

TECHNISCHE UNIVERSITÄT MÜNCHEN

Physik-Department
Lehrstuhl für Funktionelle Materialien

Dual Thermo-Responsive Diblock Copolymer Thin Films

Lucas P. Kreuzer, M. Sc.

Vollständiger Abdruck der von der Fakultät für Physik der Technischen Universität München zur Erlangung des akademischen Grades eines

Doktors der Naturwissenschaften (Dr. rer. nat.)

genehmigten Dissertation.

Vorsitzender: Prof. Dr. Martin Zacharias

Prüfer der Dissertation: 1. Prof. Dr. Peter Müller-Buschbaum
2. Prof. Dr. Friedrich C. Simmel

Die Dissertation wurde am 09.06.2021 bei der Technischen Universität München eingereicht und durch die Fakultät für Physik am 22.07.2021 angenommen.

Abstract

The behavior of dual thermo-responsive diblock copolymer (DBC) thin films in changing environmental conditions is investigated. The DBCs consist of a zwitterionic poly(sulfo betaine) (PSB) and a nonionic poly(acrylamide) (PAM) block. Systematical studies are performed that investigate how external stimuli, including temperature, the composition of the surrounding vapor, and the salt content within the films, affect the thin-film behavior, regarding its thickness, solvent uptake and release, polymer-polymer, and polymer-solvent interactions. For this purpose, mainly neutron scattering techniques and infrared spectroscopy are used. To enable these scientific studies, a sample environment for *in-situ* thin film experiments, providing precise control of the environmental surrounding, is developed and realized.

Zusammenfassung

Das Verhalten von dual thermo-responsiven dünnen Diblock Copolymerfilmen (DBC) wird in wechselnden Umgebungsbedingungen untersucht. Das DBC besteht aus einem zwitter-ionischem Poly(sulfo betain) (PSB) und einem nicht-ionischem Poly(akrylamid) (PAM) Block. In systematischen Studien wird der Effekt von externen Stimuli wie der Temperatur, der Zusammensetzung der Umgebungsatmosphäre, und des Salzgehalts in den Filmen, auf das Filmverhalten, mit Blick auf Filmdicke, Lösungsmittelgehalt, sowie Polymer-Polymer und Polymer-Lösungsmittel Wechselwirkungen, erforscht. Dazu werden hauptsächlich Neutronenstreuungsmethoden und Infrarotspektroskopie verwendet. Für die wissenschaftlichen Untersuchungen, wird eine flexible Probenumgebung entwickelt und realisiert, welche eine präzise Einstellung der Umgebung der dünnen Filme sicherstellt.

Contents

Abstract	i
List of abbreviations	vii
1. Introduction	1
2. Theoretical background	5
2.1. Phase behavior of diblock copolymers	5
2.1.1. Diblock copolymers in solution	9
2.1.2. Swelling behavior of polymer thin films	11
2.2. Stimuli-responsive polymers	14
2.2.1. Thermo-responsive polymers	15
2.2.2. Co-nonsolvency effect	21
2.3. Basics concepts of neutron scattering	23
2.3.1. Specular reflection (or neutron reflectivity)	26
2.3.2. Diffuse scattering	31
2.3.3. Time-of-flight mode	34
3. Thin film characterization	37
3.1. Structural characterization in real space	38
3.2. Structural characterization in reciprocal space	41
3.3. Spectroscopic characterization	46
3.4. Sample environments	51
3.4.1. Pre-existing experimental setup	51
3.4.2. 'FlexiProb' sample environment	54
4. Thin film preparation	59
4.1. Materials	59
4.2. Functional polymers	61
4.3. Si substrate and pre-deposition treatment	66
4.4. Thin film preparation	68

5. Isotope-sensitive thin film swelling and exchange kinetics	73
5.1. Investigation of the equilibrated thin film states	76
5.2. Swelling behavior	79
5.3. Exchange behavior	89
5.4. Conclusion	99
6. Co-nonsolvency effect in polymer thin films	101
6.1. PSPE and PNIPMAM thin films in mixed water/methanol vapor	104
6.2. Conclusion I	112
6.3. PSPE- <i>b</i> -PNIPMAM thin films in mixed water/methanol vapor	114
6.3.1. Investigation of the equilibrium states	116
6.3.2. Thin film behavior upon water swelling and methanol exchange	121
6.4. Conclusion II	131
7. Phase transition kinetics of orthogonally dual thermo-responsive thin films	133
7.1. Investigation of the equilibrated thin film states	136
7.2. Swelling behavior	139
7.3. Phase transition behavior	147
7.4. Temperature-dependent thin film morphology	154
7.5. Conclusion	160
8. Temperature-dependent cyclic thin film swelling and drying kinetics	163
8.1. Comparability of the equilibrated swollen and dry thin film states	165
8.2. Temperature-dependent cyclic swelling behavior	170
8.3. Temperature-dependent cyclic drying behavior	181
8.4. Conclusion	185
9. Thermal behavior of 'salty' thin films	187
9.1. Investigation of the equilibrated thin film states	189
9.2. Salt-dependent swelling and phase transition behavior	194
9.3. Conclusion	205
10. Summary and outlook	207
A. Appendix for Chapter 1	213
B. Appendix for Chapter 2	215
C. Appendix for Chapter 3	223

D. Appendix for Chapter 4	225
E. Appendix for Chapter 5	229
Bibliography	237
List of publications	267
Acknowledgements	279

List of abbreviations

AFM	atomic force microscope
APE	antipolyelectrolyte effect
BCP	block copolymer
cmc	critical micelle concentration
cmt	critical micelle temperature
CP	cloud point
CP'	clearing point
DBC	diblock copolymer
DC	drop-casting
DPDAK	directly programmable data analysis kit
DWBA	distorted-wave Born approximation
EIA	effective interface approximation
ESS	European Spallation Source
FRM II	Forschungsreaktor München II
FTIR	fourier-transform infrared spectroscopy
GFM	gasflow meter
GFS	gasflow system
GISANS	grazing-incidence small-angle neutron scattering
HLC	horizontal line cuts
ILL	Institut Laue-Langevin

IR	infra-red
ISIS	ISIS Neutron and Muon Source
IUPAC	International Union of Pure and Applied Chemistry
KWS-1	Kleinwinkelstreuapparatur
LCST	lower critical solution temperature
LMA	local monodisperse approximation
MLZ	Heinz Maier-Leibnitz Zentrum
NMC	neutron measurement chamber
NMR	nuclear magnetic resonance
NR	neutron reflectivity
ODT	order-to-disorder transition
OM	optical microscope
OOT	order-order transition
PAM	poly(acrylamide)
PCB	flexible printed circuit board
PID	proportion-integral-derivative
PMMA	poly(methyl methacrylate)
PNIPAM	poly(<i>N</i> -isopropylacrylamide)
PNIPMAM	poly(<i>N</i> -isopropylmethacrylamide)
PS	poly(styrene)
PSB	poly(sulfobetaine)
PTFE	poly(tetrafluoroethylene)
SANS	small angle neutron scattering
SC	spin-coating

List of abbreviations

SDD	sample-detector-distance
SKADI	small-K advanced diffractometer
SLD _N	neutron scattering length density
SLD _X	x-ray scattering length density
SLM	selective laser melting
SR	spectral reflectance
SVA	solvent vapor annealing
ToF	time-of-flight
UCST	upper critical solution temperature
UV	ultra-violet
vis	visible
VLC	vertical line cuts
XRR	x-ray reflectivity

1. Introduction

Selective, responsive, reversible. These are the essentials of a material that is referred to as smart or intelligent. In nature these properties are combined in perfection: To sustain life, nature develops selectively-tailored building blocks that inherit specific chemical and physical functions. These are able to change (reversibly) as response toward an external stimulus [1]. The mimicry of nature's behavior in synthetic polymer systems enables a most diverse application field ranging from artificial muscles [2, 3], over controlled drug delivery and release systems [4-6], to responsive surfaces and coatings [7-12].

Stimuli-responsive polymers are capable of responding to a modified chemical and physical environment or to external stimuli by changing their polymer properties, *e.g.*, solubility, viscosity, conductivity, or color [1, 13]. The response is reversible, hence the polymer returns to its initial state, once a counter-stimuli is applied (heating/cooling or light on/off). These polymers impress with their versatility and a diverse range of polymers responsive to external stimuli such as temperature [14], pH [15], electric and magnetic fields [16, 17] or the addition of small molecules [18] has been synthesized and analyzed. Furthermore, the individual response is highly tunable by adjusting *e.g.*, the molecular weight, polymer architecture or tacticity.

Among the multiplicity of responses to the stimuli described above, the response to temperature is the most studied one. Thermo-responsive polymers feature a miscibility gap, meaning they are insoluble above [8, 19] or below a critical temperature [20-23]. The lower critical solution temperature (LCST) and the upper critical solution temperature (UCST) are the lowest and highest temperatures, respectively, at which a demixing occurs. Suited homopolymers featuring a different response to the same stimulus, here an LCST- and UCST-type homopolymer, can be combined to an orthogonally dual thermo-responsive diblock copolymer (DBC) [24, 25]. In aqueous solution, they are able to self-assemble into micellar structures with a hydrophobic core and a hydrophilic shell. Upon temperature change, the micellar structure can be inverted, *i.e.*, the hydrophobic core becomes the hydrophilic shell and vice versa. Dependent on the relative positions of the respective clearing and cloud points (CP'_{UCST} and CP_{LCST}), the DBC passes through an insoluble or a molecularly dissolved intermediate regime [26, 27]. This behavior is called 'schizophrenic' and the unique structure inversion is of high interest for (smart) emulsification and the release of hydrophobic solubilizates [28-30]. Schizophrenic DBCs

systems can even be further tuned by gaining control over CP'_{UCST} and CP_{LCST} . In recent studies, this was done by introducing a second external stimulus, *e.g.*, the addition of small molecules such as salts or organic co-solvents (methanol, ethanol or acetone), or by adjusting polymer-specific parameters, such as molar mass, polymer block ratio, or polymer architecture [26, 27, 31–34]. Naturally, the combination of two (or more) stimuli-responsive polymer blocks within one system offers new possibilities, while simultaneously encounters new challenges. A higher number of external stimuli, to which the system is responsive, increases the versatility but also results in a system with narrower boundary conditions and a potential superposition of multiple stimuli. In order to avoid an interference of different stimuli, it is of high importance to design multi-responsive polymer systems, in which the individual stimuli selectively address the desired polymer blocks.

In general, stimuli-responsive polymer materials can be divided into three-dimensional (3D) systems, *e.g.*, colloids, micelles, and core-shell particles, and two-dimensional (2D) film systems, *e.g.*, thin films, brushes, layer-by-layer films, and membranes [1]. Both systems mainly differ in the respective polymer concentration. While 3D polymer materials are typically dissolved in dilute aqueous solution, a substance-rich regime is present in 2D polymer film systems. One could also describe the 3D system as polymer dissolved in water, whereas the 2D systems resembles water in a polymer matrix. So far, the behavior of (multi-) responsive polymers in diluted solution has been well-studied [1, 13, 35], however less is known once polymer concentration increases. The sample geometry, be it a polymer solution, a grafted polymer brush, or a polymer thin film, matters. Compared to solution, polymer thin films have increased interfacial areas (substrate-polymer and polymer-surrounding media), which have a strong impact on dynamic and kinetic processes such as the diffusion of a small molecules into the thin film. Furthermore, the high polymer concentration results in altered polymer-polymer and polymer-solvent interactions. Entropic effects, including confinement and chain packing, gain an increasing influence as the film thickness decreases. As a consequence, thin films show physical and mechanical properties that differ significantly from the well-studied bulk solution behavior and it is impossible to predict how an orthogonally dual thermo-responsive DBC behaves upon temperature variation in thin film geometry, from its solution behavior.

Regarding the challenges described above, the present thesis aims for a fundamental understanding of the response mechanisms of a polymer thin film system upon changing environmental parameters. The polymer system under investigation is a DBC consisting of a zwitterionic and a nonionic polymer block. Zwitterionic describes the same numbers of anionic and cationic charges within one constitutional monomer unit. In this

thesis, poly(sulfobetaine)s (PSB) are used as a zwitterionic block. Due to their zwitterionic character, a complex balance between attractive and repulsive polymer-polymer and polymer-water interactions is present, which eventually results in an UCST-type phase transition. The position of this transition is highly tunable by the addition of salt additives, but also other parameters, such as molar mass, polymer architecture, and the choice of solvent, have a considerably impact on the UCST. The nonionic block is either poly(*N*-isopropylacrylamide) (PNIPAM) or poly(*N*-isopropylmethacrylamide) (PNIPMAM). Both polymers show an LCST-type behavior, whereas the respective LCST values differ strongly, due to the additional methyl group in the backbone of PNIPMAM ($\text{LCST}_{\text{PNIPAM}} = 32\text{ }^\circ\text{C}$, $\text{LCST}_{\text{PNIPMAM}} = 44\text{ }^\circ\text{C}$).

The experimental studies in this thesis contribute to a better understanding of responsive polymer thin films, whereas every chapter focuses on individual scientific questions and challenges. Figure 1.1 schematically presents the scientific scope of the individual projects. The Chapters 5 and 6 investigate the DBC thin film system under study, in mixed vapor compositions. In particular, the role of deuterated solvents during swelling and exchange processes is of interest. In Chapter 7 the response of the DBC thin films to temperature jumps is investigated. This study focuses specifically on how the increased polymer concentration in thin film geometry affects the UCST- and LCST-type phase transitions of the individual polymer blocks. Chapter 8 analyzes the reversibility and reproducibility of thin films swelling and drying cycles at different temperatures. Regarding potential thin film applications, reversible and reliable dynamic processes are crucial. In Chapter 9, the influence of salt additives on the swelling and thermal thin film behavior is described. In this project, two external stimuli are present, temperature and salinity. The focus is on how the salt additive alters the thermal behavior of the DBC thin film and if a superposition of both stimuli is present.

Probing the response of responsive polymer thin films *in-situ* is highly challenging. While imaging techniques such as optical and atomic force microscopy offer a straightforward measurement protocol and data analysis, they are limited to the surface topography. To probe not only the thin film's surface, but also the inside, advanced neutron scattering techniques, *e.g.*, time-of-flight neutron reflectivity (ToF-NR) and grazing-incidence small-angle neutron scattering (GISANS) are used, which yield information about its swelling degree, the amount of absorbed solvent, and characteristic lateral thin film structures. Very small incident angles increase the illuminated area on the sample and thus, thin film kinetics during diffusion and exchange processes can be followed *in-situ* with high time resolution and statistical relevance. By using deuterated solvent species, excellent contrast between the polymer and the solvent is achieved, via the ToF mode, detailed information about the vertical film composition are obtained. In the present thesis, these mesoscopic

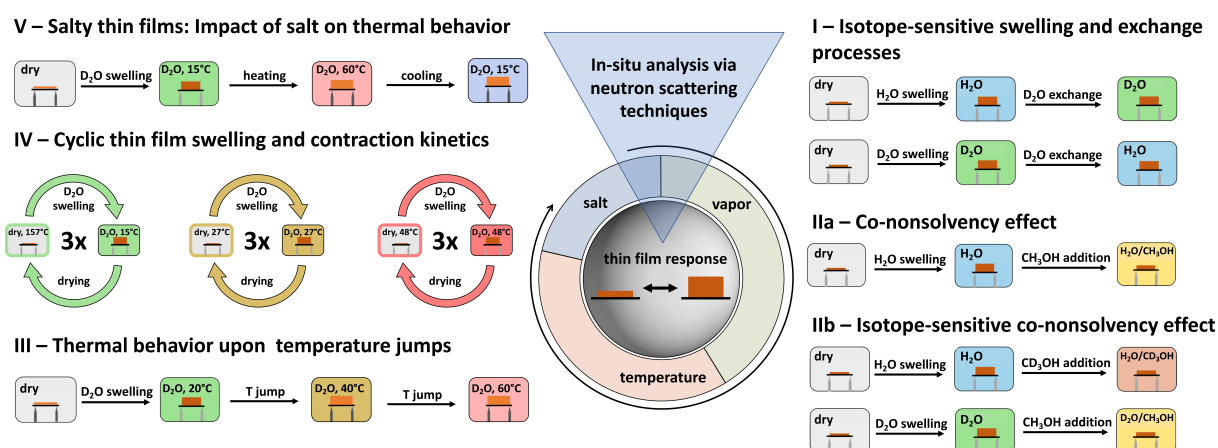


Figure 1.1.: Schematic overview of the individual research topics addressed in the present thesis. The numbers of the individual chapters are explained in the text. Adapted with permission from AMERICAN CHEMICAL SOCIETY, Copyright 2019, 2020, and 2021 [36–39].

parameters (thickness, solvent content, and 'bulk' thin film morphology) are compared to molecular information, obtained with Fourier-transform infrared spectroscopy (FTIR). The combination of scattering techniques and FTIR is highly beneficial as it enables to link molecular information to an overall thin film behavior on the mesoscale.

This introductory part is followed by Chapter 2, in which the theoretical background of DBCs in dilute solution and in thin film geometry, responsive polymers, and the principles of advanced neutron scattering techniques is provided. The Chapters 3 and 4 describe the used measurement techniques, the used materials, and the thin film preparation protocols. The scientific results are discussed in the Chapters 5 to 9. Finally, all findings obtained in this thesis are put into context in Chapter 10, thus answering the above posted questions. Based on this summary, an outlook for future research projects is given in the end, which aims to stimulate and inspire a future generation of open-minded and motivated scientists to work in the field of responsive 3D and 2D polymer materials.

2. Theoretical background

This chapter provides the theoretical principles of diblock copolymers (DBC) and stimuli-responsive polymer, which will be helpful to understand how such materials behave in non-constant environments. The first part, Section 2.1, describes the solution behavior of DBCs and the swelling behavior of DBC thin films. Section 2.2 introduces stimuli-responsive polymers, in solution and in thin film geometry. The last Section 2.3 addresses the basics of neutron scattering.

2.1. Phase behavior of diblock copolymers

Block copolymers (BCPs) consist of two or more polymer blocks that are made from chemically distinct repeating units [40, 41]. The blocks are covalently bound to each other, thereby forming various polymer architectures dependent on the number of blocks and on the type of connection, *i.e.*, linear, ring-shaped, star-shaped, or grafted. This thesis investigates BCPs with two polymer blocks, thus they have a linear architecture and are referred to as diblock copolymers (DBC). Figure 2.1 shows a simple linear DBC, which is made from block A and block B. Its nomenclature follows the guidelines of the International Union of Pure and Applied Chemistry (IUPAC): poly(A)-*block*-poly(B), or simply PA-*b*-PB.

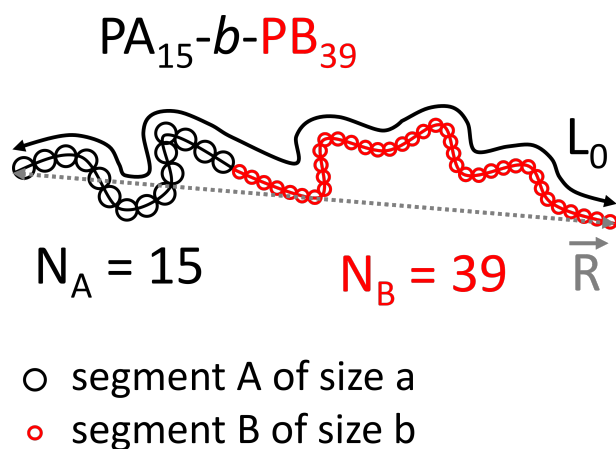


Figure 2.1: Schematic representation of a linear diblock copolymer. The two polymer blocks A and B with corresponding monomer segment sizes a and b are indicated as black and red open circles. The end-to-end distance-vector \vec{R} and the contour length L_0 are marked with a dashed gray and a continuous black arrow, respectively.

The DBC can be described accurately with the following characteristic properties: The polymers degree of polymerization N , which gives the number of repeating units (or segments) within one polymer block. For a linear DBC, N is the sum of all polymer segments in block A and B, which is denoted N_A and N_B , respectively. The block ratio r_a is calculated according to the following equation.

$$r_a = \frac{N_A}{N_A + N_B} \quad (2.1)$$

The molar mass describes the polymer weight. One distinguishes between the number average molar mass M_n , the weight average molar mass M_w , and the centrifugal average molar mass M_z (often denoted as Z -average). In the framework of this thesis only the first two molar masses are used, which are calculated for PA-*b*-PB according to the following equations.

$$M_n = \frac{\sum n_i M_i}{\sum n_i} = \frac{(n_A M_A) + (n_B M_B)}{n_A + n_B} \quad (2.2)$$

$$M_w = \frac{\sum n_i M_i^2}{\sum w_i} = \frac{(w_A M_A^2) + (w_B M_B^2)}{w_A + w_B} \quad (2.3)$$

The number and weight of the respective monomers A and B are denoted with n_i and w_i , respectively, while M_i is the molar mass of the respective monomers. Not all polymers are of equal length and molar mass, but show a certain distribution, thus M_n and M_w represent the average molar masses. The width of the distribution is described by the polydispersity index \mathcal{D} .

$$\mathcal{D} = \frac{M_w}{M_n} \geq 1 \quad (2.4)$$

Different polymerization techniques yield different \mathcal{D} values. The commonly used free radical polymerization yields a rather broad size distribution, resulting in higher \mathcal{D} values, while certain techniques, such as controlled or living polymerization, achieve very narrow distributions with \mathcal{D} values close to 1. The volume fraction f_A of polymer block A is calculated by dividing the molecular weights $M_w(A)$ and the mass density ρ_A of block A with the sum of the molecular weights and densities of all polymer blocks.

$$f_A = \frac{M_w(A)}{\rho_A} \left(\sum \frac{M_w(i)}{\rho_i} \right) \quad (2.5)$$

The contour length L_0 , which is the sum of the corresponding lengths b_i of all monomers, gives the total length of the polymer chain.

$$L_0 = \sum N_i b_i \quad (2.6)$$

While the contour length is the theoretical length of the polymer chain in its fully elongated state, the polymer chain usually is coiled and not in its most stretched state. Therefore, typically the radius of gyration R_g is given, which describes the polymer chain by the distance vectors \vec{s}_i of the polymer segments to the center of mass of the polymer chain.

Phase behavior of homopolymer and DBC melts

In general, mixing of two chemically different homopolymers is energetically not favored, and a system of two or more homopolymers tends to minimize its energy by decreasing interfacial areas. In consequence, macrophase separation occurs, which is usually in the order of several micrometers [42]. In the case of a DBC, interfacial areas are also decreased, however, due to the covalently bound polymer blocks, the phase separation occurs on a much smaller scale and is therefore referred to as micro-phase separation. The resulting domain sizes (typically 10 - 100 nm) can be tuned by adjusting the lengths and the volume fractions f_i of the corresponding polymer blocks.

The Flory-Huggins solution theory describes the miscibility of two homopolymers or the interactions of two polymer blocks in a DBC. The interaction between the segments i and j of a DBC can be quantified by the interaction parameter χ_{ij} [43, 44], which is defined according to the following equation.

$$\chi_{ij} = \frac{z}{k_B T} \left(\epsilon_{ij} - \frac{\epsilon_{ii} + \epsilon_{jj}}{2} \right) \quad (2.7)$$

Here, z is the coordination number, k_B is the constant of Boltzmann, T is the temperature, and ϵ_{ij} , ϵ_{ii} , and ϵ_{jj} are the respective contact energies between segment i and j . For simplification χ_{ij} will be written as χ in the following. A further definition of χ , as a parameter of the free energy, was found empirically [45].

$$\chi = \chi_S \frac{\chi_H}{k_B T} \quad (2.8)$$

An entropic term χ_S and a temperature-dependent enthalpic term χ_H contribute to χ . For negative χ values, the interaction between two homopolymers, or two polymer blocks in a DBC, respectively, is favored, which results in one homogeneous phase. In contrast, positive χ values indicate unfavored polymer interactions and thus a demixing (or microphase separation in case of DBCs) occur. The polymer conformation and the distance between the chain ends contribute to the entropic χ_S part. Since the end-to-end distance is larger for DBC than for the corresponding homopolymers, the entropic part is more significant for DBCs [42]. Therefore, also the values of their interaction parameters are higher, which means that microphase separation of a DBC is more likely to

occur than macroscopic phase separation of homopolymers. With increasing temperature, the enthalpic contribution χ_H becomes smaller, thus a high temperature counteracts microphase separation and favors miscibility. The phase behavior of a homopolymer blend or of a DBC can also be described by the free energy of mixing ΔG_{mix} .

$$\Delta G_{mix} = k_B T n \left(\frac{f_A}{N_A} \ln f_A + \frac{f_B}{N_B} \ln f_B + \chi f_A f_B \right) \quad (2.9)$$

The number of moles of a polymer is n . From the right side of the equation, the first two terms contribute entropically, while the third term contributes enthalpically to the free mixing energy. The entropic part scales with N^{-1} , the enthalpic part with χ , and therefore the free mixing energy and the phase behavior depend on the product of $N\chi$. For very small, or negative $N\chi$ values, mixing is favored. If $N\chi$ exceeds a critical threshold $(N\chi)_c$, macro- or microphase separation occurs. It should be mentioned, that due to the covalent bonds between both polymer blocks in a DBC, the Flory-Huggins theory is not able to fully describe the phase behavior and the occurring microphase separation.

For DBCs, the critical $(N\chi)_c$ value is around 10.5, which leads to the following characteristic segregation regimes [40]. For $N\chi < (N\chi)_c$, the interaction between polymer block A and B is favored, they intermix into a single-phase, and microphase separation is prevented. In this mixed, disordered phase, monomer concentration fluctuations are present, due to the covalent connections between block A and B [40, 46]. For larger $N\chi$ values close to 10.5, the blocks spontaneously phase separate and the segregated block domains form an ordered phase. As $N\chi$ is dependent on the temperature, this point is also referred to as the order-to-disorder transition (ODT) temperature. For $N\chi \approx (N\chi)_{ODT}$ the so-called weak segregation limit (WSL) is approached and the DBC slowly transits from a disordered to an ordered, micro-phase separated phase, where the different blocks A and B are still partly intermixed at the arising interfaces. For $N\chi \gg (N\chi)_{ODT}$ the strong segregation limit (SSL) is reached and the polymer blocks fully separate. In contrast to the weak segregation, the interfaces are well defined and barely intermixed [40, 42, 46].

The microphase separation results in different morphologies, dependent on $N\chi$ values and the volume fractions of the polymer blocks, f_A and f_B . These morphologies can be predicted according to the mean-field calculations by Bates et al. [40] and Leibler [46]. The resulting DBC structures are formed by the minority block, embedded in a matrix of the majority block. While experimental studies confirm these theoretical calculations, one has to note that the chemical difference of the monomers A and B results in asymmetric phase diagrams. Various effects, *e.g.*, deviations in polymer chain conformation of both polymer blocks A and B, crystallization, and polymer confinement, in particular present in thin film geometry, further intensify the asymmetry of the phase diagrams.

2.1.1. Diblock copolymers in solution

The previous section describes the phase behavior of homopolymers and DBCs melts, while in the following, DBCs in solution are described. Dependent on the polymer concentration of the solution, the DBC behavior differs.

Diblock copolymers in dilute solutions

In dilute solutions, polymer chains form random coils with an end-to-end distance R_{ee} of

$$\langle R_{ee} \rangle \simeq bN^{3/5} \quad (2.10)$$

and a radius of gyration R_g of

$$\langle R_g \rangle = \frac{\langle R_{ee} \rangle}{\sqrt{6}} . \quad (2.11)$$

The polymer chains are isolated and interactions between them occur only during brief times of encounter. This changes, when the polymer concentration increases. Figure 2.2 indicates a critical concentration ϕ_{c*} , at which the polymer molecules become closely packed and start to interpenetrate. This regime is called a semi-dilute solution. In concentrated solutions, with polymer concentrations above ϕ_{c**} , all polymer chains overlap with each other and space is strongly limited. Teraoka found that for good solvents, the transitions typically occur at ϕ_{c*} of 0.01 and ϕ_{c**} of 0.2 - 0.3 [47]. In poor solvents, the polymer collapses into globules and precipitates. These thermodynamic processes can be described by the Flory-Huggins theory, analogously to a homopolymer blend, which is described earlier (cf. Equation 2.9).

$$\Delta G_{mix} = k_B T n \left(\frac{\phi_P}{N} \ln \phi_P + (1 - \phi_P) \ln(1 - \phi_P) + \chi_{PS} \phi_P (1 - \phi_P) \right) \quad (2.12)$$

Here, χ_{PS} represents polymer-solvent interactions. For χ_{PS} values below 0.5, the solvent is a good solvent, for values above 0.5, it becomes a bad solvent. At $\chi_{PS} = 0.5$, the solvent is a so-called theta solvent, *i.e.*, the polymer chains behave as ideal chains without any volume effects [47]. In the case of DBCs, the solvent can be further classified as non-selective and selective, with respect to the solubility of the individual polymer blocks. If the solubility of both blocks is equally good or bad, the solvent is called non-selective. In contrast, for a deviating solubility of the blocks, the solvent is called a selective solvent. A well-studied class of DBCs, for which water is a selective solvent, are amphiphilic DBCs, which consist of a hydrophobic and a hydrophilic part. In an aqueous solution, below a certain polymer concentration, called the critical micelle concentration (cmc), they are molecularly dissolved as unimers. By increasing the polymer concentration above the cmc

the polymer chains self-assemble into micellar structures, while the concentration of dissolved unimers remains constant [48, 49]. The hydrophobic part of the amphiphilic DBC is in a collapsed state and forms the micelle core, the hydrophilic part is fully hydrated and forms the micellar shell. The free energy of the micellar structure is dependent on the interactions of the polymer blocks with each other and with the solvent. As these interactions are dependent on the temperature, the formation of micelles at a given polymer concentration can also be induced by temperature, which is referred to as critical micelle temperature (cmt).

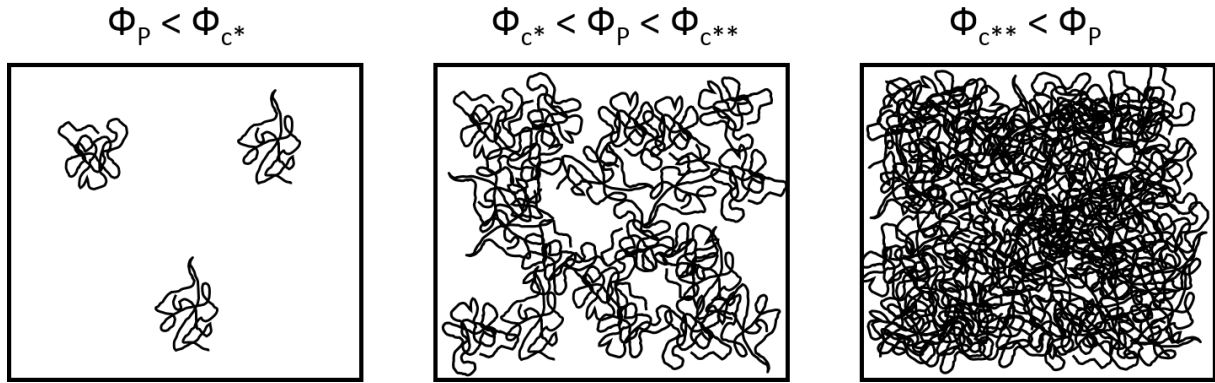


Figure 2.2.: Dilute, semi-dilute, and concentrated polymer solution. The critical polymer concentration ϕ_{c^*} divides the dilute (left) from the semidilute solution (center). Above a concentration solution limit $\phi_{c^{**}}$ the solution is called concentrated (right).

Concentrated solution and thin film geometry

With increasing polymer concentration, interactions between block A and B become more dominant, which strongly influences the solution and self-assembly behavior of a DBC. The behavior is described by the effective interaction parameter χ_{eff} , which depends on the polymer concentration as well as on the nature of the solvent. Ideal selective solvents diffuse exclusively in one specific polymer block, which leads to an increase in the volume fraction, and eventually enables an order-order transition (OOT) [50]. Thus, ordered spheres, may become cylinders and even lamellae during a selective swelling. Upon mixing, most solvents induce a plasticization of the polymer block or blocks, which means the respective glass temperature T_g is decreased [51]. As a result, disorder is favored and the temperature range of a glassy polymer state is diminished upon diluting the DBC solution.

The control over structure, mobility, and self-assembly behavior of DBCs via the addition of a solvent is exploited during solvent vapor annealing (SVA). This technique is commonly used for thin films. The DBC is exposed to a saturated solvent vapor and typically undergoes a swelling and plasticization. The polymer chain mobility increases, which eventually leads to a healing of structural defects and removal of kinetically frozen polymers (for non-selective solvents), or even to highly ordered morphologies (for selective solvents). Literature provides numerous examples of the SVA technique applied to DBCs [50, 52-57].

2.1.2. Swelling behavior of polymer thin films

In thin films, the polymer concentration is even further increased. While a dilute polymer solution can be seen as a polymer in a water matrix, a thin film is rather water molecules within a polymer matrix, and polymer-polymer interactions become more dominant. In the following, the swelling of a polymer thin film in a saturated vapor is described. Please note, that the sample system now changed from a polymer in solution to a polymer thin film in a vapor phase. All performed experimental studies, described in the Chapters [5] to [9], involve thin film swelling, and therefore, the theoretical basis required for the evaluation of a swelling behavior, is provided here. Furthermore, the theory is supported with a practical outline of the applied evaluation routine.

Swelling of a thin film occurs, when solvent molecules, usually a good solvent for at least one block of the DBC, diffuse into the thin film. The miscibility is described by the interaction parameter χ according to the Flory-Huggins solution theory. Typically, the diffusion process is driven by the osmotic pressure, and is accompanied by thickening and, as described above, plasticization of the polymer thin film [58-60]. Due to adhesive forces between the substrate and the polymer, the thin film swells mainly in the direction along the surface normal. In the present thesis, the swelling, *i.e.*, the measured film thickness normalized to its initial thickness, referred to as swelling ratio d/d_{ini} , is followed by neutron reflectometry (NR), and spectral reflectance (SR) *in-situ*. Other techniques, such as x-ray reflectivity, are also capable of determining the thin film thickness.

In particular NR is a suited technique, as it allows to follow a change in film thickness as well as a change in scattering length density (SLD) simultaneously and independently from each other. Since the latter is related to the vertical (neutron) density composition of the thin film, the incorporated solvent content and its vertical location in the film can be determined. As the SLD of organic polymers usually is low ($0.6 - 1 \times 10^{-6} \text{ \AA}^{-2}$), the selection of a solvent with a high SLD, *e.g.*, deuterated solvents (*e.g.*, $\text{SLD}_{\text{D}_2\text{O}} = 6.34$

$\times 10^{-6} \text{ \AA}^{-2}$), is beneficial for a strong contrast in the neutron scattering measurements. The amount of absorbed solvent $\Phi_S(t)$ is calculated via Equation 2.13.

$$\Phi_S(t) = \frac{SLD(t) - SLD_{ini}}{SLD_S - SLD_{ini}} \quad (2.13)$$

Here, the measured SLD at a given measurement time t , of the dry thin film, and of the pure solvents, are denoted with $SLD(t)$, SLD_{ini} , and SLD_S , respectively. Since the majority of the later presented experiments follow the swelling of a thin film in water vapor, water instead of solvent will be used in the following.

In general, the free energy of mixing results in the diffusion of water molecules into a polymer film. As explained in the previous sections, these processes were investigated experimentally and theoretically. However, for thin films, the situation is more complex. The geometrical restriction of the polymer, the increased interfacial areas (substrate-polymer and polymer-surrounding media, which in the present thesis mostly is air or saturated water vapor), and the increased polymer concentration lead to altered polymer-polymer and polymer-water interactions as compared to bulk polymers. As a consequence, diffusion and exchange processes strongly deviate from each other depending on the sample geometry [61–65]. In polymer thin films, absorbed water first fills up the accessible free volume, or simply air voids, and leads to a continuous decrease in T_g . Once these voids are filled, further water uptake results in an increase in film thickness [36, 59, 66, 67]. The swelling degree is strongly dependent on the nature of the individual polymer blocks. While hydrophilic blocks promote water uptake, the mechanical stability is poor. Introducing a glassy hydrophobic block improves mechanical stability, but hampers water uptake [68].

The thin film kinetics upon water swelling are described quantitatively with a humidity-sensitive swelling model, which was developed by Li and Tanaka [69] and further modified by Jaczewska et al. [70]. This model respects the intrinsic, diffusion-driven, swelling kinetics as well as non-constant relative humidity (RH). The swelling kinetics can be expressed according to Equation 2.14 [69–73].

$$\frac{d(t)}{d_{ini}} = \frac{d_{max}}{d_{ini}} - \left(\frac{d_{max}}{d_{ini}} - 1 \right) B \exp\left(\frac{-t}{\tau}\right) \quad (2.14)$$

The equation contains the swelling ratio d/d_{ini} , as well as the maximum swelling ratio d_{max}/d_{ini} , which expresses a theoretical limit to which the DBC thin film is able to swell at a given ambient RH. A specific time, which describes the diffusion process of water molecules into the thin film is denoted with τ . The parameter B is related to the sample geometry and ranges between 0.5 and 0.75 for thin films [69]. After an infinite swelling time t , the thin film reaches a saturated state, in which the concentration gradient of the

water molecules is in equilibrium with the water absorption. There, the thin film reaches its maximum swelling ratio d_{max}/d_{ini} .

$$\frac{d_{max}}{d_{ini}} = \frac{\frac{d(t)}{d_{ini}} - B \exp\left(\frac{-t}{\tau}\right)}{1 - B \exp\left(\frac{-t}{\tau}\right)} \quad (2.15)$$

The swelling process, in particular at later stages, is governed by the RH and the non-constant RH is taken into account via Equation 2.16 [70, 74].

$$\ln\left(\frac{\rho}{\rho_{sat}}\right) = \ln\left(1 - \frac{d_{ini}}{d_{max}}\right) + \left(1 - \frac{V_W}{V_{DBC}}\right) \frac{d_{ini}}{d_{max}} + \chi_{eff} \left(\frac{d_{ini}}{d_{max}}\right)^2 \quad (2.16)$$

The diffusion of water molecules from the vapor phase into the thin film is similar to a dissolution process of a polymer in liquid water. Equation 2.16 describes the equilibrated maximum swelling ratio at a given ambient RH according to the regular solution theory [70]. V_W and V_{DBC} are the molar volumes of water and the DBC, respectively. Typically, the volume fraction of polymers is much larger compared to the volume fraction of water, thus, the fraction ratio V_{water}/V_{DBC} effectively becomes 0 and therefore, can be neglected. From the model, the effective Flory-Huggins parameter χ_{eff} and the time τ are extracted. χ_{eff} describes the interaction of the DBC with water. One has to note, that substrate-polymer interaction are not included, and therefore, the parameter cannot be seen as an absolute Flory-Huggins parameter. As is already described earlier, the χ_{eff} parameter is a measure of the hydrophilicity of the DBC. Small values, below 0.5, indicate favored polymer-water interaction and thus, good miscibility. The time τ yields information about the timescales of the occurring dynamic processes, *e.g.*, diffusion, exchange, and deuteration processes.

The evolution of the RH and the film thickness during a typical water swelling experiment is shown in Figure 2.3. Generally, the swelling of thin films can be divided into two regimes. At early stages, the increase in RH is faster than the diffusion of water molecules into the thin film. Consequently, there, the swelling process is mainly governed by the diffusion, following Equation 2.14 and the intrinsic diffusion kinetic is the limiting factor for the swelling process. Therefore, this regime is called diffusion-limited. Note, that the maximum swelling ratio is considerably higher than the actual swelling ratio, as the ambient RH theoretically would allow for a higher swelling ratio. At later stages, the increase in RH slows down, reaches an equilibrium state, and eventually becomes the limiting parameter for the swelling process. This regime is called humidity-limited and the swelling process predominantly follows Equation 2.16.

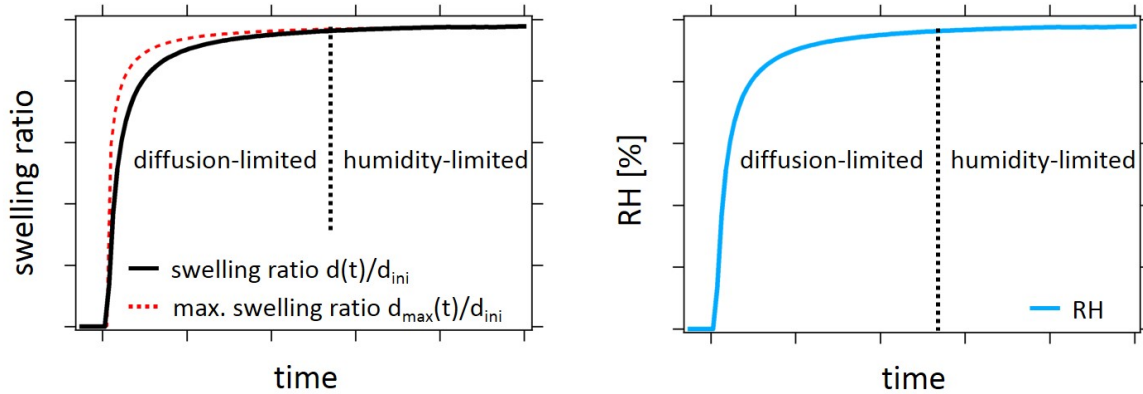


Figure 2.3.: Thin film swelling at a non-constant RH. The swelling process (left) is diffusion-limited at early stages, as the rapidly increasing RH (right) would theoretically allow for a higher maximum swelling ratio. With a decelerated RH increase, the swelling process becomes humidity-limited, and both, the maximum (dashed red line) and measured swelling ratio (black line) merge. Both regimes are divided by a vertical dashed, black line. Adapted from the dissertation of Dr. Lorenz Bießmann [75].

Since swelling occurs mainly in the direction of the surface normal, the water content Φ_{water} is linked with the increase in film thickness and can be determined according to

$$\frac{d(t)}{d_{ini}} = \frac{1}{1 - \Phi_{water}(t)} . \quad (2.17)$$

As the free volume within the thin film is filled first, and the subsequent swelling process is slightly delayed, this obtained water content is only an approximation. Still, the water content can be compared with the water content obtained experimentally via ToF-NR in order to further verify the Flory-Huggins χ_{eff} and time τ parameters.

2.2. Stimuli-responsive polymers

Stimuli-responsive polymers are able to dramatically change their properties, *e.g.*, solubility or viscoelasticity, in response to an external stimulus, including temperature, pH, electromagnetic fields, mechanical force, and chemicals [1, 13, 76–79]. By applying such stimuli, the polymer chain changes its chain conformation, *i.e.*, an initial random coil either collapses or elongates. Also a cleavage of chemical bonds is possible. One possibility to govern the self-assembly behavior in DBC, is to change the solubility of one or both blocks via an external stimulus. The resulting reversible structure control is a highly desired characteristic in numerous biomedical applications [80–82], responsive thin films and surface coatings [83–86], and in artificial muscles and pumps in soft robotics

[2, 3, 87-90]. Since all polymers are sensitive toward temperature, it is the most studied stimulus, while it is also easy to apply and to reverse.

2.2.1. Thermo-responsive polymers

Thermo-responsive polymers undergo abrupt changes in their chain conformation at a specific temperature [1, 76, 77, 91-93]. Generally, there are two types of thermo-responsive polymers, that phase separate from solution either upon heating or upon cooling. Below the lower critical solution temperature (LCST) and above the upper critical solution temperature (UCST), the polymer is miscible with a certain solvent. Consequently, the isobaric phase diagrams of the LCST- and UCST-type polymers, which typically display the temperature as a function of the polymer concentration, feature a miscibility gap, below the UCST and above the LCST. A schematic representation of such phase diagram is given in Figure 2.4.

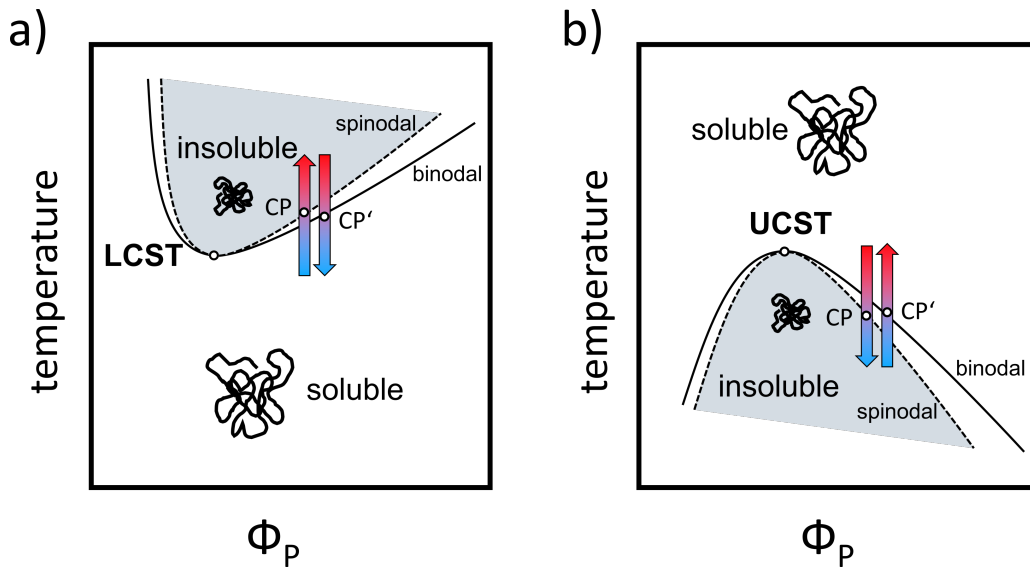


Figure 2.4.: Temperature-concentration phase diagrams of thermo-responsive polymers.

The (a) LCST and (b) UCST-type polymers feature a soluble and insoluble phase, separated by the spinodal (dashed black line) and binodal (black line). The concentration-dependent transitions between the soluble and the insoluble phase are marked with colored arrows. CP and CP' mark the cloud and clearing point, respectively. The LCST and UCST are labelled accordingly.

The binodal and spinodal curves separate the homogeneous one-phase and the heterogeneous two-phase regime from each other. In-between them a metastable regime exists. The UCST and LCST are the respective maximum or minimum of both, the binodal and the spinodal. Therefore, they are only observed at one distinct critical polymer concen-

tration. At concentrations below or above the critical polymer concentration, the phase transition occurs at the phase transition temperature. Once the solvent changes from a good to a bad solvent, the polymer chains undergo a coil-to-globule transition and form collapsed globules, which aggregate into particle clusters due to favored polymer-polymer interactions. For LCST-type polymers, this transition occurs upon heating, while UCST-type polymers undergo a coil-to-globule transition upon cooling. The formation of these polymer aggregates can be seen by the naked eye as the solution turns cloudy and turbid and the temperature, at which this happens is commonly referred to as cloud point CP. By reversing the temperature stimulus, the solution turns transparent at a certain temperature, which is called clearing point CP'. One has to note, the cloud and clearing point do not match with the phase transition temperatures, due to kinetic hindrance and aging effects in the collapsed polymer state. Furthermore, the CP upon heating and the CP' upon cooling show a certain offset, which is named hysteresis [94].

Thermodynamically, the phase separation can be understood as a balance between enthalpic and entropic contributions to the free energy, which is based on the Legendre transformation of the Gibbs equation.

$$\Delta G_{mix} = \Delta H_{mix} - T\Delta S_{mix} \quad (2.18)$$

ΔH_{mix} is the mixing enthalpy, ΔS_{mix} is the mixing entropy. This equation is already seen earlier in this chapter, in Equations [2.9] and [2.12], which described the mixing energy for DBCs blends and DBCs in dilute solution. If a polymer is soluble or not in a certain solvent is indicated by the sign of ΔG_{mix} . Thus, the solubility of a polymer can be described by four different scenarios, presupposed ΔH_{mix} and ΔS_{mix} are independent of temperature [95].

For a negative ΔH_{mix} and a positive ΔS_{mix} term, the polymer is soluble at all temperatures. In contrast, for a positive ΔH_{mix} but a negative ΔS_{mix} term, the polymer is insoluble at all temperatures. These two scenarios describe a non-thermo-responsive polymer. Once ΔH_{mix} and ΔS_{mix} are both negative or both positive, the sign of ΔG_{mix} will be determined by temperature. If both terms are negative, the sign of ΔG_{mix} will switch from negative to positive at a critical temperature T_c .

$$T_c = \frac{\Delta H_{mix}}{\Delta S_{mix}} \quad (2.19)$$

This corresponds to an UCST-type behavior, as the polymer becomes soluble at temperatures above T_c . Accordingly, the opposite case, where both ΔH_{mix} and ΔS_{mix} are positive, describes a LCST-behavior. At temperatures below T_c , the sign of ΔG_{mix} is negative and the polymer is soluble. The sign of ΔG_{mix} and therefore, the solubility of

2.2. Stimuli-responsive polymers

the polymer changes, once the temperature exceeds T_c . All scenarios are summarized in Table 2.1

Table 2.1.: Thermodynamic contributions of ΔH_{mix} , ΔS_{mix} , and ΔG_{mix} , and the resulting solubility of a polymer-solvent mixture [95].

scenario	ΔH_{mix}	ΔS_{mix}	ΔG_{mix}	solubility	polymer-type
I	+	+	- ($T > T_c$)	soluble	UCST
			+ ($T < T_c$)	insoluble	
II	+	-	+	insoluble	insoluble
III	-	-	+ ($T > T_c$)	insoluble	LCST
			- ($T < T_c$)	soluble	
IV	-	+	-	soluble	soluble

The complexity of the phase behavior of polymer solutions often exceeds the predictions of the Flory-Huggins theory. A non-zero volume change of mixing as well as non-constant free volumes for the polymer and the solvent are not taken into account. Furthermore, the solvent nature is neglected and ΔS_{mix} is considered to be fully combinatorial. As a consequence, ΔS_{mix} would always be positive, which stands in strong contrast to the experimentally observed LCST-type behavior.

In particular, hydrophobic interactions, but also hydrogen bonding and ionic interactions play a non-negligible role. Hydrophobic hydration is especially observed in aqueous solutions, which decreases the entropy of water upon mixing and eventually might outperform the combinatorial part of ΔS_{mix} . One should note here, a theoretical description of the solution behavior of, in particular LCST-type polymers, is still missing.

In aqueous solutions of polymers, commonly a thermo-responsive LCST-type behavior is observed [19]. The UCST-type behavior is mostly found in organic solvents, while only very rare polymer types show such behavior in aqueous solution [22, 96]. Since throughout the present thesis water is mainly used as solvent, the following sections focus on thermo-responsive DBCs in aqueous solution, or on thin films surrounded by water vapor.

DBC with only one thermo-responsive polymer block, exhibit two potential types of transition [25], which are both sketched in Figure 2.5a [1, 7, 30, 97-99]. During the first type, a fully hydrophilic and water-soluble DBC forms an amphiphilic DBC (transition I to II/II'), while the second type includes the transition of amphiphilic DBC to a fully hydrophobic and water-insoluble DBC (transition II/II' to III). Both transition types are induced by crossing the CP_{LCST} and CP'_{UCST} , respectively, and are fully reversible.

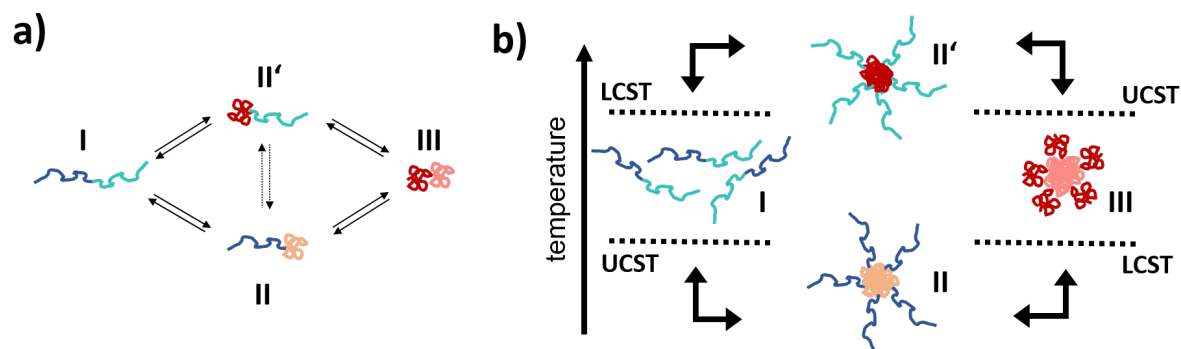


Figure 2.5.: Transition scenarios for orthogonally dual thermo-responsive DBCs. (a) The transition sequence from regime I-II/II'-III represents cumulative switching, while the sequences II-I-II' and II-III-II' stand for schizophrenic switching behavior. Furthermore, simultaneous switching between regime II and II' is possible. Blue and red colors indicate water-soluble and water-insoluble polymer blocks of the DBC. (b) The dashed black lines indicate the clearing point of the UCST-type block (CP'_{UCST}) and the cloud point of the LCST-type block (CP_{LCST}). The resulting four regimes I, II, II', and III correspond to the regimes in (a). Structural inversion is realized via regime I ($CP_{LCST} > CP'_{UCST}$) or III ($CP_{LCST} < CP'_{UCST}$).

In contrast to these single thermo-responsive DBCs, orthogonally dual thermo-responsive DBC, *i.e.*, an LCST-type and an UCST-type polymer block, feature a much more complex phase behavior [100–103]. In addition to the above-mentioned transitions, different transition sequences occur, which differ fundamentally from each other (Figure 2.5b). Either the soluble-insoluble transitions of both blocks occur cumulatively [104, 105], which corresponds to transition I - II/II' - III. Or the respective soluble-insoluble transitions of the individual blocks are counteracting each other [106–108], resulting in a transition II - I - II' or II - III - II'. In the latter transition sequence, the roles of the hydrophilic and hydrophobic polymer blocks are inverted, which is often referred to as 'schizophrenic' behavior [109–112]. Suited UCST- and LCST-type homopolymers can be combined to generate 'schizophrenic' DBCs. In this thesis, poly(sulfobetaine)s are used as UCST-type polymers and poly(acrylamide)s, such as poly(*N*-isopropylacrylamide) (PNIPAM) and poly(*N*-isopropylmeth acrylamide) (PNIPMAM) are used as LCST-type polymers. In the following, both polymer classes and their thermal responses are briefly introduced.

Poly(sulfobetaine)s - zwitterionic UCST-type polymers

Poly(sulfobetaine)s (PSBs) are zwitterionic polymers, which contain an anionic sulfonate and a cationic quarternary ammonium group within one constitutional repeat unit [113, 114]. The charged groups are linked via covalent bonds. Typically, the charges are dipolar species with high dipole moments, which are not electronically conjugated with

2.2. Stimuli-responsive polymers

each other [115]. The most widespread chemical structures of PSBs contain quaternary esters ('PSPE') and amides of (meth)acrylic acid ('PSPP'), as can be seen in Figure 2.6.

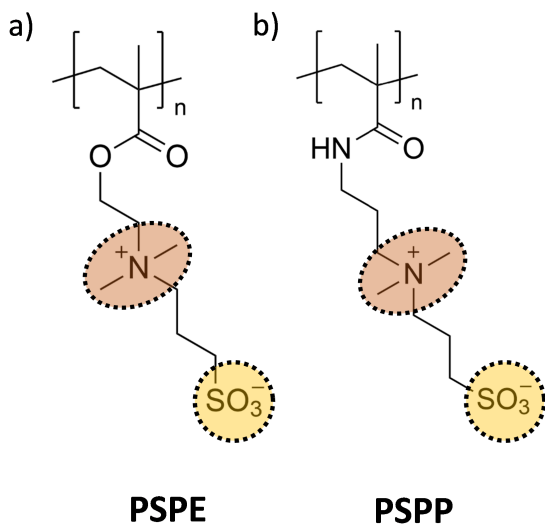
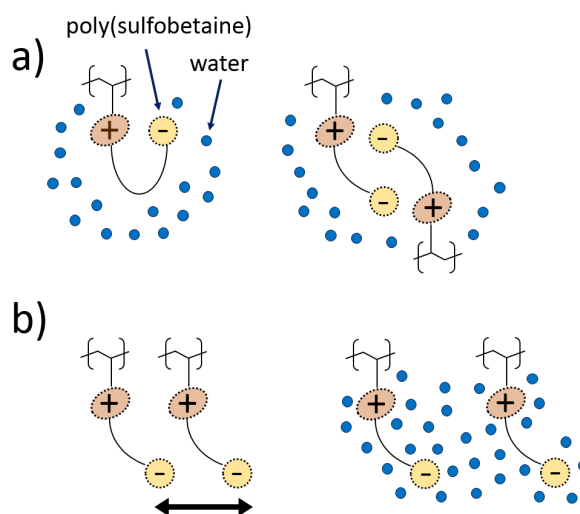


Figure 2.6: Chemical structure of poly(sulfobetaine)s. (a) Quaternary ammonium ester of methacrylic acid (PSPE) and (b) quaternary ammonium amide of methacrylic acid (PSPP). The charged groups are marked with colored circles.

Due to their high chemical stability, their structural similarity to zwitterionic phospholipids, and their electrically neutral behavior over a broad pH window, they are used for drug and gene delivery, biocompatible lubrication and antifouling materials, and as ultrafiltration membranes [116–121]. The overall net charge of PSBs is zero, which is also referred to as 'point of zero charge'. Thus the charged groups of PSBs form inner salts and attractive as well as repulsive interactions between and within individual polymer chains are present. Eventually this results in a hybrid behavior combining features of ionic and nonionic hydrophilicity. This is schematically indicated in Figure 2.7. Hence, the solubility strongly depends on the chemical nature of the ion pair and the resulting balance of interactions. While almost all PSBs are insoluble in water at low or room temperatures, many of them feature an UCST-type phase transition upon increasing temperature (cf. Figure 2.4) [106, 122, 123]. According to Equation 2.18, this transition is entropy-driven. For an aqueous solution of a low molar mass component, such UCST-type behavior is the standard behavior, however, this is rarely observed for polymer solution. Moreover, PSBs are insoluble in aprotic (chloroform, acetone, dimethyl sulfoxide) and often also in protic solvents (methanol, ethanol), while, they are mostly soluble in very polar solvents such as trifluoroethanol and hexafluoroisopropanol as well as in aqueous salt solutions [122, 124, 125].

The phase transition temperature, or the clearing point CP'_{PSB} of PSBs, is highly sensitive to molar mass, solvent isotopes, *e.g.*, $\text{H}_2\text{O}/\text{D}_2\text{O}$, polymer architecture, and in particular to the addition of salts to the solution [20, 26, 27, 36, 127–130]. In aqueous salt solution, the solubility behavior of PSBs is governed by the balance of all (non-covalent)

Figure 2.7: Interactions in zwitterionic polymers. a) attractive intra- (left) and intermolecular (right) polymer-polymer, and repulsive polymer-water interactions. b) repulsive intermolecular polymer-polymer interactions and attractive polymer-water interactions. Water molecules are indicated as blue circles. Adapted from the dissertation of Dr. Viet Hildebrand [126].



attractive and repulsive interactions. This includes added salt ions, water molecules, and polymer-polymer interactions. An enhanced solubility due to added salt is referred to as antipolyelectrolyte effect (APE) [119]. The minimal salt concentration needed for polymer dissolution is called the critical salt concentration [131, 132]. Besides the salt amount, also the nature of the salt, in particular of the anion, affects the water solubility of PSBs. In contrast, the effect of the corresponding cation is rather small [133, 134]. According to the Hofmeister series, chaotropic anions, typically large ions of low charge density (*e.g.*, Br^- , I^- , SCN^-), lead to dissolution of the polymer (salting-in effect). They induce disorder in the water structure and therefore, increase the solubility of the polymer chain. In contrast, kosmotropic anions, generally small ions of high charge density (*e.g.*, F^-) lead to precipitation (salting-out effect). They are considered to support the structure of water, in which a dissolved polymer chain is seen as a defect or a failure spot [131, 135]. To minimize the defect area, the polymer chain rearranges into a small globule and precipitates. It should be noted here that this concept considers the ions only as different sized point charges [136]. Furthermore, it is still under debate, which interaction dominates, or whether it is a combination of several or all interaction types [135, 137].

PNIPAM and PNIPMAM - nonionic LCST-type polymers

PNIPAM and PNIPMAM are nonionic polymers with an amide and an isopropyl group in their sidechains. Compared to PNIPAM, PNIPMAM has an additional methyl group in its backbone. The chemical structure of both is shown in Figure 2.8.

Typically, thermo-responsive nonionic polymers feature an LCST in aqueous solution, which is a priori driven by the enthalpy (cf. Equation 2.18). In comparison to the UCST behavior of the zwitterionic PSBs, this behavior is much more common in an aqueous solution. PNIPAM is among the most-studied thermo-responsive polymers, featuring an

2.2. Stimuli-responsive polymers

LCST of $\approx 32^\circ\text{C}$ [19, 138, 139]. The coil-to-globule transition upon heating, is attributed to changes in the number of hydrogen bonds between the PNIPAM chain and water molecules [140–142]. The transition temperature is close to the human body temperature, which makes PNIPAM a promising candidate for various biomedical applications [143–145]. In contrast, its derivative PNIPMAM features a higher LCST of $\approx 44^\circ\text{C}$. The additional methyl group on its backbone leads to a different hydration and structural behavior around the phase transition, and eventually to a higher LCST [146]. In contrast to the clearing point of PSBs (CP'_{PSB}), the cloud points of PNIPAM (CP_{PNIPMAM}) and PNIPMAM (CP_{PNIPMAM}) are rather stable and nonsensitive to parameters such as salt addition, molar mass, and solvent isotopes [19, 27, 31, 147].

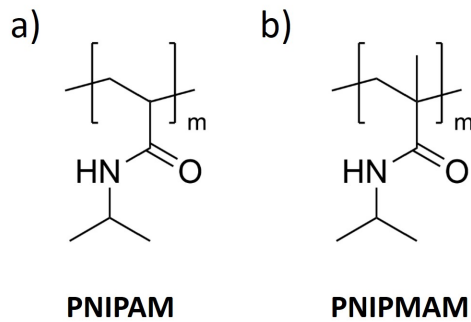


Figure 2.8: Chemical structure of poly(acrylamide)s. (a) poly(*N*-isopropylacrylamide) (PNIPAM) and (b) poly(*N*-isopropylmethacrylamide) (PNIPMAM).

2.2.2. Co-nonsolvency effect

Besides temperature, also the mixing of solvents can either decrease or increase the solvation of polymers. While most water-soluble polymers dissolve better in mixtures, which is referred to as cosolvency, some polymers feature a so-called co-nonsolvency effect. Co-nonsolvency describes the counterintuitive phenomenon that two miscible and individually good solvents for a polymer, become a poor solvent for the same polymer when mixed. For thermo-responsive LCST- and UCST-type polymers this is due to a decreased CP_{LCST} or increased CP'_{UCST} , respectively. A co-nonsolvency effect in mixtures of water and a number of organic co-solvents, *e.g.*, ethanol, methanol, and acetone, has been reported for various polymers, typically poly(acrylamide)s, and in particular for PNIPAM [32–34, 92, 148–150]. The first studies about a co-nonsolvency effect of PNIPAM in mixtures of water and methanol date back to the early 1990s [91, 150]. Since then, the research on co-nonsolvency has extended to more complex systems, such as diblock copolymer micelles [151], polyelectrolytes [152, 153], crosslinked microgels [154, 155], and grafted polymer brushes [156–158]. The increasing scientific attention resulted in various applications, *e.g.*, force actuation [159], the detection of volatile organic compounds [160], the capture and release of nanoparticles [161, 162], friction tuning [163], and the selective

precipitation of biomacromolecules, such as DNA [164]. While all these studies and applications focus on the co-nonsolvency effect of polymers in solution, it was shown recently, that homopolymer and DBC thin films feature a co-nonsolvency effect in a mixed solvent vapor phase [39, 165, 166]. The behavior can be explained by a decreased volume phase transition temperature (VPTT), the thin film analogon of a cloud point. This enables potential new fields of applications, but also a new perspective of the examination of the co-nonsolvency characteristics in the very substance-rich part of the phase diagrams. The co-nonsolvency effect in mixed solution and mixed solvent vapors is schematically shown in Figure 2.9.

Besides these experimental studies, a still limited, but growing number of computer simulation studies has emerged, which usually deal with chemically specific details [167–172]. However, the origin of the molecular mechanism behind the change in polymer conformation in a mixture of solvents is still not fully resolved, yet [91, 92]. Most researchers agree upon the major impact of polymer–solvent interactions on the polymer transition. Hence, several models emerged, that focus on competitive hydrogen bonding of the solvent and co-solvent with the polymer [167, 169, 173, 174], a bridging of two individual polymer chains by the co-solvent [167, 175], and hydrophobic hydration of particular functional groups of the polymer [176].

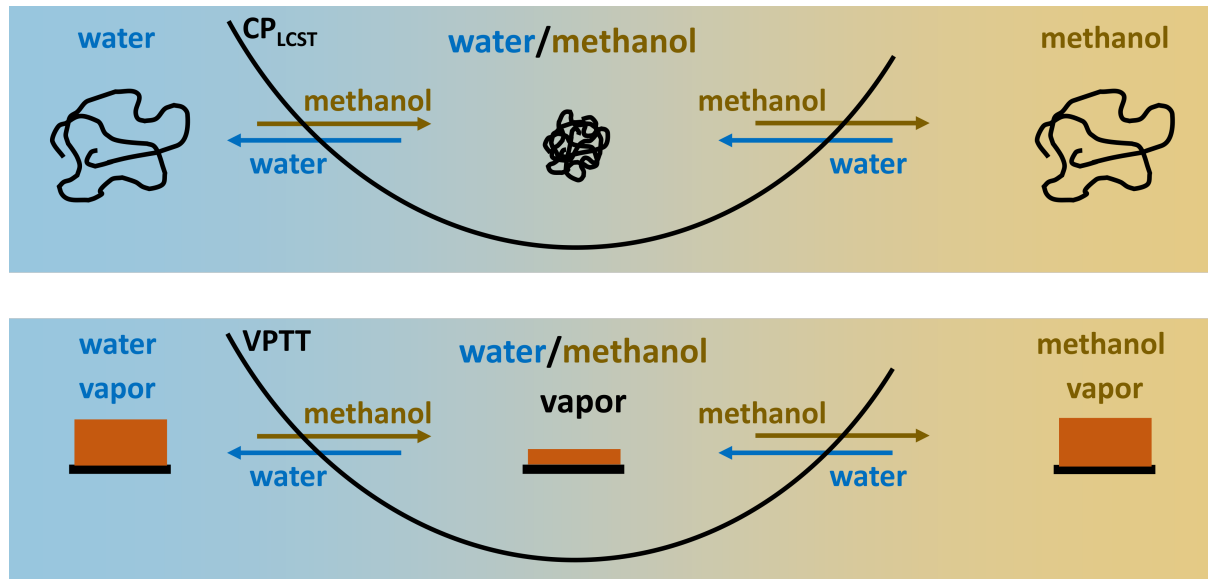


Figure 2.9.: Co-nonsolvency effect of a polymer in mixed solution and of a polymer thin film in mixed vapor. Top: A polymer is dissolved in pure water (blue) and methanol solution (yellow), but de-mixes in water/methanol mixture, due to a decreased CP_{LCST} (black line). Bottom: A thin film is swollen in pure water and methanol vapor, but contracts in mixed water/methanol vapor, due to a decreased VPTT (black line).

2.3. Basics concepts of neutron scattering

In the present thesis, neutron scattering techniques are used. In contrast to real space imaging techniques, scattering with neutrons provides statistical information about the thin films' structural properties. In the framework of this thesis, elastic scattering is performed, *i.e.*, the incoming and final scattered neutron beam are of the same energy. Basic concepts of elastic scattering are described first, before neutron reflectivity (NR) and grazing-incidence small-angle neutron scattering (GISANS) are introduced in detail. In a final section, the theory of the time-of-flight mode, which is applied in both, the NR as well as the GISANS technique, is provided. This section is partly based on the lecture notes by Daillant and Gibaud [177].

Neutron sources

A neutron scattering experiment aims to extract information about either the structure or the dynamics of the sample system under investigation, whereas these systems range from small crystals or colloidal systems, to macromolecules and their nanostructures. Similar to real-space imaging techniques, the spatial resolution of scattering techniques, which probe the sample in reciprocal space, is limited by the wavelength of the neutrons. The neutron wavelength in scattering experiments, typically ranges from 1 to 25 Å, and therefore, such experiments are very well suited to obtain information on the nanoscale level.

Before neutron scattering experiments can be carried out, a reliable and suited neutron beam has to be generated at a neutron source. There are two main types of neutron sources [178]. A spallation source, where a target, typically from metals such as Mercury, Tantalum, or Lead is bombarded by an accelerated proton beam. Due to the pulsed nature of the proton beam, the neutron beam is pulsed as well. A reactor is the second type of neutron source, and all neutron experiments, presented in this thesis, are performed at a neutron reactor. There, the uranium isotope ${}_{92}^{235}\text{U}$ captures a thermal neutron (wavelength of 0.5 to 5 Å), becomes unstable, splits, and emits two to three fast neutrons, among other fission products. One of the emitted fast neutrons is slowed-down by a moderator (typically D₂O), in order to induce a new nuclear fission. The other neutrons are further slowed-down until they have a suited wavelength for neutron experiments (1 to 25 Å, so-called cold neutrons). In contrast to a spallation source, a reactor source produces a constant neutron flow.

Neutron-nucleus interactions

The underlying concept of a neutron scattering phenomenon is the interaction of the incoming neutrons with the atomic nuclei. The scattering event is either elastic, *i.e.*, the energy of neutron is unaltered during the scattering, or inelastic, meaning the energy of the neutron changes in consequence of scattering. The following will focus on elastic neutron scattering. Figure 2.10 schematically images the scattering of a neutron from a single atomic nucleus. The incident neutron can be described as a wave with the following wave function.

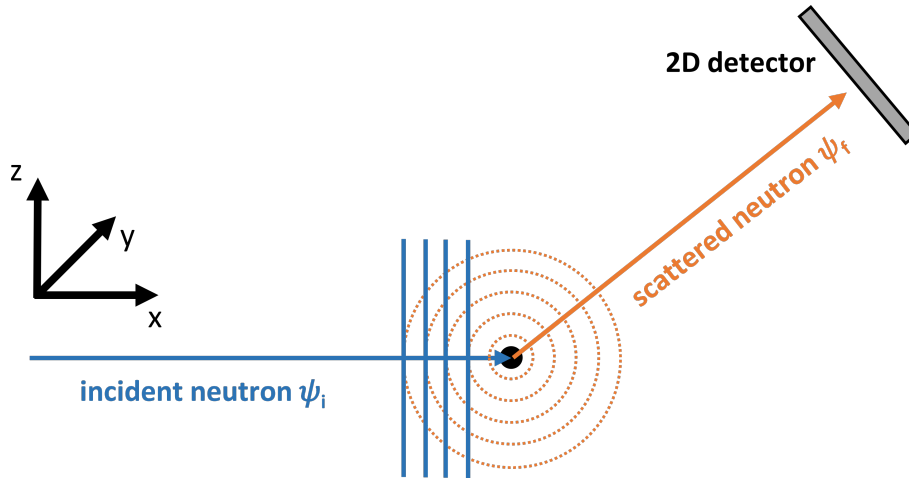


Figure 2.10.: Neutron scattering geometry from a single nucleus. The incident neutron has a plane wavefront (solid vertical, blue lines), the scattered neutron after the interaction propagates with a spherical wave front (dashed orange circles). The detector is far away from the nucleus.

$$\psi_i(\vec{r}) = \psi_0 \exp(i\vec{k}_i \cdot \vec{r}) \quad (2.20)$$

Here, k_i is the wave vector of the incident neutron, ψ_0 is related to the present neutron flux of the beam, and r is the distance between the neutron and the nucleus. The neutron-nucleus interaction occurs only near the nucleus ($\approx 10^{-15}$ m), which is a significantly smaller length scale than the wavelengths of the incident neutrons, which always are larger than 1 Å. Therefore, nuclei can be seen as point-like scatters, emitting isotropic spherical waves. The wave function of the final scattered beam can be described according to the following equation.

$$\psi_f(\vec{r}) = -b \frac{\psi_0}{r} \exp(i\vec{k}_i \cdot \vec{r}) \quad (2.21)$$

2.3. Basics concepts of neutron scattering

Due to elastic scattering, the scattered neutron has the same wave vector k_f as the incident neutron k_i , however, with a different direction, and k is the magnitude of the wave vector. Φ_0/r is proportional to the neutron flux and assures, that the flux is independent of r . The term b in Equation 2.21 is the coherent scattering length of each atom j per unit volume V , and indicates how strong the neutron interacts with the nucleus. Naturally, it strongly depends on the nucleus and the spin state of the neutron. The scattering length density, inside a given volume, can be described with Equation 2.22.

$$SLD_N = \frac{1}{V} \sum_{j=1}^N b_j \quad (2.22)$$

If the composition of the material is known, the SLD can be described with the materials density ρ and molar mass M .

$$SLD_N = \frac{\rho N_A}{M} \sum_{j=1}^N b_j \quad (2.23)$$

The SLD_N is the neutron equivalent of the refractive index n , which is defined via Equation 2.24 [179].

$$n(\vec{r}, \lambda) = 1 - \delta(\vec{r}, \lambda) + i\beta(\vec{r}, \lambda) \quad (2.24)$$

The refractive index consists of a dispersive $\delta(\vec{r}, \lambda)$ and an absorbing part $\beta(\vec{r}, \lambda)$, which are defined as follows [180, 181].

$$\delta(\vec{r}, \lambda) = \frac{\lambda^2}{2\pi} Nb \quad (2.25)$$

$$\beta(\vec{r}, \lambda) = \frac{\lambda}{4\pi} N\alpha_a \quad (2.26)$$

Typically, the dispersion is very small ($\approx 10^{-6}$) and the absorption is even smaller ($\approx 10^{-12}$), thus the refractive index values are close to 1 [180]. In order to distinguish two or more individual materials via scattering techniques, a strong difference in SLD_N is required. By using different or similar SLD_N values, contrast matching is achieved, which enhances or reduces the scattering contribution of a specific component of the sample. Since neutrons interact with the atomic nuclei, which is described by the SLD_N , neutron scattering is highly sensitive to isotopes. This allows for a differentiation of chemically very similar elements or materials.

The probably best-known example, is the difference in SLD_N of the hydrogen 1H and deuterium atom 2H or D [182]. Since hydrogen is ubiquitous in natural and synthetic macromolecules, this is in particular helpful in the field of polymer science [183]. By deuterating specific components of a polymer, a high neutron contrast is achieved as was shown in the very first GISANS experiment [184]. The above mentioned contrast matching can be realized by preparing polymer solutions, with the desired SLD_N , from mixtures of hydrogenated and deuterated solvents (mostly H_2O/D_2O) with specific ratios. A negative SLD_N value describes the scattering event during which a neutron phase shift of 180° occurs [185]. Table 2.2 lists the SLD_N values of commonly used materials.

Table 2.2.: SLD_N values (real part) for commonly used compounds. The values are independent of the neutron wavelength [186].

compound	air	Si	SiO ₂	H ₂ O	D ₂ O	CH ₃ OH	CD ₃ OH	org. polymer
SLD_N [10^{-6} \AA^{-2}]	0	2.07	3.47	-0.56	6.34	-0.37	3.90	$\approx 0.6 - 1$

Specular and diffuse scattering

In a neutron scattering experiment, a well-defined, collimated beam with a wave vector \vec{k}_i impinges under the incident angle α_i onto an interface. For now, a monochromatic neutron beam and a perfectly smooth interface without roughness is assumed. The final exiting beam is denoted as \vec{k}_f . Figure 2.11 schematically images the scattering geometry, along with the definitions of the respective angles, wave vector, and planes. The difference of the final and the incident neutron beam gives the scattering vector q , which describes the momentum transfer from a sample to the final, scattered neutron beam [42].

$$\vec{q} = \vec{k}_f - \vec{k}_i \quad (2.27)$$

In the following, two scattering scenarios are described: Neutron reflectivity, based on specular reflection, and diffuse scattering, based on off-specular reflection.

2.3.1. Specular reflection (or neutron reflectivity)

In case of specular reflection, the incident beam is, similar to optics, partially reflected with an exit angle $\alpha_f = \alpha_i$ and partially refracted with an angle α_t into the sample. The refraction is described by the refractive indices of the respective media according to Snell's law.

$$\sin(\alpha_i) = \frac{n_2}{n_1} \sin(\alpha_t) \quad (2.28)$$

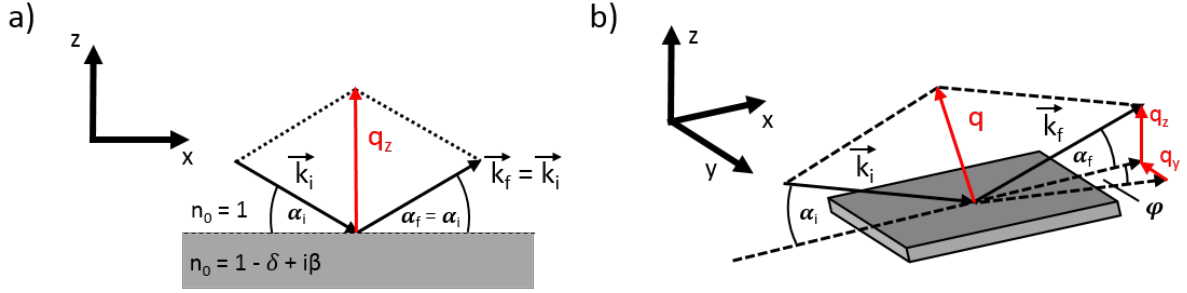


Figure 2.11.: Neutron scattering geometry for specular and diffuse scattering. (a) In specular reflection geometry ($\alpha_i = \alpha_f$) the momentum transfer occurs only in z -direction, while in (b) diffuse scattering geometry, the off-specular reflection is detected and the momentum transfer in y -direction with the scattering angle ψ has to be considered as well.

Due to $\alpha_f = \alpha_i$ the scattering vector q has only a z -component and is denoted with q_z . For elastic scattering, q_z describes a change in the direction of the final beam, with respect to the incident beam. Its modulus remains constant and is defined according to Equation [2.29](#)

$$q = q_z = \frac{4\pi}{\lambda} \sin(\alpha_f) \quad (2.29)$$

Since scattering is based on the response of the incoming beam to a change in refractive index, and the SLD_N can be seen as an equivalent to the refractive index, the ratio of the refractive indices of two media n_1 and n_2 (see Figure [2.11](#)) can be expressed as follows.

$$\frac{n_2}{n_1} = \sqrt{1 - \frac{\lambda^2}{\pi}(\rho_2 - \rho_1)} \cong 1 - \frac{\lambda^2}{\pi}(SLD_2 - SLD_1) \quad (2.30)$$

Analogously to optics, the refractive index depends on the neutron wavelength. Typically, the neutron beam impinges onto a solid (sometimes liquid) interface from air, which basically has an SLD of 0. Since most isotopes have a positive SLD, most media have a refractive index of less than 1. At an incident angle below a critical value, total reflection occurs. This critical angle α_c can be determined by setting $\alpha_f = 0$ in Equation [2.28](#) and using Equation [2.30](#).

$$\alpha_c \cong \lambda \sqrt{\frac{SLD_2 - SLD_1}{\pi}} \quad (2.31)$$

While the critical angle α_c depends on the neutron wavelength, the corresponding critical value of the scattering vector q_z is wavelength-independent. Combining Equations [2.29](#) and [2.31](#) yields Equation [2.32](#).

$$q_c \cong 4\sqrt{\pi(SLD_2 - SLD_1)} \quad (2.32)$$

It should be noted, that Equation 2.31 is only valid for a negligible absorption coefficient ($\beta \ll \delta$), which is typically the case for neutron scattering [180].

According to Fresnel, the reflection and transmission coefficients r and t of the incident and transmitted beam are defined as

$$r = \frac{k_{i,z} - k_{t,z}}{k_{i,z} + k_{t,z}} \quad \text{and} \quad t = \frac{2k_{i,z}}{k_{i,z} + k_{t,z}} \quad . \quad (2.33)$$

Here, $k_{i,z}$ and $k_{t,z}$ are the z -components of the incident and transmitted wave vectors, respectively and amount to $k_{i,z} = k \sin(\alpha_i)$ and $k_{t,z} = k \sqrt{(n^2 - \cos^2(\alpha_i))}$. Dependent on the absorption coefficient β , the reflection and transmission intensities $R_F = |r|^2$ and $T_F = |t|^2$ significantly change around the critical angle α_c , which is schematically imaged in Figure 2.12.

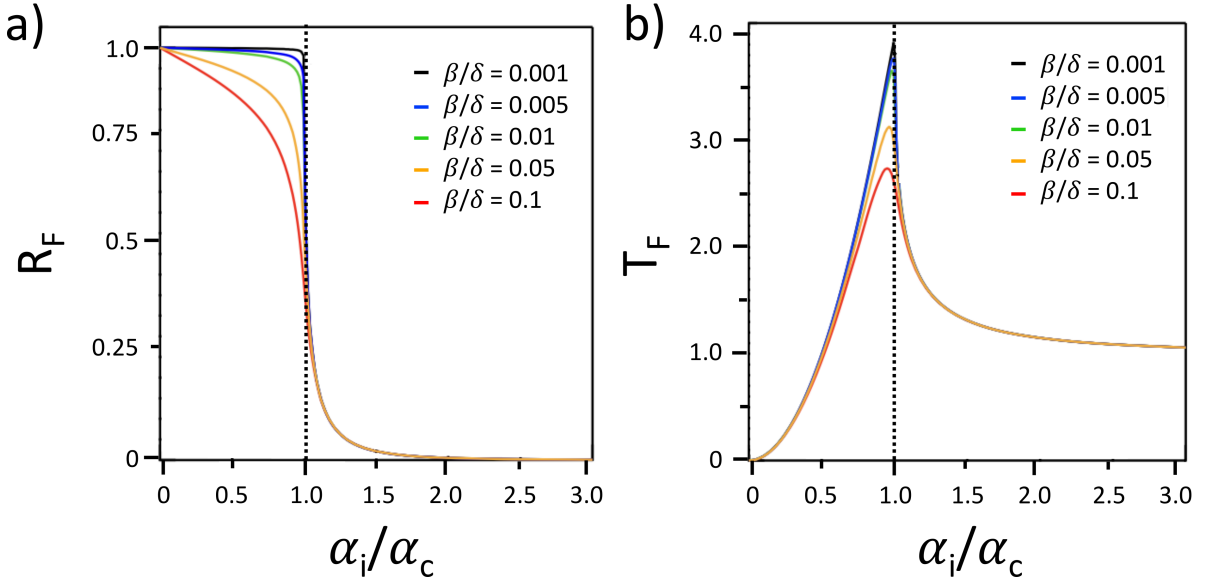


Figure 2.12.: Reflection and transmission functions according to Fresnel. The (a) reflectivity R_F and (b) transmission function T_F are plotted as a function of α_i/α_c . Total reflection occurs for $\alpha_i/\alpha_c < 1$ (a), while interference of the reflected and transmitted wave leads to a four times enhanced intensity (b). An increased absorption ($\beta > 0$) results in a damped intensity of R_F and T_F . Vertical dashed black lines mark $\alpha_i = \alpha_c$. Adapted with permission from ELSEVIER B.V, Copyright 2009 [187].

Below α_c , total reflection occurs, whereas at incident angles of $\alpha_i > \alpha_c$, reflection strongly decays. In contrast, the transmitted intensity T_F features a maximum around the critical angle α_c . There, the reflected and the transmitted neutron beam shortly propagate in phase along the surface and constructively interfere with each other, which leads to an enhancement of the transmitted beam amplitude by a factor of two [179].

Eventually, this yields a four-times amplified transmission T_F . An increasing absorption coefficient β damps both, the reflection as well as the transmission function.

A reflectivity experiment, measures the evolution of R_F (in the following denoted as R) as a function of q_z , which is defined as the following ratio of q_z and q_c .

$$R = \left| \frac{q_z - \sqrt{q_z^2 - q_c^2}}{q_z + \sqrt{q_z^2 - q_c^2}} \right|^2 \quad (2.34)$$

Figure 2.13a displays the reflectivity for the sharp zero roughness air/silicon interface, including the characteristic q_z -regimes. According to the evolution of R_F shown in Figure 2.12, total reflection occurs below q_c or q_c and the reflectivity is always unitary. It should be noted that due to quantum-mechanical effects, the neutron has a non-zero probability to tunnel through the interface into the medium with the higher refractive index - even at the conditions below q_c . Above q_c , the probability of neutrons crossing the interface is significantly greater, and R values decrease strongly. At $q_z \gg q_c$, reflectivity scales to a power law of q^{-4} . Figure 2.13 shows also typical q_z values, ranging between 0.001 to about 0.3 Å. In theory, no reflection should be detected for large q_z values. In reality, incoherent scattering and artefacts or noise coming from the neutron instrument is observed, but at very low intensity of around the order of $10^{-6} - 10^{-7}$.

Multi-layer systems

Most of the systems studied with neutron reflectivity are multi-layer systems. Such systems can be described as a stack of different media (1, 2, ..., i), with different SLD values (SLD_{N-1} , SLD_{N-2} , ..., SLD_{N-i}) and thicknesses (d_1 , d_2 , ..., d_i). The Si substrate and the surrounding media (in this thesis mostly air or a saturated water vapor) are not considered as layers but as semi-infinite front and backing media with a fixed SLD (cf. Table 2.2). Since the momentum transfer occurs perpendicular to the respective interfaces (z -direction), the SLD distribution within the multi-layer sample also depends only in this direction. Figure 2.13b displays the reflectivity as a function of q_z for a multi-layer polymer system. Analogously to the spectrum of a single Si layer in Figure 2.13a, total reflection occurs at $q_z < q_c$. Above the critical angle, a certain number of interference maxima and minima appear. This characteristic pattern, with the so-called Kiessig fringes is due to the superposition of the neutrons reflected at the various interfaces (Figure 2.13c). The position of the Kiessig fringes strongly depends on the SLD_N and the thickness of the respective layers. In order to obtain a reflectivity maximum, the difference in optical path between the reflected neutrons at two interfaces, has to be equal to an integer number N

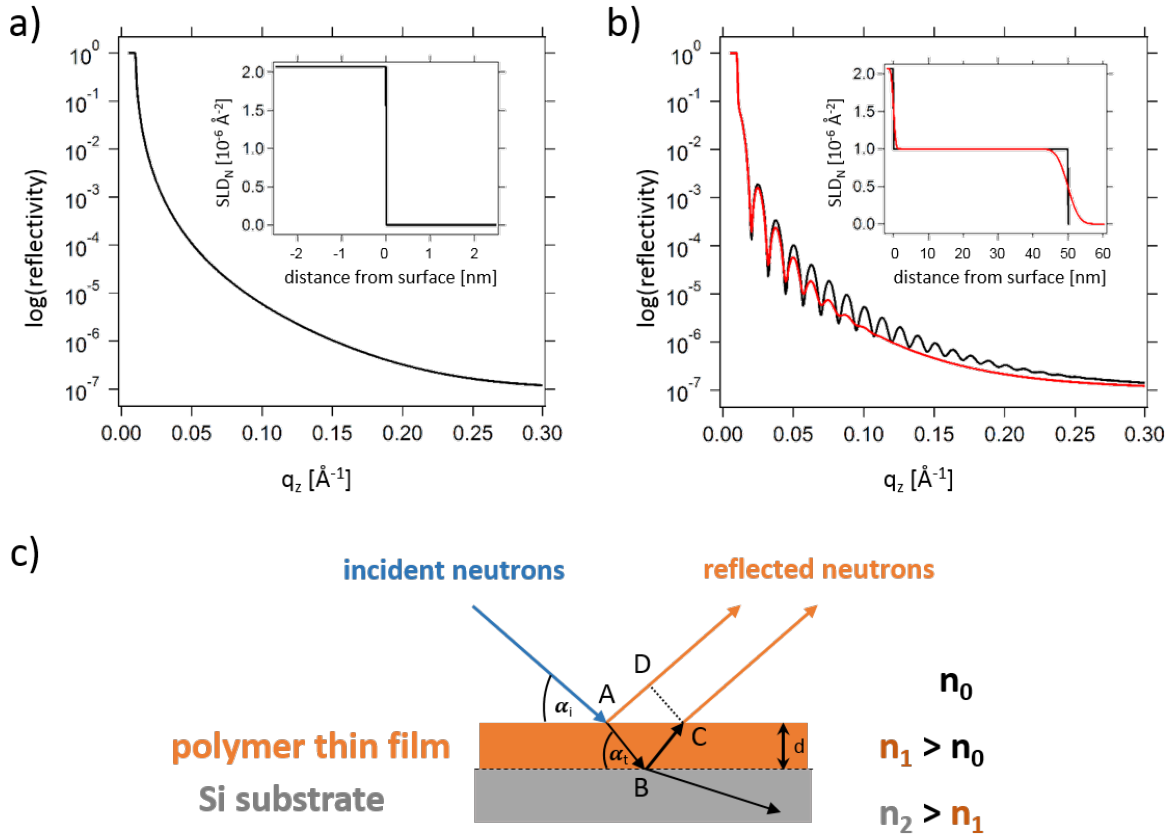


Figure 2.13.: Neutron reflectivity on polymer thin films. Typical neutron reflection pattern from (a) a bare Si substrate and from (b) a polymer coated Si substrate with (red) and without any roughness (black). The insets in (a) and (b) show the corresponding SLD profiles. (c) Superimposition of reflected neutron waves generated at different interfaces. The difference in optical path is given by $\overline{AB} + \overline{BC} - \overline{AD}$.

of wavelengths. This is similar to Bragg's law in crystallography and happens when the following condition is full filled.

$$q_z \cong \frac{2\pi}{d_i} N \quad (2.35)$$

Equation [2.35](#) shows the relationship between real-space length scales (d_i) and reciprocal space information (q_z). Thus, the distance of two reflection maxima is smaller, when the thickness of the corresponding layer is thicker. By using the recursive Parratt formalism, which hypothesizes a continuous wave function and a continuous first derivative at each interface, the experimentally reflection pattern can be modelled [\[188\]](#).

Roughness

The interfaces in a multi-layer stack are not perfectly smooth, as was assumed so far, but show a certain degree of roughness. In addition to specular reflection, this leads to off-specular or diffuse scattered neutrons. The amount of diffuse scattering is an indicator of how smooth and homogeneous the probed interface is, and very often the amount is small, compared to specular reflection. Nevertheless, it is crucial to prepare very homogeneous samples in order to carry out neutron reflectivity experiments, where the diffuse scattering signal is low. The surface roughness can be described effectively via a statistical approach. This approach is based on the assumption that the deviation of the real interface from an ideal flat geometric plane is randomly distributed. Consequently, a certain point on the interface has a probability $P(\Delta z)$ of being higher or lower of Δz with respect to the average, which can be described by a Gaussian function.

$$P(\Delta z) = \frac{1}{\sqrt{2\pi\sigma^2}} \exp\left(-\frac{(\Delta z)^2}{2\sigma^2}\right) \quad (2.36)$$

The profile of the refractive index as a function of z at an interface (between medium i and medium $i + 1$) is defined as follows.

$$n(z) = \frac{n_i + n_{i+1}}{2} - \frac{n_i - n_{i+1}}{2} \operatorname{erf}\left(\frac{\Delta z}{\sqrt{2\sigma^2}}\right) \quad (2.37)$$

Here, σ is the roughness of the interface, while erf is the error function. As an increasing roughness enhances the diffuse scattering signal, it has to be taken into account in the Parratt approach. This is done via a damping factor, that reduces the depth of the oscillations in the obtained reflectivity pattern.

2.3.2. Diffuse scattering

Diffuse scattering describes the off-specular reflection ($\alpha_i \neq \alpha_f$), which contains a momentum transfer in y -direction. This is indicated by an additional scattering angle ψ in Figure 2.11b. Typically, the off-specular intensity is very low, as compared to the specular reflection, in particular for thin film samples, where the scattering volume (in transmission mode) is very low. In order to compensate for that, incident angles of smaller than 1° are chosen. This is then called neutron scattering under grazing-incidence.

Grazing-incidence small-angle neutron scattering (GISANS)

Very small incident angles (typically $\alpha_i < 1^\circ$) allow to probe thin film samples, as compared to transmission mode, the illuminated area under grazing-incidence is significantly increased. Furthermore, the penetration depth can be adjusted, either by small changes of the incident angle or the neutron wavelength, which results in an enhancement of the thin film signal (compared to the signal of the substrate). Grazing-incidence small-angle neutron scattering (GISANS) is used to probe characteristic lateral structures in thin film samples, which typically range between 10 nm and 1-2 μm [181, 184, 189–193]. Incoming neutrons are scattered diffusely at these structures (cf. Figure 2.11b), *i.e.*, the scattering vector \vec{q} has, besides the z -component, also a y - and x -component [181, 194, 195].

$$\vec{q} = \begin{pmatrix} q_x \\ q_y \\ q_z \end{pmatrix} = \frac{2\pi}{\lambda} \begin{pmatrix} \cos(\alpha_f)\cos(\psi_f) - \cos(\alpha_i)\cos(\psi_i) \\ \cos(\alpha_f)\sin(\psi_f) - \cos(\alpha_i)\sin(\psi_i) \\ \sin(\alpha_f) + \sin(\alpha_i) \end{pmatrix} \quad (2.38)$$

The incident angle with respect to the xy -plane, ψ_i is typically 0 and Equation 2.38 simplifies.

$$\vec{q} = \begin{pmatrix} \cos(\alpha_f)\cos(\psi_f) - \cos(\alpha_i) \\ \cos(\alpha_f)\sin(\psi_f) \\ \sin(\alpha_f) + \sin(\alpha_i) \end{pmatrix} \quad (2.39)$$

Thus, \vec{q} depends on the incident angle α_i as well as on the exiting angles α_f (in the xz -plane) and ψ_f (in the xy -plane). It has to be noted that this chapter considers only elastic neutron scattering, thus, the photon energy as well as the incident and final wave vectors, \vec{k}_i and \vec{k}_f are not altered during the scattering event. However, due to multi-layered system, multiple scattering and reflection events occur for an individual neutron, and the incoming and exiting neutron beam can not be described as a plane wave anymore. In order to account for this, first-order corrections are implemented in the Born approximation, leading to the so-called distorted-wave Born approximation (DWBA) [196–198]. This model combines all possible scattering combinations (scattering and reflection) for the incoming and outgoing neutron beam. Figure 2.14 provides a schematically overview. The DWBA model also includes refraction, which are, for better clarity, not included in the schematic representation.

While there are already some software available that allow to simulate diffuse scattering data, *e.g.*, GISANS experiments, within the DWBA framework, they still require quite an amount of computational power and experience [195, 199, 200]. Therefore, in the present thesis, the DWBA theory is further simplified for the analysis of GISANS data as will be described in the following.

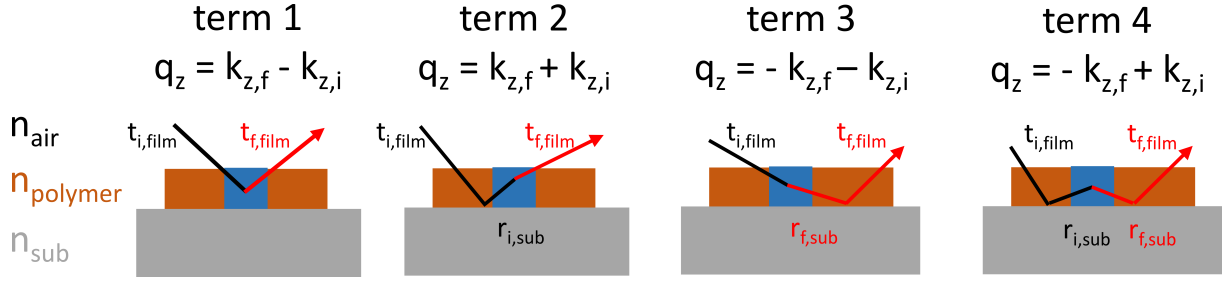


Figure 2.14.: Schematic representation of the scattering terms considered in the DWBA.

For the different scattering scenarios, the reflection (r) and transmission (t) coefficients of the incident (i) and final, scattered (f) neutron beam are labeled accordingly. The refractive indices of air, the polymer film, and the Si substrate are n_{air} , n_{film} , and n_{sub} , respectively. The refraction at the air-polymer interface is neglected.

Yoneda peak

The intensity maximum of the Fresnel transmittance (Figure 2.12b), close to the critical angle α_c was first observed by Yoneda in 1963, and thus is commonly referred to as Yoneda peak [201]. Since the critical angle of a material depends on its SLD_N (cf. Equation 2.31), also the Yoneda peak is sensitive to the materials SLD_N and density. For a material, consisting of two or more components, individual Yoneda peaks can be distinguished, assuming a sufficient scattering contrast is provided. By performing vertical line cuts (VLC) along q_z at $q_y = 0$ only the z -component is considered and individual Yoneda peaks can be identified, which yield information about the vertical film composition. Horizontal line cuts (HLC) around the Yoneda region at a fixed q_z value, give information about characteristic lateral correlations within the thin film. In the framework of this thesis, this is done via the effective interface approximation (EIA), which describes the height-height correlation function of the sample with only one effective interface [202, 203]. In GISANS measurements, the differential cross section of a single scatterer within a sample is defined as follows [195, 203].

$$\frac{d\sigma}{d\Omega} = \frac{A\pi^2}{\lambda^4} |\Delta n|^2 |t_i|^2 |t_f|^2 P(\vec{q}) \quad (2.40)$$

As the incident angle is fixed, the illuminated area A remains constant throughout the GISANS measurement, as well as the wavelength of the incoming neutrons λ . The Fresnel transmittance coefficients for the incident and exiting neutron beam depend on the scattering contrast $|\Delta n|^2$. Since for static GISANS experiment, the scattering contrast does not change during the measurement, the scattering intensity only scales with the scattering factor $P(\vec{q})$. This scattering factor includes a form factor $F(\vec{q})$ and a structure factor $S(\vec{q})$. While $F(\vec{q})$ assumes a homogeneous refractive index of mesoscopic objects

(cf. Equation 2.24), $S(\vec{q})$ takes coherent scattering from ordered, characteristic objects of similar geometric dimensions into account [203-205].

$$P(\vec{q}) \propto N|F(\vec{q})|^2 S(\vec{q}) \quad (2.41)$$

The equation assumes a homogeneous distribution of monodisperse scattering objects with a number density N , which does not correlate to reality, as the object distribution in terms of size, shape, and distance to each other, usually varies. The local monodisperse approximation (LMA) and the decoupling approximation (DA) takes this into account. Consequently, the scattering factor $P(\vec{q})$ describes a superposition of j scattering factors. The individual contribution of the different scatterer types, *i.e.*, differently sized geometric objects, can be extracted independently from each other according to Equation 2.42.

$$P(\vec{q}) \propto \sum_j N_j \langle |F_j(\vec{q})|^2 \rangle S_j(\vec{q}) \quad (2.42)$$

A full explanation of the applied model is provided in the dissertations of Dr. Christoph Schaffer and Dr. Johannes Schlipf [206, 207]. In this thesis, the HLC are modeled with the LMA and EIA of standing cylinder-shaped nanodomains, distributed on a 1D paracrystal lattice in combination with the DWBA [190, 208]. The used approximation results in a low computational effort, while simultaneously the size of the lateral, periodic objects [via $F(\vec{q})$], their distances to each others, as well as their order [via $S(\vec{q})$], are described properly [209].

2.3.3. Time-of-flight mode

A neutron scattering pattern is obtained either by using a monochromatic neutron beam and a varying incident angle α_i or by using a fixed incident angle α_i and a polychromatic neutron beam, *i.e.* the wavelength or energy of the incoming neutrons change. Usually the latter is the case for neutron scattering, as this provides a larger q range. Furthermore, surface-sensitive and bulk-sensitive information are obtained simultaneously, which is due to the wavelength-dependence of the critical angle α_c . The ToF mode can be applied to (specular) neutron reflectivity [210-212] as well as to GISANS experiments [191, 213].

The ToF mode describes the cropping of the incoming neutron beam with a chopper system. In addition, every detected neutron has not only a x - and y -coordinate on the detector but also characteristic information about its time-of-flight. These information enable the calculation of the velocity v_n and de Broglie wavelength λ_B .

$$\lambda_B = \frac{h}{p(v_n)} \quad (2.43)$$

2.3. Basics concepts of neutron scattering

The Planck's constant and the velocity-dependent momentum of the neutron are denoted with h and $p(v_n)$. As neutrons have a mass, they are exposed to gravity effects, which is strongest for the slowest neutrons. This principle is indicated schematically in Figure 2.15. The downfall in z -direction of the neutrons leads to a distribution of real incident angles α_{real} that deviate from the horizontal incident angle α_i according to $\alpha_{real} = \alpha_i + \alpha_{gravity}$ (cf. blue line in Figure 2.15b). The direct transmitted and the specular reflected neutron beam are subject to the same degree of gravitational effects, which can be used to calculate the real incident angle α_{real} via the small-angle approximation according to the following geometric expression.

$$\tan(\alpha_{real} + \alpha_f) \stackrel{\alpha_f = \alpha_{real}}{=} \tan(2\alpha_{real}) = \frac{\Delta z'}{SDD} \quad (2.44)$$

SDD is the sample-detector-distance. If the individual neutrons are detected in the event-mode, they can be binned according to their wavelengths, with an arbitrary time resolution. While for ToF-NR usually a time resolution of 1 - 30 seconds is achieved, ToF-GISANS experiments are considerably slower. As a neutron reactor emits a heterogeneously distributed neutron spectrum with a relatively low intensity of in particular the slower neutrons, it takes significantly longer times (up to 24 - 36 hours) to obtain scattering data with sufficient statistical relevance.

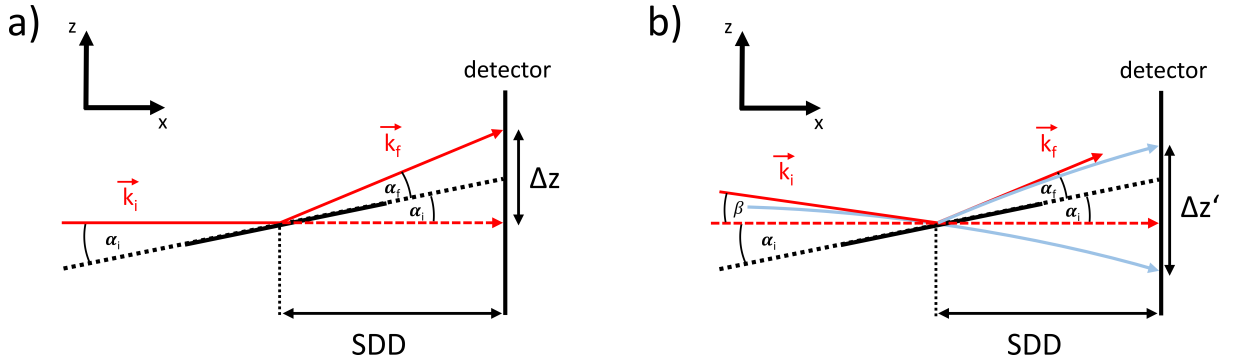


Figure 2.15.: Schematic representation of gravitational effects in neutron scattering experiments. The incident and reflected neutron wave vector k_i and k_f (a) without and (b) with the influence of gravity. Gravitational effects lead to an increased real incident angle ($\alpha_{real} = \alpha_i + \alpha_{gravity}$) and a parabolic neutron trajectory (indicated in pale blue). SDD stands for sample-detector-distance. Adapted from the dissertation of Dr. Lorenz Bießmann [75].

3. Thin film characterization

This chapter introduces the experimental techniques employed for thin film characterization. Real-space imaging techniques, such as optical microscopy (OM), profilometry, and atomic force microscopy (AFM) characterized the surface topography of the thin films. X-ray reflectivity (XRR) was used, to obtain information about film thickness, density, and surface roughness with high statistical relevance. Time-of-flight neutron reflectivity (ToF-NR) provided mesoscopic thin-film parameters, *e.g.*, film thickness and solvent content, and was performed *in-situ* upon varying environmental conditions. The lateral thin-film morphology was probed using grazing-incidence small-angle neutron scattering in ToF mode (ToF-GISANS). Notably, the data from XRR, ToF-NR, and ToF-GISANS was obtained in reciprocal space and therefore, had to be translated to real-space structures. To complement imaging and scattering techniques, spectroscopic methods were employed. Spectral reflectance (SR) followed the film thickness and refractive index, while Fourier-transform infrared (FTIR) spectroscopy measured the vibrational and rotational energy of molecular bonds *in-situ* upon changing environmental parameters. The extracted molecular information were linked to the results on the mesoscopic thin film behavior obtained with ToF-NR and ToF-GISANS.

Environmental parameters, such as temperature and relative humidity (RH), had to be controlled precisely during *in-situ* studies. For that reason, specialized measurement equipment was used. The last part of this chapter, describes already pre-existing experimental setups, and the newly designed 'FlexiProb' sample environment, which was realized together with Tobias Widmann.

3.1. Structural characterization in real space

Optical microscopy, profilometry, and atomic force microscopy were used for direct imaging of the thin film surfaces in real-space. They are discussed briefly in the following.

Optical microscopy

An optical microscope uses visible light and a lens system to create magnified real space images of small objects. Therefore, it is suited, to resolve structures on the micrometer scale and determine the (macroscopic) quality and homogeneity of polymer thin film surfaces.

Instrument: All images, shown in this thesis, were recorded with an Axiolab A microscope (Carl Zeiss, Jena, Germany). The magnification was in the range from 1.25-fold to 100-fold. The optical microscope was coupled with a PixeLink USB Capture BE 2.6 charge coupled device camera, which permitted digital image acquisition with a resolution of 1280 x 1024 pixels. A halogen lamp (Hal 100) assured constant illumination, whereas a reflected-light geometry was used to enable the magnification of non-transparent films and substrates. The Rayleigh criterion describes the resolution limit of a conventional optical microscope in the focal plane.

$$R = \frac{1.22 \lambda}{2 NA} \quad (3.1)$$

NA is the numerical aperture and λ is the wavelength of the illumination source. The values for NA , R , and the empirically determined pixel sizes for different magnification objectives are listed in Table [3.1](#).

Table 3.1.: Magnification, NA , R , and pixel size for the available objectives of the Axiolab A optical microscope. The pixel sizes were determined empirically.

magnification	NA	R ($\lambda = 700$ nm) [μm]	pixel size [μm]
1.25	0.035	12.2	6.258
2.5	0.075	5.7	3.2
10	0.20	2.1	0.8
50	0.70	0.61	0.16
100	0.75	0.57	0.08

Profilometry

A profilometer obtains the surface profile of a thin film, which yields the film thickness and the surface roughness. For this purpose, thin films were scratched from the silicon substrate and the profilometer measured the height-profile perpendicular to the scratch.

Instrument: In the present thesis a DektakXT was used (Bruker Nano Surface Division, Karlsruhe, Germany). The scratched thin films were placed on a high precision xy -stage. A diamond tip, with a stylus radius of $2\ \mu\text{m}$, was pressed to the sample surface with a small vertical force (corresponding to 2-3 mg). Subsequently, the xy -stage, equipped with an additional actuator for continuous and precise movement, moved in measurement direction perpendicular to the scratch with a scanning speed of $35\ \mu\text{m s}^{-1}$. For better statistics, several measurements at different spots along multiple scratches, distributed over the sample surface were performed. Figure 3.1 schematically displays the measurement routine.

The vertical deflection of the tip was translated into a height profile, thereby yielding the height level outside (H_o) and inside of the scratch (H_i). This was transformed into an average film thickness, using the software Vision64. One has to note, due to penetration of the sample by the tip, and residual material within the scratch, the measurement might yield a false film thickness. Thus, several measurements for one thin film sample were performed in order to reduce the uncertainty. Profilometry provided very fast, first information about the film thickness, which was used as a reference point for the fitting routine of more statistical data, *e.g.*, obtained by x-ray and neutron reflectivity.

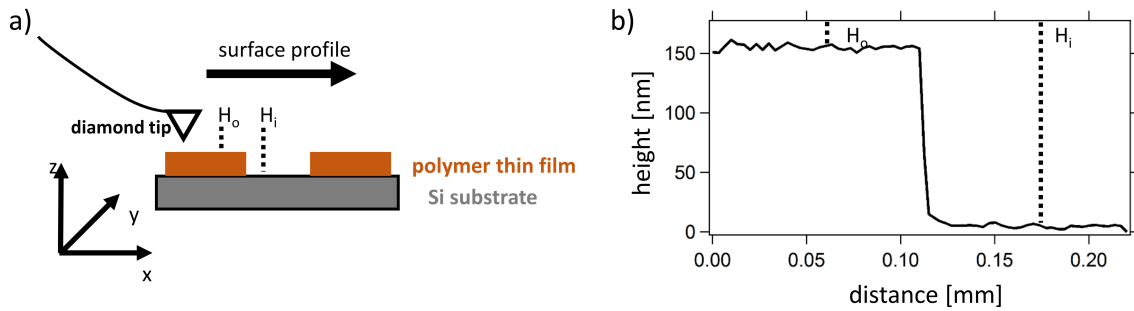


Figure 3.1.: Working principle of a profilometer. (a) Schematic overview of the profilometer setup. Scanning direction was along the x -axis. b) Typical profilometer scan with the heights H_o , outside, and H_i inside of the scratch.

Atomic force microscopy

An atomic force microscope (AFM) probes the topography of a surface and yields information about its homogeneity and roughness, based on the interaction of a sharp tip

(radius of 8 - 12 nm) and the surface of a sample. While the tip, located at the end of a cantilever, scans over the surface, its interaction with the sample changes, following the Lennard-Jones potential. Figure 3.2a shows the schematic setup of an AFM.

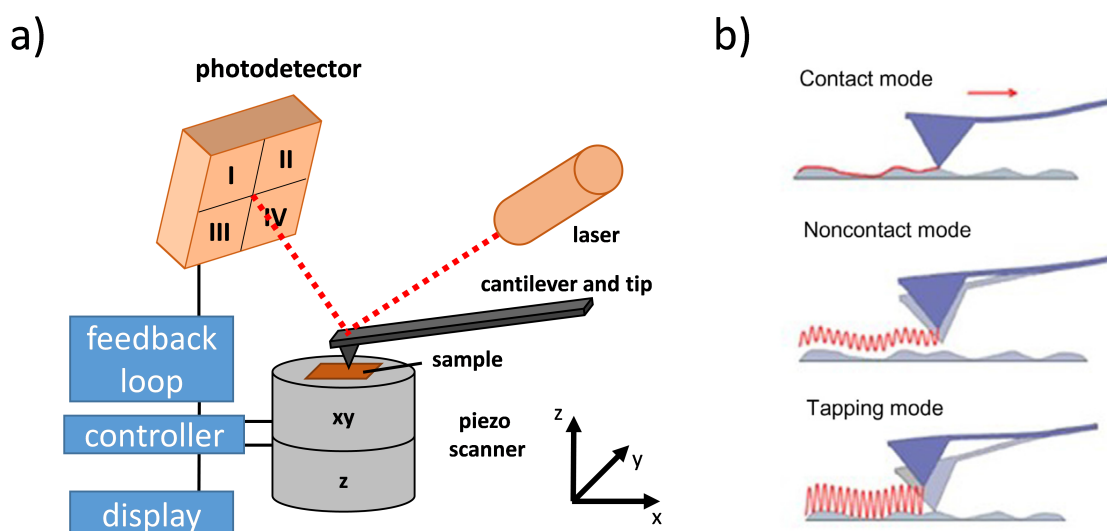


Figure 3.2.: Working principle of an AFM. (a) Schematic overview of the AFM setup. (b) Overview of the three different operation modes. Adapted with permission from ELSEVIER BOOKS, Copyright 2019 [214].

Depending on the distance of the tip to the thin film surface the AFM operates either in the non-contact mode or in the contact mode. In the non-contact mode, attractive interaction due to polarization interactions between atoms, dominate, whereas, in the contact mode, the distance between the tip and the surface is so small, that overlapping of the electronic orbitals results in repulsive interactions. While the cantilever in the non-contact mode vibrates above its resonance frequency (amplitude ≈ 10 nm), in contact mode it is in physical contact with the surface and therefore does not vibrate. In a third mode, the tapping mode, the cantilever vibrates below its resonance frequency, with an amplitude of approximately 100 - 200 nm. Figure 3.2b provides an overview of the three commonly used AFM modes. In all three modes, the deflections of the cantilever, due to topographical features, are detected with a laser, which is reflected at the end of the cantilever and hits a 2-dimensional photodetector. A feedback loop continuously responds to the cantilever deflection in order to keep it constant and equal to a preset set point value. This is done via the proportion-integral-derivative (PID gains) control. The gain has to be chosen very accurately, since the PID loop is not able to keep the set point constant if the gains are set too low. If it is set too high, the resulting image will

contain feedback noise. Besides the topographical imaging, AFM is also capable of phase imaging, where the surface topography is obtained via the phase shift between the drive signal to the cantilever and its response. This results in very high spatial information, based on the properties of the material such as adhesion, viscoelasticity, and stiffness. It is noteworthy, that this can only be done in tapping mode.

Instrument: The AFM instrument, used in this thesis, was an MFP-3D AFM (Oxford Instruments Asylum Research, High Wycombe, United Kingdom). All measurements were performed in tapping mode at room temperature. To obtain the surface roughness, an area of $1.5 \times 1.5 \mu\text{m}$ was scanned with a scan rate of 0.1 Hz. For evaluation, the software Gwyddion v2.52 was used [215].

3.2. Structural characterization in reciprocal space

In the present work, scattering techniques using x-rays and neutrons were applied to characterize the thin film samples and to follow their response to an external stimuli *in-situ*. A detailed introduction to neutron scattering is given in Chapter 2.3. For further reading, literature provides detailed overviews, especially about neutron scattering methods under grazing-incidence [181, 189, 192–194, 216].

X-ray reflectivity

X-ray reflectivity probes the vertical (electron) density profile of homogeneous and smooth thin films. X-rays are scattered at the electrons of the atomic shell and therefore, are sensitive to the x-ray scattering length density (SLD_X), *i.e.*, the material's electron density. In reflectivity mode, incident and exit angle α_i and α_f are equal, thus, the momentum transfer occurs along the surface normal (defined as z -axis). Consequently, XRR yields very accurate information about the vertical phase separation, *e.g.*, the formation of electron-dense layers. Furthermore, the film thickness, overall (scattering length) density, and roughness of the interfaces are obtained with high statistical relevance.

Figure 3.3 schematically images a typical XRR device. X-rays are generated by an anode (most commonly a Cu-K_α anode), monochromatized by a Goebel mirror, and collimated by various slits. The reflection of x-rays on a thin film sample follows the same physical principles as is explained in Section 2.3 for the reflection of neutrons.

Instrument: XRR measurements were performed with a D8 Advance Diffractometer (Bruker, Billerica, United States of America). A Cu-K_α anode was used to generate x-rays, which were monochromatized to a wavelength of $\lambda = 1.54 \text{ \AA}$. The x-ray beam was collimated with a 0.2 mm sized slit. A tantalum knife-edge, located closely above the sample, blocked part of the beam. Hence, over-illumination of the sample, especially at

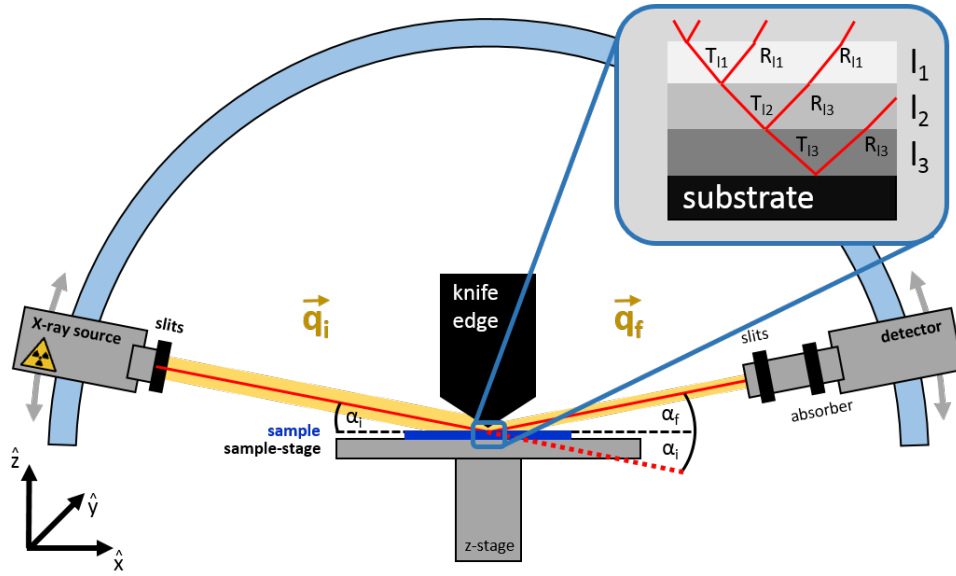


Figure 3.3.: Schematic representation of an x-ray reflectometer. (a) X-rays are generated by a $\text{Cu-K}\alpha$ anode. The monochromatized and collimated x-ray beam impinges on the thin film surface under the angle α_i and is reflected with an angle of $2\alpha_i$ (with respect to the incoming beam). The intensity of the specular reflected beam is recorded with a detector. The coupled $\alpha_i - 2\alpha_i$ signal is translated to a momentum transfer \vec{q}_z . The z -position of a tantalum knife-edge is adjusted, in order to prevent over-illumination of the thin film. The inset displays a multi layer system (here, three layers on a substrate are displayed). Each layer may or may not differ in thickness, scattering length density, and surface roughness.

very low incident angles α_i , where the x-ray footprint might be larger than the sample, was prevented. After interacting with the sample, the reflected beam was collimated with a second 0.1 mm sized and a third 0.05 mm sized slit, before reaching the detector. An automated rotary absorber protected the detector against over-saturation. Prior to the measurement, a direct beam measurement was performed to determine the position of the direct x-ray beam ($\alpha_i = 0^\circ$). In addition, a z -scan and rocking scan were performed in order to align the height, and the sample surface parallel to the direct beam. The alignment process was usually repeated 2-3 times. Typical settings for an XRR measurement performed in the framework of this thesis, was a scan range of $0 - 5^\circ$ with a step size of 0.02° . The reflectivity pattern was modeled with the Parratt algorithm [188], as explained in Section 2.3, executed by the Igor Pro v7.0 software by Wavemetrics in combination with the Motofit plugin [217].

Time-of-flight neutron reflectivity

Section 2.3 provides the basic principles of neutron reflectivity (NR) in time-of-flight (ToF) mode.

Instruments: ToF-NR measurements were performed at the RefSANS instrument at the Heinz Maier-Leibnitz Zentrum (MLZ) at the neutron source FRM II, Garching Germany [218–220], and at the D17 instrument at the neutron source ILL, Grenoble, France [221, 222]. The instrument-specific settings are described in the following.

RefSANS: The RefSANS instrument was operated in the ToF mode, *i.e.*, in addition to the exact xy -position of every neutron on the detector, the time-of-flight was recorded. According to Equation 2.29, a reflectivity curve was obtained by varying either the incident angle α_i or the neutron wavelength λ . The latter was applied for all ToF-NR measurements (at RefSANS and D17) presented in this thesis. A chopper system cut the neutron beam into pulses with a suited wavelength band, ranging from 3 to 21 Å. Due to the event-mode, the time resolution of the RefSANS instrument was only limited by the signal intensity. After data acquisition, gravity-induced trajectory deviations were corrected by the local contacts and the neutrons were binned with an effective time resolution of 30 s.

D17: Also the D17 instrument was operated in ToF-mode. A chopper system generated a suited wavelength band, ranging from 2 to 27 Å. In contrast to the event-mode of the RefSANS instrument, D17 used iterative measurements for data acquisition, *i.e.*, the measurement time defined the time resolution. One has to note, while individual measurement files can be summed up in order to improve the statistics, they cannot be splitted in order to improve the time resolution. For ToF-NR measurements at the D17 instrument a time resolution of 5.5 s was achieved.

The following section addresses ToF-NR measurements at both instruments, RefSANS and D17. Static (thin film is in equilibrium) and kinetic (thin film is not in equilibrium) ToF-NR measurements were performed. The settings of both, regarding incident angle α_i , acquisition time, wavelength band, resolution, as well as the sample-detector-distance (SDD), are summarized in Table 3.2. For realizing static and kinetic ToF-NR measurements in a precisely controlled environment, the thin film samples were mounted in a specialized measurement chamber (cf. Section 3.4).

The obtained reflectivity curves were fitted using the Motofit plugin for the Igor Pro software [217], which provided the film thickness (and swelling ratio), surface roughness, and a vertical SLD profile of the thin films, from which the solvent content was determined via Equation 2.13.

Table 3.2.: Parameters of the RefSANS and D17 instrument for static and kinetic ToF-NR measurements. Note, the $\frac{\Delta\lambda}{\lambda}$ resolution is given for the RefSANS instrument, while for the D17 instrument the $\frac{\Delta q}{q}$ resolution is listed.

RefSANS	α_i [°]	acquisition time [min]	wavelength band [Å]	resolution $\frac{\Delta\lambda}{\lambda}$ [%]	SDD [m]
angle 1 (static)	0.60	20	3 - 21	4	10.32
angle 2 (static)	2.40	100	3 - 21	4	10.32
angle 3 (kinetic)	0.76	30 s time resolution	3 - 21	8	10.32
D17				$\frac{\Delta q}{q}$ [%]	
angle 1 (static)	0.5	15	2 - 27	10	3.10
angle 2 (static)	2.5	30	2 - 27	10	3.10
angle 3 (kinetic)	1.0	5 s time resolution	2 - 27	10	3.10

Grazing-incidence small-angle neutron scattering

The basic principles of neutron scattering under grazing-incidence is introduced in Section 2.3.2. The following section describes the experimental procedure, data acquisition, and data analysis.

Instrument: GISANS measurements were performed at the RefSANS instrument at the Heinz Maier Leibnitz Zentrum (MLZ) at the neutron source FRM II, Garching Germany [218–220]. Analogously to NR, also GISANS measurements were carried out in ToF mode. Therefore, the summed-up detector image was divided into different wavelengths (or energy) channels. Since the critical angle α_c of a material is dependent on the wavelength of the incident neutrons, different critical angles were observed for different wavelengths. Hence, the material was probed at incident angles below, at, and above the critical angle simultaneously. This allowed for probing surface-sensitive and bulk-sensitive information simultaneously. On the one hand the lateral thin film morphology near the surface could be compared to surface-probing real-space techniques, such as OM and AFM, while on the other hand ToF-GISANS provided insight, how the surface mor-

phology evolved within the thin film. The settings of the performed ToF-GISANS measurements, regarding the incident angle α_i , the acquisition time, the wavelength band, its resolution, and the sample-detector-distance (SDD) are summarized in Table 3.3.

The neutrons, available for GISANS measurements at the RefSANS instrument, differed not only in wavelength but also in intensity as is shown in Figure 3.4a. Therefore, especially the surface-sensitive neutrons featured a longer wavelength, and it took longer times, to obtain a scattering image with sufficient statistical relevance. In order to compensate for the relatively low neutron intensity on the detector, the RefSANS instrument sent five single neutron beams on the sample, which were re-focused on the detector. A measurement time of ≈ 24 hours was needed, to carry out a reasonable ToF-GISANS measurement on polymer thin films. In contrast to ToF-NR, it was not possible to follow thin film kinetics with ToF-GISANS. For realizing ToF-GISANS measurements in a precisely controlled environment, the thin film sample were mounted in a specialized measurement chamber. This is explained in Section 3.4.

Table 3.3.: ToF-GISANS settings at the RefSANS instrument.

RefSANS	α_i [°]	acquisition time [h]	wavelength band [Å]	resolution $\frac{\Delta\lambda}{\lambda}$ [%]	SDD [m]
angle 1 (static)	0.5	24	3 - 21	10	10.32

A typical GISANS scattering pattern is schematically shown in Figure 3.4b. Both, transmitted and scattered neutrons were detected. The transmitted signal contained remnants of the direct beam (D), while the scattered signal showed a pronounced specular peak (S), the Yoneda region (Y), and weak off-specular scattering. The horizon H separated the transmitted from the scattered signal. Trajectory deviations induced by gravity effects were corrected after data collection by the local contacts of the RefSANS instrument. For every wavelength or energy channel, vertical line cuts (VLCs), in q_y direction at $q_z = 0$, and horizontal line cuts (HLCs), in q_z direction at the Yoneda position, were performed. While the VLCs provided information about the (scattering length) density and hence about the material composition, the HLCs gave information about the lateral film morphology. The scattering data was analyzed using the directly programmable data analysis kit (DPDAK) in combination with the monodisperse approximation (LMA) and effective interface approximation (EIA) of vertical standing cylindrical-shaped nanodomains distributed on a 1D paracrystal lattice within the framework of the distorted-wave Born approximation (DWBA).

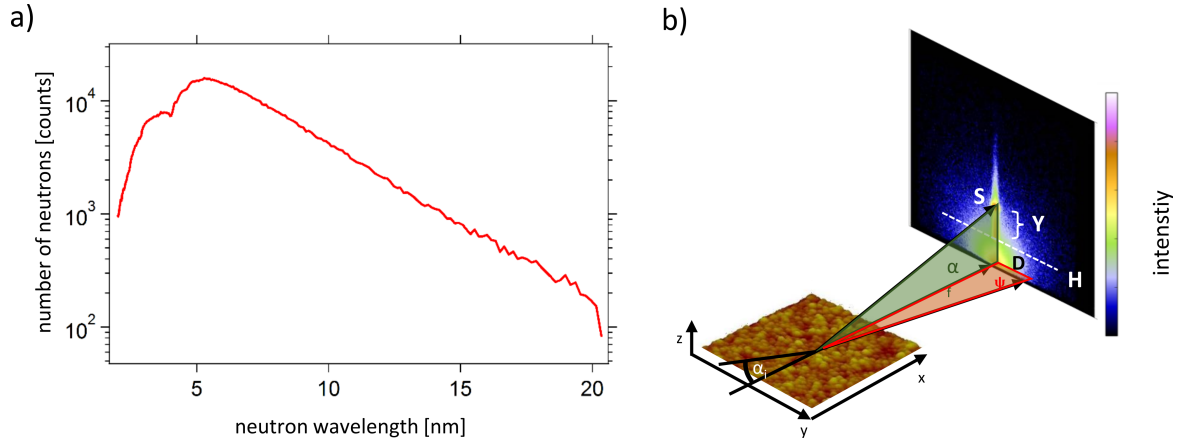


Figure 3.4.: GISANS at the RefSANS instrument (a) Intensity of the available neutrons for GISANS measurements as a function of their wavelength at RefSANS. (b) Schematic working principle of a GISANS measurement. The sample is aligned in the x - and y -plane, with the neutron beam along the x -axis. α_i and α_f mark the incident and exit angle, respectively. The out-of-plane angle is labelled with ψ . A logarithmic intensity scale is used to visualize the intensity of the detected neutrons. The typical 2D scattering pattern displays the specular peak (S), the Yoneda region (Y), the horizon (dashes white line denoted with H), and remnants of the direct beam (D).

3.3. Spectroscopic characterization

Spectral reflectance (SR) and Fourier-transform infrared (FTIR) spectroscopy were used for a spectroscopic characterization of the investigated thin films. They are discussed briefly in the following.

Spectral reflectance

Spectral reflectance (SR) measures the film thickness and the effective refractive index via interference effects in thin films. Light, typically in the UV and visible regime, is reflected at the interfaces of a thin film, *e.g.*, the air-polymer and the polymer-substrate interface. The reflected light waves interfere with each other, leading either to an enhancement or a reduction of the reflected light. By using Snell's law, the conditions for constructive and destructive interference dependent on thickness and refractive index of the thin film, and the incident angle θ_2 (incident angle on the lower boundary, here the Si substrate) of the incoming light, are given by Equations 3.2 (constructive) and 3.3 (destructive), respectively.

$$2 n_{film} d_{film} \cos(\theta_2) = \left(m - \frac{1}{2}\right) \lambda \quad (3.2)$$

3.3. Spectroscopic characterization

$$2 n_{film} d_{film} \cos(\theta_2) = m \lambda \quad (3.3)$$

The refractive index and thickness of the film is denoted with n_{film} and d_{film} , while λ is the wavelength of the incoming light, and m is an integer. Figure 3.5a schematically represents this working principle. Since the refractive index of the polymer thin film is higher than that of air, and the refractive index of the Si substrate is higher than that of the polymer thin film, two phase shifts by 180° (or by π) occur at the corresponding interfaces (highlighted by blue circles in Figure 3.5).

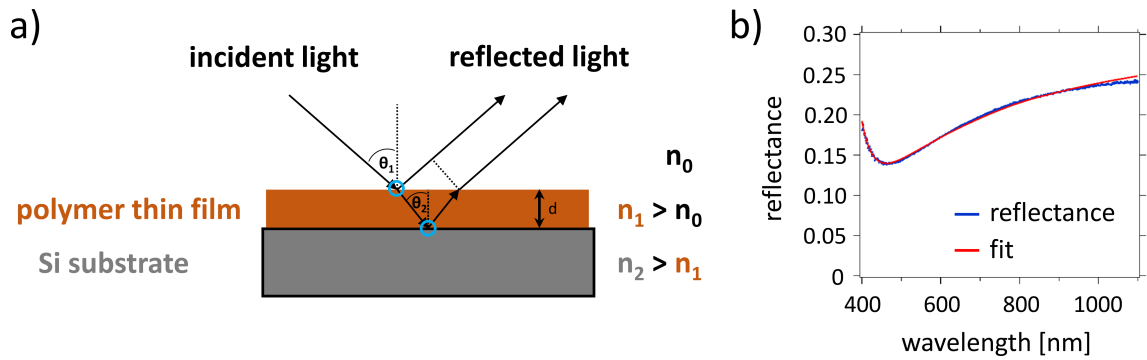


Figure 3.5.: Schematic representation of spectral reflectance. (a) Light waves are reflected at the upper and the lower interfaces of a thin film sample. Due to the difference in path length, constructive and destructive interference occur. Phase shifts of 180° , as described in the main text, are highlighted with blue circles. (b) Exemplary reflectance pattern (blue) of a polymer thin film in the visible regime, together with the best model fit (red).

Instrument: For SR measurements, a Filmetrics F20 Thin Film Measurement System (Filmetrics Inc., San Diego, United States of America) was used. The setup came with two light sources, a deuterium lamp, for light in the UV range (180 - 360 nm), and a halogen lamp for light in the visible and near-infrared range (360 - 1100 nm). Both light sources were connected via an optical fiber, guiding light waves to the sample. By adjusting the distance between the sample and the end of the optical fiber, the spot size of the incident light beam on the sample was varied between 0.5 and 1.0 mm. Prior to the actual SR measurement, the intensity of the raw signal was maximized by aligning the position of the lamp and the angle of the incoming light beam. A reference spectrum of a bare Si wafer and a background spectrum of a black cardboard (to mimic background illumination from interfering light) were measured and stored in the Filmetrics software.

Since the incident light consisted of multiple wavelengths, certain wavelengths fulfilled Equation 3.2, while others fulfilled Equation 3.3. Therefore, a characteristic interference pattern with one to several oscillations was obtained. The film thickness and the refractive

index were obtained by matching their positions and amplitudes via a model fit (Figure 3.5b). Best fits usually were achieved by a two-layer (SiO₂ and one polymer layer), a three- or a four-layer model (SiO₂, one main polymer layer, and one or two solvent enrichment layers). During swelling experiments in a saturated solvent vapor (mainly water vapor), the film thickness as well as the refractive index changed due to water absorption. As a result, both parameters were strongly coupled with each other and featured large uncertainties. To decouple them and reduce the uncertainties, the product of the film thickness and the refractive index of the DBC was used according to Magerl et al. [73].

$$d_{opt} = d_{film} \cdot n_{DBC} \quad (3.4)$$

The refractive index of the swollen polymer thin film was estimated via the Lorentz-Lorenz effective medium approximation according to Equation 3.5

$$\frac{n_{film}^2 - 1}{n_{film}^2 + 2} = \frac{d_{ini}}{d_{film}} \frac{n_{DBC}^2 - 1}{n_{DBC}^2 + 2} + \frac{d_{film} - d_{ini}}{d_{film}} \frac{n_{DBC}^2 - 1}{n_{DBC}^2 + 2} \quad (3.5)$$

Here, the refractive indices of the pure polymer and the pure solvent (in this case water) were used. Their volume fractions were calculated with d_{ini}/d_{film} , and $(d_{film} - d_{ini})/d_{film}$, respectively. By introducing d_{opt} , the film thickness was calculated via Equation 3.6

$$\frac{d_{opt}^2 - d_{film}^2}{d_{opt}^2 + 2 d_{film}^2} = \frac{d_{ini}}{d_{film}} \frac{n_{DBC}^2 - 1}{n_{DBC}^2 + 2} + \frac{d_{film} - d_{ini}}{d_{film}} \frac{n_{DBC}^2 - 1}{n_{DBC}^2 + 2} \quad (3.6)$$

Consequently, the uncertainty of the obtained film thickness and the refractive index was reduced significantly. The described procedure was applied to all SR measurements.

For realizing *in-situ* studies, the thin film samples were mounted in a specialized measurement chamber. This is explained in Section 3.4

Fourier-transform infrared spectroscopy

Fourier-transform infrared spectroscopy (FTIR) probes the molecular structure of a sample [223, 224]. This is used to obtain information about polymer-polymer, polymer-solvent interactions, the hydration state of certain functional groups, and the general solvent content within the thin film samples. The obtained FTIR spectrum usually gives the absorption or transmission intensity as a function of the wavenumber, which is defined to be the spatial frequency of a wave (here an IR light wave), during a certain distance. The frequencies of the absorbed radiation match the vibrational frequencies of molecules. A vibrational mode of a molecule is IR active if it is associated with changes in the molecules dipole moment. Figure 3.6 provides an overview of the different vibrational modes. These

3.3. Spectroscopic characterization

frequencies are assigned to a particular mode of motion and are strongly affected by the masses of the corresponding atoms, the shape of the molecular potential energy surface, and the associated vibronic coupling. Therefore, an FTIR spectrum reveals detailed information about the chemical environment of a (macro)molecule. Hence, dynamic processes, such as diffusion, hydration, and phase transitions of a polymer, where the vibrational frequencies of the polymer change as a consequence of a varied chemical environment, are followed in great detail.

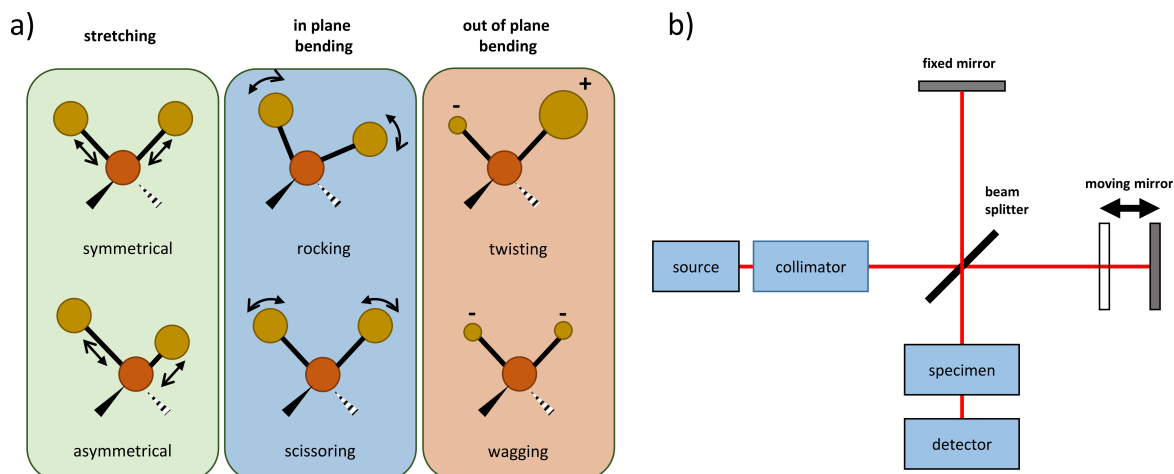


Figure 3.6.: Stretching and bending types of molecules measured with a Michelson interferometer. (a) Possible vibrational modes of molecules. These sketches do not represent the recoil of the center atom (indicated as red sphere), which is necessary to balance the overall movements. (b) Schematic overview of the Michelson interferometer setup.

Instrument: In this thesis, an Equinox 55 FTIR Spectrometer from Bruker Corporation (Billerica, United States of America) was used, which followed the working principle of a Michelson Interferometer. This is shown in Figure 3.6b. A beam splitter divided the incoming IR beam into two beams that were reflected at a fixed and at a moving mirror. This resulted in a difference in the optical pathway of the two IR beams and a superposition of the different wavelengths. The superposition can be expressed mathematically with Equation 3.7.

$$I(x) = I_0 \left[1 + \cos(2\pi\nu x) \right] \quad (3.7)$$

This easy and precise principle was used, to generate constructive interference for all wavelengths, while the intensity was dependent on the optical path length δ according to Equation 3.8.

$$I(\delta) = \int_{-\infty}^{+\infty} I(\nu) \cos(2\pi\nu\delta) d\nu \quad (3.8)$$

Following the Euler equation, the sinus contribution vanishes for even functions, such as a cosine function. Therefore, the Fourier-transformation of Equation 3.8 corresponds to the complex Fourier-transformation, as written in Equation 3.9.

$$I(\nu) = \int_{-\infty}^{+\infty} I(\delta) D(\nu) e^{i 2\pi\nu\delta} d\delta \quad (3.9)$$

With this equation, the IR spectrum $I(\nu)$ was calculated from the interferogram $I(x)$. An exemplary interferogram, a reference spectrum of a bare Si substrate, and the final FTIR spectrum of a polymer thin film are shown in Figure 3.7.

A typical FTIR spectrum was recorded with a resolution of 2 cm^{-1} within a wavenumber range from $300 - 8000 \text{ cm}^{-1}$. The final signal was averaged over 256 scans, which takes approximately 7 min. The FTIR device was constantly purged with a dry and CO_2 filtered air stream, in order to minimize the concentration of IR active molecules, such as H_2O and CO_2 in the beam pathway. A reference of the Si substrate was taken first, and the FTIR spectrum of the thin film sample was recorded under the very same environmental conditions (RH, temperature) and settings (resolution, wavenumber range, scan number). The obtained data of the spectrum underwent the following post-treatment using the software Opus provided by Bruker. First, the spectrum was cut into a suited wavenumber range, which typically was from $600 - 4000 \text{ cm}^{-1}$. Subsequent, a baseline correction via the concave rubber band method was applied. In a final step, an atmospheric compensation removed the remaining vibrational modes of atmospheric H_2O and CO_2 molecules.

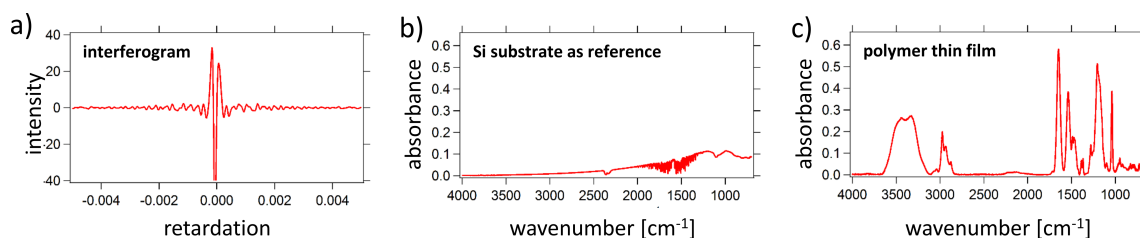


Figure 3.7.: From the interferogram to the FTIR spectrum. (a) The superposition of the incident IR wavelengths results in an interferogram. (b) Typical FTIR spectrum of a bare Si substrate used as reference. (c) Typical FTIR spectrum of a polymer thin film sample.

For analysis, vibrational modes, *e.g.*, O-H and O-D stretching vibrations were integrated with fixed integration limits, which indicated the amount of solvent within the thin films. Integration of the protonated amide II and deuterated II' modes yielded information about deuteration processes. In addition, the peak maximum shifts of functional groups were analyzed in order to reveal their local hydration behavior. Their peak maxima were determined by Gaussian fits.

3.4. Sample environments

The investigation of the response behavior of thin films toward external stimuli *in-situ* is the scientific core of the present thesis. However, the realization of these *in-situ* studies, regarding the control of environmental conditions such as relative humidity (RH), temperature, and vapor composition, is not trivial. It is especially not trivial, considering the space and time limitations, usually present at large scale neutron facilities. In order to tackle these challenges, customized experimental setups were used. In the first part of this section, pre-existing measurement chambers, developed and built by former members of the chair, are described. The second part introduces the 'FlexiProb' sample environment, which was developed and realized in close collaboration with Tobias Widmann.

3.4.1. Pre-existing experimental setup

The following three sub-sections describe older, pre-existing measurement chambers for ToF-NR and ToF-GISANS, SR, and FTIR experiments.

Sample environment for ToF-NR and ToF-GISANS

The measurement chamber was developed by Dr. Panagiotou Panteleimon [225]. It is made from high purity aluminum to avoid element activation upon neutron radiation and consists of a base plate and a lid. Figure 3.8 schematically displays the layout of the measurement chamber. Liquid channels embedded in the base plate were connected to a thermal bath, in order to adjust the temperature inside the chamber. For better thermal isolation, a PTFE plate was placed between the base plate of the chamber and the goniometer setups of the corresponding neutron beamlines. The thin films were mounted vertically (as shown in Figure 3.8) or horizontally on three standing aluminum pins that are located on top of the base plate. A solvent reservoir was placed underneath the mounted thin film sample. By means of a syringe, which was pierced through a septum in the lid, solvents were injected into and removed from the closed chamber, in order to control the ambient RH. A connector to a vacuum pump, located on top of the lid, was used to rapidly decrease the RH within the chamber. Two circular windows, covered with 0.1 mm thick aluminum foil, allowed the neutron beam to enter and exit the chamber with angles of up to 5°. A temperature and RH sensor (usually an SHT31 sensor of the Sensirion AG), soldered to a flexible printed circuit board (PCB) cable, was placed inside the measurement chamber. The PCB cable was pinched between the base plate and the lid and connected to a computer. The described sample environment was used for ToF-NR and ToF-GISANS measurements, discussed in the Chapters 5, 7, and 8.

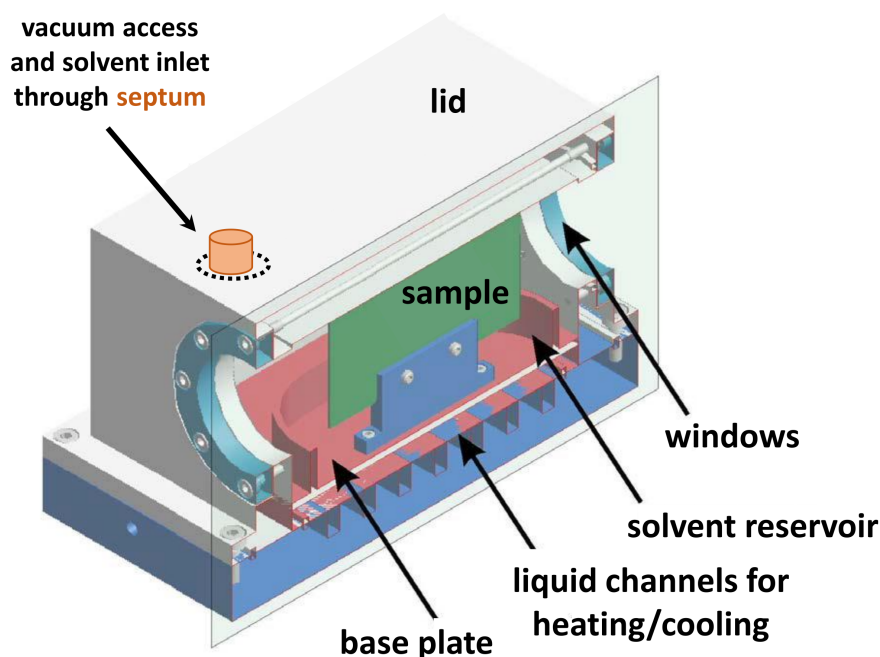


Figure 3.8.: Schematic representation of the pre-existing neutron measurement chamber (for ToF-NR and ToF-GISANS). Adapted from the dissertation of Dr. Panagiotou Panteleimon [225].

Sample environment for SR

The measurement chamber was developed by Dr. Weinan Wang [226]. It is made from stainless steel and is schematically displayed in Figure 3.9. Liquid channels within the base plate and the lid were connected to a thermal bath for temperature control inside the chamber. The thin films were placed horizontally on a sample stage, surrounded by a solvent reservoir. Through a septum in the chamber lid, solvents were injected into and removed from the chamber via a syringe in order to generate a saturated RH. The RH and temperature, were followed with an SHT31 sensor, soldered to a flexible PCB cable. The incident visible light, generated by a halogen lamp, was guided via an optical fiber, to the SR optics, located on top of the chamber lid, and through a highly transmissive CaF_2 window. The light impinged on the thin film after a pathway of approximately 3 cm. The reflected light was guided via the same optical fiber to a detector. In order to prevent condensation at the CaF_2 window, it was heated with a power source. The described sample environment was used for SR measurements, discussed in the Chapters 5, 7, and 8.

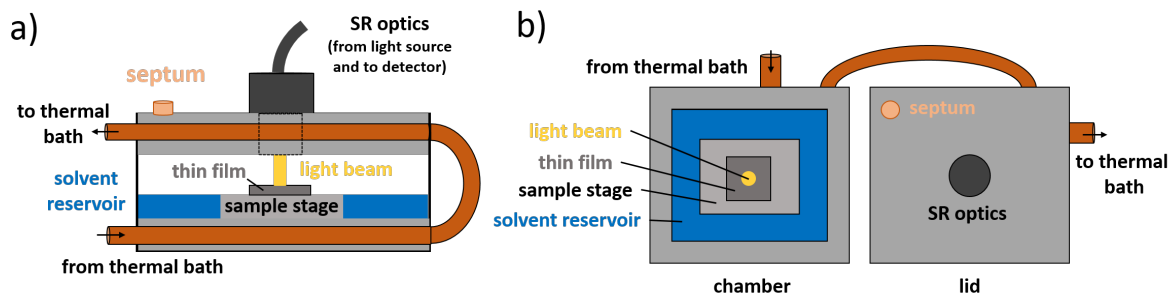


Figure 3.9.: Schematic representation of the pre-existing SR measurement chamber.

Sample environment for FTIR

The FTIR measurement chamber was developed by Prof. Alfons Schulte [227]. It is made from copper and is imaged schematically in Figure 3.10.

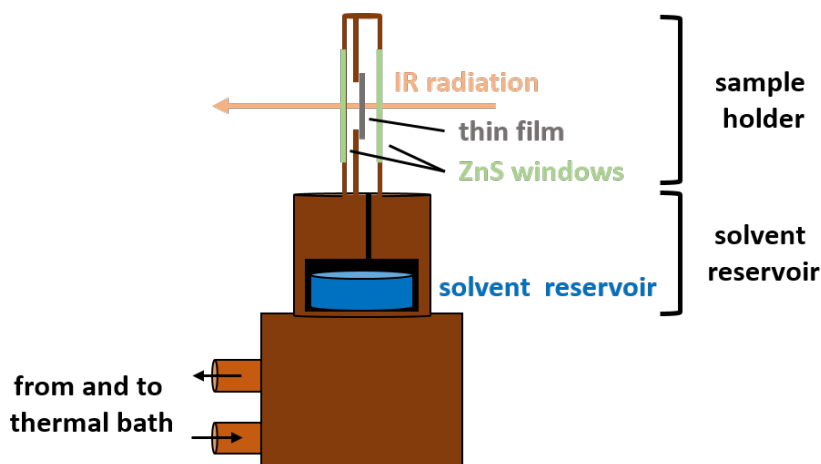


Figure 3.10.: Schematic representation of the FTIR measurement chamber. Adapted from the master thesis of Christian Herold [228].

A solvent reservoir within the lower part of the chamber was connected by a narrow tube with the upper part, which functioned as a sample holder. Once the reservoir was filled with a solvent and screwed to the upper part, the RH inside the sample chamber, increased very slowly. This artificially slowed down increase in RH enabled *in-situ* FTIR measurements. The thin films were fixed with double-faced adhesive tape to a copper ring inside the upper part of the measurement chamber. The copper ring was sandwiched between two ZnS windows, that are highly transmissive to IR radiation. The whole measurement chamber was screwed onto a copper block, which was connected to a thermal bath. RH and temperature inside the chamber were followed with an SHT31 sensor on a PCB cable, which was pinched between the copper ring and one of the ZnS windows. All FTIR measurements presented in this thesis, were performed with the described mea-

surement chamber. For the FTIR experiments described in Chapter 6, a gas flow setup, which is introduced in Section 3.4.2, was connected to the FTIR chamber.

3.4.2. 'FlexiProb' sample environment

The 'FlexiProb' sample environment enables the investigation of polymer thin films in stable and tunable environment conditions, regarding temperature, relative humidity, and vapor composition. This setup, including all components, was developed and realized over the course of this PhD thesis, in close collaboration with Tobias Widmann [229, 230].

The 'FlexiProb' project

The 'FlexiProb' project is an ongoing joint project of three soft-matter groups from the universities of Bielefeld, Darmstadt, and Munich [230–232]. Within this project, each group developed a specialized sample environment, using the same, universal carrier system. In the future, the realized 'FlexiProb' sample environments will be implemented at the small-K advanced diffractometer (SKADI) beamline at the European Spallation Source (ESS), which is currently under construction in Lund, Sweden. Once the ESS is completed, it will provide 22 neutron beam instruments, that are assembled around a spallation neutron target, which is fed by a 5 MW proton accelerator [233]. The ESS will be a pulsed neutron source and will deliver very long neutron pulses of 2.86 ms, with a very high flux and sufficient wavelength resolution *e.g.*, for small-angle scattering applications.

The great advantage of a high-flux pulse is accompanied by new challenges. While measurement times decrease significantly, it will become extremely valuable and an efficient usage of that time is of high importance. Therefore, the developed sample environments can be exchanged via a simple and fast plug and play principle, by using the same carrier platform, and by providing full software integration and control. This enables maximum flexibility with minimal downtimes of the SKADI instrument. In perspective, the project also aims on partially automate the sample change, as due to the high neutron flux, higher radiation is expected at the sample location.

'FlexiProb' sample environment

The Munich 'FlexiProb' sample environment consists of several components. The heart of the sample environment is a 3D-printed UNiVersal Chamber for Observation of Reflectivity with Neutrons (UniCORN) [229]. Other key elements are a gas flow system, a thermal bath, an additional SR device, and a motion control unit [230]. The individual components of the sample environment can be easily installed, connected, substituted,

and dismantled, which reduces the installation of the experimental equipment to a minimum time and effort. In particular, during the scientific tests of the 'FlexiProb' setup at large-scale facilities, this resulted in a highly reliable experimental performance. Furthermore, the unified setup, regarding connectors and adapters, was basically ready-to-use at any given neutron instrument, which significantly reduced the number of meetings and consultations with the corresponding local contacts, prior to the actual measurements. The individual components are briefly described in the following.

UniCORN

UniCORN is a 3D-printed and spherical measurement chamber [229]. It was printed from an aluminum-based AlSi10Mg alloy via selective laser melting (SLM). It was designed by Tobias Widmann via the software SolidWorks 2019. The 3D-printing was done by PROTIQ GmbH (Blomberg, Germany). The spherical and almost edge-less shape prevents condensation and potential solvent spilling on the polymer thin film. Figure 3.11 provides the final chamber draft and the finished 3D-printed UniCORN.

UniCORN consists of two parts, the measurement chamber and the corresponding lid. The measurement chamber contains a sample holder stage, which is fixed on three vertical pillars. On the stage, different sample holder systems can be installed, thereby allowing different sample sizes (from $1 \times 1 \text{ cm}^2$ to $7 \times 7 \text{ cm}^2$) and geometries (vertical and horizontal). Two elliptical windows, covered with 0.1 mm thick aluminum foil, function as an entry and exit window for the neutron beam (maximum exit angle of $\alpha_i = 5^\circ$).

The chamber features connections for a thermal bath (golden connectors), a gas flow system (blue connectors), and an additional LEMO plugin for electronics, such as sensors, light systems, or additional measurement techniques as shown in Figure 3.11. The main feature is a continuous 6 mm broad liquid channel within the chamber and lid walls. The total length of the channel is 2.4 m, and even though, its walls are only 2 mm in thickness, the SLM technique provides sufficient stability. Through these channels a heating or cooling liquid was guided through, which provided excellent thermal control during the performed experiments. In addition, fast temperature changes were feasible. Detailed information to UniCORN is provided in reference [229].

Implementation of a gas flow system

A gas flow system was developed in order to generate a stable and tunable vapor inside UniCORN. A schematic overview of the designed and realized gas flow system can be seen in Figure 3.12. The gas flow system consists of three individual gas streams, which were controlled by three gas flow meters (GFMs) via an RS232 connection. Nitrogen was used as a carrier gas. GFM1 led pure, dry nitrogen directly to UniCORN and was

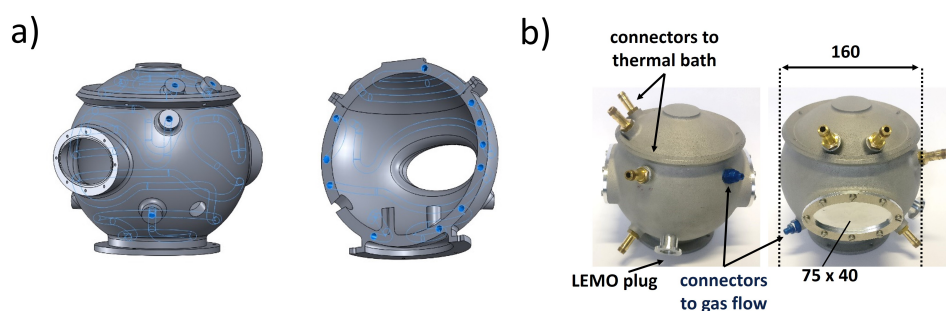


Figure 3.11.: 3D-printed UniCORN. (a) The final draft of the 3D-printed UniCORN. The blue channel indicate the liquid channel within the walls. The cross-section (right) shows the pillars, on which different sample holder systems can be mounted. (b) Real images of UniCORN. The length scales of the chamber itself, the elliptical windows, and the different adapters are labeled accordingly. Adapted with permission from reference [229].

used for drying. GFM2 and GFM3 led the nitrogen through washing bottles, that were filled either with the same or with different solvents, depending on whether the performed experiment required a pure or a mixed vapor. In both cases, the RH within UniCORN was adjusted between 0% RH (GFM1 = 100%, GFM2 = GFM3 = 0%) and a maximum RH of $\approx 96\%$ (GFM1 = 0%, GFM2 = GFM3 = 100%). By mixing the saturated solvent streams with the dry N_2 stream, an intermediate RH was achieved very precisely. Further information to the gas flow system is provided in references [229, 230].

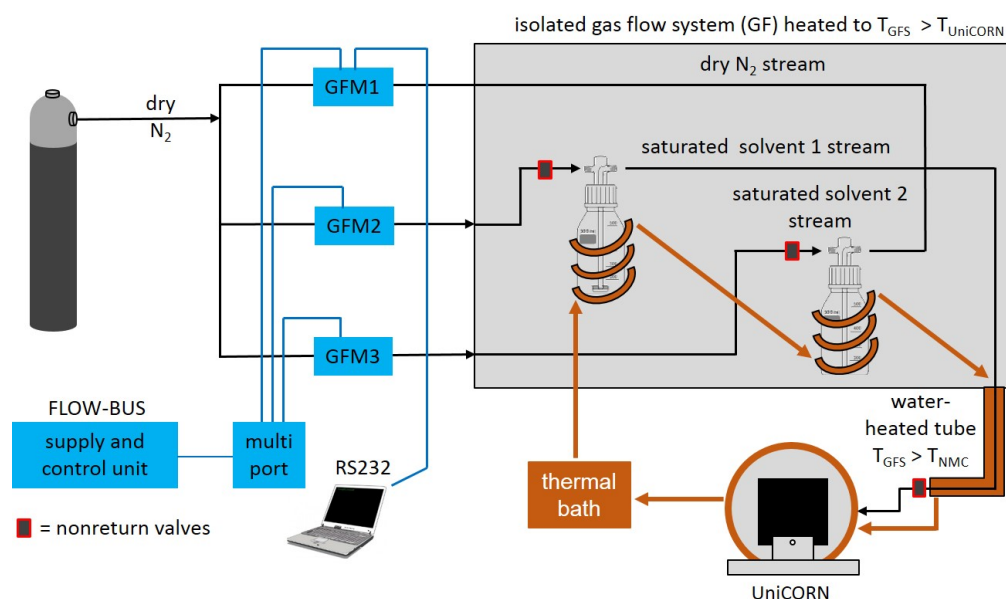


Figure 3.12.: Schematic representation of the designed gas flow system. The gas flow is indicated in black, the heating/cooling circuit in orange, and the electronic control system in blue. Figure adapted with permission from reference [230].

Coupling with spectral reflectance

The coupling of two or several measurement techniques enables to probe a sample at the same environmental conditions. While the inevitable effort may not be underrated, the results are very promising. In the framework of the 'FlexiProb' sample environment, a SR device was successfully coupled with UniCORN [230].

The SR device consisted of a light source (halogen lamp for visible, deuterium lamp for UV light), the spectrometer, optical fiber cables, and an optics extension. The optics extension was attached to the lid of UniCORN. All components are shown in Figure 3.13a. The light beam entered UniCORN through a CaF₂ window (highly transparent for UV/vis light) and was reflected at the mounted thin film sample after a beam pathway of 10 cm (Figure 3.13b). Following the modular approach, it was easy and fast to couple and decouple the SR device. If it was not needed, another lid, without CaF₂ window (cf. Fig. 3.11b) was used.

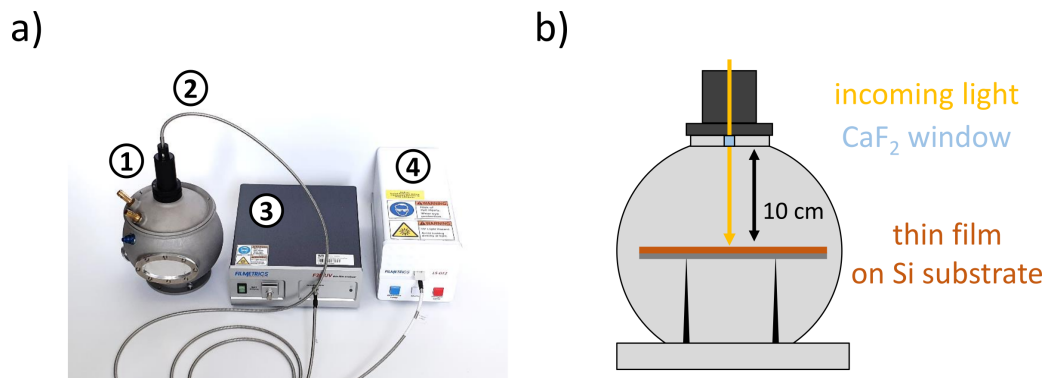


Figure 3.13.: UniCORN coupled with SR device. (a) All components of the coupled SR device and UniCORN. The SR device includes (1) the optics, (2) the optical fiber cables, (3) the spectrometer, and (4) the light source. (b) Schematic drawing of the incoming white light beam (yellow), and a thin film sample (orange) within UniCORN at a distance of 10 cm. Figure adapted with permission from reference [230].

4. Thin film preparation

This chapter provides a full overview of the thin film preparation routine. The first part introduces all materials and polymers used in the thesis. The second part describes the pre-treatment of the substrate material. The last part includes the thin film preparation protocols via different deposition techniques, and potential post-deposition treatments.

4.1. Materials

The chemical structure of all used materials, *i.e.*, solvents, acids, and additives, is shown in Figure 4.1. While TFE was used as solvent for all homo- and diblock copolymers (DBC), de-ionized water, deuterated water, methanol, and deuterated methanol-d3 were used to humidify the vapor around the thin films during measurements. Hydrochloric acid, hydrogen peroxide, and sulfuric acid were used for cleaning purposes. Sodium bromide was added to the polymer solutions prior to spin-coating and drop-casting the thin film samples discussed in Chapter 9. The respective properties and suppliers are briefly described in the following.

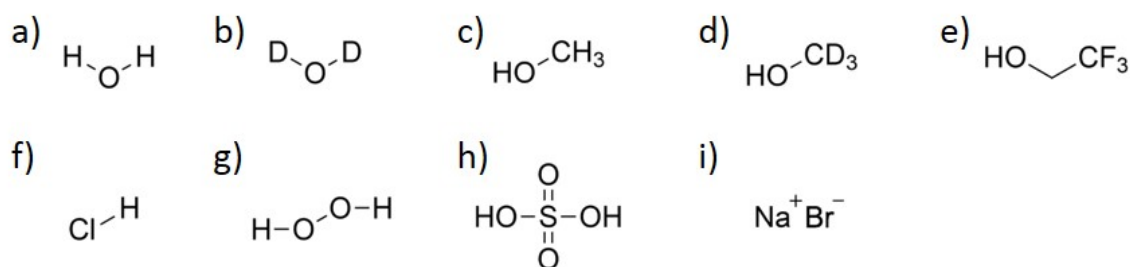


Figure 4.1.: Chemical structure of the used materials. (a) water (H₂O), (b) deuterated water (D₂O), (c) methanol (CH₃OH), (d) deuterated methanol-d₃ (CD₃OH), (e) 2,2,2-Trifluoroethanol (TFE), (f) hydrochloric acid (HCl), (g) hydrogen peroxide (H₂O₂), (h) sulfuric acid (H₂SO₄), and (i) sodium bromide (NaBr).

De-ionized water

Water (H₂O) was de-ionized using a Purelab Chorus 1 purification system (Veolia Water Technologies Deutschland GmbH, Celle, Germany). The de-ionized water featured a resistivity of 18.2 M Ω cm throughout all thin film preparation steps and experimental procedures.

Deuterated water

Deuterated water (D₂O - CAS: 7789-20-0) was used to achieve high contrast in neutron reflectivity and neutron scattering experiments. The D₂O used in the present thesis was purchased from Deutero GmbH (Kastellaun, Germany), and had a purity of 99.95%. It was used without further purification.

Methanol and deuterated methanol-d3

Both, hydrogenated methanol (CH₃OH - CAS: 67-56-1) and deuterated methanol-d3 (CD₃OH - CAS: 1849-29-2) were used to generate a mixed water/methanol vapor as is described in Chapter 6. CH₃OH has a slightly lower molar mass (32.04 g mol⁻¹) and density (0.791 g cm⁻³ at 25 °C) than CD₃OH (35.04 g mL⁻¹ and 0.867 g cm⁻³ at 25 °C). Thus, the vapor pressure of the CH₃OH (13.02 hPa) is higher than of CD₃OH (12.90 hPa), which was taken into account for the calculation of the water/methanol ratio in the mixed vapor. Both methanol species exhibit the same boiling point of 65 °C. Methanol with a purity of ≥ 99.99% was purchased from Carl Roth GmbH + Co. KG (Karlsruhe, Germany), while CD₃OH with a purity of 99.5% was purchased from Deutero GmbH (Kastellaun, Germany). Both solvents were used without further purification.

2,2,2-Trifluoroethanol

2,2,2-Trifluoroethanol (TFE - CAS: 75-89-8) was used as a polar solvent for all homo- and diblock copolymers unless stated otherwise. TFE has a molar mass of 100.02 g mol⁻¹, a density of 1.373 g cm⁻³ (at 25 °C), and a boiling point of 73.6 °C. The solvent was purchased from Sigma-Aldrich Chemie GmbH (Taufkirchen, Germany) with a purity of 99.9% and was used without further purification.

Hydrochlorid acid

Hydrochloric acid, (HCl - CAS: 7647-01-0), is a strong inorganic acid with an acid dissociation constant (pK_a) of -6, a molar mass of 36.46 g mol⁻¹, and a density of 1.19 g cm⁻³ at 25 °C. It was purchased with a purity of 37% from Carl Roth GmbH + Co. KG (Karlsruhe, Germany) and was used for acidic cleaning of the Si substrates without further treatment.

Hydrogen peroxide

Hydrogen peroxide (H₂O₂ - CAS: 7722-84-1) is a weak organic acid (pK_a of 11.8) and a strong oxidation agent. Its molar mass is 34.02 g mol⁻¹ and its density is 1.19 g mL⁻¹. It

was purchased with an assay of 29 - 32% from Carl Roth GmbH + Co. KG (Karlsruhe, Germany) and was used for acidic cleaning of the Si substrates without further treatment.

Sulfuric acid

Sulfuric acid (H_2SO_4 - CAS: 7664-93-9) is similar to HCl a strong inorganic acid with a pK_a of -3. It has a molar mass of 98.08 g mol^{-1} and a density of 1.84 g mL^{-1} at $25 \text{ }^\circ\text{C}$. It was purchased with a purity of 95 - 98% from Carl Roth GmbH + Co. KG (Karlsruhe, Germany) and was used for acidic cleaning of the Si substrates without further treatment.

Sodium bromide (NaBr)

Anhydrous sodium bromide (NaBr - CAS: 7647-15-6) is an inorganic salt with a cubic crystal structure. The white solid has a molar mass of $102.89 \text{ g mol}^{-1}$ and a density of 3.21 g mL^{-1} . NaBr was added to the polymer solution before spin-coating and drop-casting thin film samples that are discussed in Chapter 9. It was purchased from Sigma-Aldrich Chemie GmbH (Taufkirchen, Germany) and was used without further purification.

4.2. Functional polymers

The following sections give an overview of the investigated homopolymers and DBCs. Their chemical structures are imaged in Figure 4.2. At the end of this section, Table 4.1 summarizes the polymer characteristics, *e.g.*, the molecular weight M_n and the respective block lengths. Furthermore, the chapters, in which the respective polymers are investigated, are provided. All polymers were synthesized and characterized by the Chair of Applied Chemistry (Prof. André Laschewsky) of the Chemistry Institute at the University of Potsdam. The dissertation of Dr. Viet Hildebrand provides detailed information about the respective synthesis routes and polymer characterizations. The respective UCST- and LCST-type transitions (also denoted as clearing and cloud point CP'_{UCST} and CP_{LCST} in the following) of the polymers were determined via turbidimetry measurements on polymer solutions with a concentration of 5 wt% [126].

PSPE₂₇₀

Poly(3-((2-(methacryloyloxy)ethyl)dimethylammonio) propane-1-sulfonate) (PSPE) belongs to the polymer class of zwitterionic polymers. Zwitterionic means, the polymer exhibits the same amount of anionic and cationic charges within one constitutional repetition unit. Poly(sulfobetaine)s (PSBs) possess a cationic quarternary ammonium and an anionic sulfonate group. Both ionic groups are located in the side chain of the carbon backbone. The letters 'P' and 'E' in the abbreviation PSPE, refer to the spacing between the ester and the quarternary ammonium cation, and to the spacing between the quarternary ammonium to the sulfonate group, which is three C-atoms (Propyl group)

and two C-atoms (Ethyl group) in length, respectively. Figure 4.2a gives the chemical structure of PSPE, while Section 2.2.1 provides further information to the polymer class of PSBs.

The studied PSPE homopolymer has 270 repetition units, with a theoretical molecular weight of 76 kg mol^{-1} . UV-vis analysis, via the end groups, gave a M_n of 88 kg mol^{-1} (cf. Table 4.1). This PSPE homopolymer features an UCST-type transition at 55°C in H_2O and 68°C in D_2O , respectively (cf. Table 4.2), which was determined via turbidimetry by our partners from Potsdam [126]. The polymer was received as yellowish powder and was used as received.

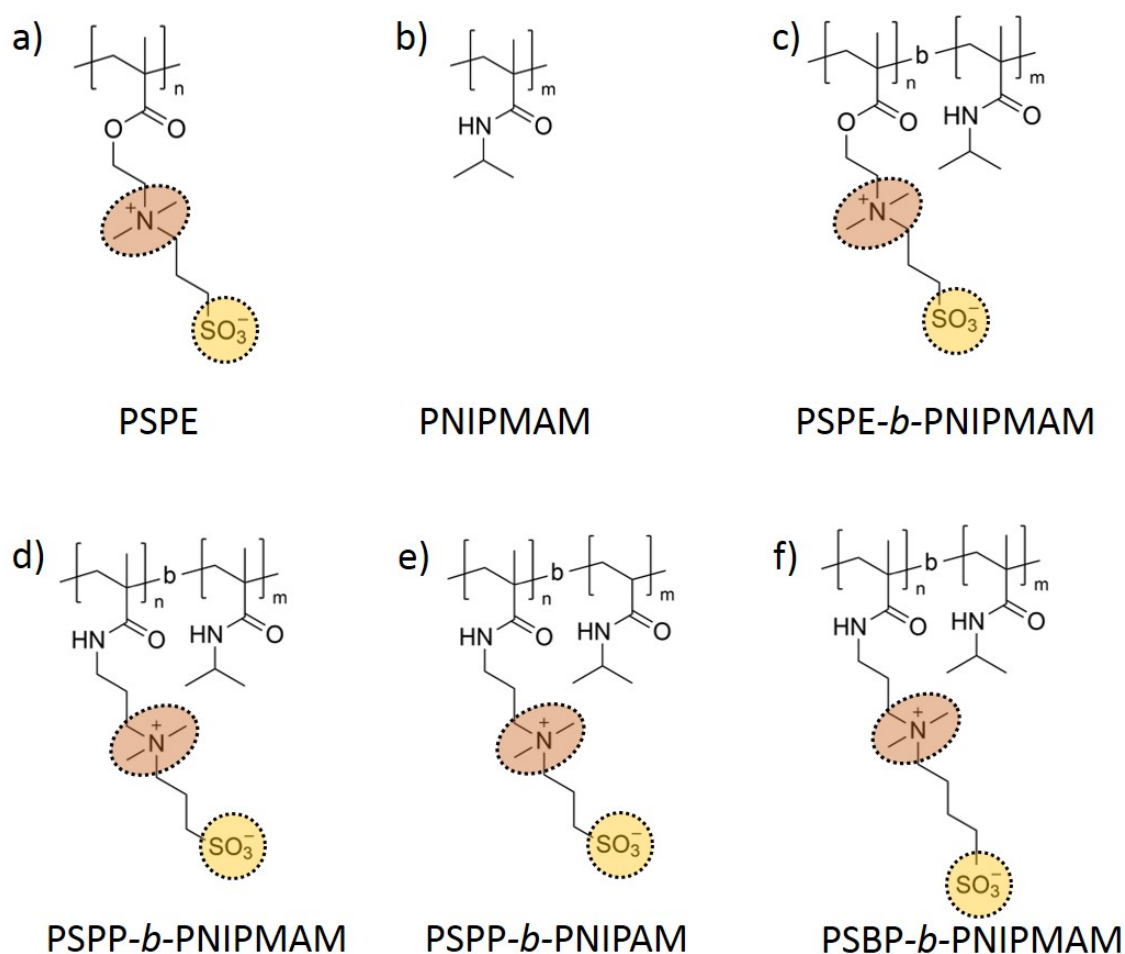


Figure 4.2.: Chemical structures of the polymers under investigation. (a) PSPP ($n = 270$), (b) PNIPMAM ($m = 65$), (c) PSPE-*b*-PNIPMAM ($n = 270$, $m = 60$), (d) PSPP-*b*-PNIPMAM ($n = 500$, $m = 150$), (e) PSPP-*b*-PNIPAM ($n = 80$, $m = 105$), and (f) PSBP-*b*-PNIPMAM ($n = 245$, $m = 105$). The charged groups of the zwitterionic PSBs are highlighted.

PNIPMAM₆₅

In contrast to the zwitterionic PSBs, poly(*N*-isopropylmethacrylamide) (PNIPMAM) is a nonionic homopolymer. Its side chain contains a hydrophilic amide group and a hydrophobic isopropyl group. PNIPMAM features a lower critical solution temperature (LCST), and therefore undergoes a coil-to-globule collapse transition upon heating. One should note, with increasing molecular weight, the LCST increases as well. Section 2.2.1 provides further information about the thermal behavior of PNIPMAM.

PNIPMAM was received as white powder. The characterization, done by our collaboration partners in Potsdam, yielded a theoretical molecular weight of 9 kg mol⁻¹, which was confirmed by UV-vis spectroscopy and corresponds to a block length of 65 monomer units per polymer chain. Turbidimetry measurements revealed a LCST-type transition at 32 °C in H₂O and 33 °C in D₂O, respectively (cf. Table 4.2) [126]. The homopolymer was used as received without further treatment.

PSPE₂₇₀-*b*-PNIPMAM₆₀

Appropriate homopolymers, featuring an UCST and a LCST, can be connected to orthogonally dual thermo-responsive diblock copolymers. Section 2.2.1 provides detailed information about the behavior of such polymers.

PSPE₂₇₀-*b*-PNIPMAM₆₀ consists of the zwitterionic PSPE and the nonionic PNIPMAM blocks. The chemical structure is provided in Figure 4.2c. The DBC was received as a yellowish powder and was used without further treatment. Turbidimetry measurements yielded an UCST-type transition at 54 °C in H₂O and 57 °C in D₂O, as well as a LCST-type transition at 47 °C in H₂O and 46 °C in D₂O, respectively (cf. Table 4.2) [126]. Thus, the CP'_{UCST} is lower, while the CP_{LCST} is higher than the critical solution temperatures of the corresponding homopolymers. This demonstrates the high sensitivity of both blocks to the polymer architecture and the impact of the PSPE on the PNIPMAM block and vice versa.

PSPP₅₀₀-*b*-PNIPMAM₁₅₀

PSPP₅₀₀-*b*-PNIPMAM₁₅₀ consists of a zwitterionic poly(*N,N*-dimethyl-*N*-(3-methacrylamidopropyl)-ammonio-propane sulfonate) (PSPP) block and a nonionic PNIPMAM block. The chemical structure of the PSPP block (cf. Figure 4.2d), slightly differs from the PSPE block, that is introduced above, as the ester group was substituted by an amide group. The distance between the amide and the quarternary ammonium, as well as between the quarternary ammonium to the sulfonate group, was three C-atoms in length.

PSPP₅₀₀-*b*-PNIPMAM₁₅₀ was received as a yellowish powder and was used without further treatment. The critical solution temperatures are listed in Table 4.2. Characterization via turbidimetry yielded an UCST-type transition at 24 °C in H₂O and 31 °C in D₂O, and a LCST-type transition at 48 °C in H₂O and 49 °C in D₂O (cf. Table 4.2) [126].

PSPP₈₀-*b*-PNIPAM₁₃₀

PSPP₈₀-*b*-PNIPAM₁₃₀ consists of the zwitterionic block PSPP and the nonionic block PNIPAM (cf. Figure 4.2e). The LCST-type transition was found at ≈ 32 °C, while the UCST-type transition was below 26.5 °C. One has to note that the exact values of the CP'_{UCST} and the CP_{LCST} were not measured within the framework of this thesis and also not by our collaboration partners in Potsdam. The examination of PSPP₈₀-*b*-PNIPAM₁₃₀, as described in Chapter 5, is performed at 26.5 °C, which is supposed to be above the clearing point of the PSPP block (CP'_{PSPP}) and still below the cloud point of the PNIPAM block (CP_{PNIPAM}), due to the following reasons:

Vishnevetskaya and coworkers presented the transmission curve of a 10 g L⁻¹ PSPP₄₃₀-*b*-PNIPAM₂₀₀ solution in salt-free D₂O [26]. It also consists of a PSPP and PNIPAM block, however with different block lengths. While the CP'_{PSPP} was around 18 °C, the CP_{PNIPAM} was around 34 °C. In addition, Hildebrand et al. [127] demonstrated, a shorter block length leads to a lower CP'_{PSPP} . Hence, we conclude, the CP'_{PSPP} of the here investigated PSPP₈₀-*b*-PNIPAM₁₃₀ is lower than 18 °C in D₂O. According to Niebuur et al. the CP'_{PSPP} was even lower in H₂O solution [130].

Furthermore, it was found, the CP'_{PSPP} of a 5wt% solution of the homopolymer PSPP₈₀ (same block length than the PSPP block used in Chapter 5) was 8.7 °C in H₂O and 14.7 °C in D₂O [130]. According to reference [26] the CP'_{PSPP} was even further decreased by adding a PNIPAM block to the PSPP block. Thus, the CP'_{PSPP} of PSPP₈₀-*b*-PNIPAM₁₃₀ should be lower than 8.7 °C and 14.7 °C in H₂O and D₂O, respectively.

The M_n of PNIPAM was found to have a minor impact on the CP_{PNIPAM} [139]. Thus, the CP_{PNIPAM} of PSPP₈₀-*b*-PNIPAM₁₃₀ should not vary significantly from the CP_{PNIPAM} of PSPP₄₃₀-*b*-PNIPAM₂₀₀ (34 °C in D₂O). Furthermore, recent studies showed, neighboring blocks had no (if the neighboring block is hydrophobic) or small (if the neighboring block is hydrophilic) impact on the CP_{PNIPAM} of the PNIPAM block [234, 235]. Thus, the PSPP block of PSPP₈₀-*b*-PNIPAM₁₃₀ would lead to a shift of CP_{PNIPAM} to higher temperatures and the hydrophilic range would even increase.

Summarized, the chosen measurement temperature of 26.5 °C in 5 is above the CP'_{PSPP} and below the CP_{PNIPAM} of the corresponding PSPP and PNIPAM blocks, in H₂O and D₂O solution.

PSBP₂₄₅-*b*-PNIPMAM₁₀₅

PSBP₅₀₀-*b*-PNIPMAM₁₄₅ consists of a zwitterionic poly(4-((3-(methacrylamidopropyl)dimethylammonio)butane-1-sulfonate) (PSBP) block, which features a butyl group between the quarternary ammonium and the sulfonate group, and a nonionic PNIPMAM block. Its chemical structure is provided in Figure 4.2f. Turbidimetry measurements revealed an UCST-type transition of above 26.5 °C and a LCST-type transition of ≈ 32 °C in H₂O and D₂O solution (cf. Table 4.2) [126]. PSPP₅₀₀-*b*-PNIPMAM₁₄₅ was received as yellowish powder and was used without further treatment.

Table 4.1.: Analytical data of the polymers used in the respective chapters. The values are taken from the dissertation of Dr. Viet Hildebrand [126].

^{a)}the signal intensity was too weak to allow a reliable integration.

polymer	M _n [kg mol ⁻¹]			Chapter
	theoretical	by ¹ H-NMR	by UV-vis	
PSPE ₂₇₀	76	n.d. ^{a)}	88	6
PNIPMAM ₆₅	9	9	9	6
PSPE ₂₇₀ - <i>b</i> -PNIPMAM ₆₀	84	79	77	6
PSPP ₅₀₀ - <i>b</i> -PNIPMAM ₁₅₀	165	156	151	7 and 8
PSPP ₈₀ - <i>b</i> -PNIPAM ₁₃₀	n.d. ^{a)}	n.d. ^{a)}	n.d. ^{a)}	5
PSBP ₂₄₅ - <i>b</i> -PNIPMAM ₁₀₅	88	83	86	9

Table 4.2.: Temperatures of the UCST-type and LCST-type transitions of the polymers used in this thesis in 5wt % H₂O and D₂O solution, respectively. The values are taken from the dissertation of Dr. Viet Hildebrand [126].

^{a)}These values were determined based on the argumentation in the main text.

polymer	UCST-type transition [°C]		LCST-type transition [°C]	
	in H ₂ O	in D ₂ O	in H ₂ O	in D ₂ O
	PSPE ₂₇₀	55 °C	68 °C	–
PNIPMAM ₆₅	–	–	32 °C	33 °C
PSPE ₂₇₀ - <i>b</i> -PNIPMAM ₆₀	54 °C	57 °C	47 °C	46 °C
PSPP ₅₀₀ - <i>b</i> -PNIPMAM ₁₅₀	24 °C	31 °C	48 °C	49 °C
PSPP ₈₀ - <i>b</i> -PNIPAM ₁₃₀	< 26.5 °C ^{a)}	< 26.5 °C ^{a)}	≈ 32 °C ^{a)}	≈ 32 °C ^{a)}
PSBP ₂₄₅ - <i>b</i> -PNIPMAM ₁₀₅	> 47 °C	> 47 °C	49 °C	49 °C

4.3. Si substrate and pre-deposition treatment

Substrate effects contribute greatly to the thin film behavior. Thus, the choice of the substrate is of high importance, and throughout the present thesis silicon (Si) was used as substrate material. Its low surface roughness provides excellent conditions for thin film deposition. Furthermore, Si is nontransparent for ultra-violet (UV) and visible light, but transparent for infrared (IR) light. Thus, it is an optimal substrate material for spectral reflectance (SR) (UV and visible light is reflected) and Fourier-transform infrared (FTIR) spectroscopy (IR light is transmitted).

Si substrate

Silicon substrates, purchased from Silicon Materials (Kaufering, Germany) were used throughout all measurement in this thesis. The p-doped, round-shaped Si wafers were 100 mm in diameter, 0.525 mm in thickness, and had a resistivity of 10 - 20 Ω cm. The wafers were polished on one side, thus exposing the (100) crystal orientation. The surface roughness of the polished side was $R < 0.5$ nm. The wafers were pre-scratched by a diamond cutter to a desired substrate size. They were broken along the scratch, which gave sharp and well-defined edges. Typical substrate sizes were: 1 × 1 cm² for FTIR, 2 × 2 cm² for SR, and 7 × 7 cm² for ToF-NR and ToF-GISANS experiments.

Acid cleaning

Substrate-polymer interactions have a major impact on the final thin film quality, regarding its homogeneity, and morphology. Therefore, any impurities on the surface of the Si substrate must be removed prior to polymer deposition. This was done with a modified piranha acid bath [236]. A glass beaker was put in a water bath on a heating plate. Successively, H₂O (54 mL), H₂O₂ (84 mL), and H₂SO₄ (198 mL) was filled into the glass beaker and slowly heated to 80 °C. A watch glass was put on the beaker to prevent evaporation. While the acid bath heated up, the cut Si substrates were placed into a poly(tetrafluoroethylene) (PTFE) substrate holder. The Si substrates were rinsed with water to remove any dust or residual Si particles from the cutting process, and subsequent were placed in the heated acid bath. Besides the removal of any organic traces, the acid bath oxidized the silicon surface and generated a hydrophilic SiO_x layer. It is noteworthy to mention, the duration of the acid bath had a serious impact on the formation of SiO_x surface layers on top of the Si substrate. After 15 min, the substrates were removed from the acid bath and were transferred to two beakers filled with 500 mL of de-ionized H₂O. Thereby, most acidic residuals were already washed off. To assure acidic-free Si substrates, the individual substrates were rinsed again separately with another 500 mL of H₂O. To further hydrophilize the surface, an oxygen plasma was applied.

Oxygen plasma

The thin films were exposed to an oxygen plasma in a Nano Plasma Cleaner from Diener Electronic (Ebhausen, Germany). The clean and dry Si substrates were placed in a glass beaker, which then was placed in the vacuum chamber of the plasma oven. After an oxygen atmosphere with a pressure of 0.4 mbar was established, the plasma treatment was induced by applying a frequency of 40 kHz at 250 W. The combination of low-pressure and energy caused the oxygen gas to ionize and become plasma. The plasma ions hit the Si surface, which consequently oxidized. During further bombardment of oxygen ions, polar hydroxyl groups were formed. In addition, any organic compounds, that survived the acid bath, were decomposed by the oxygen radicals and were removed via a vacuum pump. After 10 min, the plasma treatment was finished, and the hydrophilized substrates were removed from the vacuum chamber. One has to note, the effect of the plasma treatment and the hydrophilized surface only lasts for several minutes. To take full advantage, polymer deposition was performed immediately after the plasma treatment. Polymer-deposition on the hydrophilized substrate results in a strong physical bonding of the thin films to the substrate, and therefore ensures an intact film surface and substrate-film interface without de-lamination or de-wetting throughout all performed experiments.

4.4. Thin film preparation

Polymer thin films were prepared via spin-coating and drop-casting. In addition, solvent vapor annealing (SVA) was applied to the the spin-coated thin films. Both deposition techniques as well as SVA are briefly introduced in the following.

Spin-coating

Spin-coating is a common technique to prepare uniform thin films by depositing usually small amounts of material on a flat substrate, that is rotating (dynamic spin-coating) or is not rotating (static spin-coating). The main advantage is, that thin films of high homogeneity are prepared on a reliable and fast basis. In this thesis, Delta6 RC TT (Süss Microtec Lithography GmbH, Garching, Germany) was used for static spin-coating. The cleaned and plasma-treated Si substrate was fixed to the rotating plate either by vacuum (for Si substrates of $2 \times 2 \text{ cm}^2$) or by a custom-made mounting system (for Si substrates of $7 \times 7 \text{ cm}^2$ in size). The polymer, dissolved in TFE, with a typical concentration of $15\text{-}30 \text{ g L}^{-1}$, was pipetted onto the substrate, thereby covering the whole substrate. The volume depended on the substrate size. Usually $250 \mu\text{L}^{-1}$ were used for $2 \times 2 \text{ cm}^2$ substrates, while $2000 \mu\text{L}^{-1}$ were used for $7 \times 7 \text{ cm}^2$ substrates. TFE is a good solvent for the respective homopolymers and DBCs and yields water-free thin films. For the thin films discussed in Chapter 9 thin films were spin-coated from TFE solution with a NaBr concentration of 0, 2, 10, and 20 mM. The spin-coating stage was covered with a glass beaker, in order to create a saturated solvent atmosphere around the thin film. This led to a slower drying process, and a longer regime of swollen and mobile polymer chains, which was beneficial for healing defects and removing kinetically frozen artefacts.

The spin-coating procedure started immediately afterwards. Parameters, such as rotation speed and time were preset and typically amount to 2500 rpm and 900 s. The acceleration of the spin-coating stage was fixed to ACL9, which was equivalent to a time of approximately 6 s until the final rotation speed was reached. While these parameters were fixed, the concentration of the polymer solution varied, in order to tune the final film thickness of the polymer thin films. The thickness d_{film} was determined by the following equation by Schubert [237].

$$d_{film} = C c_0 \omega^{-1/2} M_w^{1/4} \quad (4.1)$$

The experimental parameter C has to be determined empirically for each sample system. Since the samples under investigation are very similar, this parameter is considered to be constant. The polymer concentration c_0 is the key factor for the final film thickness d . ω

4.4. Thin film preparation

denotes the angular velocity and M_w is the molecular weight of the solvent. A schematic overview of the spin-coating procedure is provided in Figure 4.3.

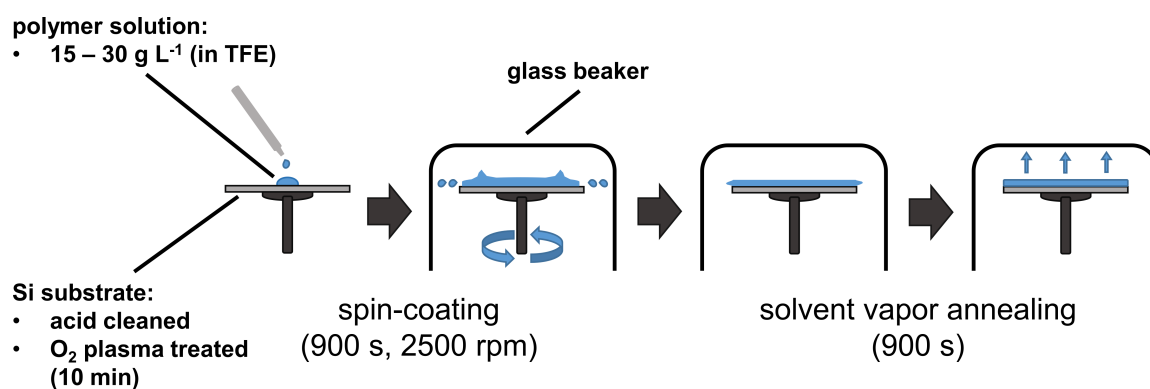


Figure 4.3.: Schematic overview of the spin-coating deposition protocol.

Since TFE is a very polar solvent, it was highly challenging to achieve homogeneous thin films out of TFE solution and included a lot of parameter screening. Furthermore, it was not trivial to spin-coat thin films with a homogeneous polymer distribution on large Si substrates ($7 \times 7 \text{ cm}^2$). To overcome these two main challenges, the spin-coating time was set to 900 s and SVA annealing was applied to all thin films directly after the spin-coating process had finished, for further 900 s. Figure 4.4 displays the effect of optimized spin-coating parameters and the subsequent SVA on the homogeneity of the thin films.

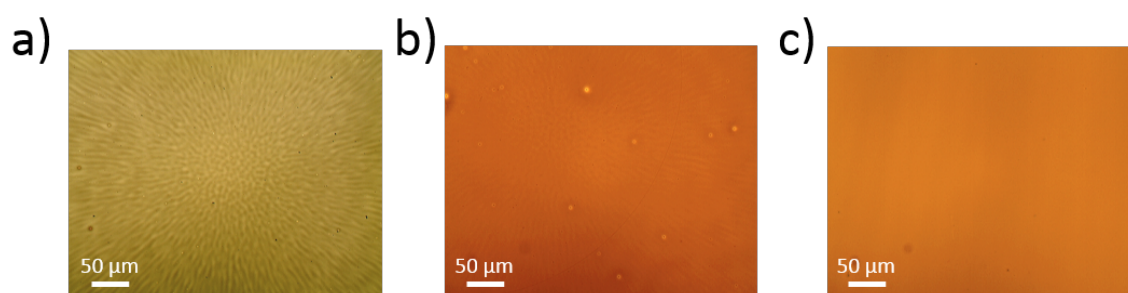


Figure 4.4.: Effect of spin-coating parameters and SVA on homogeneity of the resulting polymer thin film. (a) pronounced spin-coating star due to omission of SVA. (b) Spin-coating with non-optimized parameters and subsequent SVA results in a weakly pronounced spin-coating star. (c) Optimized spin-coating parameters (2500 rpm, 900 s) and SVA lead to a homogeneous polymer thin film. The different colors are due to different thin film thicknesses.

Despite the high homogeneity of the sample surface, edge effects occurred, due to the squared substrate geometry as well as due to rough edges (from the cutting process). While these edge effects might not affect local techniques, *e.g.*, AFM, SR, and FTIR, they affect neutron reflectivity and scattering techniques, as these methods typically illuminate a large sample area. Thus, the Si substrates, used in neutron experiments were pre-scratched prior to spin-coating deposition, and the edges were cut off after the spin-coating and SVA had finished. Figure 4.5 displays edges of the Si substrate with a deposited polymer thin film on top, where the increased film thickness at the edges and multiple macroscopic thin film defects are clearly visible.

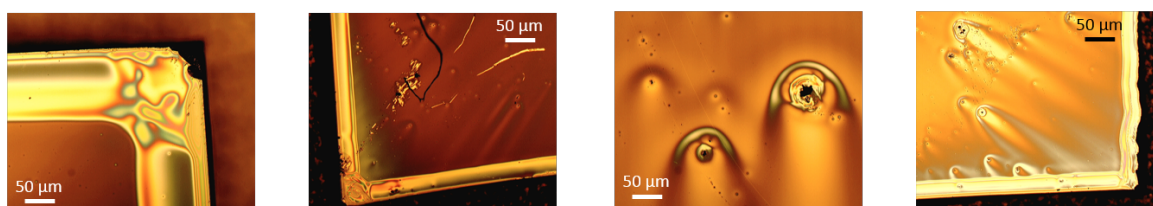


Figure 4.5.: Edge effects after polymer deposition via spin-coating. An increased film thickness and macroscopic thin film defects are observed at the substrate edges.

Drop-casting

Drop-casting is a very fast and easy deposition technique that yields thin films with a thickness in the μm range. The prepared thin films were dome-shaped and featured a stronger surface curvature as well as a higher heterogeneity than the spin-coated samples. Hence, interference effects on thin films were suppressed, which was in particular beneficial for FTIR measurements. Furthermore, the drop-cast films were thicker and provided longer pathways of the IR radiation through the thin film, thereby yielding an improved signal to noise ratio. Typically, the polymer solution had a concentration of 30 g L^{-1} . For drop-casting a solution volume of only $7\text{-}10 \mu\text{L}$ was pipetted onto a Si substrate. The substrate had a size of $1 \times 1 \text{ cm}^2$ and was cleaned via an oxygen plasma for 10 min. In order to enhance the curvature of the polymer solution even more, a time of 25 min after the plasma treatment and before the drop-casting, was waited. This led to a better de-wetting behavior of the polymer solution, and therefore, to thicker thin films with a higher surface curvature. A schematic overview of the drop-casting procedure is provided in Figure 4.6

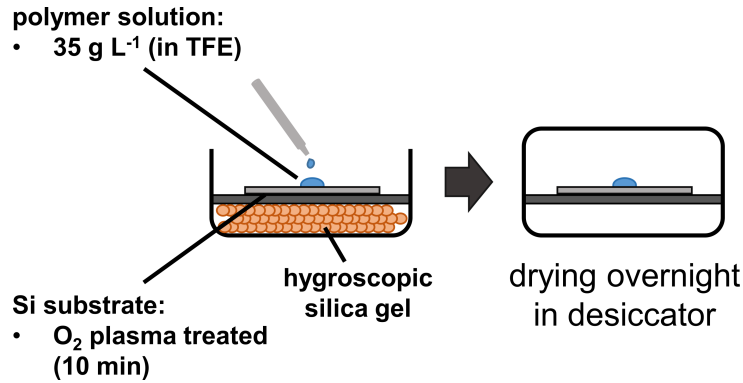


Figure 4.6.: Schematic overview of the drop-casting technique.

Solvent vapor annealing

Solvent vapor annealing (SVA) is a commonly used, thermodynamically-driven technique to generate highly homogeneous thin films. It is also applied to enhance microphase separation of DBCs in thin film geometry [50, 52-57]. Thin films are exposed to a saturated atmosphere of one or more solvents (typically several minutes to few hours) at a temperature well below the bulk glass transition temperature T_g of the polymer (or the polymer blocks in a DBC). This causes the polymer to swell and therefore, its chain mobility increases. While non-selective solvents heal defects and remove kinetically frozen artefacts, selective solvents lead to highly ordered thin film morphologies (different from the bulk). The SVA treatment was applied immediately after the spin-coating procedure had finished as is indicated in Figure 4.3. The thin films, remained on the spin-coating stage and under the glass beaker in a saturated TFE atmosphere for another 900 s. Table 4.3 summarizes the settings of the spin-coated (SC) and drop-cast (DC) thin film deposition protocols.

Table 4.3.: Applied settings for the spin-coating (SC) and drop-casting (DC) thin film deposition protocols.

deposition method	acid bath	O ₂ plasma	SC speed [rpm]	SC time [s]	c [g L ⁻¹]	V [μ L]	SVA
SC (2 × 2 cm ²)	yes	yes	2500	900	15 - 30	250	yes
SC (7 × 7 cm ²)	yes	yes	2500	900	15 - 30	2000	yes
DC (1 × 1 cm ²)	no	yes	–	–	35	7 - 10	no

5. Isotope-sensitive thin film swelling and exchange kinetics

This chapter is based on the publication 'Swelling and Exchange Behavior of Poly(sulfo betaine)-Based Block Copolymer Thin Films' (L. P. Kreuzer et al., *Macromolecules* **2019**, 52, 3486-3498; DOI: 10.1021/acs.macromol.9b00443) [36]. Reprinted with permission from AMERICAN CHEMICAL SOCIETY, Copyright 2019. Experiments were performed in collaboration with bachelor student Leander Peis [238].

Responsive polymers are able to change their chain conformation as response to even slight variations in their surroundings. While in responsive polymer hydrogels, this behavior can be used to store and release large quantities of water in response to an external stimulus [1, 76, 77], responsive polymer thin films are able to switch between a swollen and a contracted thin film, which refers either to elongated or to coiled polymer chains. Due to the dimension on the nanoscale, responsive thin films are often applied in the fields of soft-robotics [2, 3], sensors [13, 87, 90, 239], and responsive surfaces or coatings [7, 8, 10, 12]. For these fields, a controlled sorption, release, and diffusion of gaseous and liquid penetrants is crucial. Inevitably, polymer thin films are exposed to a surrounding atmosphere, which in most cases is simply air, containing a certain amount of water and other small molecules. As the diffusion of these molecules is driven by the osmotic pressure, they can easily penetrate into the thin film. Recent studies revealed, this was typically accompanied by a swelling and plasticization, *i.e.*, the film became thicker and softer [58-60]. Also, its morphology and other film properties might be altered. Prior to the implementation in potential future applications, a fundamental understanding of the underlying mechanisms of the sorption and release of water is essential, especially for new types of polymers. Such a new type of responsive polymer is introduced and analyzed in the following.

Introduction

Within the last years, more and more scientific attention was paid to orthogonally dual thermo-responsive, so called 'schizophrenic' DBCs that consisted of a zwitterionic poly(sulfobetaine) (PSB) block and a nonionic poly(*N*-isopropylacrylamide) (PNIPAM) or a poly(*N*-isopropyl methacrylamide) (PNIPMAM) block [25, 27, 31]. In these DBCs the PSB block featured an upper critical solution temperature (UCST), the PNIPAM and PNIPMAM block were well known for their lower critical solution temperature (LCST). Section 2.2.1 provides a detailed description of these two polymer types and their corresponding DBCs.

The phase behavior of PSBs and PNIPAM homopolymers in dilute and concentrated solutions was described and analyzed in great detail, as was the behavior of their bulk hydrogels, micellar systems, and brushes in various solvents [91, 127, 128, 130, 240-242]. Literature provides also information, although to a smaller extent, about the behavior of diblock copolymers (DBC), made from PSBs and PNIPAM, in aqueous solution [25-27, 31, 127, 235]. In particular, the phase transition temperature of PSB, usually denoted as clearing point CP'_{PSB} , was found to be highly sensitive to various parameter, such as molar mass, monomer architecture, and salt additives [20, 26, 27, 129, 242]. Furthermore, recent studies demonstrated a strong isotope sensitivity of the CP'_{PSB} , most prominently toward different water species and typically, the CP'_{PSB} was located at lower temperatures in H_2O than in D_2O [130, 242]. This was mainly addressed to an altered nature of H- and D-bonds, respectively, due to H_2O and D_2O having a different mass, electronegativity, and dipole moment. The cloud point of PNIPAM (CP_{PNIPAM}), was found to be stable in both water types [19].

In contrast to the solution behavior, less is known about their behavior of such dual thermo-responsive DBCs in thin film geometry. Due to the high polymer concentration, the thin film behavior is mainly governed by polymer-polymer interactions, and not by polymer-solvent interactions as it is the case in dilute solutions. Also, interfacial effects gain influence on dynamic diffusion or exchange processes and therefore, an extrapolation of the polymer solution behavior to thin film geometry is impossible. So far, very few studies investigated thin film swelling processes in saturated water vapor, and in most studies the focus was set on standardized DBCs systems, *e.g.*, poly(styrene)-*b*-poly(methylmethacrylate) (PS-*b*-PMMA) or PNIPAM-*b*-PMMA, in which only one polymer block was stimuli-responsive [59, 68, 243]. Further information to thin films in saturated vapors is provided in Section 2.1.2

While a fundamental understanding of PSB-based dual thermo-responsive DBCs in thin film geometry is still missing, the present thesis aims to close this gap. In a first step, we investigate the swelling and exchange behavior of such thin films in H_2O and

D₂O. The DBC under investigation consists of a zwitterionic poly(*N,N*-dimethyl-*N*-(3-(methacrylamido)propyl)ammonio-propanesulfonate) (PSPP) block and a longer nonionic PNIPAM block (PSPP₈₀-*b*-PNIPAM₁₃₀). In the following, the DBC is referred to as PSPP-*b*-PNIPAM. Its chemical structure together with a detailed characterization can be found in Section 4.2 (cf. Figure 4.2e).

The following study is based on two individual experiments. In a first experiment, the swelling of the PSPP-*b*-PNIPAM thin film in H₂O vapor is followed, before the vapor is changed from H₂O to D₂O (will be named 'D₂O exchange' hereafter). A second experiment follows first the swelling in D₂O vapor, before it is exchanged to a H₂O vapor ('H₂O exchange'). Figure 5.1 schematically displays the experimental protocol. This study yields new insights into the swelling and in particular into the exchange mechanisms in thin films. Furthermore, the isotope sensitivity of the PSPP block is addressed by using different water species. Please note, in aqueous solution, the corresponding PSPP homopolymer featured a significant lower UCST-type transition in H₂O (8.7 °C) than in D₂O (14.7 °C) [130]. For this first study, the temperature is kept constant at 26.5 °C throughout both experiments. At this temperature, both polymer blocks are expected to be soluble in H₂O and D₂O (cf. also Section 4.2), which promotes a large water uptake.

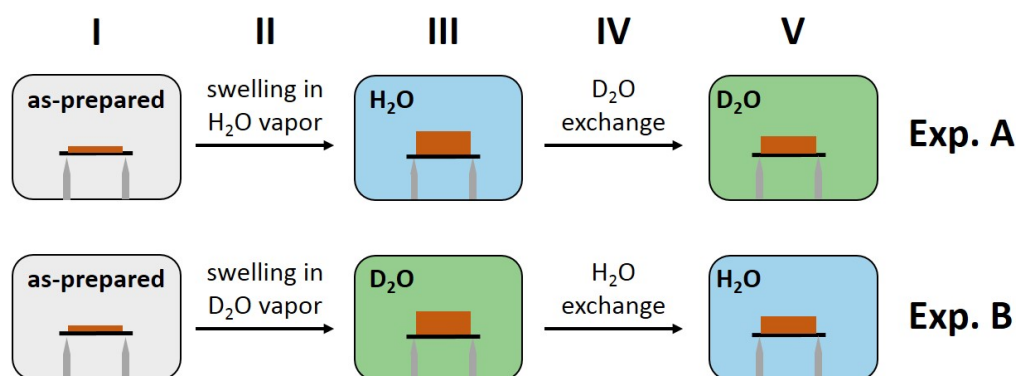


Figure 5.1.: Isotope-sensitive thin film swelling and exchange kinetics: Schematic representation of the performed experiments. In experiment A, the swelling in H₂O vapor is followed by the D₂O exchange while in experiment B the swelling in D₂O is followed by the H₂O exchange. The thin film states in equilibrium (stage I, III, and V) are probed with static ToF-NR, while the thin film kinetics of the swelling (stage II) and exchange (stage IV) processes are followed with kinetic ToF-NR, SR, and FTIR *in-situ*. The ambient surrounding, the H₂O, and the D₂O vapor, are indicated in gray, blue, and green, respectively. Adapted with permission from AMERICAN CHEMICAL SOCIETY, Copyright 2019 [36].

The chapter is structured as follows: Static ToF-NR experiments probe the DBC thin films in their equilibrated states (stage I, III, and V). Subsequent, the dynamic processes, the swelling (stage II) and exchange (stage IV), followed with spectral reflectance (SR),

kinetic time-of-flight neutron reflectivity (ToF-NR), and Fourier-transform infrared spectroscopy (FTIR) *in-situ*, are described. Particular attention is given to potential differences in film thickness and water content, dependent on the deuteration level of the used water species. This mesoscopic information is complemented with molecular information about the polymer-water interactions, obtained by FTIR measurements. A conclusion summarizes the finding at the end of this chapter.

ToF-NR measurements are performed at the RefSANS instrument at the MLZ neutron source in Garching, Germany [218–220]. Details to ToF-NR, SR, and FTIR can be found in the Sections 3.2 and 3.3. For realizing *in-situ* measurements, corresponding sample environments described in the subsection 'Pre-existing experimental setup' in Section 3.4 are used [229, 230]. The thin film samples are prepared according to Section 4.4. A pre-characterization of the thin film samples is done via optical and atomic force microscopy, and x-ray reflectivity. All techniques reveal highly homogeneous and smooth thin films as can be seen in the Appendix A.

5.1. Investigation of the equilibrated thin film states

The environmental parameters, *i.e.*, the relative humidity (RH) and the temperature are monitored throughout both experiments (cf. Figure 5.1a). Both, as a function of time are plotted in Figure 5.2. A strong increase in RH is seen during the swelling in water vapor while during the exchange processes it remains relatively stable. The slight variations, in particular upon the vapor exchange result from a specific calibration of the humidity sensor to H₂O. The temperature is kept constant at 26.5 °C.

Static ToF-NR probes the thin films in their equilibrated as-prepared (stage I), water swollen (stage III), and exchanged states (stage V), and yields a first impression how the thin films behave in H₂O and D₂O vapor. The NR curves together with their model fits are shown in Figure 5.3. The as-prepared states are fitted with a two-layer model (SiO₂ and one main polymer layer), while two additional water enrichment layers at the substrate-polymer and polymer-water vapor interfaces, in the swollen and exchanged states necessitated a four-layer fit model. The extracted film thickness, which is normalized to the initial film thickness for better comparability (gives swelling ratio d/d_{ini}), and the average thin film $\langle SLD \rangle$ (in the following simply written as SLD) are listed in Table 5.1. From the SLD, the water content Φ is calculated according to Equation 2.13 in Section 2.1.2.

The as-prepared thin films are homogeneously distributed and of similar size in both experiments [(35 ± 1) and (32 ± 1) nm], which is crucial as the initial film thickness has a strong impact on the swelling behavior [74]. The measured SLD in the as-prepared state

5.1. Investigation of the equilibrated thin film states

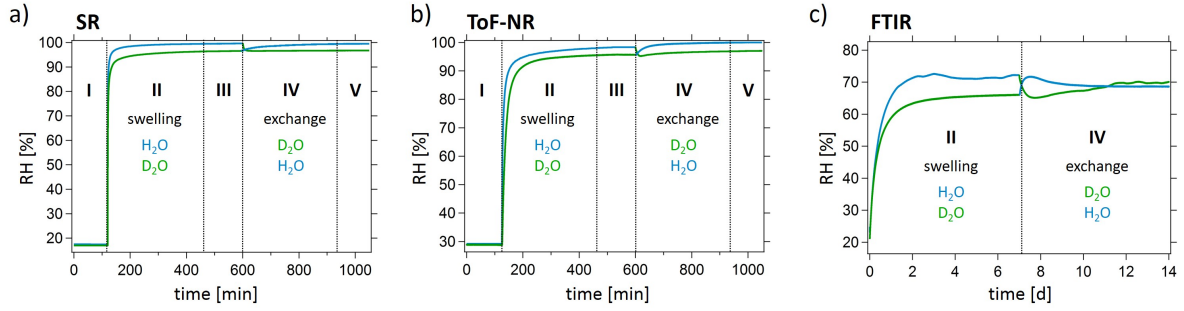


Figure 5.2.: RH and temperature during swelling in water vapor and the subsequent exchange process. Both parameters are plotted as a function of time for the (a) SR, (b) ToF-NR, and (c) FTIR measurement chamber. The temperature is kept constant at 26.5 °C (black solid line). The thin film stages are labelled according to Figure 5.1. The use of H₂O and D₂O is indicated in blue and green, respectively. Adapted with permission from AMERICAN CHEMICAL SOCIETY, Copyright 2019 [36].

is slightly lower $[(0.73 \pm 0.02) \times 10^{-6} \text{ \AA}^{-2}]$ than the theoretical SLD ($0.85 \times 10^{-6} \text{ \AA}^{-2}$) [182], which is due to a minor amount of H₂O molecules inside the thin films.

Table 5.1.: Film thickness (sum of all polymer layers), swelling ratio d/d_{ini} , SLD (via integration of the SLD profile), and the water content Φ (via Equation 2.13) extracted from static ToF-NR curves and the corresponding SLD profiles (Figure 5.3).

H ₂ O swelling - D ₂ O exchange				
thin film state	film thickness d [nm]	swelling ratio d/d_{ini}	SLD [10^{-6} \AA^{-2}]	water content Φ [V%]
as-prepared	35 ± 1	1.00 ± 0.03	0.73 ± 0.02	–
H ₂ O swollen	59 ± 1	1.69 ± 0.06	0.15 ± 0.01	65 ± 8 (H ₂ O)
D ₂ O exchanged	61 ± 2	1.74 ± 0.04	2.99 ± 0.05	45 ± 4 (D ₂ O)
D ₂ O swelling - H ₂ O exchange				
as-prepared	32 ± 1	1.00 ± 0.02	0.75 ± 0.01	–
D ₂ O swollen	51 ± 2	1.59 ± 0.02	3.82 ± 0.08	48 ± 4 (D ₂ O)
H ₂ O exchanged	59 ± 1	1.84 ± 0.05	1.26 ± 0.03	50 ± 2 (H ₂ O)

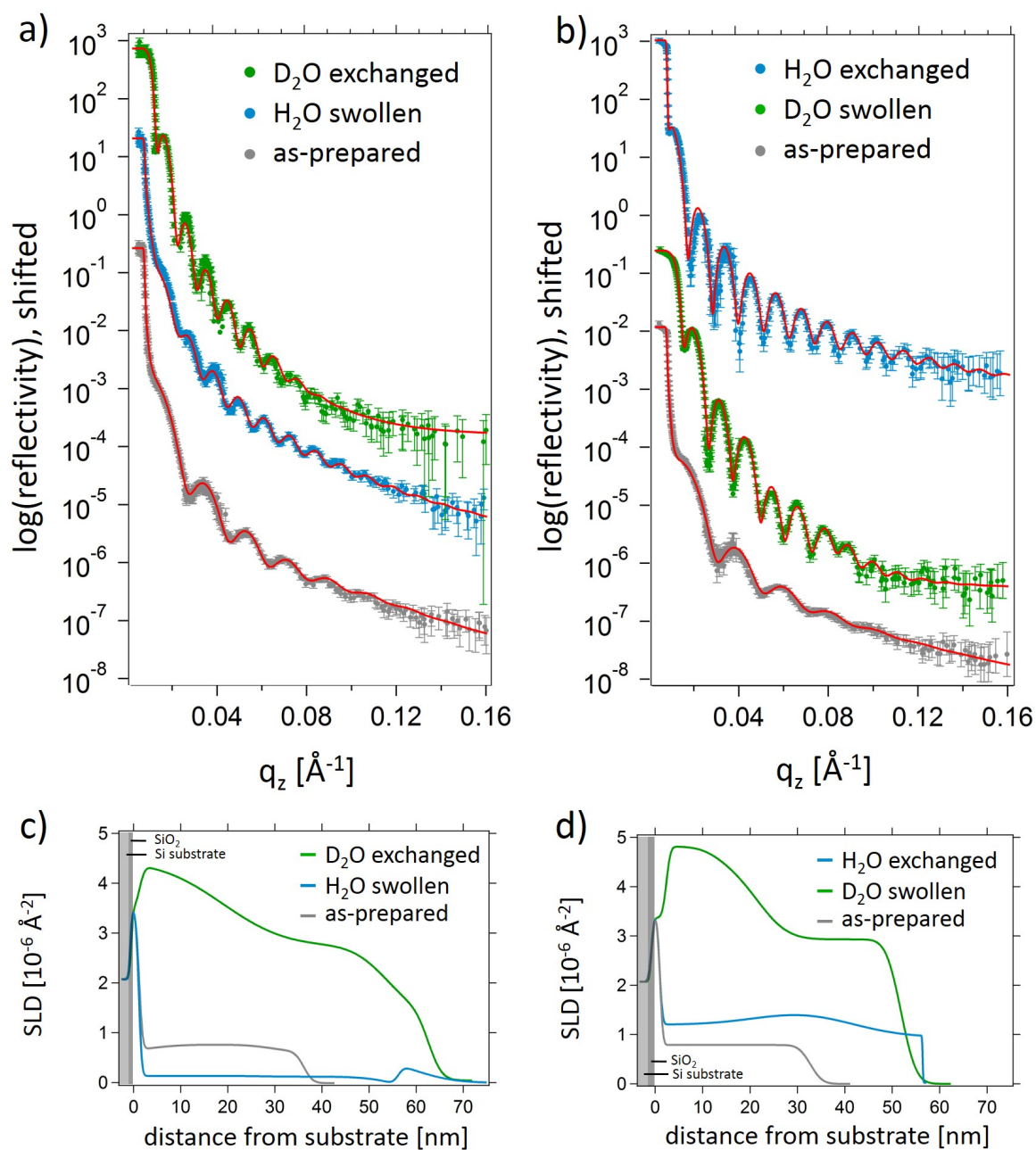


Figure 5.3.: Static ToF-NR measurements. ToF-NR curves of the thin film in their equilibrium states in (a) experiment A and (b) experiment B. The curves of the as-prepared (stage I), swollen (stage III), and exchanged thin film state (stage V) are indicated in gray, blue (in H₂O vapor), and green (in D₂O vapor). Best fits are achieved with a two-layer model for the as-prepared state, and a four-layer model for the swollen and exchanged states (red lines). Corresponding SLD profiles of (c) experiment A and (d) experiment B are shown below the NR curves. Adapted with permission from AMERICAN CHEMICAL SOCIETY, Copyright 2019 [36].

After the swelling in water vapor, both thin films feature an increased water content and swelling ratio. Interestingly, a higher swelling degree is reached during the swelling in H₂O vapor. In addition, water enrichment layers appear near the Si substrate, which is due to the attractive hydrophilic interactions between the SiO₂ layer and water [67, 109].

These layers are more pronounced after the swelling in D₂O vapor, which is due to the better contrast in SLD of the DBC and D₂O, as compared to H₂O. After the H₂O exchange, a further increase in thickness, accompanied with an H₂O uptake is observed, while after the D₂O exchange, the swelling ratio and water content remain constant. These findings already indicate differences in interactions of the DBC with different water species, which we mainly address to the PSPP block and its strong H/D isotope sensitivity. As described in the Introduction, the CP'_{PSPP} is at lower temperatures in H₂O than in D₂O vapor. Thus, the water compatibility of the PSPP block and therefore or the whole thin film might be higher in H₂O vapor. Water enrichment layers near the substrate are also present in the final exchanged thin film state (stage V).

The final SLD values after the water exchange (stage V), suggest, that in both experiments, both water species are present within the thin films, and thus the exchange processes are incomplete. For a completed water exchange, *i.e.*, all H₂O molecules are exchanged by D₂O molecules and vice versa, the SLD values are too low in case of the D₂O exchange and too high in case of the H₂O exchange, respectively.

To further explore the isotope sensitivity of the DBC, the dynamic swelling and exchange processes are followed in real-time. While the static ToF-NR measurements revealed the impact of different water species on the equilibrated thin film states, the kinetic ToF-NR measurements allow to monitor the swelling and exchange behavior, regarding changes in film thickness, water content, and polymer-water interactions, in real time.

5.2. Swelling behavior

To further explore the isotope sensitivity of the DBC, the dynamic swelling (stage II) and exchange processes (stage IV) are followed in real-time. SR and ToF-NR are used to obtain information about mesoscopic parameters such as film thickness and the absorbed water content, while FTIR spectroscopy complements these information on a molecular level and probes the polymer-water interactions. The first part, discusses the thin film behavior upon swelling in water vapor, while the second part describes the exchange behavior.

Film thickness and water content

Figure 5.4 shows the swelling ratio d/d_{ini} obtained from SR measurements during the swelling in H₂O (blue) and D₂O vapor (green) as a function of time. A single SR spectrum is recorded every 10 seconds, which defines the time resolution. With increasing RH, the thin films undergo a strong swelling process, which equilibrates after roughly 400 min at a swelling ratio of $d/d_{ini} \approx 2$. While SR experiments yield similar swelling ratios for the swelling with H₂O and D₂O, the obtained swelling degrees are higher as the swelling degrees determined via static ToF-NR. This might be due to differences in the measurement technique. SR probes only a small area of the thin film, while ToF-NR illuminates a larger region and therefore, exhibits a significant higher statistical relevance. Furthermore, different measurement chambers are used (cf. Section 3.4.1).

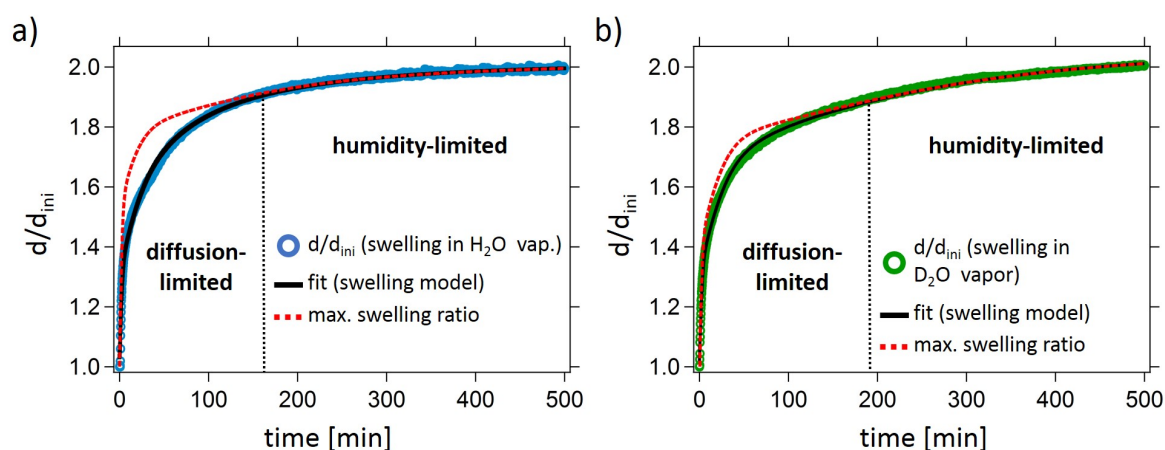


Figure 5.4.: Swelling in water vapor followed with SR *in-situ*. The swelling ratio d/d_{ini} as a function of time during the swelling in (a) H₂O and (b) D₂O vapor. A swelling model is applied to the data as explained in the main text (solid black line). The maximum swelling ratio d_{max}/d_{ini} is plotted as dotted red line. The vertical dotted black line divides the swelling process in a diffusion-driven and a humidity-driven regime. Adapted with permission from AMERICAN CHEMICAL SOCIETY, Copyright 2019 [36].

Figure 5.4 also shows the maximum swelling ratio d_{max}/d_{ini} , which is calculated by Equation 2.15. It describes the limit, to which the polymer thin film could (theoretically) absorb water molecules, at a given RH, if intrinsic diffusion processes are absent (or are neglected). At early stages, the maximum and the measured swelling ratio feature a strong deviation, which identifies the intrinsic diffusion process as a limiting factor, since the very rapidly increasing RH would allow for higher swelling ratios. At later stages, both curves merge, *i.e.*, the swelling process is limited by the RH. Interestingly, the diffusion-limited regime is shorter for the swelling process in H₂O vapor (≈ 177 min) than in D₂O vapor

(≈ 195 min). Thus, the H₂O diffusion is promoted, which indicates a higher affinity of the DBC toward H₂O.

To quantify the swelling data, a swelling model is applied to the evolution of swelling ratio. This model respects the intrinsic swelling kinetics, which is driven by the diffusion of water into the thin film, as well as a non-constant RH. From the model, the effective Flory-Huggins interaction parameter χ_{eff} between the DBC and the respective water species is extracted. In addition, the model yields a time τ , which describes the time scales of the occurring swelling (or later on, exchange) processes. Please note, that interactions of the DBC with the Si substrate are excluded from the swelling model. An detailed description of the swelling model is given in Section 2.1.2. Table 5.2 lists the extracted χ_{eff} and τ values. The applied swelling model yields lower χ_{eff} and (slightly lower) τ values, for the swelling in H₂O as compared to D₂O vapor. While the lower χ_{eff} value indicates a higher affinity of the DBC towards H₂O, the lower τ value hints toward a faster H₂O diffusion into the thin film. This is in good agreement with the shorter diffusion-limited regime, for the swelling in H₂O vapor. Summarized, the thin films are able to incorporate an greater H₂O amount faster than a lesser D₂O amount.

water swelling	χ_{eff}	τ [min]
H ₂ O swelling	0.55 ± 0.01	42 ± 1
D ₂ O swelling	0.73 ± 0.01	46 ± 1

Table 5.2: Swelling model applied to the SR data shown in Figure 5.4.

To investigate the water swelling kinetics in more detail, ToF-NR measurements are performed. In contrast to SR, ToF-NR enables to determination the film thickness and the absorbed water amount independently from each other. To assure a high time resolution as well as a high statistical relevance, a single NR curve is obtained every 30 s. Selected, representative NR curves for swelling in H₂O and D₂O vapor, are shown in Figure 5.5. A four-layer model is used for the fitting procedure (SiO₂, water enrichment layers at both interfaces, one main polymer layer).

The local reflectance maxima, the so-called Kiessig fringes, move closer together, therefore indicating an increasing film thickness (cf. Equation 2.35). Notably, this is more pronounced during the swelling in H₂O vapor. The shift of the critical edge (vertical dashed black line) demonstrate a change in the average thin film SLD, as water molecules diffuse into the thin films. Figure 5.6 displays the swelling ratio and water content as a function of time. A higher swelling ratio and water content are reached during the swelling with H₂O as compared to D₂O. Again, this is referred to a lower CP'_{PSP} in H₂O than in D₂O, and the resulting higher H₂O compatibility of the DBC. Also, the maximum swelling ratio follows the same trend, as is found in the SR swelling data (cf. Figure 5.4). It shows

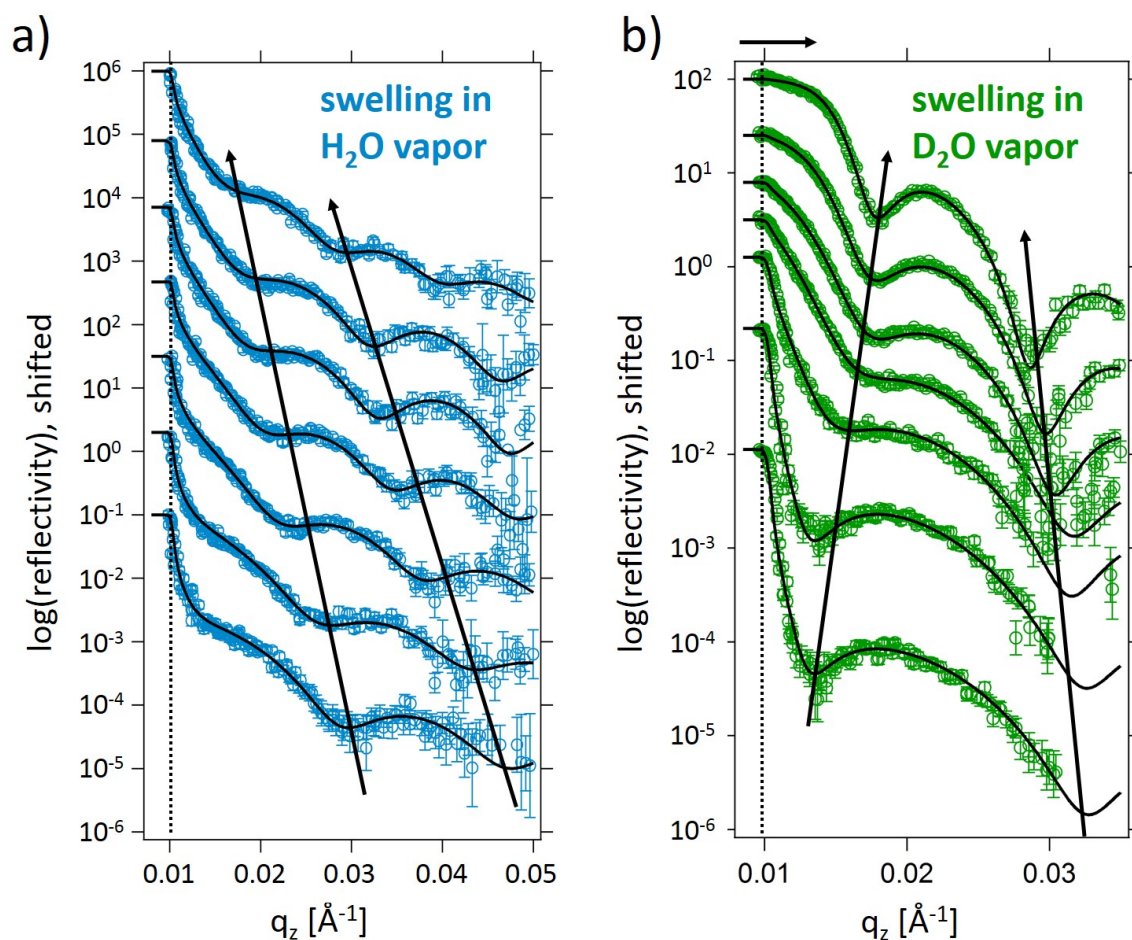


Figure 5.5.: Representative selection of ToF-NR curves for the swelling in water vapor. Representative ToF-NR data (open blue and green circles) are shown with best model fits obtained via a four-layer model (black lines) for the swelling in (a) H₂O and (b) D₂O vapor. From bottom to top the time increases: $t = 0.5, 7, 15, 40, 45, 90,$ and 360 min after swelling is induced. The curves are shifted along the y -axis for clarity. The vertical dashed black line marks the critical edge of the as-prepared thin film. The black arrows inside the graphs indicate the shift of the Kiessig fringes, while the black arrow on top of (b) indicates the shift of the critical edge. Adapted with permission from AMERICAN CHEMICAL SOCIETY, Copyright 2019 [36].

a significant offset from the actual measured swelling ratio in the early stages before both curves merge, thereby demonstrating a swelling process that is diffusion-limited at early stages and humidity-limited at later stages. While this swelling mechanism applies for both, the swelling in H₂O and D₂O vapor, the respective time scales differ considerably. Analogously to the SR data, the swelling in H₂O vapor is diffusion-limited for shorter times (≈ 150 min) than the swelling in D₂O vapor, which again is addressed to the higher

5.2. Swelling behavior

affinity of the DBC to H₂O. In order to further quantify the swelling data obtained from ToF-NR, the swelling model is applied. Table 5.3 lists the extracted χ_{eff} and τ values.

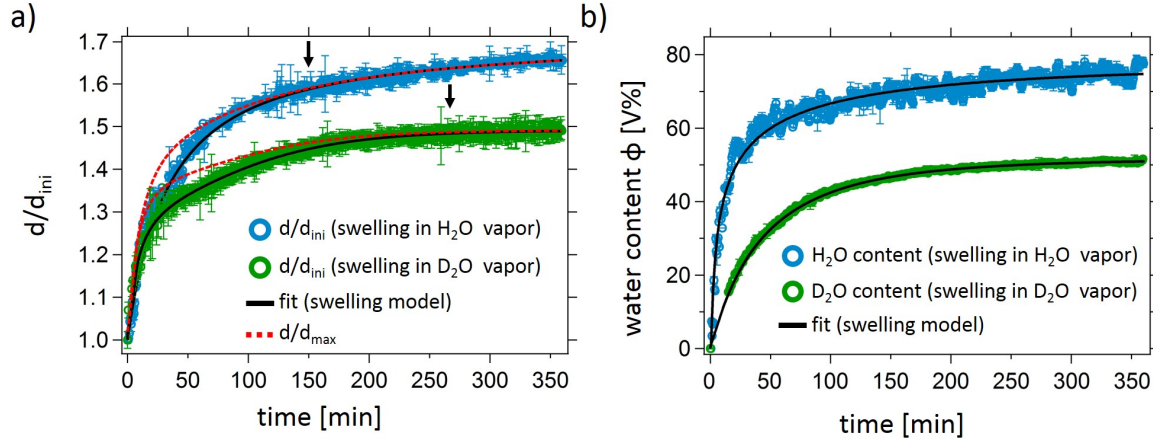


Figure 5.6.: Swelling in water vapor followed with kinetic ToF-NR *in-situ*. The (a) swelling ratio d/d_{ini} and (b) water content Φ as a function of time for the swelling in H₂O (blue circles) and D₂O vapor (green circles). Both are fitted with the swelling model (black line) as explained in the main text. The maximum swelling ratio d_{max}/d_{ini} is plotted as dotted red line. Black arrows in (a) mark the time, at which the swelling process is no longer diffusion-limited, but limited by the RH. Adapted with permission from AMERICAN CHEMICAL SOCIETY, Copyright 2019 [36].

swelling in	χ_{eff}	τ [min]	extracted from
H ₂ O vapor	0.85 ± 0.01	30 ± 1	ToF-NR (d/d_{ini}) ^a
D ₂ O vapor	0.83 ± 0.01	162 ± 7	ToF-NR (d/d_{ini}) ^a
H ₂ O vapor	0.32 ± 0.01	83 ± 5	ToF-NR (Φ) ^b
D ₂ O vapor	0.50 ± 0.01	80 ± 3	ToF-NR (Φ) ^b

Table 5.3: Swelling model applied to the ToF-NR data shown in Figure 5.6a,b.

In particular, the $\tau(d/d_{ini})$ values differ significantly from each other, and indicate a much faster H₂O diffusion, which is in good agreement with the shorter diffusion-limited regime during the swelling in H₂O vapor. $\chi_{eff}(\Phi)$ values suggest a higher affinity of the DBC toward H₂O, which confirms the findings from SR and static ToF-NR measurements. The $\tau(\Phi)$ values are similar for both swelling processes, which hints toward an equally fast H₂O and D₂O uptake, despite favored interaction of the DBC to H₂O.

Polymer-water interactions

In order to identify the molecular origin of the disparity in interactions between PSPP-*b*-PNIPAM and the different water species, the swelling processes are followed with FTIR spectroscopy. A single spectrum is recorded every 7 minutes, which is a considerably lower time resolution as compared to ToF-NR and SR. Thus, to realize *in-situ* measurements and to enable a certain comparability between the different measurement techniques, the increase in RH is decelerated by using a specialized FTIR measurement chamber (cf. Section 3.4). The obtained FTIR spectra upon the swelling in H₂O and D₂O vapor are displayed in Figure 5.7.

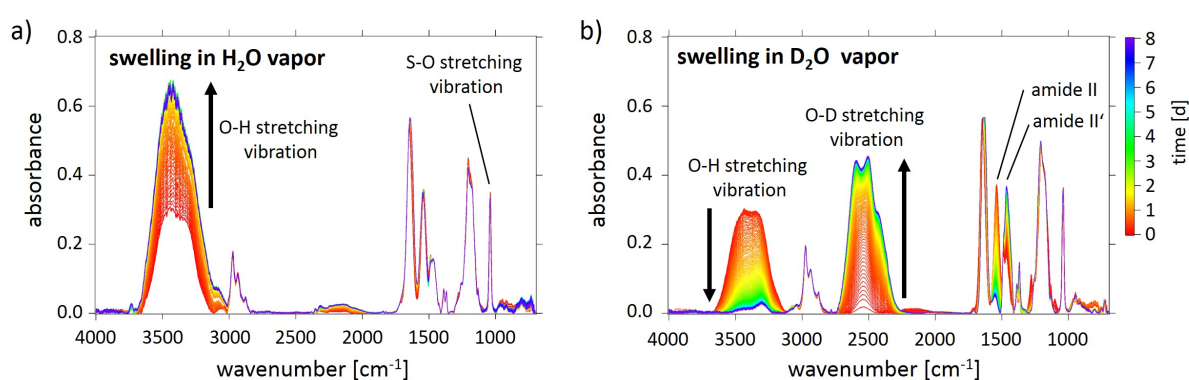


Figure 5.7.: Swelling in water vapor followed with FTIR *in-situ*. FTIR spectra during the swelling in (a) H₂O and (b) D₂O vapor. The red curve marks the initial ($t = 0$ d), while the purple curve marks the final measurement ($t = 8$ d). Characteristic absorption peaks are labelled accordingly. Black arrows mark the increase and decrease of the O-H and the O-D stretching vibration. Numbers next to the arrows indicate the sequence order of increase and decrease steps. Adapted with permission from AMERICAN CHEMICAL SOCIETY, Copyright 2019 [36].

The two very prominent absorption peaks, located at around 3400 cm^{-1} and 2500 cm^{-1} , are assigned to the O-H and O-D stretching vibrations. Both peaks can be divided into several sub-modes that correspond to energetically different O-H and O-D vibrations [244, 245]. These differences result from variations in H- and D-bonds of water to the polymer (especially to the amide group, which is present in both, the PSPP and PNIPAM block). Also free water, *i.e.*, not bound by H- or D-bonds to the polymer chain, contributes to these large peaks. In-between, a three-fold peak is detected. It is addressed to the asymmetric (2974 cm^{-1}) and symmetric stretching vibration (2886 cm^{-1}) of the CH₃ groups, which are bound to the quaternary amines of the PSPP, and in the isopropyl groups of PNIPAM. The asymmetric stretching vibration of the CH₂ groups located in the backbones and sidechains of the polymer blocks, appears at 2938 cm^{-1} . Since their vibrational signals remain mostly unaffected during the hydration with either H₂O or D₂O,

5.2. Swelling behavior

they are used for normalization, in order to account for deviating thin film thicknesses. By integration over the broad O-H and O-D peaks information about the general water content inside the thin films is obtained. Figure 5.8 shows their normalized peak areas as a function of time during both water swelling processes. Note, due to the decelerated increase in RH within the measurement chamber, the time axis is in days. Both signals initially increase with time, indicating that water molecules diffuse into the thin films, and equilibrate after two to three days, with the O-H signal reaching a higher plateau compared to that of the O-D signal. This clearly demonstrates, that the thin film is capable of absorbing more H₂O than D₂O molecules and confirms the ToF-NR and SR results on a molecular level. The deviating molar extinction coefficient ϵ_λ of the O-H and O-D peak is already taken into account. Although the swelling kinetics followed with FTIR occur on a significant longer time scale than the kinetics followed with ToF-NR and SR, the swelling process itself is induced by an increasing RH. Therefore, the swelling model is applied to the FTIR data as well. Table 5.4 lists all extracted values. The swelling in H₂O vapor yields lower $\chi_{eff}(\Phi)$ and $\tau(\Phi)$ values, than the swelling in D₂O vapor, indicating a higher affinity of the DBC to H₂O, as well as a faster H₂O diffusion. This is also consistent with SR and ToF-NR results.

The strong advantage of FTIR spectroscopy is the precise differentiation between protonated and deuterated compounds due to a deviating binding energy. Besides the monitoring of the water content, this also enables the detection of potential deuteration processes. Once deuterated solvents are involved in swelling (or exchange) processes, the polymer chain undergoes deuteration at the acidic hydrogen atom within the amide group, which is present in both, the PSPP and PNIPAM block. At 1645 cm⁻¹ and 1537 cm⁻¹, the absorption peaks of this group are located, which are denoted as amide I and II. The amide I band includes the C=O stretching mode of the carbonyl group and also contributions from the N-C stretching vibration [246–248]. The amide II band arises from the N-H in-plane bending with contributions from C-H stretching vibrations [227].

Table 5.4.: Swelling model applied to the FTIR data shown in Figures ^a5.8a and ^b5.9a.

water swelling	χ_{eff}	τ [d]	extracted from
H ₂ O swelling	0.55 ± 0.01	0.5 ± 0.1	FTIR [Φ (O-H stretch. vib.)] ^a
D ₂ O swelling	0.66 ± 0.01	2.5 ± 0.1	FTIR [Φ (O-D stretch. vib.)] ^a
H ₂ O swelling	0.91 ± 0.01	0.11 ± 0.01	FTIR (S-O stretch. vib.) ^b
D ₂ O swelling	0.77 ± 0.01	0.13 ± 0.01	FTIR (S-O stretch. vib.) ^b

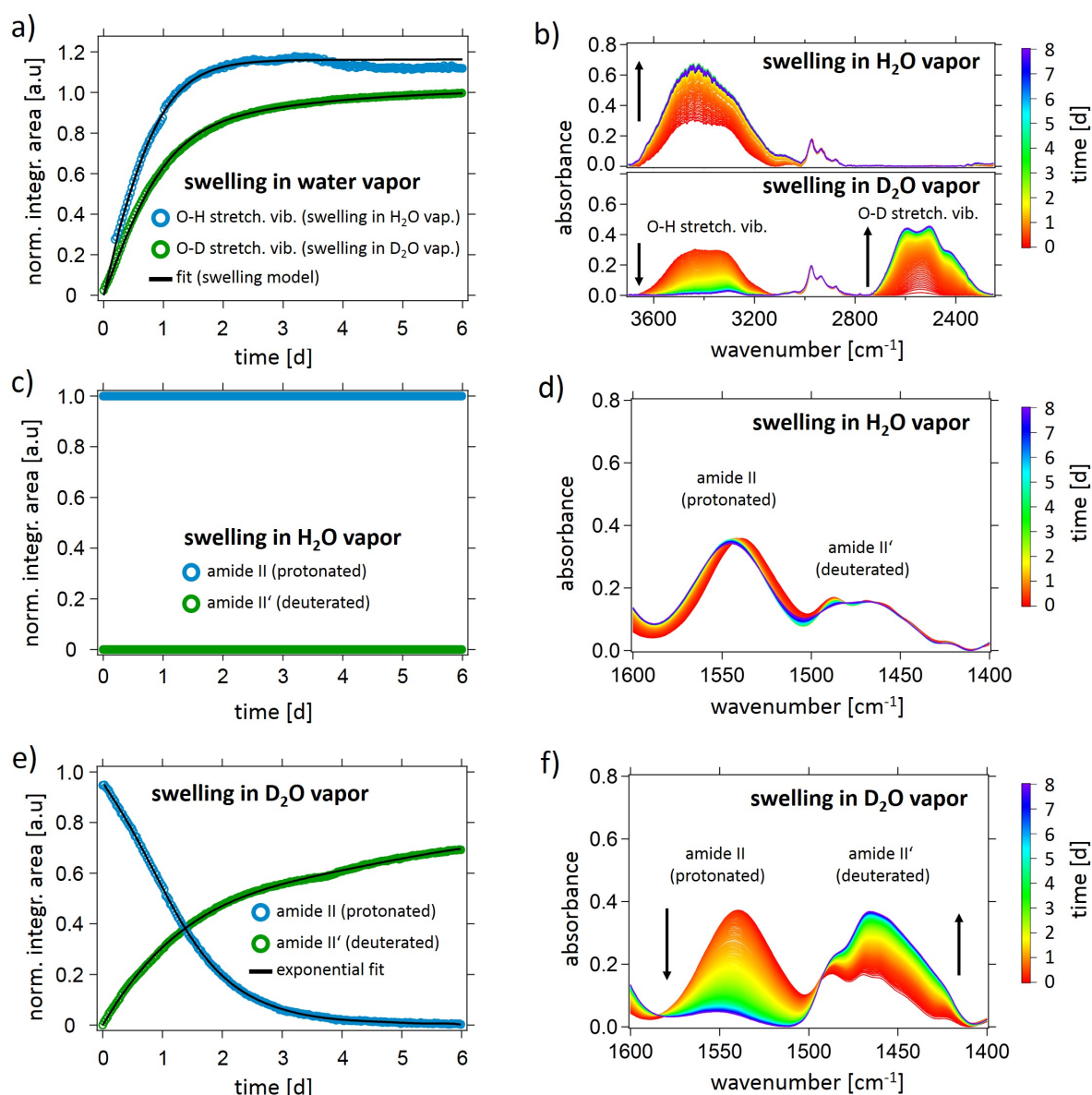


Figure 5.8.: Integration areas extracted from FTIR spectra during swelling in water vapor. Normalized integration areas of the (a) O-H (blue) and O-D (green) peaks, and the protonated and deuterated amide II and II' peak during the swelling in (c) H₂O and (e) D₂O vapor. The corresponding absorption modes are imaged besides the integration areas (b,d,f). The integration areas of the O-H and O-D peaks as a function of time in (a) are fitted with a swelling model (black line) as explained in the main text. The integration areas of the amide II and II' peaks in (c,e) are fitted with an exponential fit as explained in the main text. Black arrows indicate increasing and decreasing absorption modes. Adapted with permission from AMERICAN CHEMICAL SOCIETY, Copyright 2019 [36].

While the amide I band is mainly affected by changes in the polymer's secondary structure, the amide II is sensitive to deuteration. The stretching vibration energies of N-H and N-D differ, so that a peak resulting from the deuterated amide group, denoted with amide II', is detectable at around 1550 cm^{-1} . The deuteration rate can be quantified, by integrating the corresponding protonated amide II and the deuterated amide II' peak. Figure 5.8c,e shows the evolution of the obtained integration area.

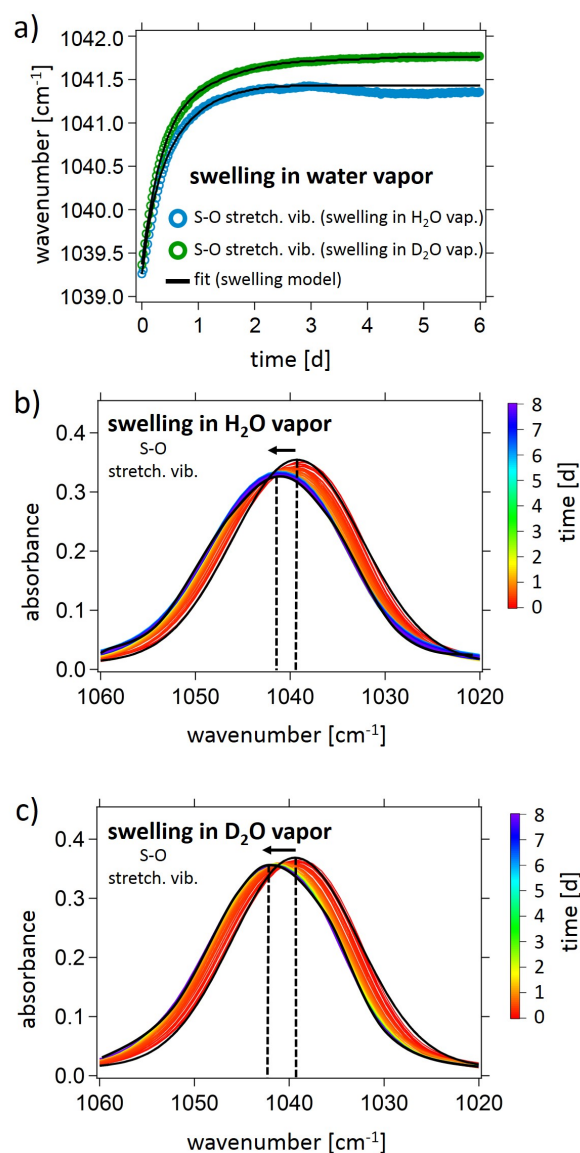
The amide II signal upon swelling in H_2O vapor can be seen as a reference, as obviously no deuteration occurs since no deuterated water is involved. In contrast, during the D_2O swelling, the intensity of the protonated amide II band decreases, while the intensity of the deuterated amide II' increases, which clearly proves ongoing deuteration processes. Note, that the absorbance of the amide II and II' peak in their equilibrated states deviate, which is due to the different extinction coefficients. Interestingly, the deuteration equilibrates only after roughly 5 days, and therefore deuteration occurs significantly longer than the water is absorbed.

This might be due to inaccessible amide groups, as in particular, the isopropyl groups of the PNIPAM side chain might shield the amide groups from diffusing D_2O molecules. The evolution of the amide II and II' peaks are fitted with a logarithmic growth and decay function, respectively. The obtained growth $[(2.0 \pm 0.2)\text{ d}]$ and decay $[(1.5 \pm 0.2)\text{ d}]$ rates prove, that every hydrogen atom is replaced by a deuterium atom. As a result of the deuteration process, a third water species namely HDO is generated, which is assumed to adopt characteristics in-between H_2O and D_2O , regarding its affinity to the DBC and diffusion speed.

While a changing integration area gives information about the amount of a certain compound, *e.g.*, H_2O and D_2O , or N-H and N-D, a shifting peak position yields insights into local hydration effects. The development of a hydration shell around a characteristic group, alters its chemical environment and affects the vibrational binding energy. Consequently, the peak maximum shifts either to lower or higher wavenumbers, dependent on the impact of the changed environment toward a higher or a lower vibrational energy. In the finger print region of the FTIR spectra, a sharp peak at 1039 cm^{-1} is visible, which is due to the symmetric S-O stretching mode of the SO_3^- group, located at the end of the PSPP side chain. Based on its prominent location and the negative charge, it is assumed to play a major role in swelling and exchange processes. Figure 5.9a gives its peak maximum position as a function of time.

The peak shift is slightly more pronounced during the swelling in D_2O vapor. Apparently, the hydration with D_2O has a stronger influence on the vibrational energy of the S-O stretching vibration than with H_2O . This might be due to the higher mass of D_2O , however, the difference in the peak shifts is too large, to be explained only by this.

Figure 5.9: Peak maximum position extracted from FTIR spectra during swelling in water vapor. (a) The peak position of the symmetric S-O stretching vibration upon the swelling in H₂O (blue) and D₂O vapor (green) is extracted via an Gaussian fit from the corresponding absorption modes shown in (b,c). A Gaussian fit (applied to all FTIR curves) is shown in (b,c) as black line for each first and final absorption peak. Black arrows indicate the shifting peak position of the S-O stretching vibration. Dashed black lines indicate the peak maxima. The S-O peak position as a function of time is fitted with a swelling model (black line) as explained in the main text. Adapted with permission from AMERICAN CHEMICAL SOCIETY, Copyright 2019 [36].



Therefore, also deviating interactions between the SO_3^- group and the respective water species are assumed. The applied swelling model confirms this observation. The obtained $\chi_{eff}(S-O)$ values are lower for the swelling in D₂O vapor, thereby attributing the SO_3^- group a higher affinity toward D₂O than H₂O. These findings are extremely interesting, as they seem at first to oppose the previous results. However, they indicate a deviating general and local thin film behavior. The very small $\tau(S-O)$ values (smaller than $\tau(\Phi)$ values) underline this assumption. Upon swelling, water initially accumulates around the SO_3^- group, before the hydration of the remaining polymer chain follows thereafter. After the swelling in water vapor, both thin films are in equilibrium. The thin film has absorbed more H₂O and is swollen to a higher degree than the thin film after the D₂O swelling. The respective exchange processes are performed subsequently to the swelling processes.

5.3. Exchange behavior

The exchange kinetics are induced, by changing the H₂O to a D₂O vapor and vice versa. ToF-NR, SR, and FTIR are used to follow the exchange kinetics of the PSPP-*b*-PNIPAM thin films *in-situ*. Analogously, to the swelling kinetics, the obtained mesoscopic thin film characteristics are described first, and subsequent they are linked to molecular information.

Film thickness and water content

Figure 5.10 displays the swelling ratio d/d_{ini} as a function of time during the D₂O (green) and H₂O (blue) exchange.

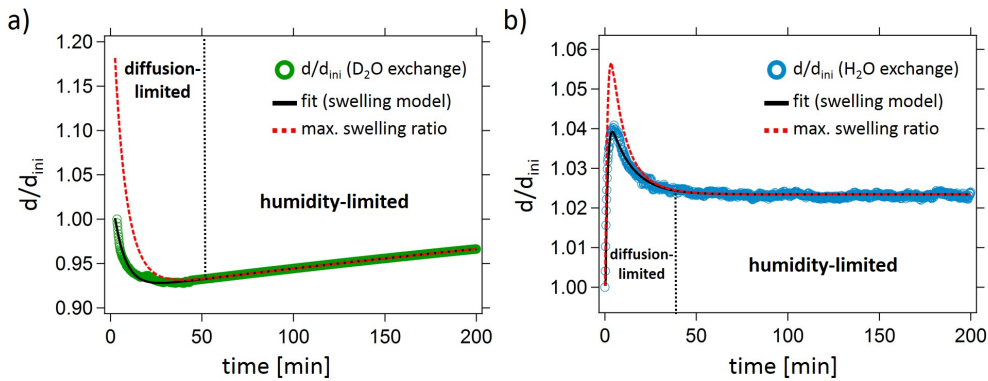


Figure 5.10.: Water swelling followed *in-situ* with SR. Swelling ratio d/d_{ini} as a function of time during the (a) D₂O and (b) H₂O exchange. The exchange data is fitted with the swelling model (black line) as explained in the main text. The maximum swelling ratio d_{max}/d_{ini} is plotted as dotted red line. The vertical dotted black line divides the swelling process in the diffusion-driven and humidity-driven regime. Adapted with permission from AMERICAN CHEMICAL SOCIETY, Copyright 2019 [36].

During the D₂O exchange, the film thickness decreases (during the first 40 min) until a local minimum is reached. Subsequent, the thin film re-swells to roughly its swelling ratio after the swelling. The film thickness during the H₂O exchange follows the reversed trend. First, the film thickness increases (during the first 5 min) before the film contracts and equilibrates at roughly its initial swelling ratio. While the local minimum and the slightly lower swelling ratio during the D₂O exchange indicates a decreased water compatibility of the DBC thin film, the opposite is the case during the H₂O exchange. The DBC thin film exhibits a higher H₂O compatibility, suggested by the local maximum and the slightly higher final swelling ratio. This might be due to a lower CP'_{PSPP} in H₂O as compared to D₂O vapor. As a consequence, further H₂O uptake is promoted, while in D₂O vapor,

the thin film 'de-mixes' and H₂O molecules are released. The subsequent re-swelling and contraction processes, result from re-arrangement processes of the polymer chains. Analogously to the swelling data, the swelling model is applied. The values for χ_{eff} and τ are listed in Table 5.5.

Table 5.5.: Swelling model applied to SR data shown in Figure 5.10

water exchange	χ_{eff}	τ [min]	extracted from
D ₂ O exchange	0.96 ± 0.01	6 ± 1	SR (d/d_{ini}) ^a
H ₂ O exchange	0.75 ± 0.01	7 ± 1	SR (d/d_{ini}) ^a

The evolution of the film thickness, already indicates favored polymer-H₂O interactions, as the D₂O swollen thin film absorbs even further H₂O molecules. In contrast, the H₂O swollen film releases H₂O molecules in D₂O vapor. The applied swelling model confirms this: A lower χ_{eff} value is obtained for the H₂O exchange. Regarding the τ values, both exchange processes occur on the same time scale, which indicates a similar diffusion of H₂O and D₂O molecules through a D₂O and H₂O swollen thin film, respectively. Interestingly, the τ values are much lower for the exchange than for the swelling processes, thus suggesting, the water diffusion through an already hydrated thin film is eased as compared to a dry or partially hydrated thin film. The trend of the maximum swelling ratio d_{max}/d_{ini} indicates a diffusion-limited regime at early stages of the exchange processes, while the later stages are limited by the RH. The diffusion-limited regime is generally shorter during the water exchange as compared to the swelling, which is due to the rather minor changes of the RH. Furthermore, it is found to be slightly longer for the D₂O exchange, which indicates a slightly slower D₂O diffusion through the thin film.

The water exchange processes are further investigated with kinetic ToF-NR measurements. Figure 5.11 provides a selection of representative NR curves together with the best four-layer model fits (SiO₂, two water enrichment layers at both interfaces, one main polymer layer). A clear shift of the critical edge to higher q_z values is observed during the D₂O exchange, which indicates an increasing average thin film SLD due to the exchange of H₂O molecules by D₂O. The spacing of the Kiessig fringes remain relatively constant, thereby confirming the stable film thickness (cf. Figure 5.10). The NR curves of the H₂O exchange evolve differently. The critical edge shifts back to lower q_z values, due to the exchange of D₂O molecules by H₂O. The Kiessig fringes move closer together, which indicates an even further increasing film thickness. Noticeably, the measured SLD after the D₂O exchange is lower than the theoretically calculated value for a complete exchange. The opposite is the case for the H₂O exchange. Thus, in the respective final exchanged

5.3. Exchange behavior

thin film states, a mixture of H₂O and D₂O molecules is present in the thin films. In order to calculate the water content Φ from the measured SLD, Equations 5.1 and 5.2 are used. Since the water exchange involves more than one water species, the equations deviate slightly from Equation 2.13, which is described in Section 2.1.2.

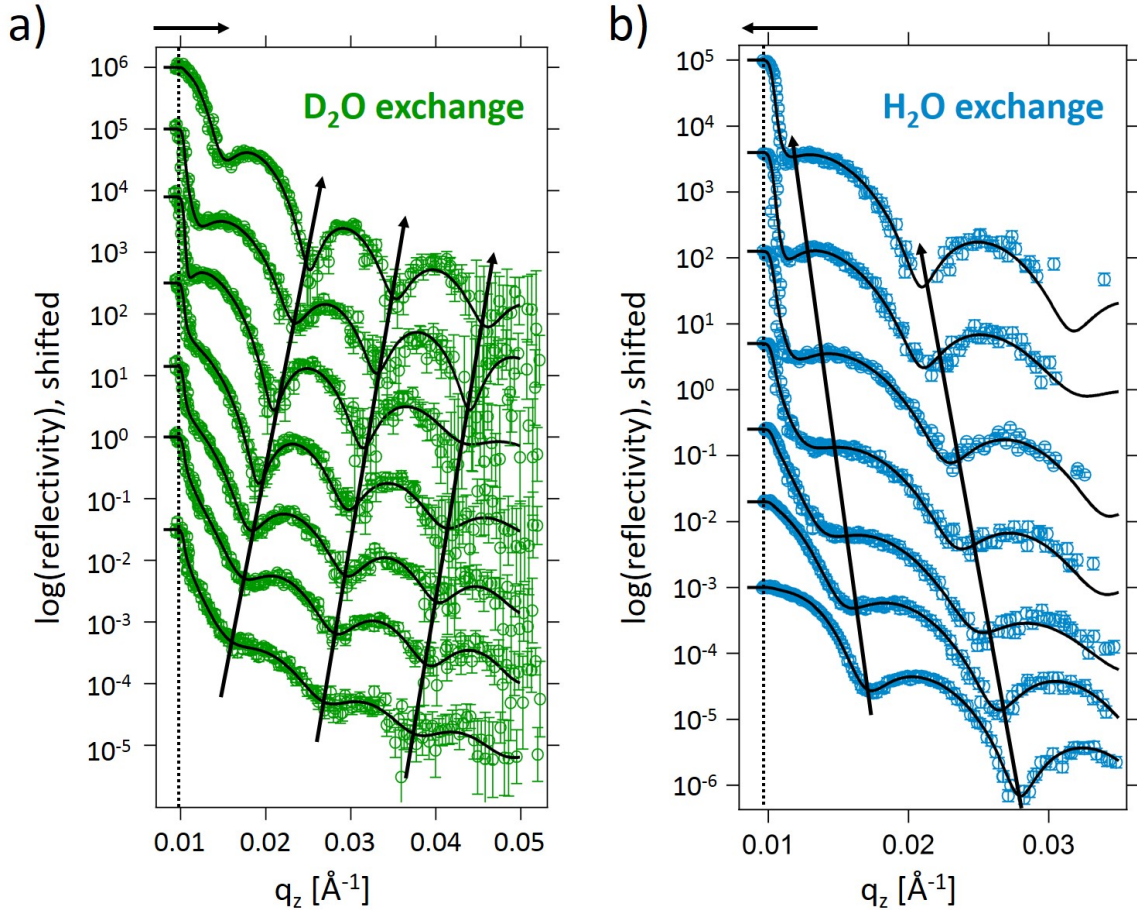


Figure 5.11.: Representative selection of ToF-NR curves for the exchange processes. Representative ToF-NR data (open green and blue circles) are shown with best model fits obtained via a four-layer model (black lines) for the exchange with (a) D₂O and (b) H₂O. From bottom to top the time increases: $t = 0.5, 2.5, 5, 10, 15, 20,$ and 360 min after the exchange process is induced. The ToF-NR curves are shifted along the y -axis for clarity. The vertical dashed black line marks the critical edge of the as-prepared thin film. The black arrows on top of the graphs marks the shift of the critical edge, while the black arrows inside the graphs indicate the shift of the Kiessig fringes. Adapted with permission from AMERICAN CHEMICAL SOCIETY, Copyright 2019 [36].

$$\Phi_{D_2O} = \frac{SLD_{meas}(t) - SLD_{H_2O-swollen}}{SLD_{D_2O} - SLD_{H_2O-swollen}} \quad (5.1)$$

$$\Phi_{H_2O} = \frac{SLD_{D_2O-swollen} - SLD_{meas}(t)}{SLD_{D_2O-swollen} - SLD_{H_2O}} \quad (5.2)$$

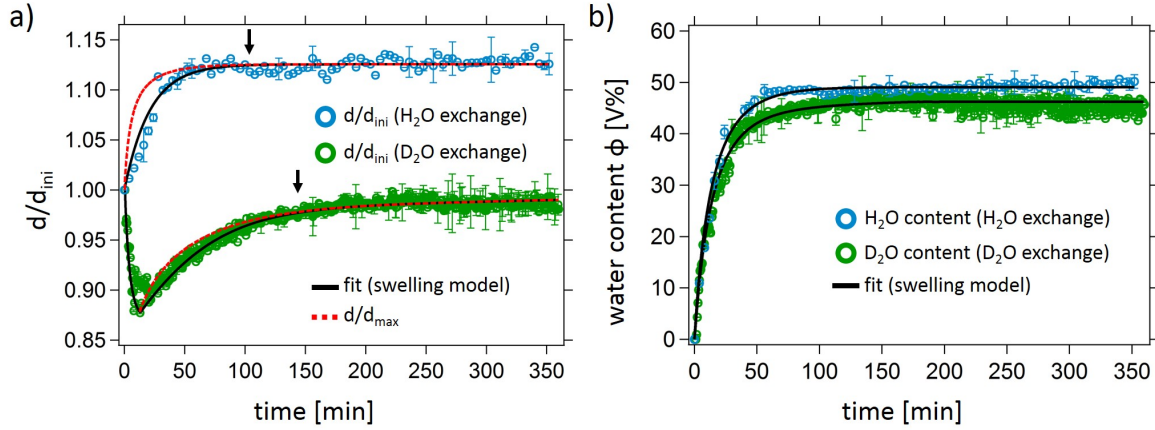


Figure 5.12.: Water exchange followed *in-situ* with ToF-NR. The (a) swelling ratio d/d_{ini} and (b) water content Φ as a function of time for the H₂O (blue circles) and D₂O exchange (green circles). Both are fitted with the swelling model (solid black line) as explained in the main text. The maximum swelling ratio d_{max}/d_{ini} is plotted as dotted red line. Black arrows in (a) mark the time, at which the swelling process is no longer diffusion-limited, but limited by the RH. Adapted with permission from AMERICAN CHEMICAL SOCIETY, Copyright 2019 [36].

Here, the SLD_{meas} is the extracted SLD of the polymer thin film, obtained via integration of the SLD profile over all polymer layers and divided by the total film thickness, at a given time t . The SLD values for the H₂O swollen and D₂O swollen film states are obtained from the static ToF-NR measurements (cf. Table 5.1). Both, the water content Φ and the swelling ratio d/d_{ini} are shown in Figure 5.12 as a function of time.

The trends of the swelling ratios during the respective water exchange processes differ enormously from each other. During the D₂O exchange, the film thickness first decreases (until ≈ 15 min), before it re-swells, due to re-arrangement processes of the polymer chains, back to roughly its initial thickness. Upon H₂O exchange, the film thickness increases during the first 60 min and equilibrates. Again, the decrease and increase in film thickness during the exchange with D₂O and H₂O, respectively, can be explained by a shift of CP' _{PSPP} to lower temperatures. The solvent change leads to a shift of the consolute phase boundary towards higher (D₂O exchange) or lower (H₂O exchange) temperatures and eventually results in repulsive (D₂O exchange) or attractive (H₂O exchange) PSPP-water interactions. The evolution of the water content Φ shows a slightly higher H₂O

5.3. Exchange behavior

incorporation, once again underlining the higher affinity of the DBC to H₂O, as compared to D₂O and again, this is attributed to the altered H- and D-bonds between water and the polymer chain. To further analyze these processes, the swelling model is applied to the data. All extracted χ_{eff} and τ values are summarized in Table 5.6.

Table 5.6.: Swelling model applied to ToF-NR data shown in Figure 5.12a,b.

water exchange	χ_{eff}	τ [min]	extracted from
D ₂ O exchange	1.34 ± 0.01	42 ± 2	ToF-NR (d/d_{ini}) ^a
H ₂ O exchange	1.65 ± 0.01	21 ± 4	ToF-NR (d/d_{ini}) ^a
D ₂ O exchange	0.73 ± 0.01	24 ± 1	ToF-NR (Φ) ^b
H ₂ O exchange	0.78 ± 0.01	20 ± 1	ToF-NR (Φ) ^b

The fitting procedure of the time-dependent swelling ratios yields lower $\chi_{eff}(d/d_{ini})$ and $\tau(d/d_{ini})$ values for the H₂O exchange than for the D₂O exchange. Since the higher affinity of the DBC toward H₂O and the faster H₂O diffusion as compared to D₂O, is well known by now, this is expected. The situation becomes more complex when the swelling model is applied to the evolution of the water content. Here, the model yields similar $\chi_{eff}(\Phi)$ and $\tau(\Phi)$ values, which indicates no particular difference between the both exchange processes. However, one has to note, that the complexity of the exchange processes, regarding two competing water species, occurring re-arrangement processes of the polymers, and deuteration of the polymer chains, pushes the applied swelling model to its limit. The obtained water content Φ as a function of time, calculated from the measured SLD is most likely a combination of water absorption and release. Hence, it is hard to determine an exact ratio of the two water species present in the thin film. However, the overall thin film behavior, in particular regarding the further increase in thickness and the higher amount of incorporated H₂O molecules during the H₂O exchange, is a strong indicator for a general higher affinity of the DBC toward H₂O.

In order to distinguish between H₂O and D₂O, FTIR measurements are conducted. FTIR enables to decouple the exchange process in a water release and a water uptake, with respect to the different water species. As a consequence, the evaluation via the swelling model becomes meaningful, as individual processes are isolated and can be analyzed separately.

Polymer-water interactions

The overall FTIR spectra of the water exchanges are shown in Figure 5.13. The characteristic absorption modes can be assigned to the corresponding molecular groups, as is explained earlier in Section 5.2. A change in absorbance intensity of the O-H and O-D peaks demonstrates that during the D₂O exchange, H₂O molecules are released, while D₂O molecules are absorbed. The reversed behavior can be seen during the H₂O exchange. The normalized peak areas as a function of time are shown in Figure 5.14.

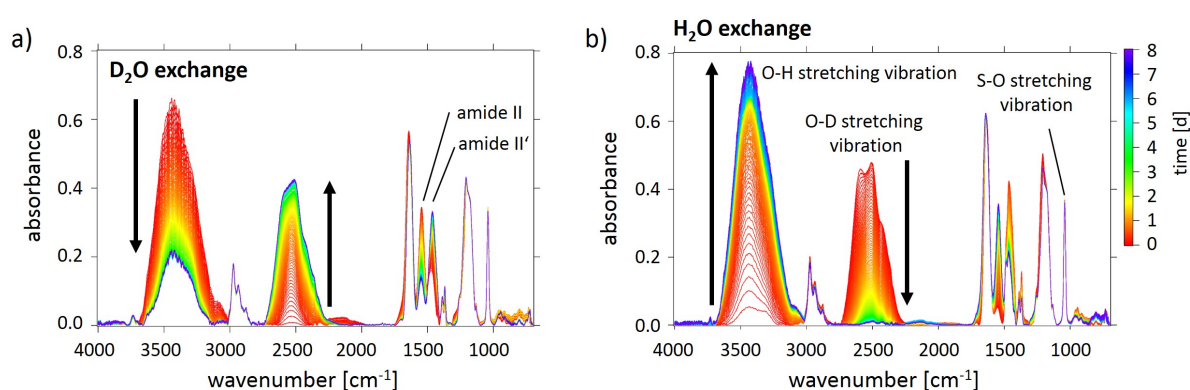


Figure 5.13.: Water exchange followed with FTIR *in-situ* FTIR spectra during the (a) H₂O and (b) D₂O exchange. The red curve marks the initial ($t = 0$ days), while the purple curve marks the final measurement after 8 days, with respect to the induce of the water exchange. Characteristic absorption peaks are labelled accordingly. Black arrows mark the increase and decrease of the O-H and the O-D stretching vibration. Adapted with permission from AMERICAN CHEMICAL SOCIETY, Copyright 2019 [36].

Similar to the swelling kinetics, the O-H peak reaches a higher plateau as compared to the O-D peak (the different molar extinction coefficient of the O-H and O-D stretching vibration is taken into account). This clearly proves a higher H₂O incorporation during the H₂O exchange, as compared to the D₂O incorporation during the D₂O exchange. Most interestingly, the final O-H and O-D peak areas, reach a similar integration area than after the water swelling, *i.e.*, after the D₂O exchange a similar amount of D₂O is incorporated in the thin film than after the swelling in D₂O vapor and vice versa for the H₂O exchange. Therefore, the particular order of the applied vapors, first H₂O, then D₂O, or vice versa, does not matter regarding the individual H₂O or D₂O content in the final equilibrium states of the thin film. However, the order does matter for the total water content, as different amounts of water are released during the exchange processes. Notably, the exchange processes are not complete, as a mixture of both water species is present in the thin films after the water exchange process has equilibrated. This is in good agreement with the findings from ToF-NR.

5.3. Exchange behavior

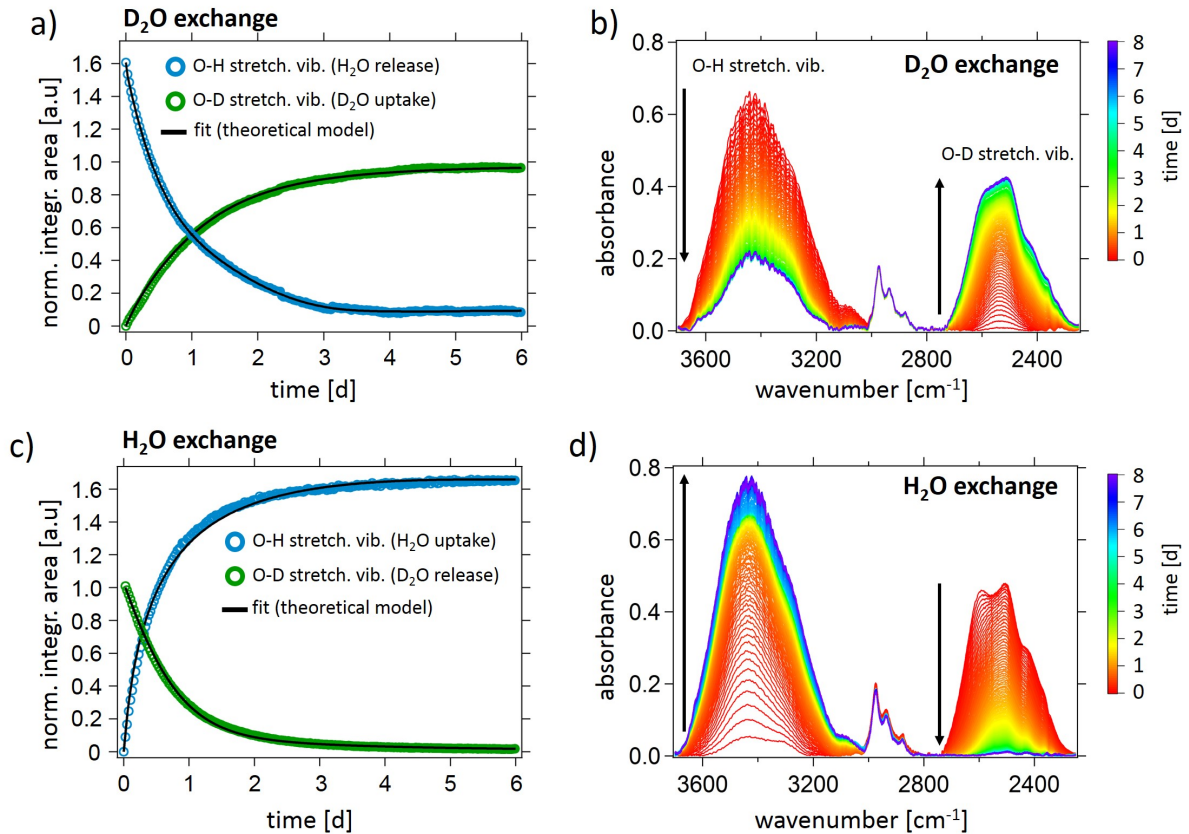


Figure 5.14.: Extracted integration areas from FTIR spectra during water exchange. The integration areas of the O-H (blue) and O-D stretching vibration (green) during the exchange with (a) D₂O and (c) H₂O are extracted from the absorption modes shown in (b,d). The integration areas as a function of time (a,b) are fitted with a swelling model (black line) as explained in the main text. Adapted with permission from AMERICAN CHEMICAL SOCIETY, Copyright 2019 [36].

The swelling model is applied to both, the water release and water uptake process during the water exchange. While it yields similar $\chi_{eff}(\Phi\text{-uptake})$ values for the water uptake processes (cf. Table 5.7), indicating no specific preference of the DBC toward H₂O or D₂O, the $\chi_{eff}(\Phi\text{-release})$ values show the by now well-known higher affinity of the polymer towards H₂O. The $\tau(\Phi)$ values confirm this. Both, the H₂O uptake during the H₂O exchange, and the H₂O release during the D₂O exchange happens on a clearly faster time scale than the corresponding D₂O uptake and release processes, thereby demonstrating the faster diffusion of H₂O through the DBC thin film.

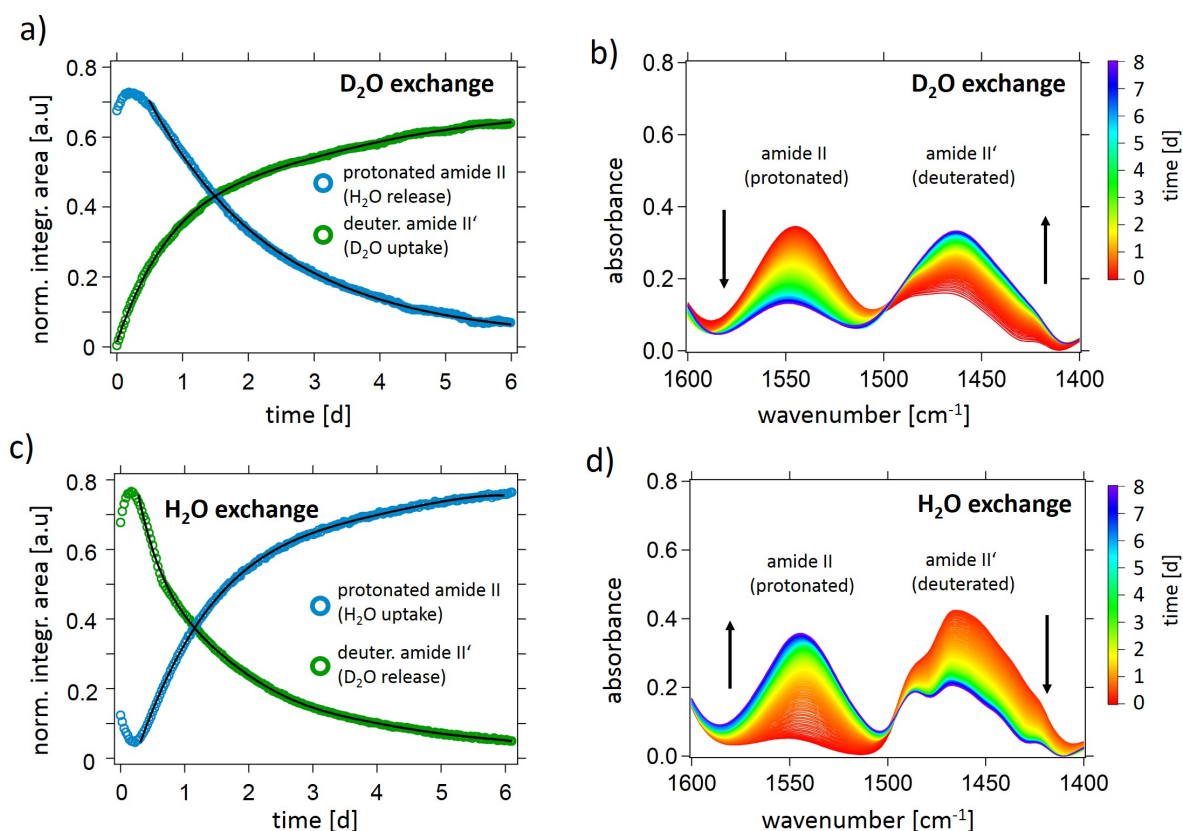


Figure 5.15.: Extracted integration areas from FTIR spectra during water exchange. The protonated amide II (blue) and the deuterated amide II' mode (green) during the exchange with (a) D_2O and (c) H_2O are extracted from the corresponding absorption modes shown in (c,d). The integration areas are fitted with an exponential fit as explained in the main text. Black arrows indicate increasing and decreasing absorption modes. Adapted with permission from AMERICAN CHEMICAL SOCIETY, Copyright 2019 [36].

Analogously to the swelling kinetics, the deuteration degree of the amide group is analyzed by integrating the absorption peaks of the amide II and II' modes. The normalized peak areas as a function of time are displayed in Figure 5.15. A clear increase and decrease in peak area of the amide II' and II mode, respectively, is obtained during the D_2O exchange, while the opposite behavior can be seen during the H_2O exchange. Hence, deuteration of the protonated amide group, as well as a re-protonation of the deuterated amide group occur upon both exchange processes. An exponential fit suggests a faster re-protonation during the H_2O exchange [amide II growth rate = (1.2 ± 0.13) d] than deuteration during the D_2O exchange [amide II' growth rate = (1.96 ± 0.20) d], which is in agreement with the previously found faster H_2O diffusion. One has to note, during the very early times of the exchange processes a slight decrease of the amide II mode during the D_2O exchange, as well as an increase and decrease of the amide II' and II modes, re-

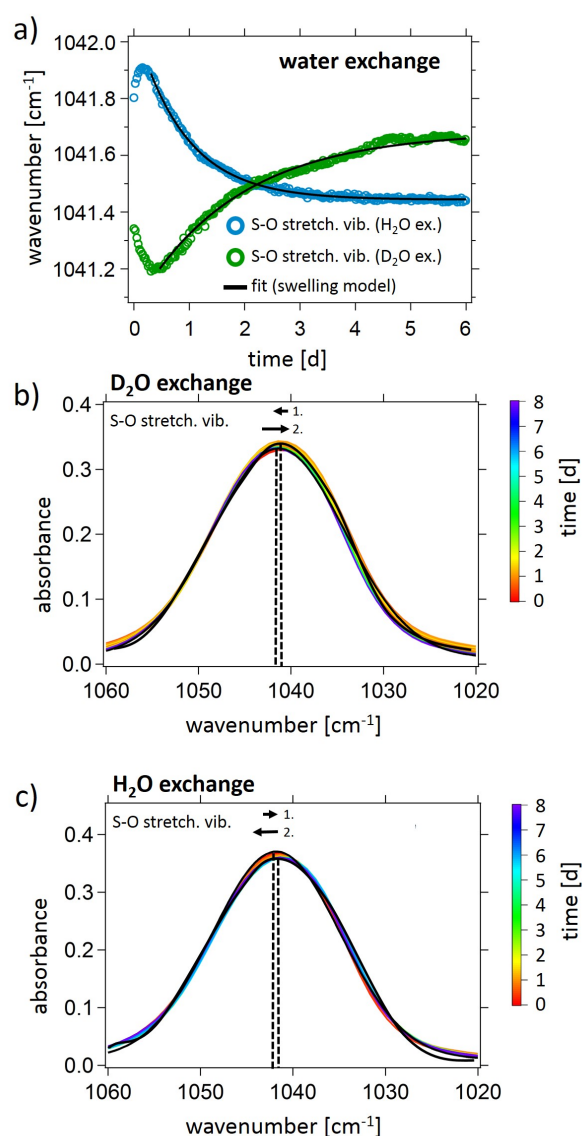
Table 5.7.: Swelling model applied to the FTIR data shown in Figures [5.14](#) and [5.16a](#).

water exchange	χ_{eff}	τ [d]	extracted from
D₂O exchange			
D ₂ O uptake	0.77 ± 0.01	1.01 ± 0.10	FTIR [Φ (O-D stretch. vib.)] ^a
H ₂ O release	0.25 ± 0.01	0.69 ± 0.17	FTIR [Φ (O-H stretch. vib.)] ^a
H₂O exchange			
H ₂ O uptake	0.79 ± 0.01	0.72 ± 0.21	FTIR [Φ (O-H stretch. vib.)] ^a
D ₂ O release	1.12 ± 0.02	2.89 ± 0.17	FTIR [Φ (O-D stretch. vib.)] ^a
D ₂ O exchange	0.85 ± 0.01	1.75 ± 0.03	FTIR (S-O stretch. vib.) ^b
H ₂ O exchange	0.88 ± 0.01	0.99 ± 0.01	FTIR (S-O stretch. vib.) ^b

spectively, during the H₂O exchange, is visible. This is accounted to a protonation (upon D₂O exchange) and deuteration (upon H₂O exchange) of the amide group, as result to re-arrangement processes of the polymer chains.

In a last step, the peak shift of the symmetric S-O stretching vibration as a function of time is analyzed. Figure [5.16](#) shows its evolution during the respective exchange processes. During the first 12 hours of the D₂O exchange, the S-O peak shifts to lower wavenumbers, before it shifts back to higher wavenumbers. Essentially, the trend is reversed during the H₂O exchange, as it first shifts to higher (during the first 8 h), and then to lower wavenumbers. The smaller initial shifts to higher and lower wavenumbers are addressed to a change in hydration due to re-arrangement processes of the polymer chains at early stages of the water exchange. The subsequent backshifts refer to a slowly exchanged hydration shell around the SO₃⁻ groups as response to the exchange of the water vapor. The peak maximum shifts are less pronounced as during the water swelling processes, since a water hydration shell is already present in the beginning of the water exchange and is only modified to a mixed D₂O and H₂O hydration shell. Similar to the swelling kinetics, the position of the S-O stretching vibration peak maximum equilibrates at higher wavenumbers during the D₂O exchange as compared to the H₂O exchange. Analogously to the swelling behavior, this is due to the higher mass of D₂O, but also due to a stronger D₂O hydration. Interestingly, the final peak positions after the swelling in D₂O vapor and D₂O exchange, and vice versa are very similar. This suggests a completed exchange process in which all water molecules within the hydration shell around the SO₃⁻ group are replaced with the respective other water species. This stands in contrast to the non-completed exchange process, regarding the overall water content within the thin film, and

Figure 5.16: Peak maximum position extracted from FTIR spectra during water exchange. (a) The peak position of the symmetric S-O stretching vibration upon the exchange in D₂O (green) and H₂O vapor (blue) is extracted via a Gaussian fit from the corresponding absorption modes shown in (b,c). A Gaussian fit (applied to all FTIR curves) is shown in (b,c) as black line for each first and final absorption peak. Dashed black lines indicate the peak maxima. The S-O peak position as a function of time as shown in (a) is fitted with a swelling model (black line) as explained in the main text. Adapted with permission from AMERICAN CHEMICAL SOCIETY, Copyright 2019 [36].



demonstrates that the local swelling and exchange behavior of particular groups does not necessarily follow the overall thin film behavior. This fits to the special role the SO_3^- holds during the water swelling and exchange.

The swelling model is applied to the peak position shift, while only the peak shift after the re-arrangement of the polymer chains is considered. The extracted values are summarized in Table 5.7. The obtained values for $\chi_{eff}(\text{S-O})$ suggest favored interactions between the SO_3^- group and D₂O as compared to H₂O, which is in agreement with the results from the swelling processes. Interestingly, the $\tau(\text{S-O})$ values indicate a slower assembly of D₂O molecules around the SO_3^- group. This is due to the generally lower affinity of the DBC towards D₂O and the observed slower D₂O diffusion speed through the thin film. Noteworthy, the $\tau(\text{S-O})$ values are higher than the respective values for the

D₂O and H₂O uptake processes, *i.e.*, the exchange of the hydration shell around the SO₃⁻ group needs longer times, than the water uptake of the thin film. This is most likely due to the complete water exchange process of the hydration shell around the SO₃⁻ group in contrast to the only partial water exchange process within the (bulk) thin film.

5.4. Conclusion

This chapter focuses on the swelling and exchange behavior of PSPP-*b*-PNIPAM thin films in H₂O and D₂O vapor. Particular attention is given to the swelling and exchange kinetics. While SR and ToF-NR yield mesoscopic parameters such as the thin film thickness and the water content, FTIR is applied to obtain information on a molecular level. This choice of measurement techniques enables to connect information about polymer-water interactions with the general thin film behavior, in particular with the absorbed and released water content and the film thickness. In addition, the two water species, H₂O and D₂O, show large differences in their SLD and binding energy, which gives excellent contrast in the ToF-NR and FTIR measurements. Thus, a comparison of the corresponding swelling and exchange processes is possible and a fundamental knowledge about the role of deuterated solvents, with particular regard to the known H/D isotope sensitivity of PSBs, is developed. By applying a swelling model, which respects a non-constant RH, the swelling and exchange processes can also be analyzed in a quantitative way.

We observe, a significant different swelling and foremost a different exchange behavior of the DBC thin films in either H₂O or D₂O vapor. Most prominently, a higher affinity of the DBC towards H₂O as compared to D₂O is found, which is mainly addressed to the isotope sensitivity of the PSPP block and the decreased CP'_{PSPP} in H₂O as compared to D₂O. This results in a larger amount of H₂O that is incorporated within the thin films, and furthermore in a stronger swelling degree and a faster saturation during both, the swelling and exchange in H₂O vapor. Most notably, the evolution of the film thickness during the exchange processes is highly opponent. During the D₂O exchange, the film first contracts before it re-swells, while the fully D₂O swollen thin film is able to undergo a further swelling process upon H₂O exchange. FTIR measurements support these findings on a molecular level. Furthermore, FTIR highlights the special role of the SO₃⁻ group and demonstrates that the behavior of individual characteristic groups might deviate from the overall polymer behavior, with respect to water affinity and hydration speed. While the shift of the peak maximum of the S-O stretching vibration suggests rather a completed exchange of the hydration shell around the sulfonate group, the overall water content, reveals that after the water exchange, a mixture of D₂O and H₂O molecules are present within the thin film. In addition, deuteration of the amide group, present in both

the PSPP and the PNIPAM block, is detected once deuterated water is involved in the swelling and exchange processes. The deuterated amide groups are re-protonated during the H₂O exchange. As a consequence, a third water species, HDO, is generated, which is assumed to adopt an intermediate role between H₂O and D₂O, regarding its affinity to the DBC and mobility within the thin film.

All these findings demonstrate strong differences in the swelling and exchange behavior of the DBC thin films, dependent on whether these processes are realized in a H₂O or a D₂O vapor. The deviating swelling and exchange mechanisms are mainly attributed to the isotope sensitivity of the PSPP block. Apparently, the differences in molar mass, dipole moment, and electronegativity influence the H- and D-bonds to the polymer chain considerably. This is expected to a certain level, however the significance of the observed differences are indeed surprising.

6. Co-nonsolvency effect in polymer thin films

This chapter is divided into two parts. The first part is about PSPE and PNIPMAM homopolymer thin films in mixed water/methanol vapor and is based on the publication 'Poly(sulfobetaine) versus Poly(*N*-isopropylmethacrylamide): Co-Nonsolvency-Type Behavior of Thin Films in a Water/Methanol Vapor Atmosphere' (L. P. Kreuzer et al., *Macromolecules* **2021**, 54, 1548-1556; DOI: 10.1021/acs.macromol.0c02281) [39]. Experiments were performed in collaboration with bachelor student Christoph Lindenmeir [249]. The second part investigates PSPE-*b*-PNIPMAM thin films in mixed water/methanol vapor. The PSPE and PNIPMAM blocks feature same block lengths as the corresponding homopolymers that are described in the first part. This part is based on the publication 'Solvation Behavior of Poly(sulfobetaine)-Based Diblock Copolymer Thin Films in Mixed Water/Methanol Vapors' (L. P. Kreuzer et al., *Macromolecules* **2021**, 54, 7147–7159; DOI: 10.1021/acs.macromol.1c01179) [250]. All Figures are re-printed with permission from AMERICAN CHEMICAL SOCIETY, Copyright 2021.

In the previous chapter, the behavior of poly(sulfobetaine)-based diblock copolymer (DBC) thin films in pure and mixed water vapors (H₂O and D₂O) is described, which is far more complex than initially assumed. In order to extend the knowledge about polymer thin films in mixed vapors, methanol is introduced as a second solvent besides water. On the one hand, methanol is chosen because it is the simplest alcohol, and on the other hand, poly(acrylamides), such as poly(*N*-isopropylacrylamide) (PNIPAM) and poly(*N*-isopropylmethacrylamide) (PNIPMAM) feature a co-nonsolvency phenomenon in mixed water/alcohol solutions (cf. Section 2.2.2).

The swelling process is performed in saturated water vapor, while the subsequent exchange process takes place in mixed water/methanol vapor. Since the last chapter reveals a highly complex exchange process, we found it necessary, to improve the understanding of the individual polymer blocks. Therefore, the behavior of a poly(sulfobetaine) (PSPE₂₇₀) and PNIPMAM homopolymer (PNIPMAM₆₅) thin film in different vapor compositions

is analyzed first, and subsequent the corresponding PSB₂₇₀-*b*-PNIPMAM₆₀ thin films are investigated.

Introduction

The counterintuitive phenomenon of two miscible and good solvents for a polymer, becoming a poor solvent for the same polymer when mixed is called co-nonsolvency effect [91, 92]. While the origin of the change in polymer conformation in the mixture of two good solvents is under vivid scientific debate, most researchers agree upon the major impact of polymer-solvent interactions on this polymer transition. Several promising models emerged over the last years that focused in particular on the competitive hydrogen bonding of the two used solvents [167, 169, 173, 174], hydrophobic hydration [176, 251], and bridging of two individual polymer chains by the co-solvent [167, 175]. A detailed description of the co-nonsolvency effect and a current state of the art is provided in Section 2.2.2.

So far, the co-nonsolvency studies known to literature investigated the polymer behavior in diluted bulk solution or hydrogels [92, 154, 170, 252–254], where the polymer concentration was intermediate. These experimental studies were supported by extensive theoretical and simulative approaches [167–170, 175, 255]. Recently, also concentrated samples systems, *e.g.*, tethered polymer brushes and microgel thin films [148, 163, 174, 256–260], were reported. While all these studies used a liquid stimuli, experiments or simulations, addressing the co-nonsolvency effect of concentrated thin films surrounded by a mixed vapor phase, were very rarely reported so far [39, 165, 166]. Since the increased polymer concentration in thin film geometry is expected to strongly alter the polymer-solvent interactions, an extrapolation of the polymer behavior from bulk solution to thin film geometry is not possible. Furthermore, the solvent concentration is lower in the vapor phase than in the by now, well-studied liquid mixtures, which is also expected to alter the co-nonsolvency mechanism. Information to thin films in saturated vapors is provided in Section 2.1.2.

In the present chapter, we aim for a deeper understanding about the behavior of orthogonally dual thermo-responsive DBC in mixed water/methanol vapors. The DBC under investigation consists of the zwitterionic poly[3-((2-(methacryloyloxy) ethyl)dimethyl ammonio) propane-1-sulfonate] (PSPE) and the nonionic PNIPMAM. The chemical structure of the DBC PSPE₂₇₀-*b*-PNIPMAM₆₀ is shown in Figure 4.2c in Section 4.2. For simplicity, it is referred to as PSPE-*b*-PNIPMAM in the following. While at temperatures below the cloud point (CP_{PNIPMAM}), PNIPMAM is soluble in water, the addition of ethanol was found to decrease the CP_{PNIPMAM} , which eventually led to a de-mixing of PNIPMAM in water/ethanol mixtures [261, 262]. For PNIPAM a co-nonsolvency behavior was also

reported in mixed water/methanol solutions [92, 154, 168, 170, 263]. Above its clearing point (CP'_{PSPE}) PSPE is soluble in water, but in contrast to PNIPMAM it is insoluble in methanol [125, 264], and therefore does not show a co-nonsolvency effect in mixed water/methanol solution. With increasing methanol content its solubility decreases, thus, according to the Flory-Huggins solution theory, methanol is a classical non-solvent to PSPE. Still, co-nonsolvency behavior in water/alcohol mixtures is not unknown to polyelectrolytes. For instance, co-nonsolvency was reported for poly(phosphatidylcholine methacrylate) in ethanol-rich water/ethanol mixtures [265].

In order to understand the role of the individual polymer blocks, the corresponding PSPE_{270} and PNIPMAM_{65} homopolymer thin films are analyzed and described in the first part of this chapter. Both homopolymer thin films are named simply PSPE and PNIPMAM hereafter. Figure 6.1 gives a schematic overview of the performed experiments. The temperature is kept constant at 22°C . In dilute aqueous solutions, a CP'_{PSPE} of $\approx 55^\circ\text{C}$, and a CP_{PNIPMAM} of 30°C was found by our collaboration partners from University of Potsdam via transmission measurements [126, 127]. Thus, the chosen measurement temperature is below both, the CP'_{PSPE} and CP_{PNIPMAM} in the binary dilute homopolymer-water phase diagrams. Hence, at 22°C PSPE is insoluble in aqueous solution, while PNIPMAM is soluble. An analogous situation is encountered in methanol, in which again PSPE is insoluble, but PNIPMAM is soluble. Therefore, we expect the PSPE thin films to be less solvated than the PNIPMAM thin films throughout the swelling in water vapor as well as upon the methanol exchange.

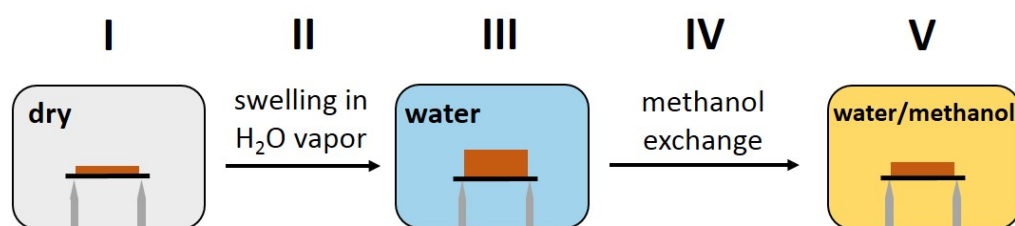


Figure 6.1.: Co-nonsolvency effect in PSPE and PNIPMAM thin films: Schematic representation of the performed experiments. PSPE and PNIPMAM thin films are exposed to water vapor first. Subsequent methanol is added to the vapor, thereby exchanging some of the water molecules (final water/methanol ratio of 70/30 V%). The thin films in their equilibrium states are labelled with I, III, and V, respectively. The thin film kinetics of the swelling in water vapor (stage II) and the methanol exchange (stage IV) are followed with SR and FTIR *in-situ*. The initial dry, the pure water, and the mixed water/methanol vapor are indicated in, gray, blue, and yellow, respectively. Adapted with permission from AMERICAN CHEMICAL SOCIETY, Copyright 2021 [39].

Both, the PSPE and PNIPMAM thin film, are first dried (stage I in Figure 6.1), and subsequently swollen in saturated water vapor (swelling in water vapor, stage II). Once the swollen films are in equilibrium (stage III), some of the water vapor is exchanged with methanol (methanol exchange, stage IV), by setting the water/methanol flow ratio to 70/30 vol%. The experiment terminates once the thin films have equilibrated (stage V). By investigating the behavior of PSPE and PNIPMAM in thin film geometry, we aim for a better understanding how an increased polymer concentration and altered polymer-water/methanol interaction affect the co-nonsolvency phenomenon in polymer thin films.

The first part about the homopolymer thin films is structured as follows. First, spectral reflectance (SR) measurements, monitoring *in-situ* the film thickness of the PSPE and PNIPMAM thin films during the swelling in water vapor and the methanol exchange are presented. Subsequently, polymer-water and polymer-methanol interactions, probed via Fourier-transform infrared spectroscopy (FTIR), are discussed. A final conclusion is provided at the end of this first part. The scientific focus lies in particular on the behavior of both polymer thin films during the methanol exchange. Based on the different nature of PSPE and PNIPMAM, *i.e.*, zwitterionic vs. nonionic, insoluble vs. soluble in methanol, UCST vs. LCST, a deviating behavior is expected. A custom-made sample environment in combination with a gas flow setup is used to realize *in-situ* measurements (cf. Section 3.4.2). The thin film samples discussed in the following are prepared according to Section 4.4. A pre-characterization of the homopolymer thin film samples is done via optical and atomic force microscopy, which reveal a highly homogeneous and smooth thin film's surface. The Appendix B provides details to the pre-characterization of the thin films.

6.1. PSPE and PNIPMAM thin films in mixed water/methanol vapor

The relative humidity (RH) and temperature are monitored throughout the swelling in water vapor. Upon the methanol exchange, two solvents are present within the measurement chamber, which makes it challenging to track the RH, as the methanol falsifies the water RH and vice versa. This is commonly known as cross-sensitivity. Since the RH evolves very similar during the swelling in water vapor of PSPE and PNIPMAM, (cf. Figure 6.2), we assume very similar conditions also during the methanol exchange.

The film thickness of the PSPE and PNIPMAM thin films during the swelling in water vapor (stage II) and the methanol exchange (stage IV) is followed with SR almost in real time as every 10 seconds a single SR spectrum is recorded. Since the thin film swelling behavior is strongly correlated with the initial film thickness [73], special attention is paid to achieving a similar initial film thickness of the PSPE and the PNIPMAM thin

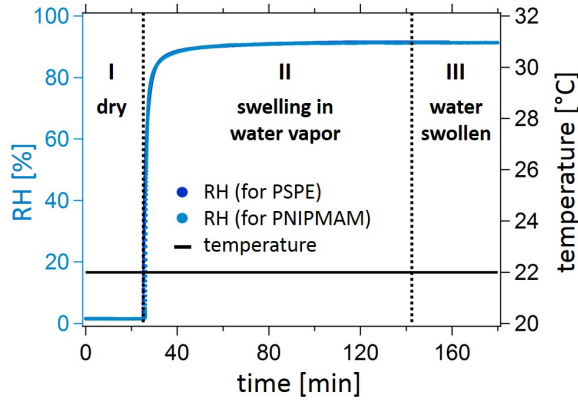


Figure 6.2: RH and temperature during swelling in water vapor The good overlap of the RH for the PSPE (dark blue) and PNIPMAM (pale blue) assures a good comparability of the two performed experiments. The RH during the methanol exchange is not followed as explained in the text. The temperature is kept constant at 22 °C (black solid line). The thin film stages are labelled according to Figure 6.1. Adapted with permission from AMERICAN CHEMICAL SOCIETY, Copyright 2021 [39].

films. Table 6.1 lists the film thicknesses in the dry state, after the swelling in water vapor, after the methanol exchange, as well as in pure methanol vapor. To account for the slight difference of the initial PSPE and PNIPMAM film thickness, the initial film thickness d_{ini} is used for normalization, and the resulting swelling ratio d/d_{ini} is used in the following discussion. Figure 6.3 gives the swelling ratio as a function of measurement time throughout swelling in water vapor and the methanol exchange. Furthermore, Figure 6.3c,d depicts the swelling ratio during the swelling in pure methanol vapor, which is performed as a reference experiment.

Table 6.1.: PSPE and PNIPMAM thin film thickness determined with SR measurements shown in Figure 6.3.

thin film	d (d/d_{ini}) (N ₂ vapor)	d (d/d_{ini}) (water vapor)	d (d/d_{ini}) (water/methanol vapor)	d (d/d_{ini}) (methanol vapor)
PSPE	34 ± 1 (1.00)	62 ± 3 (1.82)	40 ± 2 (1.18)	46 ± 1 (1.35)
PNIPMAM	28 ± 2 (1.00)	30 ± 1 (1.07)	29 ± 1 (1.04)	34 ± 2 (1.21)

The PSPE thin film reaches a significantly higher swelling ratio during the swelling in water vapor than the PNIPMAM thin film. This enormous difference in swelling degree is highly unexpected, since from dilute aqueous solution behavior, the opposite behavior is expected. At 22 °C, PSPE is insoluble in water, but PNIPMAM is. We assume, due to altered and more dominant polymer-polymer interactions in thin film geometry, a clustering of the nonpolar isopropyl groups as well as of the nonpolar backbone of PNIPMAM occurs. As a consequence, large amounts of water are prevented to solvate

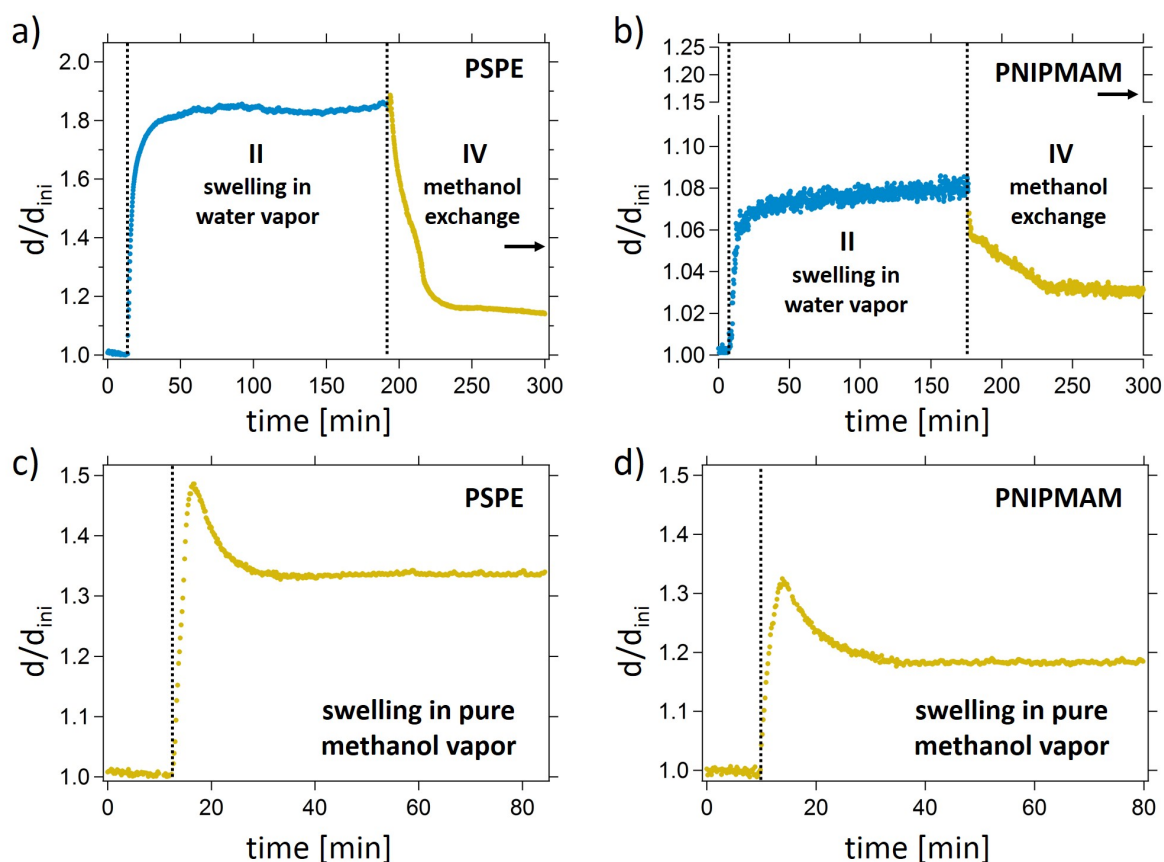


Figure 6.3.: Swelling in water vapor and the subsequent methanol exchange followed with SR *in-situ*. The swelling ratio d/d_{ini} as a function of measurement time during the swelling in water vapor (stage II) and the methanol exchange (stage IV) of the (a) PSPE and the (b) PNIPMAM thin film. The two black arrows mark the final swelling ratio of the respective thin films after swelling in pure methanol vapor, which is shown in (c) for the PSPE and in (d) for the PNIPMAM thin film. Adapted with permission from AMERICAN CHEMICAL SOCIETY, Copyright 2021 [39].

the polar amide groups. In contrast, the PSPE side chains are more polar and longer and thus, are able to accommodate and bind significantly larger quantities of water than PNIPMAM.

Once the thin films are in an equilibrated state, the methanol exchange is induced. Immediately, both thin films undergo a pronounced contraction and reach a swelling ratio that is not only lower than the swelling ratio in pure water vapor, but also lower than in pure methanol vapor (cf. Figure 6.3c,d and black arrows in Figure 6.3a,b). This may have been expected for the PNIPMAM thin film due to its known co-nonsolvency effect in mixed water/alcohol solution, however not for the PSPE thin film. PSPE is insoluble in methanol and according to the Flory-Huggins solution theory, the PSPE thin film should experience

a monotonous decrease in film thickness upon increasing methanol content. However, a behavior analogously to the co-nonsolvency-type behavior of the PNIPMAM thin film is observed. Apparently, the altered polymer-water and polymer-methanol interactions due to an increased polymer concentration in the thin film geometry, lead to a good compatibility of PSPE and methanol, and eventually to co-nonsolvency-type behavior in mixed water/methanol vapor.

While both thin films feature a contraction upon methanol exchange, the underlying contraction mechanisms deviate from each other. For the PSPE thin film a one-step contraction is observed, while the PNIPMAM thin film contracts in two individual steps. The abrupt initial contraction slows down shortly after and the contraction slows down. One has to note that the PSPE contraction also features a small shoulder, however this is not accounted for a second contraction phase, since the slopes before and after that shoulder are virtually the same. Interestingly, the time scales of the thin film contractions differ as well. While the PSPE equilibrates within a short time of approximately 20 min, it takes about 65 min for the PNIPMAM thin film to reach an equilibrated state. This hints towards different diffusion speeds and a different mobility of water and methanol within the PSPE and the PNIPMAM thin film, which naturally, are affected by the polymer-water/methanol interactions. While the PSPE thin film reaches a higher swelling ratio in pure water vapor as compared to pure methanol vapor, it is the other way round for the PNIPMAM thin film. Therefore, we assume, PSPE has a higher affinity to water, whereas PNIPMAM has a higher affinity to methanol.

While it is known, PNIPAM (and therefore we assume also PNIPMAM) shows a strong binding to the hydroxyl groups of methanol, the strong swelling degree of the PSPE thin film in pure water vapor suggests a high affinity to water. This indicates different preferred polymer-solvent interactions within the two polymer thin films. While PSPE-water interactions are favored over PSPE-methanol interactions, the opposite case is encountered in the PNIPMAM thin films and PNIPMAM-methanol interactions are favored over PNIPMAM-water interactions. These differences might explain the deviating contraction response of PSPE and PNIPMAM upon methanol exchange.

In order to analyze the molecular origin of the unexpected thin film behavior, FTIR measurements are performed according to the measurement protocol shown in Figure [6.1](#). This measurement technique enables a decoupled observation of the water release and the methanol absorption once the methanol exchange is induced and methanol is also present within the FTIR measurement chamber. In contrast to the SR measurements, every 2 minutes a single FTIR spectrum is recorded. The resulting spectra during the swelling in water vapor and the methanol exchange processes are shown in Figure [6.4](#). The prominent absorption modes appearing at around 3400 cm^{-1} and at 2986 cm^{-1} refer to the

O-H and C-H stretching vibrations. The integration areas of the absorption peaks indicate the amount of water and methanol within the thin films. A three-fold peak is detected at around 2950 cm^{-1} , which can be addressed to the asymmetric (2974 cm^{-1}) and the symmetric C-H stretching vibrations (2886 cm^{-1}) of the CH_3 groups. The asymmetric C-H stretching vibration of the CH_2 groups appears at 2938 cm^{-1} . These absorption modes in the dry thin film state (very first FTIR spectrum) are used to normalize all other peaks used for analysis, in order to eliminate the impact of varying thin film thicknesses. Figure 6.5 depicts the normalized integration areas as a function of exposure time during the swelling in water vapor and the methanol exchange.

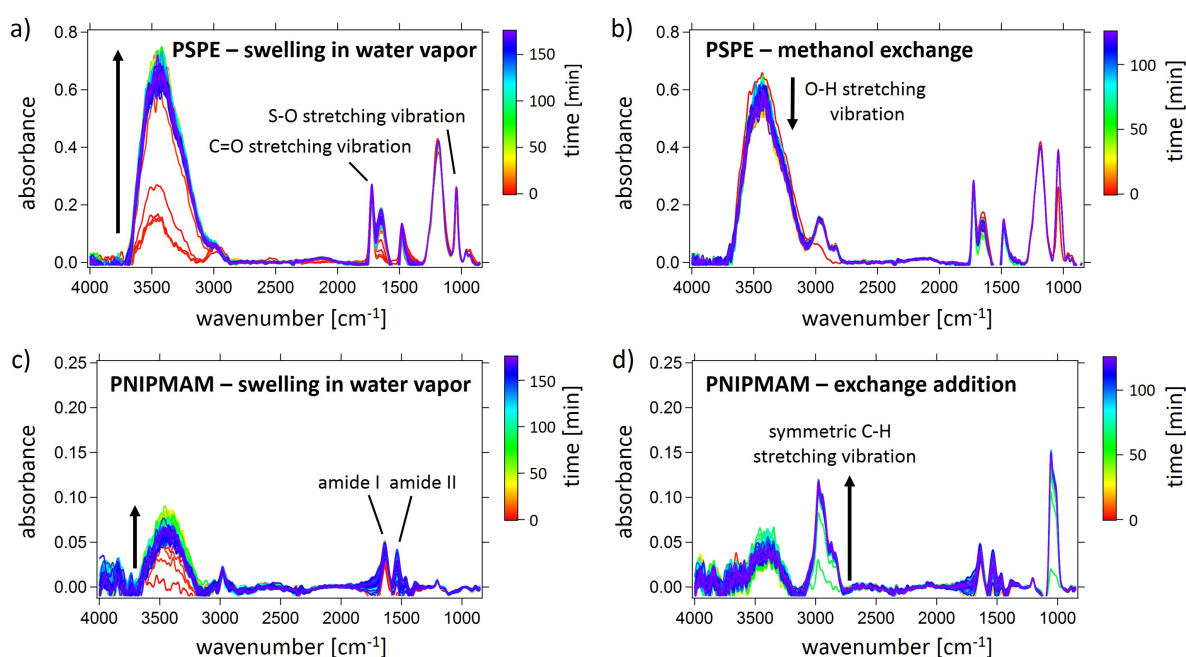


Figure 6.4.: Swelling in water vapor and the subsequent methanol exchange followed with FTIR *in-situ*. FTIR spectra during the swelling in (a,c) water vapor, as well as during the (b,d) methanol exchange for the (a,b) PSPE and (c,d) PNIPMAM thin film. FTIR spectra during the (a,c) swelling in water vapor and the (b,d) methanol exchange for the PSPE and PNIPMAM thin film. The red curve marks the initial ($t = 0$ min), the purple curve marks the final measurement after 175 min (swelling in water vapor) and 125 min (methanol exchange). Characteristic absorption peaks are labelled accordingly. Black arrows mark the increase and decrease of the water and methanol peaks. Adapted with permission from AMERICAN CHEMICAL SOCIETY, Copyright 2021 [39].

During the swelling in water vapor, the PSPE thin film clearly absorbs a considerably higher amount of water than the PNIPMAM thin film, thereby confirming the SR findings. Both thin films reach a maximal water content before a certain amount of water is released from the thin films again. This is due to polymer re-arrangement processes, which are the

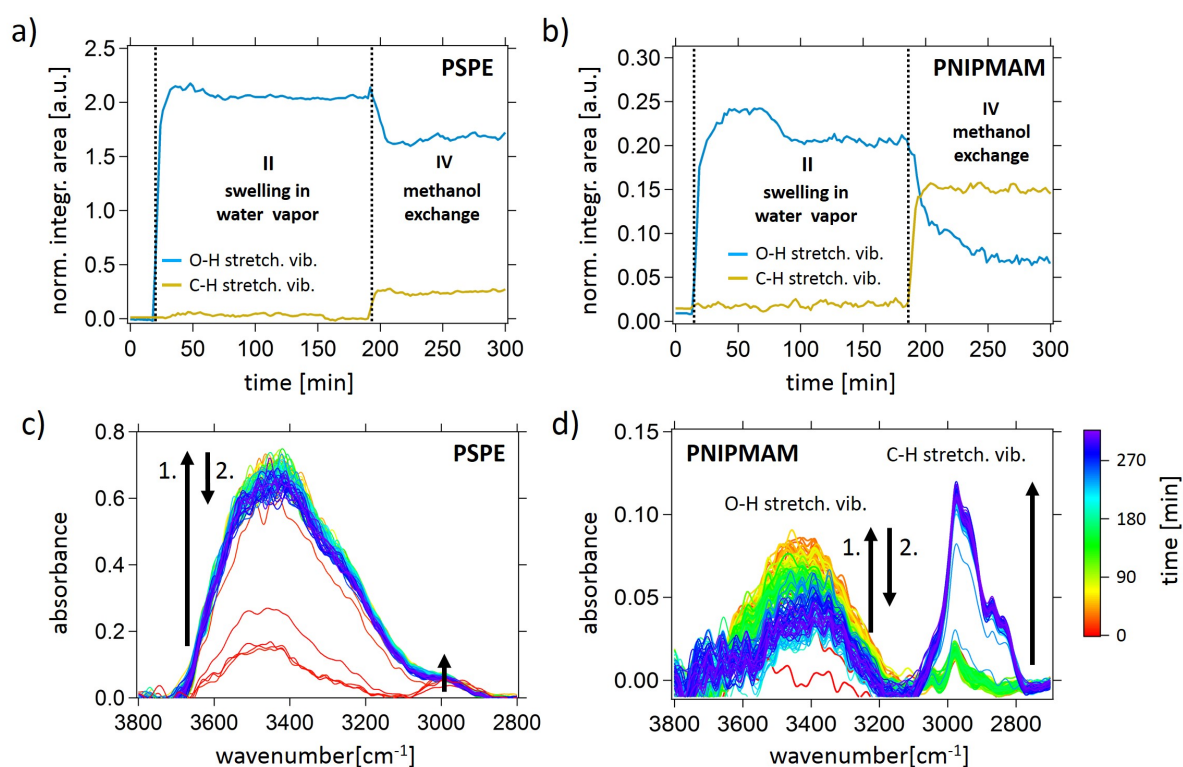


Figure 6.5.: Integration areas extracted from FTIR spectra during swelling in water vapor and the subsequent methanol exchange. The normalized peak areas of the O-H (blue) and C-H peaks (yellow) stretching vibrations are extracted as a function of time for the (a) PSPE and (b) PNIPMAM thin film from the corresponding absorption modes shown in (c,d). Black arrows indicate increasing and decreasing water and methanol absorption peaks. Numbers indicate the sequence order of increase and decrease steps. Adapted with permission from AMERICAN CHEMICAL SOCIETY, Copyright 2021 [39].

result of a higher polymer chain mobility with increasing water content. Immediately after the methanol exchange is induced, both thin films absorb methanol and release water. The methanol absorption occurs in one single step for both the PSPE and PNIPMAM thin films and is finished roughly around 10 minutes. The water release mechanism deviates in both thin films. While the PSPE thin film features a fast one-step water release, the PNIPMAM thin film releases water in two-steps. During the first 10-12 min, water is released rapidly, before the release is significantly slowed down and the thin film reaches an equilibrium state after roughly 60 min following the methanol exchange. The different water release regimes could hint toward the presence of two water species, *i.e.*, hydrophobic hydration water around the isopropyl group and water bound by H-bonds, which are substituted by methanol at different speeds. Interestingly, both release mechanisms strongly resemble the evolution of the film thickness that is observed with

SR measurements, which suggests that mainly the released water is responsible for the accompanied film thickness change.

The combined findings from SR and FTIR reveal a different behavior of the PSPE and the PNIPMAM thin film in a mixed water/methanol vapor. For PSPE, the water release and methanol absorption are closely synchronized. The accompanying decrease in film thickness takes slightly longer than the water release, indicating ongoing re-arrangements of the PSPE chains after both the water and methanol contents have already equilibrated. In the case of PNIPMAM, the methanol uptake is markedly faster than the water release and has already equilibrated, while the water uptake is still ongoing. Possibly, both water species are replaced by methanol within the same time scale in one single step. The differences in water release demonstrate the deviating polymer-water and polymer-methanol interactions in both thin films and underline how the polymer nature alters the general thin film behavior.

Interestingly, in the equilibrated state after the methanol exchange, the normalized integration areas of the O-H and C-H peaks indicate, most of the water remains within the PSPE thin film, while most of the water is released from the PNIPMAM thin film. This highlights the favored PNIPMAM-methanol and PSPE-water interactions in the respective thin films. The observed behavior might be due to the preferential and rapid binding of methanol toward PNIPMAM, which makes its sidechains appear more hydrophobic after methanol absorption [168, 266], and can be seen as the thin film equivalent to the collapsed globules in mixed solutions [267]. As a consequence, even more water is released from the PNIPMAM thin film, which is observed as a second and decelerated water release process. In contrast, the PSPE thin film does not continue to release water molecules after the methanol uptake has finished. Therefore, we assume that the methanol does not affect the binding of solvents to the PSPE chains, presumably due to the strong attractive interactions between PSPE and water. This means, for the two investigated polymer thin films, different driving forces and varying preferential interactions affect their respective swelling behavior in multiple ways. Nevertheless, both thin films undergo a distinct contraction in mixed water/methanol vapor, which is followed by a re-swelling upon increasing methanol content. Eventually, this observation requires rather a thin film-specific interpretation of the observed co-nonsolvency-type behavior than an explanation by universal co-nonsolvency theory. The origin of the observed behavior could reflect the respective hydrophilicities of the PSPE and PNIPMAM thin films at 22 °C, which differs greatly regarding the water uptake during the swelling in water vapor. This is also indicated by the SR measurements and infers a strong shift of both, the UCST-type and LCST-type transition temperatures to lower temperatures (< 22 °C), as the polymers are transferred from aqueous solution to thin film geometry.

While the peak integrals are indicative of the overall amounts of water and methanol within the thin films, the analysis of the peak positions of the polymer absorption peaks addresses the specific solvation of the corresponding functional groups, as their bonding energy is altered with a changing chemical environment. Figure 6.6 displays the peak positions of the symmetric S-O (from the SO_3^- group at the end of the PSPE side chain) and C=O stretching vibration (from the ester group in the PSPE side chain) as well as the peak shift of the amide I and II modes (amide group in the PNIPMAM side chain) as a function of measurement time.

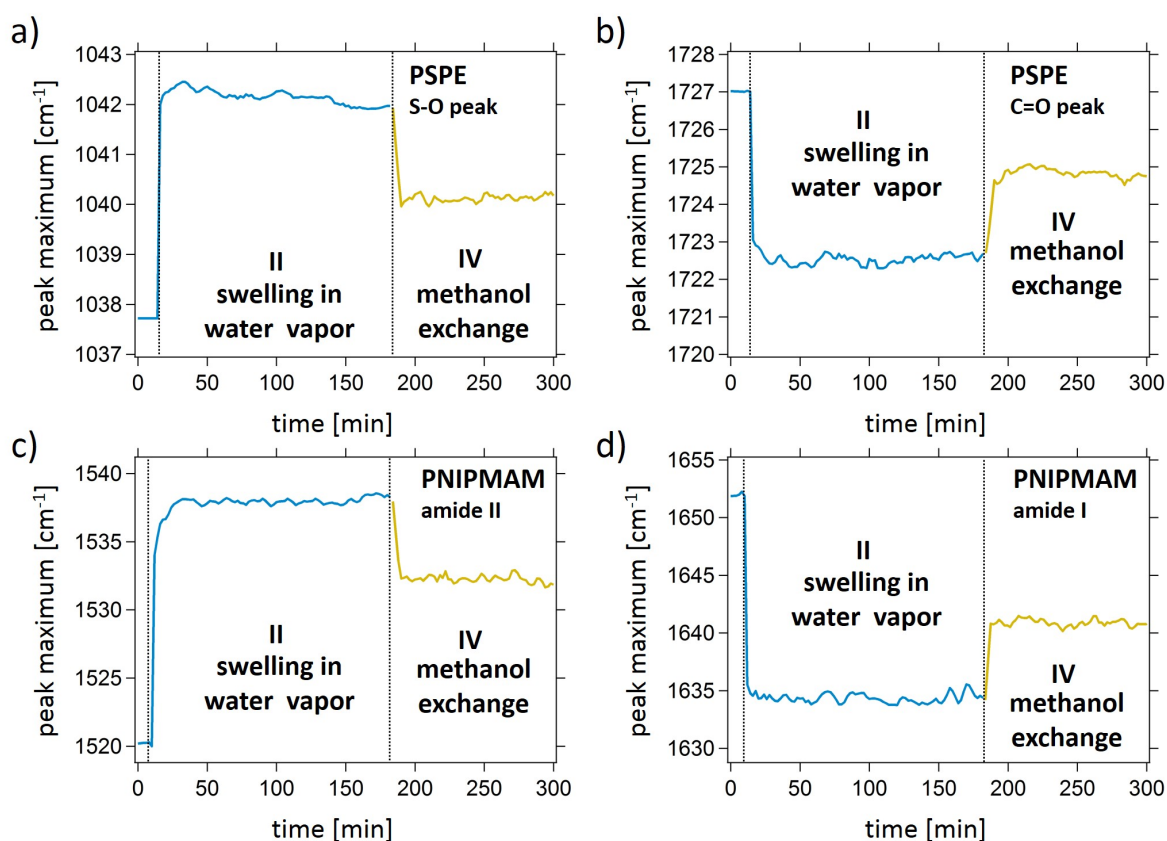


Figure 6.6.: Peak maximum position extracted from FTIR spectra during swelling in water vapor and the subsequent methanol exchange. The peak position of the (a) symmetric S-O and (b) C=O stretching vibration (of PSPE), and the (c) amide II and (d) amide I modes (of PNIPMAM) are extracted by applying a Gaussian fit to the corresponding peaks. Blue curves indicate the peak shift during the swelling in water vapor, while yellow curves represent the peak shift during the methanol exchange, respectively. A close-up of the shifting absorption modes can be found in the Appendix B. Adapted with permission from AMERICAN CHEMICAL SOCIETY, Copyright 2021 [39].

All four analyzed vibrations strongly shift during the swelling in water vapor, which indicates the development of a hydration shell around these polar groups of PSPE and PNIPMAM, as water molecules diffuse into the thin films [37, 268]. Please note, the comparatively low water uptake of the overall relatively hydrophobic PNIPMAM thin film is not contradictory to a strong hydration around the polar and hydrophilic amide groups. Once the methanol exchange starts, and methanol is present in the vapor, all bands undergo an immediate reverse shift, which, however, compensates only partially the initial shift during the swelling in water vapor. This reflects on the one hand a dehydration around those groups, which on the other hand is not a complete dehydration. The functional groups remain at least partially hydrated. All bands, the SO_3^- and ester group of the PSPE as well as the amide I and II groups of the PNIPMAM, show a sharp and defined, one-step reverse peak shift. This parallels the changes in the water and methanol peak intensities observed in the PSPE thin film, as well as the thickness changes detected by SR measurements. However, it opposes the two-step mechanism observed in the overall shrinkage and release of water, which is found for the PNIPMAM thin film. This agrees with and corroborates the scenario stated above: PNIPMAM immediately absorbs methanol, which leads to a rapid change of hydration of the amide groups due to strong methanol binding. Apparently, the replacement of the hydrophobic hydration water around the isopropyl group needs longer times. Furthermore and contrary to expectations from the solution behavior, the PSPE thin film shows a weaker tendency to release water than the PNIPMAM thin film, which is a result from the favorable PSPE-water interactions within the PSPE and favorable PNIPMAM-methanol interactions within the PNIPMAM thin film.

Therefore, the general behavior of polymer thin films cannot be predicted from their behavior in dilute solution, which implies a more hydrophilic behavior of the PNIPMAM instead of the PSPE thin film expected at a measurement time of 22 °C. Also, different driving forces of a co-nonsolvency-type thin film behavior dominate in different thin film systems, regarding the altered polymer-water and polymer-methanol interactions in the PSPE and PNIPMAM thin films. These might explain the varying swelling and contraction mechanisms of the two thin films.

6.2. Conclusion I

The swelling and co-nonsolvency-type behavior of the zwitterionic PSPE and the nonionic PNIPMAM homopolymer thin films in pure water and mixed water/methanol vapor is investigated. In particular, the response of the thin films toward methanol exchange is of interest. A constant measurement temperature of 22 °C is chosen, which is below both,

the CP'_{PSPE} and CP_{PNIPMAM} . SR follows *in-situ* the film thickness, which relates to the polymer conformations: a swollen state indicates elongated and hydrated polymer chains and a contracted state refers to coiled and dehydrated polymer chains. In addition, FTIR is applied *in-situ* to monitor changes in the molecular vibrations of the characteristic modes of PSPE and PNIPMAM and therefore, yields information about the polymer-water and polymer-methanol interactions.

The PSPE thin film is found to absorb greater amount of water than the PNIPMAM thin film during the swelling in pure water vapor. This is not predictable from aqueous solution, as PSPE features a miscibility gap in water at 22 °C. In contrast, PNIPMAM is fully soluble in water at 22 °C, at least in the (semi-)diluted regime. Thus, we mainly address these deviations from the bulk solution behavior to altered polymer-water interactions to an increased polymer concentration in thin film geometry. Upon methanol exchange, both thin films undergo a pronounced contraction, and reach a swelling ratio, that is lower than in pure methanol vapor. Therefore, we attribute a co-nonsolvency-type behavior not only to the PNIPMAM and to the PSPE thin films. While for PNIPMAM, a co-nonsolvency behavior in mixed water/ethanol solutions is known, PSPE is insoluble in methanol, and thus its co-nonsolvency-type behavior in thin film geometry is extremely surprising. In addition, the contraction mechanisms of the PSPE and the PNIPMAM thin films upon methanol exchange strongly deviate from each other. The PSPE thin film features a straight forward one-step contraction, in which the water release and methanol uptake are synchronized. In contrast, the PNIPMAM thin film contracts in two individual steps. A first, rapid contraction is followed by a second, decelerated contraction. While the methanol uptake is already finished during the first contraction step, the water release occurs during both steps. This might be due to different water types, *e.g.*, hydrophobic hydration water around the nonpolar isopropyl groups, and water bound by H-bonds to the amide groups. Observed peak shifts of the amide I and II modes confirm this. Both modes feature a rapid one-step backshift during the methanol exchange, which indicates a fast exchange of water molecules around the amide groups by methanol. Apparently, the strong PNIPMAM-methanol interactions lead to a fast release of the hydration water around the amide groups, which is responsible for the first and very fast contraction process. The replacement of the hydrophobic hydration water needs longer times, which is observed as the second and slowed down contraction.

We assume, that although both polymer thin films show a co-nonsolvency-type behavior, the differences of the contraction mechanisms of PSPE and PNIPMAM thin films are largely based on the deviating nature of PSPE and PNIPMAM, *i.e.*, UCST-type vs. LCST-type polymer, insoluble vs. soluble in methanol, zwitterionic vs. nonionic. As a result different polymer-water and polymer-methanol interactions are present in the respec-

tive thin films. While PSPE-water interactions are more favorable than PSPE-methanol interactions, the opposite case applies for the PNIPMAM thin film, where PNIPMAM-methanol interactions are favored over PNIPMAM-water interactions. Thus, the underlying co-nonsolvency mechanism depends on the specific nature of the polymer thin films, which requires a thin film-specific interpretation of the observed results, rather than a universal co-nonsolvency theory.

This first part reveals the different role of the PSPE and PNIPMAM blocks upon swelling in water vapor and in particular upon methanol exchange. Regarding the deviating contraction mechanisms and the competing interactions of water and methanol with the respective polymer system, a fundamental knowledge about the ongoing processes and a solid basis for further co-nonsolvency studies in thin films is achieved.

6.3. PSPE-*b*-PNIPMAM thin films in mixed water/methanol vapor

This second part investigates the behavior of the PSPE-*b*-PNIPMAM DBC thin films, which consist of PSPE and PNIPMAM blocks featuring the same block lengths, as the homopolymers described above. Since the PSPE and the PNIPMAM thin films showed a co-nonsolvency-type behavior, we now address the question, if the PSPE-*b*-PNIPMAM thin film, in which the PSPE and PNIPMAM blocks are covalently bound to each other, exhibit a co-nonsolvency-type behavior as well. Or if both polymer blocks interfere with each other in such a manner, that steric hindrance or repulsive interactions eventually affect a potential co-nonsolvency-type behavior of the DBC thin film. In addition, we aim to develop a versatile thin film system, that analogously to recently reported PNIPMAM-*b*-PMMA thin films [166], can achieve multiple distinct thin film regimes. In the present chapter, the hydrophobic PMMA block is replaced by the responsive PSPE block and thus multiplex (nano) switches might be enabled.

Analogously to the homopolymer study, PSPE-*b*-PNIPMAM thin films are first swollen in water vapor, before methanol exchanges some of the water molecules (ratio water and methanol is set to 70/30 V%). In order to extend the knowledge about the co-nonsolvency phenomenon in thin films, and to connect it to the previous Chapter 5 about isotope-sensitive swelling and exchange processes, we introduce deuterated water and methanol species into the system. Thus, in two individual experiments, the DBC thin films are first exposed to a saturated water atmosphere of either H₂O or D₂O, and subsequent deuterated CD₃OH exchanges some of the H₂O molecules, or protonated CH₃OH exchanges some of the D₂O molecules. Both kinetic processes, the water swelling and the methanol exchange

are followed with simultaneous time-of-flight neutron reflectometry (ToF-NR) and SR measurements, as well as with FTIR. We choose methanol as co-solvent, as it was also used for the study of the PSPE and PNIPMAM homopolymer thin films. Furthermore, the combination of protonated and deuterated solvents provides excellent contrast in the ToF-NR measurements. Since, poly(sulfobetaines) are known for their isotope sensitivity (cf. Chapter 5), the use of different protonated and deuterated water species might further tune the thin film behavior, regarding different distinct thin film regimes. In order to avoid too many different H-bonds and overly complex data, we chose the partially methanol species CD₃OH over the fully deuterated CD₃OD species. This still provides excellent neutron contrast, while isotope-sensitive results can be explicitly addressed to the different water species. Figure 6.7 illustrates the applied measurement protocol.

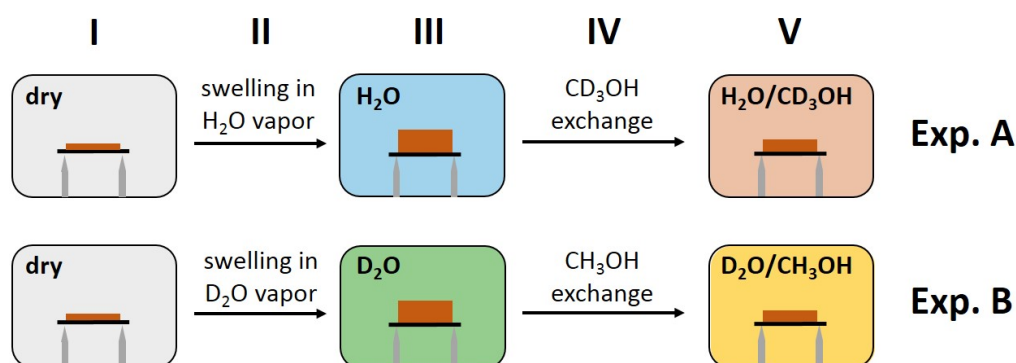


Figure 6.7.: Swelling in water vapor and the subsequent methanol exchange: Schematic representation of the performed experiments. (a) experiment A: The swelling in H₂O vapor is followed by the CD₃OH exchange, while in (b) experiment B the swelling in D₂O vapor is followed by the CH₃OH exchange. The thin film states in equilibrium (stage I, III, and V) are probed with static ToF-NR, while the thin film kinetics of the swelling (stage II) and the methanol exchange (stage IV) are followed with kinetic ToF-NR, SR, and FTIR *in-situ*. The initial dry N₂, the pure water, and the mixed water/methanol vapors are indicated in, gray, blue (H₂O), green (D₂O), red (H₂O/CD₃OH), and yellow (D₂O/CH₃OH), respectively. Adapted with permission from AMERICAN CHEMICAL SOCIETY, Copyright 2021 [250].

The equilibrated thin film stages I, III, and V, according to Figure 6.7, are probed with static ToF-NR measurements and are discussed first, followed by the dynamic swelling in water vapor and the subsequent methanol exchange. Subsequent, polymer-solvent interactions probed by FTIR are described. A final conclusion is given at the end of this chapter.

ToF-NR measurements are performed at the D17 reflectometer at the ILL neutron source in Grenoble, France [221, 222]. Sections 3.2 and 3.3 provide details to ToF-NR, SR, and FTIR spectroscopy. A custom-made sample environment, described in Section 3.4.2

is used, to realize *in-situ* measurements [229, 230]. The thin film samples are prepared according to Section 4.4. A pre-characterization of the thin film samples is done via optical and atomic force microscopy as well as with x-ray reflectivity. All techniques reveal a highly homogeneous and smooth thin film, which is shown in the Appendix B.

6.3.1. Investigation of the equilibrium states

Analogously, to the first part, the DBC thin film behavior is analyzed at a constant temperature of 22 °C. This is below the UCST-type transition ($CP'_{\text{PSPE-}b\text{-PNIPMAM}} = 54\text{ °C}$ in H_2O and $CP'_{\text{PSPE-}b\text{-PNIPMAM}} = 57\text{ °C}$ in D_2O) and also below the LCST-type transition ($CP_{\text{PSPE-}b\text{-PNIPMAM}} = 47\text{ °C}$ in H_2O and $CP_{\text{PSPE-}b\text{-PNIPMAM}} = 46\text{ °C}$ in D_2O) that were found for the DBC PSPE-*b*-PNIPMAM in solution (concentration of 50 g L⁻¹) [129]. Please note that in solution the clearing point of the PSPE homopolymer (CP'_{PSPE}) is at similar temperature than the UCST-type transition of the DBC ($CP'_{\text{PSPE}} = 55\text{ °C}$ in H_2O), while the cloud point of the PNIPMAM homopolymer ($CP_{\text{PNIPMAM}} = 30\text{ °C}$ in H_2O) is located at significant lower temperatures than the LCST-type transition of the DBC. The low CP_{PNIPMAM} value is due to a very hydrophobic end group and the short degree of polymerization ($n = 60$) [26]. This demonstrates the huge impact of the PSPE block on the transition of the PNIPMAM block, while the PSPE transition is barely affected by the PSPE block. At the measurement temperature of 22 °C the PSPE block is insoluble in water, while PNIPMAM is soluble. A similar situation is encountered in methanol, where PSPE is also insoluble but PNIPMAM is soluble. However, in thin film geometry the situation is different, as is revealed by the homopolymer study in the first part of this chapter. The PSPE homopolymer thin film features a higher water uptake than the PNIPMAM homopolymer thin film, while a methanol exchange leads to a co-nonsolvency-type behavior of both, the PSPE and PNIPMAM thin films. In the DBC thin film, we consequently expect a water hydration of both polymer blocks, while the covalent bonds between the blocks might alter a potential co-nonsolvency-type behavior upon methanol exchange.

After an initial drying process in a N_2 flow, swelling in water vapor is induced by generating a saturated H_2O (experiment A) or D_2O vapor (experiment B) via a gas flow system. After the thin films are in equilibrium, CD_3OH replaces some of the H_2O vapor (experiment A), while CH_3OH replaces some of the D_2O vapor (experiment B) with a water/methanol flow ratio of 70/30 vol%. Due to a cross-sensitivity of the humidity sensor to water and methanol, the RH is followed throughout the swelling in H_2O and D_2O vapor only. Since Figure 6.8 demonstrates a good comparability of the RH evolution during the swelling in water vapor in both experiments A and B, and both methanol species feature similar vapor pressures (12.9 and 12.8 kPa at 20 °C for CH_3OH and CD_3OH , respectively)

we also assume comparable environmental conditions during the methanol exchange in both experiments.

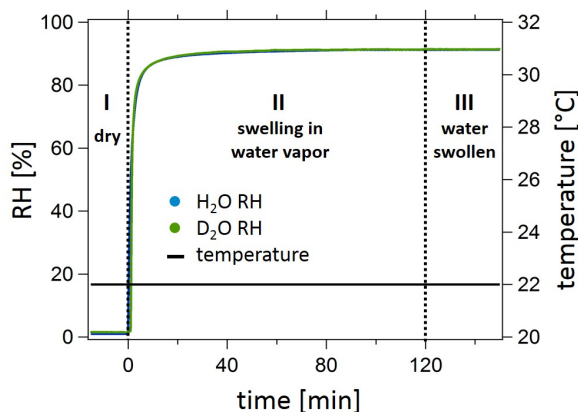


Figure 6.8: RH and temperature during swelling in H₂O and D₂O vapor. The good overlap of the RH for the swelling in H₂O (blue) and D₂O vapor (green) assures a good comparability of the two performed experiments A and B. The RH during the methanol exchange is not followed as explained in the text. The temperature is kept constant at 22 °C (black solid line). The thin film stages are labelled according to Figure 6.1. Adapted with permission from AMERICAN CHEMICAL SOCIETY, Copyright 2021 [250].

The equilibrated thin film states in their dry (stage I), swollen (stage III), and contracted (stage V) states are probed with static ToF-NR measurements. Figure 6.9 displays the obtained NR curves. In both water-swollen states (stage III), the Kiessig fringes are closer together than in the dry states (stage I), thus indicating an increased film thickness of the thin films in water vapor. The spacing becomes larger for the NR curves of both films probed in mixed water/methanol vapors (stage V), which suggests a contraction of the thin films in mixed vapors. In experiment A, the critical edge remains constant during the swelling in H₂O vapor, but moves to higher q_z values in mixed H₂O/CD₃OH vapor, while in experiment B, the critical edge shifts to higher q_z values during the swelling in D₂O vapor, and back to smaller q_z values in mixed D₂O/CH₃OH vapor. This is due to the low and high SLD values of the protonated and deuterated water and methanol species, respectively. Best fits of the static NR curves of the dry thin films are achieved with a two-layer model (SiO₂ and one main polymer layer), while a solvent enrichment layer near the Si substrates necessitates a three-layer model for all other curves. The fit procedure yields information about the film thickness and the average scattering length density $\langle \text{SLD} \rangle$ (in the following simply written as SLD), which in combination of the SLD values of the used water and methanol species (cf. Table 2.2) allows to determine the water content Φ_{water} via Equation 2.13. The neutron SLD of PSPE-*b*-PNIPMAM is calculated using the mass densities based on its composition. We assumed a typical polymer mass density of 1.000 g cm⁻³ for the PSPE block. The mass density of the PNIPMAM block is estimated from the known PNIPAM density of 1.100 g cm⁻³ [269]. Thus, the SLD of the DBC amounts to $0.772 \times 10^{-6} \text{ \AA}^{-2}$ [182].

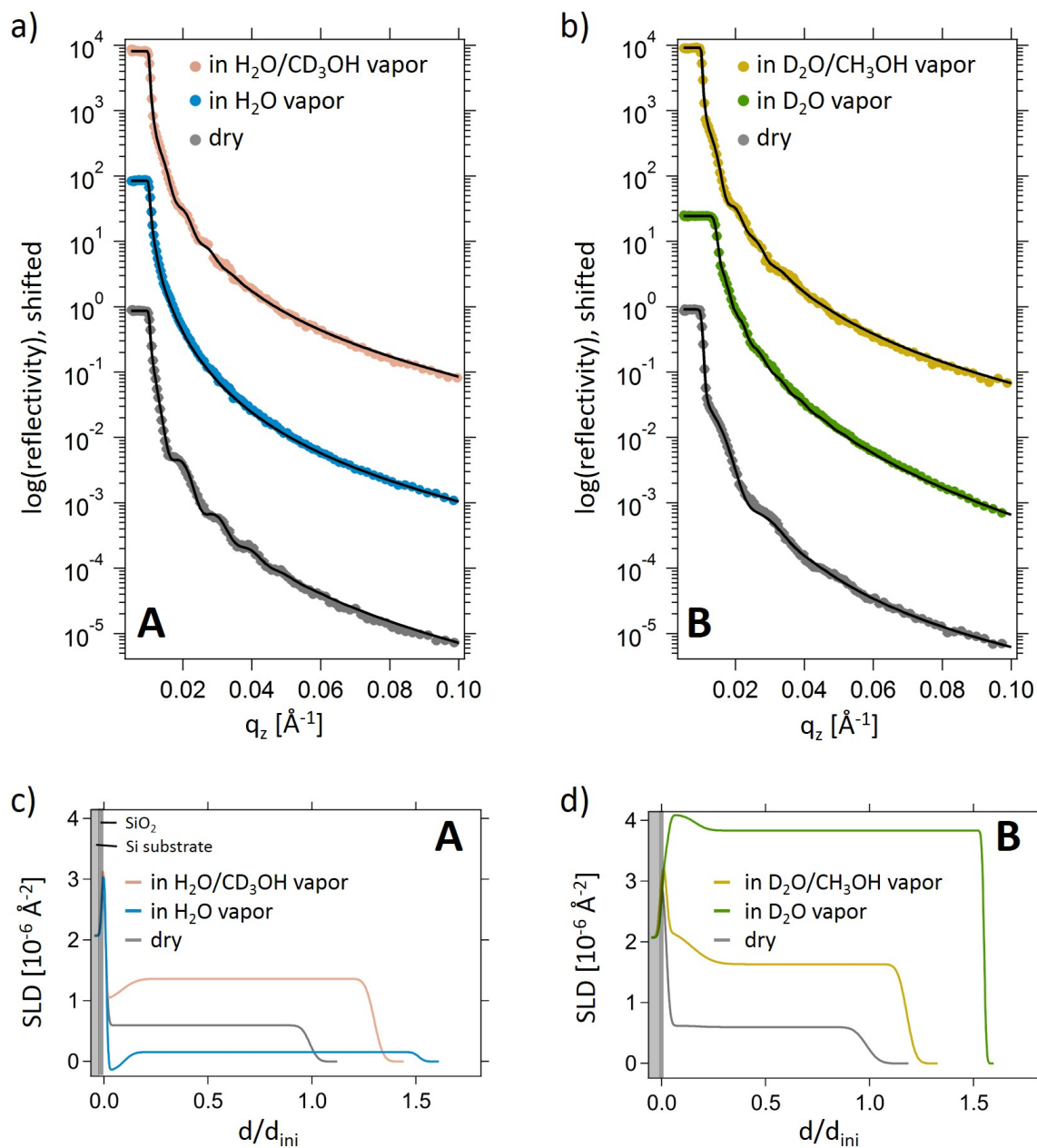


Figure 6.9.: Static ToF-NR measurements. ToF-NR curves of the thin film in their equilibrium states in (a) experiment A and (b) experiment B. The curves of the thin films in the dry (stage I), in pure water (stage III) and in mixed water/methanol vapor (stage V) are indicated in gray, blue (H_2O vapor), green (D_2O vapor), red ($\text{H}_2\text{O}/\text{CD}_3\text{OH}$), and yellow ($\text{D}_2\text{O}/\text{CH}_3\text{OH}$). Best fits are achieved with a two and three-layer model (black lines) as explained in the text. Corresponding SLD profiles of (c) experiment A and (d) experiment B are displayed below the respective NR curves. Adapted with permission from AMERICAN CHEMICAL SOCIETY, Copyright 2021 [250].

6.3. PSPE-*b*-PNIPMAM thin films in mixed water/methanol vapor

The methanol content $\Phi_{methanol}$ is calculated on the basis of this equation with the assumption, that the change in the measured SLD during the swelling in water vapor and the methanol exchange is linked linearly with the changing film thickness d , normalized to the initial film thickness d_{ini} [39, 165].

$$\Phi_{methanol}(t) = \frac{\frac{SLD_{meas}(t) - SLD_{DBC}}{\gamma \left(1 + e^{-\frac{1}{R(t)}}\right)} \left(1 - \frac{d_{ini}}{d(t)}\right) + SLD_{DBC} - SLD_{meas}}{SLD_{methanol} - SLD_{water}} \quad (6.1)$$

The volumetric conversion factor γ is introduced in order to describe the discrepancy in volume, as solvent molecules occupy different volumes in an ordered hydration shell and in solution. The factor γ is calculated according to Equation [6.2] and amounts to 0.90 for experiment A and to 0.85 for experiment B.

$$\gamma = \frac{\frac{SLD_{meas}(t) - SLD_{DBC}}{SLD_{water} - SLD_{DBC}}}{1 - \frac{d_{ini}}{d(t)}} \quad (6.2)$$

The corresponding values are taken from the equilibrium states after the swelling in water vapor (stage III) [39, 165, 166]. Additional to the comparison of the measured $SLD_{meas}(t)$ and the respective SLD values of the DBC, water, and methanol, a time-dependent deuteration rate $R(t)$ is implemented in Equation [6.1]. In the present work, deuteration barely occurs, as is seen with FTIR measurements, which will be explained later in this chapter. Nevertheless, the small effect is taken into account in Equation [6.1]. Characteristic thin film values obtained from the fitting procedure are listed in Table [6.2].

Table 6.2.: Film thickness (sum of all polymer layers), swelling ratio d/d_{ini} , SLD (via integration of the SLD profile), and solvent contents Φ_{water} and $\Phi_{methanol}$ (calculated via Equations [2.13] and [6.1]) extracted from static ToF-NR curves and the corresponding SLD profiles (Figure [6.9]).

experiment A	d [nm]	d/d_{ini}	SLD [10^{-6} \AA^{-2}]	Φ_{water} [V%]	$\Phi_{methanol}$ [V%]
dry (stage I)	52 ± 3	1	0.69 ± 0.02	9 ± 1 (H ₂ O)	—
swollen (stage III)	83 ± 6	1.60 ± 0.05	0.12 ± 0.02	67 ± 6 (H ₂ O)	—
contracted (stave V)	59 ± 5	1.33 ± 0.01	1.35 ± 0.03	24 ± 2 (H ₂ O)	37 ± 2
experiment B					
dry (stage I)	46 ± 2	1	0.70 ± 0.03	8 ± 1 (H ₂ O)	—
swollen (stage III)	69 ± 5	1.51 ± 0.04	3.82 ± 0.08	57 ± 3 (D ₂ O)	—
contracted (stave V)	59 ± 4	1.28 ± 0.03	1.68 ± 0.05	21 ± 3 (D ₂ O)	41 ± 2

The dried thin films are of similar thickness [$d_{ini} = (52 \pm 1)$ nm and (46 ± 2) nm], which is crucial in order to provide a good comparability of the respective dynamic processes [74]. The obtained film thickness is normalized to their initial value d_{ini} , which gives the swelling ratio d/d_{ini} to facilitate the comparison of the kinetic processes. The average SLD values extracted from the fits are converted into the D₂O content according to Equation 2.13. It should be noted that the SLD values of the dry thin films are lower than the theoretically calculated SLD of the pure DBC [182]. This discrepancy can be explained with a minor amount of residual H₂O inside the film. For a more detailed view of the vertical film composition profile, the SLD profiles obtained from fits to the ToF-NR data are shown in Figure 6.9c,d. The DBC is distributed homogeneously within the thin films in the dry states (stage I) of both experiments, A and B (gray line). Once the thin films undergo swelling, the distribution becomes heterogeneous along the surface normal (z -axis), as water enrichment layers are formed near the substrate–polymer interface. These layers remain unchanged in thickness upon the methanol exchange. These layers are formed during thin film swelling due to attractive interactions between the D₂O molecules and the native hydrophilic SiO₂ layer on top of the Si substrate. This is consistent with earlier studies [36, 67, 109].

It is found that during the H₂O swelling, slightly more H₂O molecules are absorbed [$\Phi_{H_2O} = (67 \pm 6)$ V%], as compared to the D₂O swelling [$\Phi_{D_2O} = (57 \pm 3)$ V%]. This is accompanied by a fractional stronger increase in film thickness [$d/d_{ini}(D_2O) = (1.60 \pm 0.05)$ and $d/d_{ini}(D_2O) = (1.51 \pm 0.04)$] of the DBC films. This difference indicates a slightly higher affinity of the DBC to H₂O than D₂O, which we mainly attribute to the isotope sensitivity of the PSPE block. Such effect is also described Chapter 5. In both experiments A and B, the film thickness is lower in mixed water/methanol vapors than in pure water vapors, whereas both thin films reach a similar swelling ratio [$d/d_{ini}(H_2O/CD_3OH) = (1.33 \pm 0.01)$ and $d/d_{ini}(D_2O/CH_3OH) = (1.28 \pm 0.03)$]. Also, the water and methanol contents are relatively similar [experiment A: $\Phi_{H_2O} = (24 \pm 2)$ V% and $\Phi_{CH_3OH} = (37 \pm 2)$ V%, experiment B: $\Phi_{D_2O} = (21 \pm 3)$ V% and $\Phi_{CD_3OH} = (41 \pm 2)$ V%]. The results might indicate a higher affinity of the DBC to H₂O, however, within the uncertainties, the thin films in mixed water/methanol vapor reach similar swelling ratios and absorb similar amounts of water and methanol.

In a reference experiment, the DBC is exposed to pure CH₃OH vapor, which leads to a higher swelling degree [$d/d_{ini}(CH_3OH) = (1.37 \pm 0.02)$] as compared to the mixed H₂O/CD₃OH and D₂O/CH₃OH vapors (cf. Figure 6.10). However, the observed difference is marginally and less pronounced than for the previous study about the PSPE and PNIPMAM homopolymers described in the first part of this chapter. Thus, a clear distinctive co-nonsolvency-type behavior cannot be observed for the PSPE-*b*-PNIPMAM

thin film. This difference to the respective homopolymers might be due to an interfering interaction of both polymer blocks of the DBC, which leads to a steric hindrance. Regarding the strong impact of the PSPE block on the transition temperature of the PNIPMAM block in solution, also cooperative hydration effects upon methanol exchange are possible, which reduce a hypothetical co-nonsolvency effect in the DBC thin film.

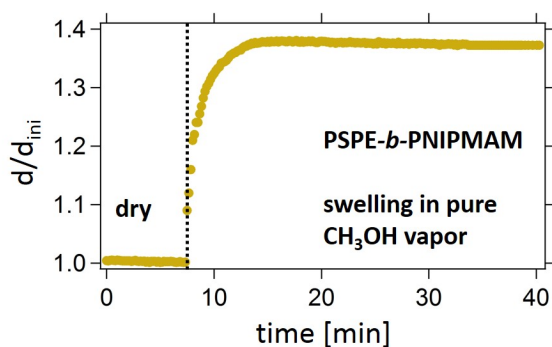


Figure 6.10: Swelling behavior of the PSPE-*b*-PNIPMAM thin film in pure methanol vapor followed with SR *in-situ*. The final swelling ratio is slightly higher than the swelling ratio reached in mixed water/methanol vapors. Adapted with permission from AMERICAN CHEMICAL SOCIETY, Copyright 2021 [250].

6.3.2. Thin film behavior upon water swelling and methanol exchange

The dynamic processes in between the equilibrated states are followed *in-situ* with SR, ToF-NR, and FTIR. First, mesoscopic information regarding the film thickness and solvent content, obtained with SR and ToF-NR are described. Subsequent, molecular information about polymer-solvent interactions are presented.

Film thickness and solvent content

The behavior of the PSPE-*b*-PNIPMAM thin film upon swelling in water vapor and methanol exchange is followed *in-situ* and simultaneously with SR and ToF-NR. Fitting of the kinetic ToF-NR curves yields information about how the film thickness and the water and methanol contents evolve. Figures 6.11 and 6.12 provide a representative selection of ToF-NR curves, together with the best fits (three-layer model). The swelling ratio d/d_{ini} extracted from ToF-NR and from SR data, as a function of measurement time throughout experiment A and B is shown in Figure 6.13. The time window in which no kinetic ToF-NR data points are plotted, correspond to the static ToF-NR measurements, which take 45 min to measure and during which the vapor composition is kept constant.

The swelling ratios, determined with ToF-NR and SR are in good agreement with each other, which hints towards a small uncertainty of these values. The thin films in both experiments undergo a strong increase in film thickness. Upon swelling in H₂O vapor, a higher swelling ratio is reached after longer times (≈ 130 min) as compared to the swelling in D₂O vapor (≈ 100 min). This was already seen in a similar poly(sulfobetaine)-based DBC thin film system, where longer diffusion pathways in thicker films resulted in longer swelling processes [38].

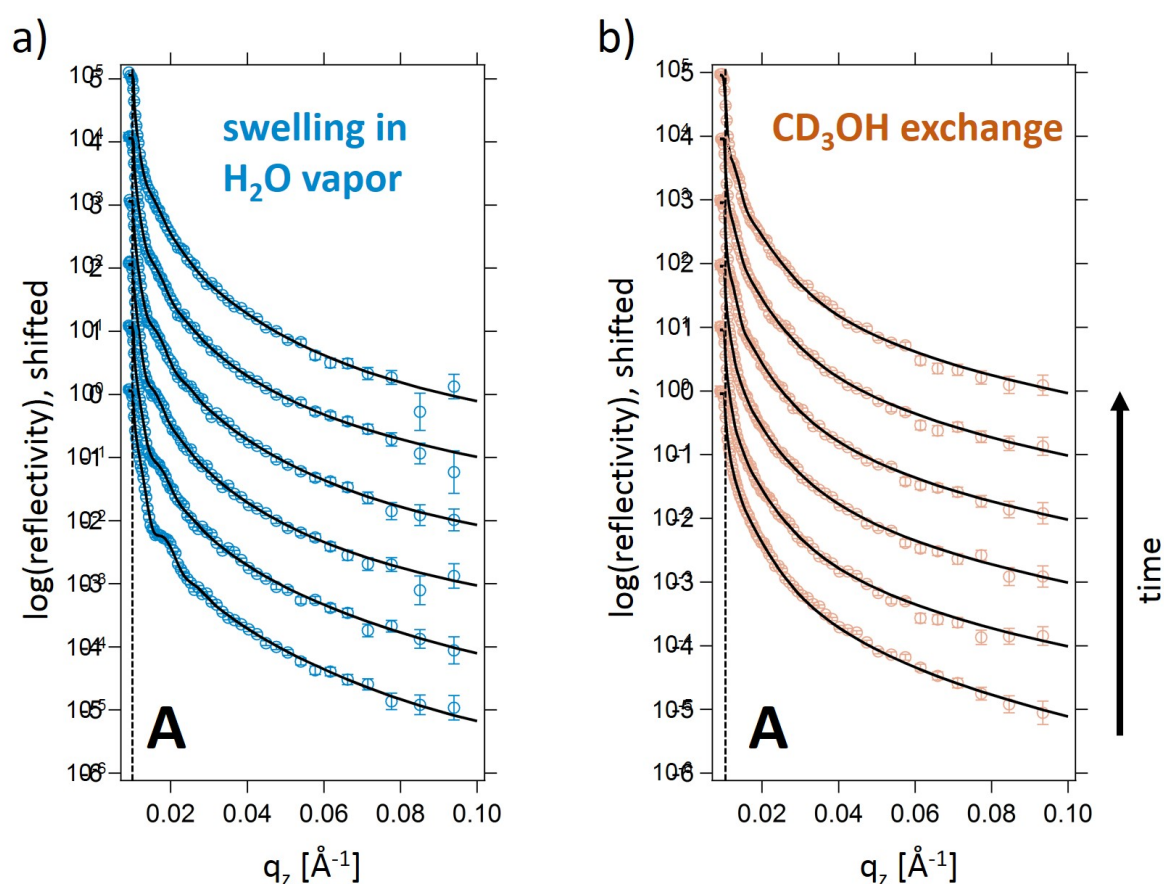


Figure 6.11.: Representative selection of ToF-NR curves for the swelling in H₂O vapor and the subsequent CD₃OH exchange. Representative ToF-NR data (open circles) during the swelling in (a) H₂O vapor and the subsequent (b) CD₃OH exchange are shown with best model fits (black lines), which are achieved with a three-layer model. From bottom to top the measurement time increases. For the swelling in H₂O vapor the curves are taken at $t = 0.5, 2, 5, 8, 10,$ and 60 min, while for the CD₃OH exchange the curves are taken at $t = 0.5, 5, 15, 30, 60,$ and 120 min. The ToF-NR curves are shifted along the y -axis for clarity. The dashed black line marks the critical edge of the as-prepared thin film. Adapted with permission from AMERICAN CHEMICAL SOCIETY, Copyright 2021 [250].

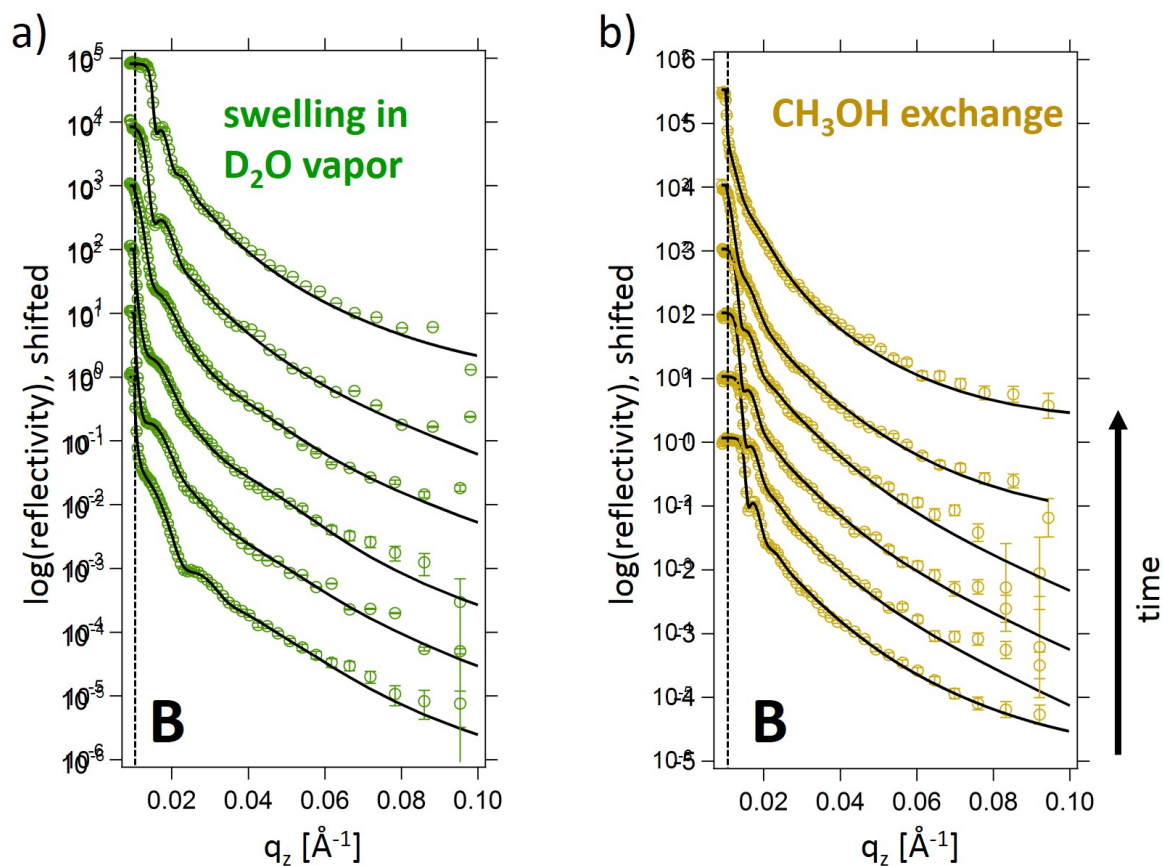


Figure 6.12.: Representative selection of ToF-NR curves for the swelling in D_2O vapor and the subsequent CH_3OH exchange. Representative ToF-NR data (open circles) during the swelling in (a) D_2O vapor and the subsequent (b) CH_3OH exchange are shown with best model fits (black lines), which are achieved with a three-layer model. From bottom to top the measurement time increases. For the swelling in D_2O vapor the curves are taken at $t = 0.5, 2, 5, 8, 10,$ and 60 min, while for the CH_3OH exchange the curves are taken at $t = 0.5, 5, 15, 30, 60,$ and 120 min. The ToF-NR curves are shifted along the y -axis for clarity. The dashed black line marks the critical edge of the as-prepared thin film. Adapted with permission from AMERICAN CHEMICAL SOCIETY, Copyright 2021 [250].

The methanol exchange is induced by changing the gas flow from a 100 vol% water flow to a 70/30 vol% water/methanol flow. In consequence, two individual thin film contractions with a certain time period of constant swelling ratio in-between are observed. The first contraction is more pronounced for the CD_3OH exchange in experiment A [$\Delta d/d_{ini}(CD_3OH) = 0.09$, $\Delta d/d_{ini}(CD_3OH) = 0.02$, where $\Delta d/d_{ini}$ denotes the difference in the swelling degree before and after the first contraction] and the subsequent time of constant swelling ratio is significantly shorter (≈ 12 min), than during the CH_3OH exchange (≈ 28 min). The second thin film contraction is of similar magnitude for both, the

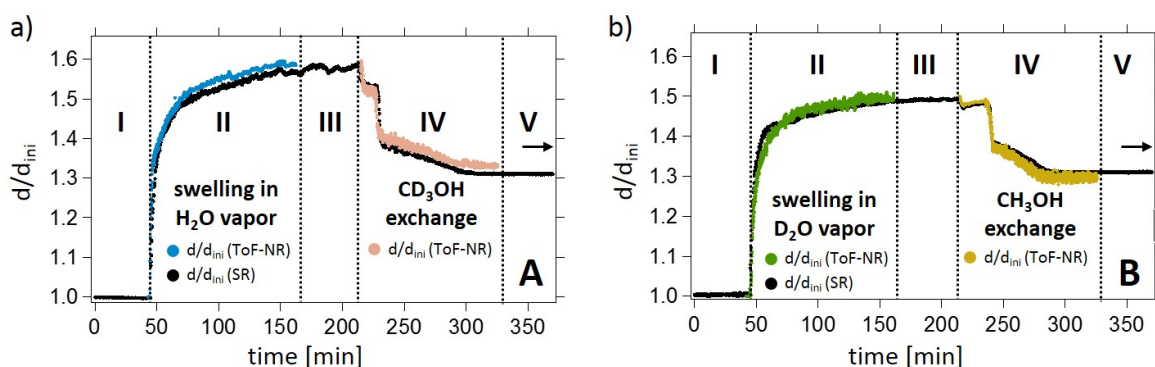


Figure 6.13.: Swelling in water vapor and the subsequent methanol exchange followed with SR and kinetic ToF-NR *in-situ*. The swelling ratio d/d_{ini} as function of measurement time during experiment (a) A and (b) B. The swelling ratio d/d_{ini} (extracted from kinetic ToF-NR) during swelling in water vapor (stage II) is colored in blue (swelling in H_2O vapor) and green (swelling in D_2O vapor), while during the methanol exchange (stage IV) it is colored in red (CH_3OH exchange) and yellow (CD_3OH exchange). The swelling ratio d/d_{ini} extracted from SR is colored black throughout all stages. No kinetic ToF-NR data is obtained at the stages I, III, and V, where the thin film is in equilibrium. The black arrows indicate the degree of swelling of the thin films reached in pure CH_3OH vapor (cf. Figure 6.10). Adapted with permission from AMERICAN CHEMICAL SOCIETY, Copyright 2021 [250].

CD_3OH and the CH_3OH exchange [$\Delta d/d_{ini}(CD_3OH)$ and $\Delta d/d_{ini}(CH_3OH) \approx 0.1$, where $\Delta d/d_{ini}$ denotes the difference in the swelling degree before and after the second contraction]. In both experiments, the second contraction slows down after approximately 5 min (with respect to the start of the second contraction), and the thin films reach equilibrium thickness after 90 min with respect to the start of the methanol exchange. The first, sharp contraction of the thin film resembles the one-step contraction that is observed for the PSPE homopolymer, even though, the contraction of the homopolymer is considerably stronger. The second one is very similar to the contraction, which is seen for the PNIPMAM homopolymer thin film (cf. Section 6.1). Therefore, we address the first contraction to the PSPE block and the second contraction to the PNIPMAM block. The observed difference of the PSPE contraction in experiment A and B, with respect to the $\Delta d/d_{ini}$ values can be explained by the deviating affinity of the PSPE block to H_2O and D_2O , respectively. In contrast, the PNIPMAM contraction is similar in both experiments, which seems logical, as PNIPMAM is relatively insensitive toward H/D isotopes [270]. Due to the individual contraction processes of the PSPE and the PNIPMAM block, four thin film regimes are obtained: initial dry, after the swelling in water vapor, after the PSPE contraction, and after the PNIPMAM contraction. These different film regimes are only triggered by the vapor composition. In addition, they can even be fur-

ther tuned, regarding their magnitude ($\Delta d/d_{ini}$) by using hydrogenated or deuterated water species. For comparison, recently a PMMA-*b*-PNIPMAM DBC film in mixed water/acetone vapors was investigated [166], which featured three distinct film thickness regimes, in dependence on the vapor composition. By replacing the hydrophobic PMMA with the responsive PSPE block, an additional thickness regime is accessible, which is a meta-stable regime. By reducing the methanol content in the vapor composition below 30 V%, the thin film might equilibrate in this distinct thin film regime, where only the PSPE block is in a collapsed state. With respect to potential applications, the here observed four nanoscale thin film regimes would give the possibility to realize quaternary (nano) switches.

In addition to the film thickness, ToF-NR yields information about the average thin film SLD. The contrast variation enables to extract a water and methanol content Φ_{water} and $\Phi_{methanol}$ according to Equations 2.13, 6.1, and 6.2. Figure 6.14 displays both as a function of measurement time.

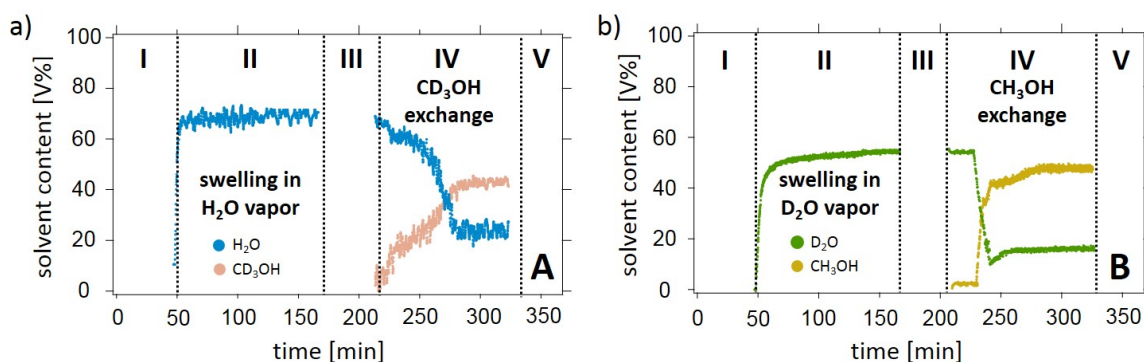


Figure 6.14.: Swelling in water vapor and the subsequent methanol exchange followed with kinetic ToF-NR *in-situ*. The water and methanol content Φ_{water} and $\Phi_{methanol}$, respectively, as function of measurement time during experiment (a) A and (b) B (extracted from kinetic ToF-NR). The H_2O and D_2O contents are colored in blue and green, while the CD_3OH and CH_3OH contents are colored in red and yellow. No kinetic ToF-NR data is obtained at the stages I, III, and V, where the thin film is in equilibrium (cf. Figure 6.13). Adapted with permission from AMERICAN CHEMICAL SOCIETY, Copyright 2021 [250].

During the swelling in water vapor (stage II), the thin films absorb more H_2O than D_2O ($\Phi_{H_2O} = 66 \pm 7$ V% and $\Phi_{D_2O} = 55 \pm 3$ V%), which is in good agreement with the higher swelling ratio and the higher affinity of the PSPE block to H_2O . In contrast, to the evolution of the swelling ration, the water content inside the thin films increase significantly faster and reaches an equilibrium state earlier. This is due to air voids present in the initially dry thin films. These voids are filled up first, before further water uptake leads to an increase in film thickness. Also, the polymer chains undergo re-arrangements

processes, which lead to further swelling, long after the water uptake has equilibrated [37, 38].

Upon the methanol exchange (stage IV), in both experiments A and B, two individual steps, analogously to the evolution in film thickness (cf. Figure 6.13) are observed. During both steps, water is released and methanol is absorbed into the thin film. In experiment A, the first water release and methanol uptake step happens directly after methanol is added to the vapor. The second contraction occurs after ≈ 225 min and follows roughly the evolution of the swelling ratio displayed in Figure 6.13a (stage IV), where the sharp collapse is followed by a long equilibration time. A different mechanism is observed for experiment B. While the first step-wise D_2O release and CH_3OH uptake is very weak, the second one is significantly more pronounced. Even an overshooting is observed during this second step, and a local minimum in D_2O content and a local maximum in CH_3OH content is reached, before the thin film relaxes and equilibrates. These local minima in D_2O and maxima in CH_3OH content are referred to re-arrangement processes of the polymer chains and are also found in the previous Chapter 5 and in the literature [36, 166]. Furthermore, we observe a long meta-stable regime in-between both steps, during which the D_2O and CH_3OH contents are constant. The differences in the water release and the methanol uptake mechanisms in experiment A and B are again attributed to the isotope sensitivity of PSPE and the resulting deviating interactions of, in particular, PSPE and water and methanol, respectively. The higher affinity to H_2O compared to D_2O , eventually leads to a slow H_2O release (experiment A) and a fast D_2O release (experiment B). The corresponding methanol species follow the trend of the water species, *i.e.*, a slow CD_3OH uptake (experiment A) and a fast CH_3OH uptake (experiment B) are observed. Despite the differences in the release/uptake mechanisms the water and methanol contents in the final equilibrium state (stage V) are relatively similar (cf. Table 6.2).

Polymer-solvent interactions

FTIR spectroscopy is applied *in-situ* following the experimental design illustrated in Figure 6.7. Figure 6.15 shows the obtained FTIR spectra. Please note, that the H_2O and D_2O swelling, as well as the CH_3OH exchange was monitored for 70 min, while the CD_3OH exchange was monitored for 240 min.

In addition to the absorption peaks that are already explained in the first part of this chapter, peaks at around 2500 cm^{-1} and 2074 cm^{-1} appear. These are assigned to the O-D and C-D stretching vibration resulting from deuterated D_2O and CD_3OH molecules, respectively. Analogously to the study of the homopolymers, integration of solvent absorption peaks indicate the amount of water and methanol present in the thin films. Figure 6.16 displays the normalized peak areas of the O-H, the O-D, the C-H, and

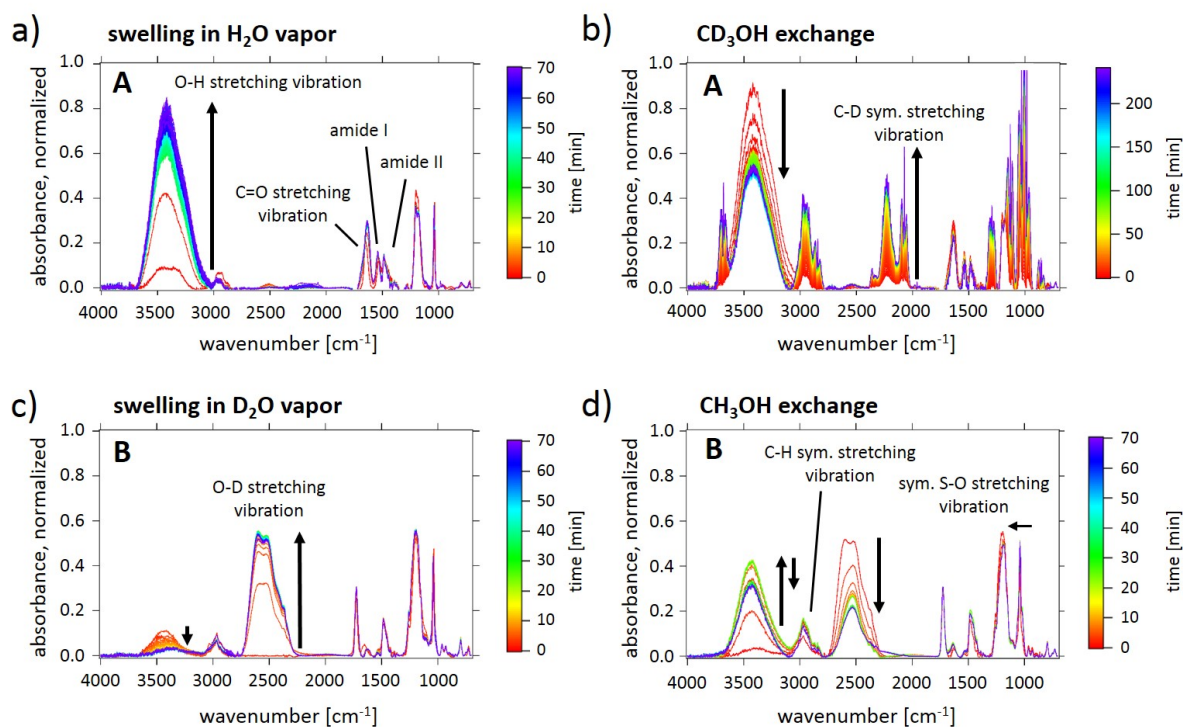


Figure 6.15.: Swelling in water vapor and the subsequent methanol exchange followed with FTIR *in-situ*. FTIR spectra during the swelling in (a) H₂O and (c) D₂O vapor, and during the (b) CD₃OH and (d) CH₃OH exchanges. The red curve marks the initial ($t = 0$ d), the purple marks the final measurement. The measurement time for all dynamic processes is 70 min, except for the CD₃OH exchange, where it is 240 min. Characteristic absorption peaks are labelled accordingly. Black arrows mark the increase and decrease of the water and methanol peaks. Adapted with permission from AMERICAN CHEMICAL SOCIETY, Copyright 2021 [250].

the C-D peaks, which consequently indicate the amount of water (H₂O and D₂O) and methanol (CD₃OH and CH₃OH) inside the thin films.

In experiments A and B, a significant and fast water uptake is observed, while more H₂O than D₂O is absorbed. This is in agreement with the findings from ToF-NR experiments and underlines once again the higher affinity of the DBC to H₂O. The observed O-H peak, upon swelling in D₂O vapor (cf. Figure 6.16b), originates from residual H₂O molecules in the thin film, which are slowly exchanged by D₂O molecules. Nevertheless, a certain amount of H₂O remains in the thin film throughout the D₂O swelling.

During methanol exchange, water is released and methanol is absorbed in a two-step process. This is also consistent with the ToF-NR data and underlines the assumption on a molecular level that both polymer blocks show an individual methanol-induced collapse. The two steps are indicated with black arrows in Figure 6.16a,b. In experiment A, H₂O is released rapidly immediately after the CD₃OH exchange is induced, while simultaneously

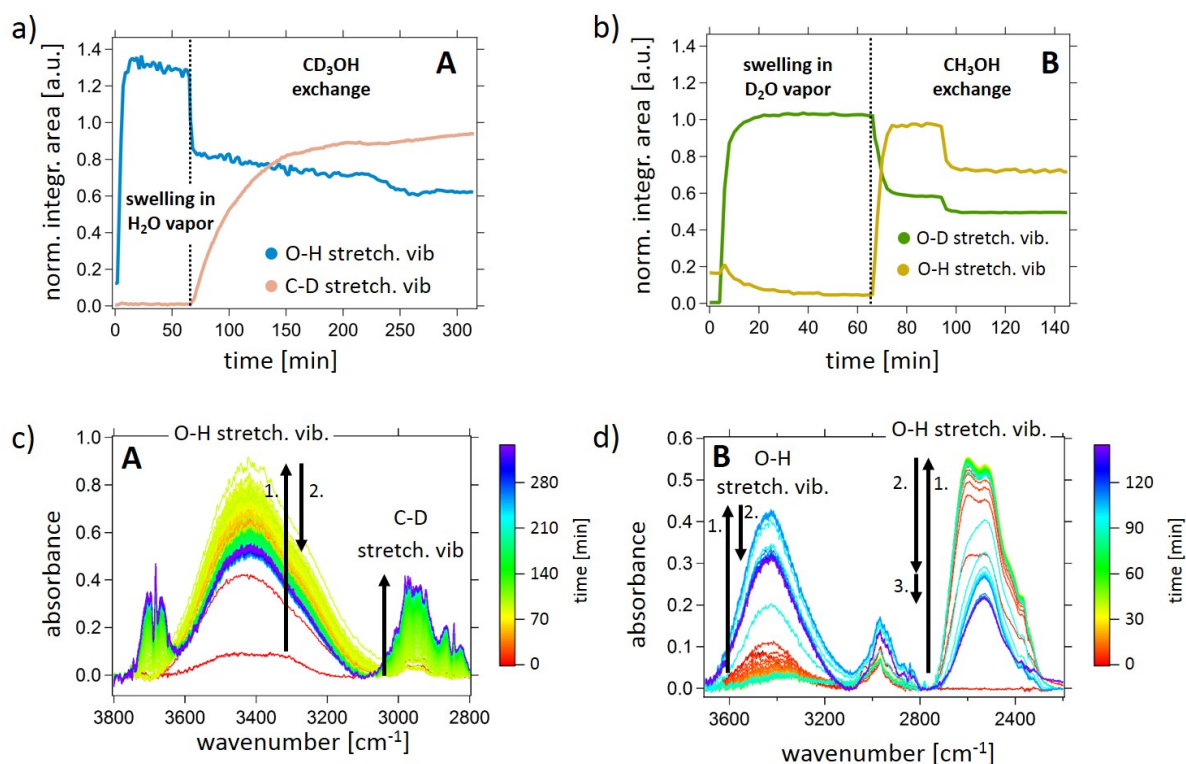


Figure 6.16.: Integration areas extracted from FTIR spectra during swelling in water vapor and the subsequent methanol exchange. The normalized peak areas of the O-H [blue in (a) and yellow in (b)] and O-D peaks (green) and the symmetric C-D (red) stretching vibration are extracted as a function of time for experiment (a) A and (b) B from the corresponding absorption modes shown in (c,d). Please note that in (b) the O-H stretching vibration indicates the H_2O content (from residual H_2O molecules) during the D_2O swelling, and the CH_3OH content during the CH_3OH exchange. The black arrows in (a,b) mark the individual collapse processes. The black arrows in (c,d) mark the increase and decrease of the water and methanol peaks. Numbers next to the arrows indicate the sequence order of increase and decrease steps. Adapted with permission from AMERICAN CHEMICAL SOCIETY, Copyright 2021 [250].

CD_3OH is absorbed but slower than H_2O is released. The release and uptake continue, albeit at a lower rate, without leveling off during the remaining time. At later times ($t \approx 225$ min) a second and weakly pronounced step occurs, where H_2O is released and CD_3OH is absorbed. In experiment B, D_2O is released and CH_3OH is absorbed very rapidly immediately after the CH_3OH exchange is induced, and the thin film levels off quickly. Shortly after this first release and absorption step, a second step occurs ($t \approx 90$ min) at which both, D_2O , and CH_3OH are released from the thin film. The appearance of two individual steps in both experiments, in which H_2O and D_2O are released is surprising and hints toward differently bound water types (via H- or D-bonds and via

hydrophobic hydration), which are replaced by CD₃OH and CH₃OH at different speeds. During the second water release step, CD₃OH is absorbed (experiment A) and CH₃OH is released (experiment B). While the further CD₃OH uptake is very small, it still indicates different interactions of CD₃OH with the H₂O-based hydration shell in experiment A, and of CH₃OH with the D₂O-based hydration shell in experiment B, respectively, during methanol exchange. Furthermore, the time scales at which the corresponding water release and methanol absorption steps occur, deviate in experiment A and B. This can be explained by the different mobility of the two water species within the thin films. The stronger affinity of the DBC to H₂O also leads to a lower mobility as compared to D₂O. Thus, H₂O release in experiment A is hindered and therefore, occurs more slowly than the D₂O release in experiment B. This might also affect the mobility of the polymer chains. Hence, the re-arrangement of the polymer chains in an H₂O/CD₃OH hydration shell takes longer times as compared to a D₂O/CH₃OH hydration shell and can explain the later film contraction upon CD₃OH exchange. One can conclude that the H-bonds of H₂O to the polymer, as compared to the D-bonds of D₂O, not only lead to a delayed, but also to a weaker H₂O release as compared to the D₂O release. In the final equilibrium state in experiment A and B, the respective water and methanol contents are similar. Thus, also on a molecular level, the release and uptake mechanisms differ significantly, while the final equilibration state and solvent contents are relatively similar.

In addition to the water and methanol content, the characteristic functional groups within the PSPE (SO₃⁻ and ester), and the PNIPMAM block (amide I and II) are analyzed. The PSPE specific C=O (of the ester group) and symmetric S-O stretching vibrations appear at 1750 cm⁻¹ and 1038 cm⁻¹. The PNIPMAM specific amide I and II modes appear at 1650 cm⁻¹ and 1540 cm⁻¹. Upon hydration their bonding energies change, which can be seen as a peak shift in the FTIR spectra. Figure 6.17 images the peak shifts of the PSPE and PNIPMAM specific functional groups, which are determined from the FTIR spectra shown in Figure 6.15.

While the symmetric S-O and the amide II peaks shift to higher wavenumbers, the C=O and the amide I peaks shift to lower wavenumbers upon hydration. This is in agreement with the behavior of the functional groups of the corresponding homopolymers as is seen in the first part of this chapter, and with literature [37, 165, 268]. In addition, all four analyzed peaks feature a stronger shift during swelling with H₂O, compared to swelling with D₂O. This is consistent with the higher amount of H₂O molecules within the thin films. During methanol exchange, both PSPE-specific peaks, the symmetric S-O and the C=O stretching vibrations, undergo two individual backshifts of their peak maxima. These backshifts clearly indicate a partial de-hydration or a change in the hydration shell, respectively, and eventually a collapse of the PSPE block. Similar to the change in solvent

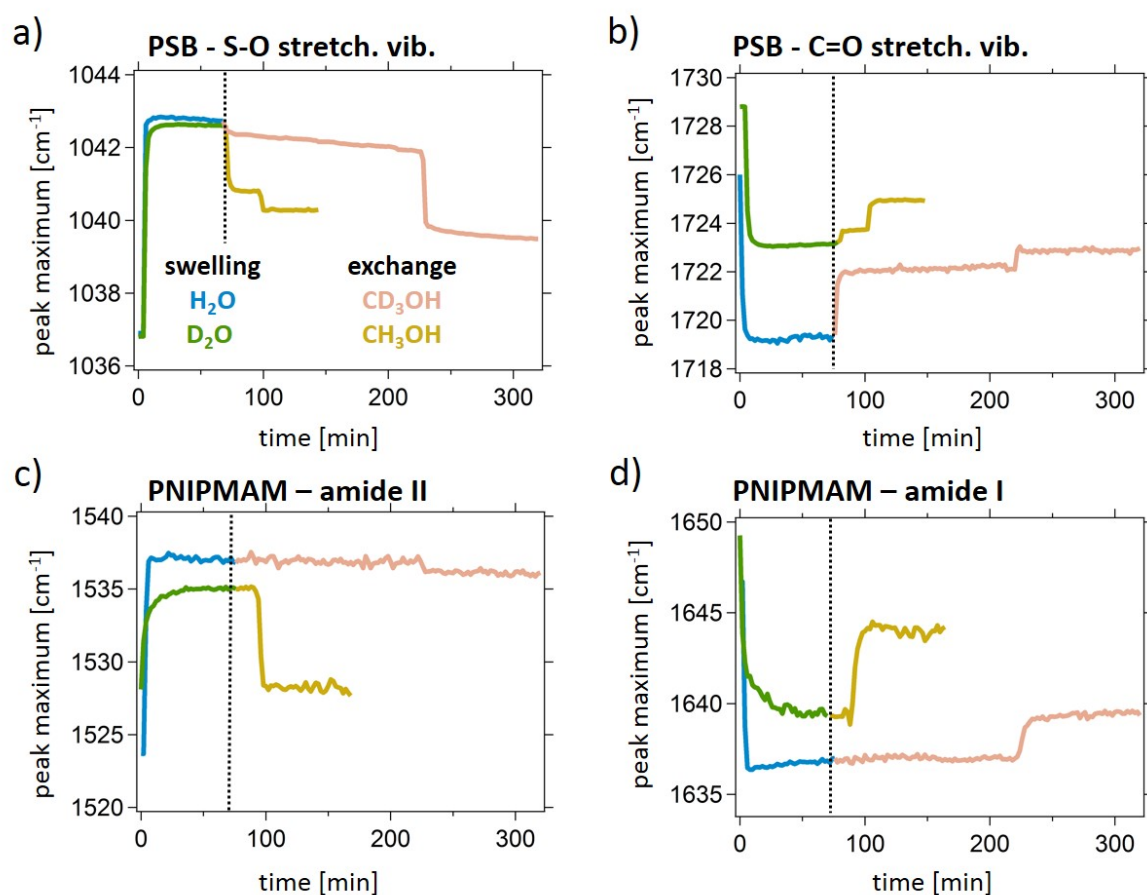


Figure 6.17.: Peak maximum position extracted from FTIR spectra during swelling in water vapor and the subsequent methanol exchange. From the FTIR spectra shown in Figure 6.15, the peak maximum shift of the (a) symmetric S-O stretching vibration, (b) the C=O stretching vibration, (c) the amide I, and (d) amide II modes are extracted by applying a Gaussian fit to the corresponding peaks. Blue and green curves indicate the peak shift during the swelling in H_2O and D_2O vapor, while red and yellow curves represent the peak shift during the CD_3OH and CH_3OH exchanges, respectively. A close-up of the shifting absorption modes can be found in the Appendix B. Adapted with permission from AMERICAN CHEMICAL SOCIETY, Copyright 2021 [250].

content (cf. Figure 6.16), the second backshift appears significantly later during the CD_3OH exchange than during the CH_3OH exchange. In contrast, the PNIPMAM-specific amide I and II modes, only show one backshift as a result of the PNIPMAM collapse. Interestingly, this backshift correlates in time with the second backshift of the PSPE-specific peaks. Thus, the collapse of the PNIPMAM block might affect the hydration behavior of the PSPE block, which results in the second backshift of the PSPE-specific groups. Vice versa this is not the case, as the collapse of the PSPE block (first backshift

immediately after the methanol exchange is induced) does not affect the peak positions of the amide I and II modes. This is interesting, since PNIPMAM is the minority component in the DBC. It might be, that the released water moves from a PNIPMAM nano domain to a PSPE nano domain and changes the environmental conditions there. Furthermore, it should be noted that all backshifts during the CD₃OH exchange are less pronounced than the backshifts upon the CH₃OH exchange. This again highlights the higher affinity of the DBC to H₂O than to D₂O.

6.4. Conclusion II

In this second part, we investigate the swelling behavior in water vapor and the subsequent behavior in mixed water/methanol vapor, of a DBC thin film, that consists of a zwitterionic PSPE block and a nonionic PNIPMAM block. The DBC thin film is able to incorporate more H₂O molecules and reaches a higher swelling ratio during swelling in H₂O vapor as compared to swelling in D₂O vapor. This is due to a higher affinity of the PSPE block to H₂O than to D₂O. Upon methanol exchange, two individual and different types of contractions of the DBC thin films are observed. By comparing both contraction types to the homopolymer study, the first contraction can be assigned to the collapse of the PSPE block, while the second contraction is addressed to the collapse of the PNIPMAM block. Since the thin films feature only a slightly higher swelling degree in pure CH₃OH vapor than in mixed water/methanol vapor, we do not attribute a pronounced co-nonsolvency behavior to the PSPE-*b*-PNIPMAM thin films. This is surprising, since a co-nonsolvency-type behavior is found for the individual PSPE and PNIPMAM homopolymer thin films. It seems that the covalently tied PSPE and PNIPMAM blocks interact with each other in the DBC, which might result in steric hindrance or repulsive interactions between the blocks. Since the collapse of the PNIPMAM block can affect the hydration behavior of the PSPE block, cooperative hydration effects are also possible, which interfere with a co-nonsolvency effect in the DBC thin film.

The fact, that the two contractions occur after one another, enables in total four different thin film regimes (initially dry, water swollen, after the PSPE collapse, and after the PNIPMAM collapse). These regimes are only dependent on the vapor composition and can be further tuned via different deuteration levels of the used solvents. Thus, compared to earlier work, where three different film thickness regimes of a PMMA-*b*-PNIPMAM DBC film were presented [166], an additional regime is provided by the replacement of the PMMA block by PSPE. In terms of possible application, the results offer the basis for a possible nanoscale switch with four states [quarternary (nano)switches]. While the contraction mechanisms differ considerably in both experiments, the water and methanol

contents are similar in the final equilibrated thin film state. FTIR confirms the two individual thin film contractions and the deviating water release and methanol uptake mechanisms on a molecular level. From, the peak shifts of the PSPE and PNIPMAM-specific absorption peaks, we find that the PNIPMAM collapse affects the hydration behavior of the PSPE block, but not vice versa.

7. Phase transition kinetics of orthogonally dual thermo-responsive thin films

The following chapter is based on the publication 'Phase Transition Kinetics of Doubly Thermo-responsive Poly(sulfobetaine)-Based Diblock Copolymer Thin Films' (L. P. Kreuzer et al., *Macromolecules* **2020**, 53, 2841-2855; DOI: 10.1021/acs.macromol.0c00046) [37]. Reprinted with permission from AMERICAN CHEMICAL SOCIETY, Copyright 2020. Experiments were performed in collaboration with bachelor student Johannes Pantle [271].

The previous chapters focus on a fundamental understanding of orthogonally dual thermo-responsive poly(sulfobetaine)-based DBC thin films and their behavior in pure and mixed vapors at constant temperature. In the present and the following chapters, the change in temperature will play a crucial role. In aqueous solution, poly(sulfobetaine)s (PSBs) feature an upper critical solution temperature (UCST), while poly(*N*-isopropyl methacrylamide) (PNIPMAM) exhibits a lower critical solution temperature (LCST). Section 2.2.1 provides a detailed description of the response of both polymer types toward temperature.

Introduction

Thermo-responsive polymers can undergo drastic changes in their chain conformation as a response to temperature variation. By physical or chemical cross-linking of thermo-responsive polymers, thermo-responsive hydrogels are created, that can hold large quantities of water. Upon temperature change, the linked polymer chains either contract or elongate, and therefore, water is either released from or absorbed into the hydrogel (see Section 2.2.1 for further reading) [1, 76, 77].

In former studies, appropriate UCST- and LCST-type homopolymers were combined to orthogonally dual thermo-responsive DBCs, which in aqueous solution self-assembled into micelles with a hydrophobic core and a hydrophilic shell [25, 106, 107, 272]. Due to the

combination of UCST and LCST-based thermo-responsive polymer blocks and their opposing thermal response, micellar inversion was induced by a change in temperature, *i.e.*, the hydrophobic core became the hydrophilic shell and vice versa [109–112]. Dependent on the relative positions of the clearing point (CP'_{UCST}) and the cloud point (CP_{LCST}), this was realized via a fully hydrophilic regime ($CP'_{UCST} < CP_{LCST}$), a fully hydrophobic regime ($CP'_{UCST} > CP_{LCST}$), or directly ($CP'_{UCST} = CP_{LCST}$). However, schizophrenic DBCs were mainly investigated in dilute aqueous solutions, and the extrapolation of the bulk solution behavior to thin film geometry is not very reliable as is described in Section 2.1.2 and in the previous Chapter 6. Thus, the present chapter focuses on the thermal behavior of a schizophrenic DBC in thin film upon two consecutive temperature jumps.

The DBC under investigation consists of a zwitterionic poly(*N,N*-dimethyl-*N*-(3-methacrylamidopropyl)-ammonio-propane sulfonate) (PSPP) block and a nonionic PNIPMAM block (PSPP₅₀₀-*b*-PNIPMAM₁₅₀), and is denoted as PSPP-*b*-PNIPMAM in the following. Its chemical structure can be found in Figure 4.2d in Section 4.2. In solution, the corresponding homopolymers showed an CP'_{PSPP} at 31.5 °C and a $CP_{PNIPMAM}$ at 44 °C in H₂O (polymer concentration of 50 g L⁻¹), respectively [26]. Interestingly, the DBC featured a slightly higher $CP'_{PSPP_{DBC}}$ at 33.5 °C and a markedly higher $CP_{PNIPMAM_{DBC}}$ at 49.5 °C [26]. Thus, the impact of the PNIPMAM block on the $CP'_{PSPP_{DBC}}$ was rather small, while the PSPP block altered the $CP_{PNIPMAM_{DBC}}$ considerably. Since the UCST-type transition of PSPP is at lower temperatures than the LCST-type transition of PNIPMAM the DBC featured a fully hydrophilic regime at intermediate temperatures at the corresponding polymer concentration of 50 g L⁻¹ (cf. Figure 2.6b in Section 2.2.1). The found transition temperatures in solution serve as reference points for the present study.

Figure 7.1 gives a schematic overview of the performed experiment, which is composed of three main parts. First, the swelling of the DBC thin film is induced by exposing it to D₂O vapor at constant temperature of 20 °C (stage II - swelling in D₂O vapor). Regarding the values for the $CP'_{PSPP_{DBC}}$ and the $CP_{PNIPMAM_{DBC}}$ in aqueous solution as reference points, the set temperature of 20 °C should be well below both. Once the swollen thin film is in equilibrium, the temperature is increased jump-wise from 20 °C to 40 °C (stage IV - first temperature jump) and from 40 °C to 60 °C (stage VI - second temperature jump). While 40 °C is in-between the UCST_{PSPP_{DBC}}-type and the LCST_{PNIPMAM_{DBC}}-type transition, 60 °C is above both. Therefore and with respect to the solution phase diagram, the applied measurement protocol covers the relevant phase diagram regimes of the DBC.

The equilibrated thin films in their as-prepared (stage I), and their swollen states at 20 °C (stage III), 40 °C (stage V), and 60 °C (stage VII) are probed with static time-of-flight neutron reflectivity (ToF-NR), in order to obtain mesoscopic information, regarding film thickness and absorbed water content. In addition, ToF grazing-incidence small-angle

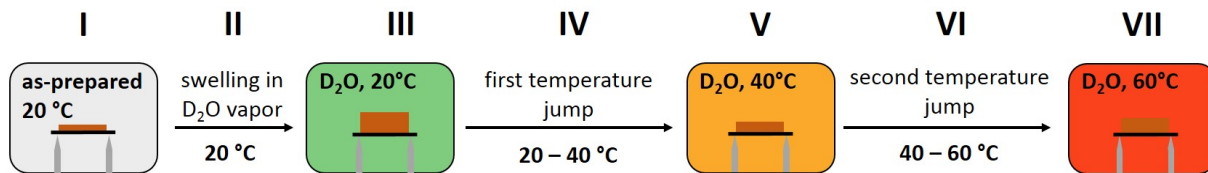


Figure 7.1.: Phase transition kinetics of orthogonally dual thermo-responsive thin films: Schematic representation of the performed experiments. The swelling in D_2O vapor is followed by a first and a second temperature jump. The thin film states in equilibrium (stage I, III, V, and VII) are probed with static ToF-NR, while the thin film kinetics of the swelling (stage II) and the two temperature jumps (stage IV and VI) are followed with kinetic ToF-NR, SR, and FTIR *in-situ*. The initial ambient, and the D_2O vapor at 20 °C, 40 °C, and 60 °C are indicated in gray, green, orange, and red, respectively. Adapted with permission from AMERICAN CHEMICAL SOCIETY, Copyright 2020 [37].

neutron scattering (GISANS) is applied, which probes the lateral thin film nanostructure. This reveals a potential DBC microphase separation that might change upon temperature increase analogously to the 'schizophrenic' micellar inversion in aqueous solution. The thin film kinetics during the swelling in D_2O vapor and the two subsequent temperature jumps are followed with spectral reflectance (SR), kinetic ToF-NR, and Fourier-transform infrared spectroscopy (FTIR) *in-situ*. FTIR measurements have a strongly limited time resolution and to enable the monitoring of the thermal response *in-situ*, a temperature ramp of 0.5 K h^{-1} , instead of fast temperature jumps is applied.

This chapter addresses the scientific questions, how the thin film geometry alters the thermal behavior of PSPP-*b*-PNIPMAM, and how the lateral thin film geometry changes upon temperature increase. For answering these, a combination of neutron scattering techniques and FTIR spectroscopy is highly beneficial as it links molecular information to the overall thin film behavior, regarding its swelling degree, water uptake, and thin film morphology, to molecular information about polymer-water interaction and the local hydration of specific functional groups.

The ToF-NR and ToF-GISANS measurements are performed at the RefSANS instrument at the MLZ neutron source in Garching, Germany [218-220]. Details to ToF-NR, ToF-GISANS, SR, and FTIR can be found in the Sections 3.2 and 3.3. For realizing *in-situ* measurements, corresponding sample environments as described in the subsection 'Pre-existing experimental setup' in Section 3.4 are used. The thin film samples, discussed in the following are prepared and pre-characterized according to Section 4.4. The Appendix C provides details to the pre-characterization of the thin films. Optical and atomic force microscopy, as well as x-ray reflectivity reveal a highly homogeneous and smooth thin film.

7.1. Investigation of the equilibrated thin film states

Throughout the experiment, the ambient conditions, regarding the relative humidity (RH) and temperature, within the SR, the ToF-NR/GISANS, and the FTIR measurement chambers are monitored. Both parameters as a function of time are displayed in Figure 7.2.

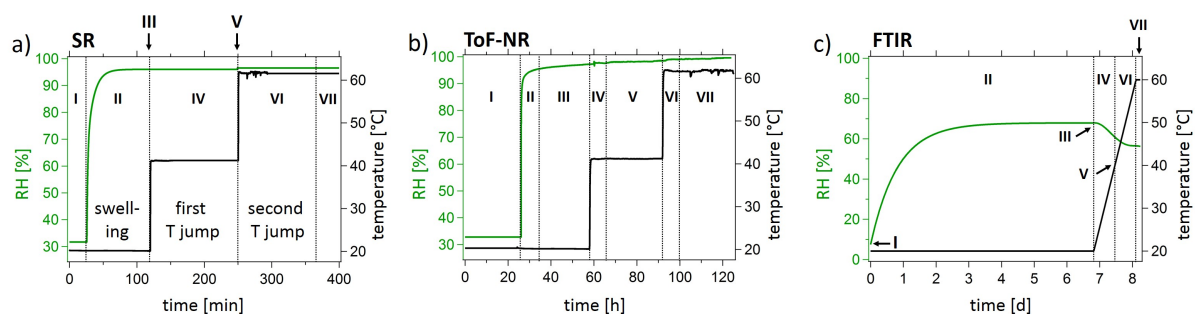
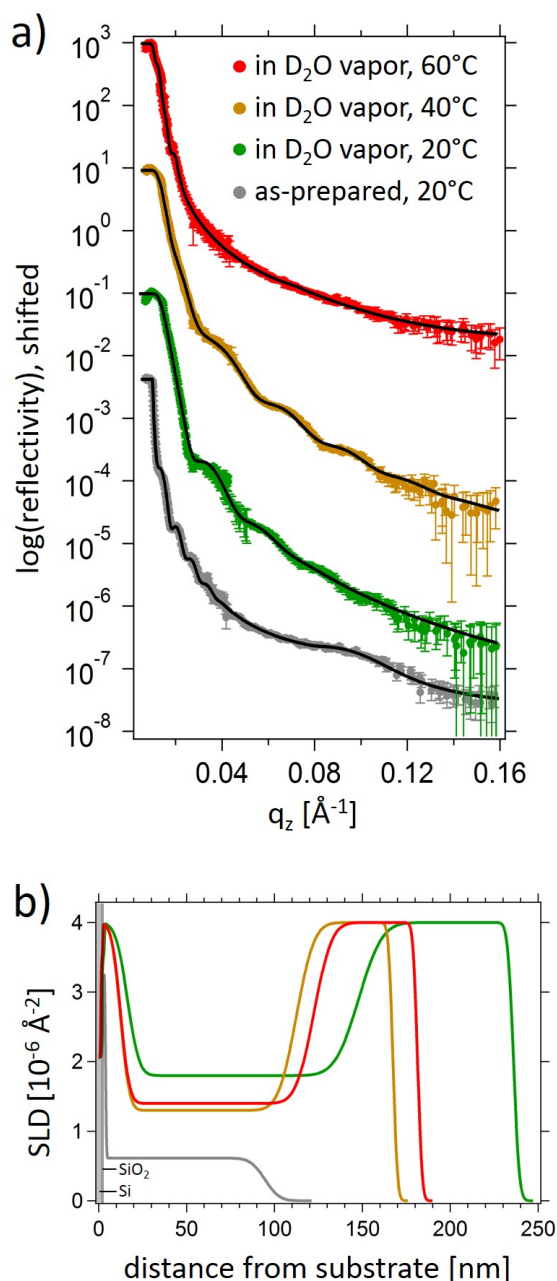


Figure 7.2.: RH and temperature during swelling in water vapor and the two temperature jumps. Both parameter are plotted as a function of time within the respective (a) SR, (b) ToF-NR and ToF-GISANS, and (c) FTIR measurement chambers. The thin film stages are labelled according to Figure 5.1. Adapted with permission from AMERICAN CHEMICAL SOCIETY, Copyright 2020 37.

The general evolution of the RH and temperature during SR and ToF-NR/ToF-GISANS experiments are very similar, except for slight deviations in the beginning of the swelling process. During the FTIR measurements, the temperature ramp results in a slight drop of the RH, which is taken into account for the analysis.

In order to get a first insight in the swelling and thermal behavior of the DBC thin film, static ToF-NR measurements probe the corresponding equilibrated thin film states, in-between the swelling process and the temperature jumps. Figure 7.3 displays the resulting NR curves together with their model fits. While the as-prepared state (stage I) is fitted with a two-layer model (SiO_2 and one polymer layer), the swollen states at 20 °C, 40 °C, and 60 °C (stage III, V, and VII) are fitted with a four layer model, due to appearing D_2O enrichment layers at the substrate-polymer and polymer- D_2O vapor interfaces. The obtained film thickness d is normalized to its initial film thickness d_{ini} , yielding the swelling ratio d/d_{ini} . From average thin film $\langle\text{SLD}\rangle$ (denoted as SLD in the following) the D_2O content Φ can be calculated, according to Equation 2.13. All extracted thin film characteristics are summarized in Table 7.1. Furthermore, the SLD is related to the vertical film composition, and yields information about the vertical water distribution within the thin film. The corresponding SLD profiles are also shown in Figure 7.3.

**Figure 7.3: Static ToF-NR measurements.**

ToF-NR curves of the thin film in its equilibrium states. The curves of the as-prepared (stage I), and the swollen states at 20 °C (stage III), at 40 °C (stage V), and at 60 °C (stage VII) are indicated in gray, green, orange, and red. Best fits are achieved with a two-layer model for the as-prepared state, and with a four-layer model for the swollen states (black lines). (b) Corresponding SLD profiles. Adapted with permission from AMERICAN CHEMICAL SOCIETY, Copyright 2020 [37].

The obtained SLD for the as-prepared thin film state is lower [$(0.53 \pm 0.03) \times 10^{-6} \text{\AA}^{-2}$] than the SLD determined theoretically, using the NIST SLD calculator [182]. This theoretical SLD determination is based on the basis of the mass density composition of the DBC and yields a SLD of $0.60 \times 10^{-6} \text{\AA}^{-2}$. For PSPP, a typical organic polymer density of 1.00 g cm^{-3} is assumed, whereas for PNIPAM, a mass density of 1.10 g cm^{-3} is estimated from the known density of PNIPAM. The small difference in measured and theoretically determined SLD is due to residual H₂O molecules in the thin film, as is also found in the previous Chapters [5] and [6]. To assure a correctly calculated water content

Table 7.1.: Film thickness (sum of all polymer layers), swelling ratio d/d_{ini} , SLD (via integration of the SLD profiles), and D₂O content Φ (via Equation 2.13) extracted from the fits of the static ToF-NR measurements, shown in Figure 7.3.

thin film state	film thickness d [nm]	swelling ratio d/d_{ini}	SLD [10^{-6} \AA^{-2}]	D ₂ O content Φ [V%]
as-prepared	91 ± 1	0.60 ± 0.03	0.53 ± 0.02	–
D ₂ O swollen at 20 °C	236 ± 4	2.59 ± 0.06	3.60 ± 0.01	52 ± 2
D ₂ O swollen at 40 °C	160 ± 3	1.76 ± 0.04	2.51 ± 0.01	33 ± 2
D ₂ O swollen at 60 °C	174 ± 2	1.91 ± 0.04	2.69 ± 0.01	36 ± 2

for the swollen thin film states (cf. Equation 2.13), the theoretical SLD value is used for the water content analysis.

From the results an already quite detailed picture can be drawn. After the swelling in D₂O at 20 °C, the thin film features an considerably increased film thickness and water content. Compared to the swollen state at 20 °C, the thickness and water content are decreased at 40 °C, while at 60 °C the thickness and water content are slightly increased, with respect to the state at 40 °C. All values are listed in Table 7.1. These results reveal some unexpected details, in particular about the trend of the film thickness and water content upon increasing temperature. From bulk solution, the opposite behavior is expected, since 20 °C is below the clearing point of the PSPP block (CP'_{PSPP}) and the cloud point of PNIPMAM ($CP_{PNIPMAM}$), while 40 °C is in-between both, and 60 °C is above both. The results oppose our expectations and indicate a considerable shift of the CP'_{PSPP} and $CP_{PNIPMAM}$ in thin film geometry. Since the terminology of clearing and cloud point rather refers to solutions than to thin films, the terms 'swelling temperature' for CP'_{PSPP} and 'collapse temperature' for $CP_{PNIPMAM}$ are used in the following. The shift of the swelling and collapse temperatures is mainly addressed to altered polymer-polymer and polymer-water interactions due to the increased polymer concentration.

In addition, the SLD profile (cf. Figure 7.3b) features a homogeneously distributed as-prepared thin film state. In the swollen states at 20 °C, 40 °C, and 60 °C, D₂O enrichment layers appear, near both interfaces, the substrate-polymer and the polymer-D₂O vapor interface. The enrichment layer near the substrate can be explained by the high hydrophilicity of the SiO₂ layer on top of the Si substrate, which results in attractive interactions to D₂O [36, 67, 109]. The second enrichment layer near the D₂O vapor interface is an accumulation layer on an already fully D₂O-saturated thin film due to the high ambient RH. While the thickness of the enrichment layer near the substrate remains relatively stable upon temperature increase, the second enrichment layer on top of the

thin film is synchronized with the evolution of the overall thickness, *i.e.*, the swollen state at 20 °C features the largest D₂O enrichment layer, while at 40 °C the D₂O enrichment layer is the thinnest.

In order to further investigate, in particular the unexpected evolution of the thin film thickness and water content upon temperature increase, SR, kinetic ToF-NR, and FTIR measurements follow the dynamic swelling and temperature jumps in-between the above described equilibrium states.

7.2. Swelling behavior

The first part of the following section, describes the swelling in D₂O vapor followed with SR and ToF-NR. Complementary, FTIR measurements are discussed in the second part. Furthermore, a swelling model is applied to the data.

Film thickness and water content

Figure 7.4 gives the evolution of the swelling ratio and the D₂O content, upon swelling in D₂O vapor, obtained from SR and ToF-NR measurements. A single SR spectrum is measured every 10 seconds, while every 30 seconds a single ToF-NR curve is recorded. Analogously to the static ToF-NR curves, the kinetic curves are fitted with a four-layer model (SiO₂, two D₂O enrichment layers, and one main polymer layer). Selected NR curves with the corresponding fits are shown in Figure 7.5.

χ_{eff}	τ [min]	extracted from
0.71 ± 0.05	31 ± 1	SR $(d/d_{ini})^a$
0.36 ± 0.02	7.5 ± 0.2	ToF-NR $(d/d_{ini})^b$
0.22 ± 0.01	2.3 ± 0.1	ToF-NR $(\Phi)^b$

Table 7.2: Swelling model applied to the SR and ToF-NR data shown in Figure 7.4a,b.

During swelling in D₂O vapor, the DBC thin film reaches a swelling ratio of ≈ 2.6 , which is accompanied with a considerable D₂O uptake of ≈ 50 V%. Both values are in good agreement with the results from static ToF-NR. Notably, the swelling process followed with SR exhibits a long dynamic regime. Even after 120 min, the film thickness still marginally increases. In contrast, ToF-NR monitors a shorter swelling process, which is already equilibrated after roughly 8 minutes. This is due to the different used measurement chambers for SR and ToF-NR measurements (cf. Section 3.4), which vary in dimensions. Thus, the RH increases on different time scales in these chambers. In order to compensate for this effect, the data is analyzed with a swelling model, that takes the

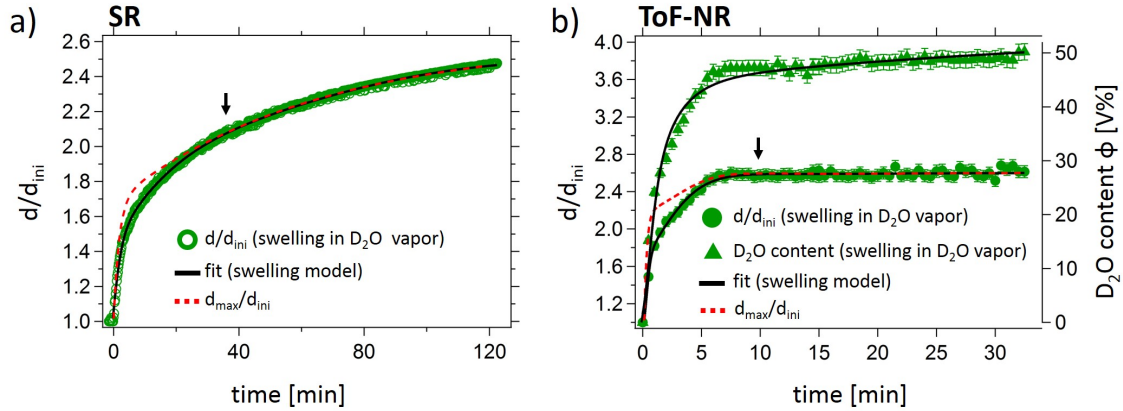


Figure 7.4.: Swelling in D₂O vapor followed with SR and ToF-NR *in-situ*. The swelling ratio d/d_{ini} as a function of time during the swelling in D₂O vapor is obtained with (a) SR (open circles) and (b) kinetic ToF-NR measurements (full circles). The maximum swelling ratio d_{max}/d_{ini} is plotted as dotted red line. Black arrows mark the time, at which the swelling process is no longer diffusion-limited, but limited by the RH. (b) D₂O content Φ (full triangles) as a function of time obtained with kinetic ToF-NR measurements. A swelling model is applied to the data as explained in the main text (solid black line). Adapted with permission from AMERICAN CHEMICAL SOCIETY, Copyright 2020 [37].

intrinsic swelling kinetics into account, *i.e.*, the diffusion of D₂O into the thin film. In addition, the model respects the non-constant RH and considers the varying evolution of the RH within the SR and ToF-NR measurement chambers. From the swelling model the effective Flory-Huggins interaction parameter χ_{eff} and a time τ are extracted. Section 2.1.2 provides a detailed description of the swelling model. Table 7.2 lists all χ_{eff} and τ values, extracted by applying the model to the SR and ToF-NR swelling data.

Even though, the swelling model takes into account the different evolution of the RH within the different measurement chambers used for SR and ToF-NR measurements, the extracted χ_{eff} and τ values still differ considerably. This might be due to different sample sizes in SR ($2 \times 2 \text{ cm}^2$) and ToF-NR measurements ($7 \times 7 \text{ cm}^2$) and the exclusion of substrate-polymer interactions in the applied swelling model. It seems, the influence of the substrate on the thin film swelling behavior is significant. Furthermore, the probed thin film area is much smaller during SR measurements as compared to ToF-NR measurement. Due to the very small incident angle of the incoming neutron beam ($\alpha_i = 0.76^\circ$), the footprint is large and therefore, the results feature a higher statistical relevance. Hence, the ToF-NR displays the general thin film behavior, while SR rather indicates a local thin film behavior. In order to interpret the results according to the guidelines of good scientific practice, the extracted χ_{eff} and τ values are only compared within the individual measurement techniques, or measurement chambers, respectively.

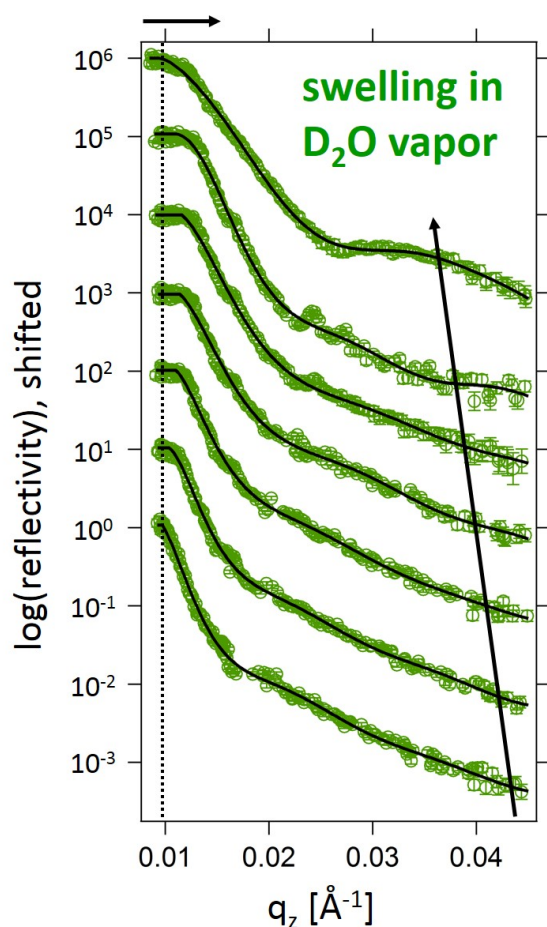


Figure 7.5: Representative selection of ToF-NR curves for the swelling in D_2O vapor. Representative ToF-NR data during the swelling in D_2O vapor are shown with best model fits (black lines). From bottom to top the time increases: $t = 0.5, 1, 2, 5, 10, 15,$ and 30 min. The ToF-NR curves are shifted along the y -axis for clarity. The dashed black line marks the critical edge of the as-prepared thin film. The black arrow on top of the graph marks the shift of the critical edge, while the black arrow inside the graph indicates the shift of the Kiessig fringes. Adapted with permission from AMERICAN CHEMICAL SOCIETY, Copyright 2020 [37].

The swelling model applied to the SR data, yields a χ_{eff} and τ value that are slightly lower as compared to observations of a similar DBC thin film (PSPP-*b*-PNIPAM), whose swelling and exchange behavior is discussed earlier in Chapter 5. These lower χ_{eff} and τ values indicate a higher water compatibility as well as a faster swelling process of the here discussed PSPP-*b*-PNIPAM thin films, than for the PSPP-*b*-PNIPAM thin films investigated in Chapter 5. One has to mention, the swelling in D_2O vapor in Chapter 5 is performed at a higher temperature of 26.5°C . Still, the comparison reveals interesting results. On the one hand, we assume a hydrophobic PSPP block at 20°C , based on its CP'_{PSPP} of 33.5°C in aqueous solution [27], while in former work it was also seen, an increased polymer concentration leads to an increased CP'_{PSPP} [127, 273]. On the other hand, in Chapter 6 we see a very strong water uptake of a similar poly(sulfobetaine) at a temperature of 22°C , which is below its CP'_{PSPE} in solution. Therefore, we attribute a strong water uptake to the here investigated PSPP block, and since the molar fraction of the PSPP block is higher than of the PSPP block in Chapter 5, we identify the PSPP block to be responsible for the better compatibility with water and the faster swelling process.

The situation is more complex for the ToF-NR data, since here the swelling model can be applied to two curves, the curve of the swelling ratio d/d_{ini} and of the water content Φ . The obtained $\chi_{eff}(d/d_{ini})$ and $\tau(d/d_{ini})$ values are smaller than the $\chi_{eff}(\Phi)$ and $\tau(\Phi)$ values. This suggests that D₂O is incorporated into the thin film on a faster time scale than the thin film increases in thickness. This is in good agreement with the previous two Chapters 5 and 6, and can be explained by air voids, present in the as-prepared state, which are filled with D₂O first, before a swelling process takes place. Furthermore, the extracted χ_{eff} and τ values are lower as compared to the values obtained in Chapter 5, thereby confirming the findings from SR measurements. Apparently, the PSPP block is mainly responsible for the strong and fast water uptake.

In addition, Figure 7.4a,b displays the maximum swelling ratio d_{max}/d_{ini} (dotted red line), which is dependent on the non-constant RH and on χ_{eff} . Hence, it expresses the theoretical limit of the swelling ratio the DBC thin film is able to reach at a given ambient RH and at a given temperature. At early stages, the maximum swelling ratio differs strongly from the actual swelling ratio, before at later stages they eventually merge (point of merging is indicated with a black arrow). Thus, the diffusion of the D₂O molecules is the limiting factor at the early stages of the swelling process, while the swelling is limited by the RH at the later stages. This is also described in Chapter 5, where the diffusion-limited regime during the swelling in D₂O vapor of the PSPP-*b*-PNIPAM thin film is clearly longer as for the PSPP-*b*-PNIPMAM thin film in the present chapter. This fits perfectly to the seemingly higher water compatibility of the PSPP-*b*-PNIPMAM thin film as is described above. As a general statement, one could conclude that a higher water compatibility of the thin film promotes diffusion processes and shortens the diffusion-limited regime. As a consequence the swelling process is limited earlier by the RH.

Polymer-water interactions

In order to analyze the thin film behavior also on a molecular level, FTIR measurements are applied *in-situ*. Please note, in order to enable *in-situ* measurements despite a long FTIR measurement time of 7 minutes, the RH increase within the FTIR measurement chamber is artificially decelerated. As a consequence, the overall D₂O swelling took 6 days to be finished. The obtained FTIR spectra are shown in Figure 7.6.

The two very prominent absorption peaks located at around 3400 cm⁻¹ and 2500 cm⁻¹ can be assigned to several sub-bands of free and bound (via hydrogen or deuterium bonds) O-H and O-D stretching vibrations, respectively. The intensity of the two peaks relates to the amount of water (H₂O and D₂O) inside the thin film at a given time. The nonzero intensity of the O-H peak indicates that prior to the swelling in D₂O vapor, H₂O molecules are already present in the as-prepared thin film. In-between these two absorption peaks, a

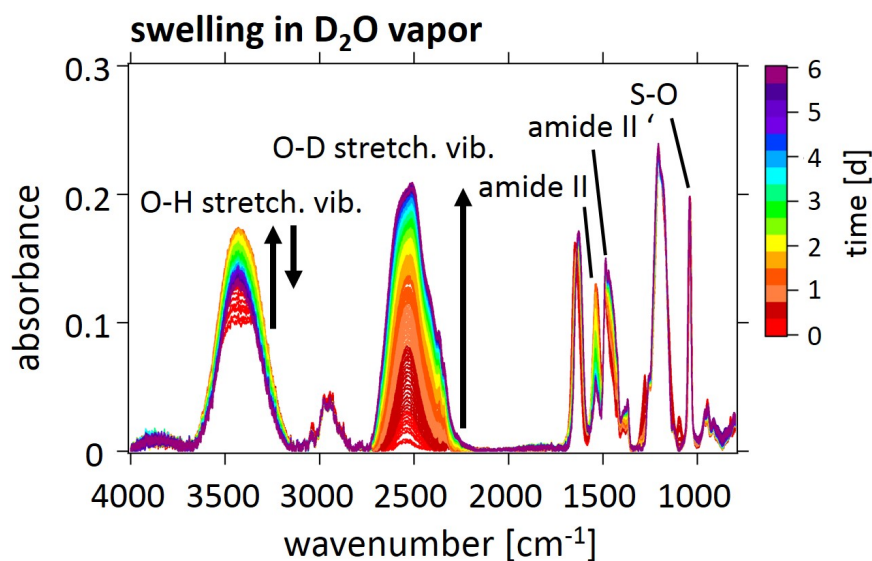


Figure 7.6.: Swelling in D_2O vapor followed with FTIR *in-situ*. The red curve marks the initial ($t = 0$ d), while the purple curve marks the final measurement ($t = 6$ d). Characteristic absorption peaks are labelled accordingly. Black arrows mark the increase and decrease of the O-H and the O-D stretching vibration. Adapted with permission from AMERICAN CHEMICAL SOCIETY, Copyright 2020 [37].

three-fold peak appears, which is addressed to the asymmetric (2974 cm^{-1}) and symmetric C-H stretching vibrations (2886 cm^{-1}) of the CH_3 groups (present at the quaternary amine of the PSPP chain and in the isopropyl group of the PNIPMAM chain). The peak at 2938 cm^{-1} refers to the asymmetric C-H stretching vibration of the CH_2 groups located in the backbones and sidechains of both polymer blocks. Since their vibrational signal remains mostly unaffected from the increasing RH during the swelling in D_2O vapor, as well as from the increasing temperature during the two temperature jumps, the integration area of these peaks of the first FTIR spectrum of the as-prepared thin film ($t = 0$), is used for normalization. At 1645 cm^{-1} and 1537 cm^{-1} , two peaks, assigned to the amide group, present in both, the PSPP and PNIPMAM block, appear. They are denoted with amide I and II band. While the amide I band is a combination of the C=O and the N-C stretching vibration, the amide II band appears due to C-H stretching vibrations and N-H in-plane bending [227, 247, 248, 274]. Both bands are highly sensitive towards hydrogen (or deuterium) bonds as they relate to the vibration and bending energy of an hydrogen bond donor (amide I) and an hydrogen acceptor (amide II). Furthermore, the amide II band allows to detect occurring deuteration of the amide group as the bending energies of N-H and N-D bonds differ. The N-D in plane bending appears at around 1550 cm^{-1} and is denoted with amide II'.

The integration of the O-D and O-H peaks yields information about the amount of D_2O and H_2O within the thin film. Since the swelling is performed in D_2O vapor, deuteration of the polymer chain, foremost at the amide group, occurs. As a consequence, a third water species, namely HDO, is present, which contributes to both, the O-D and O-H peak. Figure 7.7 gives the normalized integration areas of the O-D and O-H stretching vibrations as a function of time during the swelling in D_2O vapor. One has to note, that both peaks feature a different molar extinction coefficient ϵ_λ which is already taken into account.

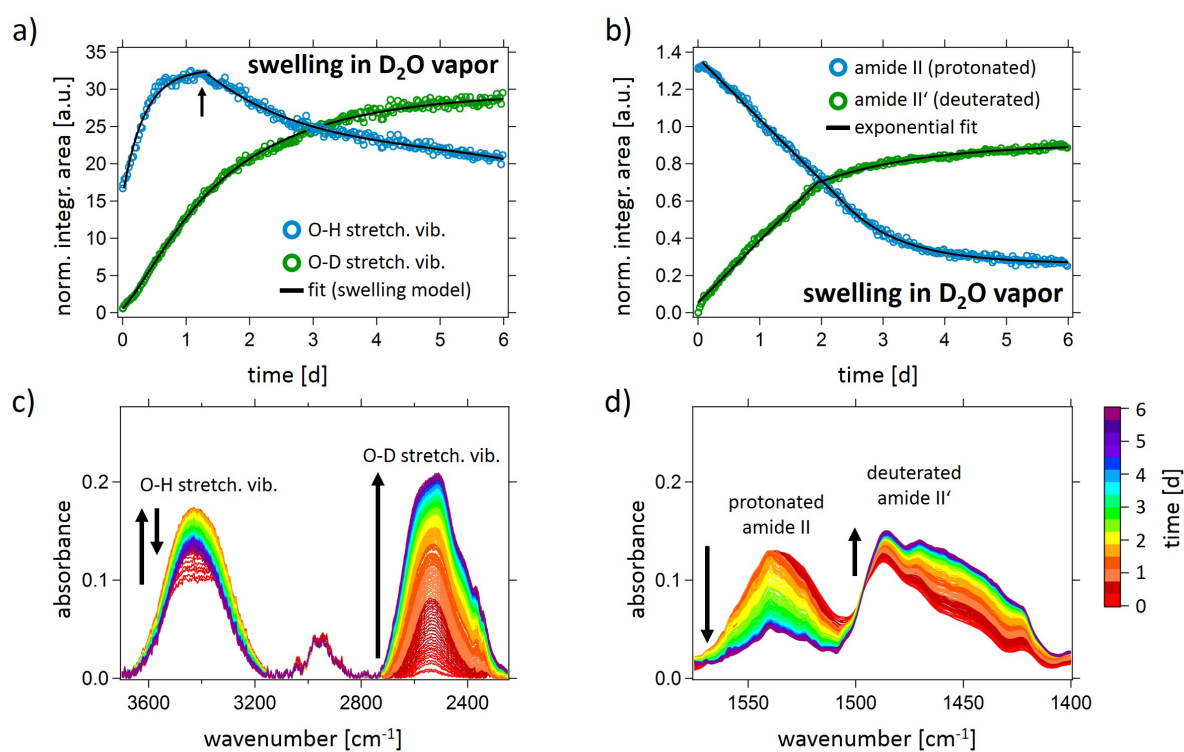


Figure 7.7.: Integration areas extracted from FTIR spectra during the swelling in D_2O vapor. Normalized integration areas of the (a) O-H (blue) and O-D (green) peaks, and the (b) protonated (blue) and deuterated (green) amide II and II' peak during the swelling in D_2O vapor. The corresponding absorption modes are imaged below the integration areas in (c,d). The integration areas of the O-H (divided into two regimes by a black arrow) and O-D peaks as a function of time in (a) are fitted with a swelling model (black line), while the integration areas of the amide II and II' peaks in (b) are fitted with an exponential fit as explained in the main text. Adapted with permission from AMERICAN CHEMICAL SOCIETY, Copyright 2020 [37].

The integration area of the O-D peak increases with time, as D_2O molecules diffuse into the thin film, and reaches an equilibrated state after roughly 5.5 d. In contrast, the integration area of the O-H peak as a function of time follows a more complex trend. As mentioned above, H_2O molecules are present within the thin film in the as-prepared

state. In Chapter 5, the change of the vapor composition leads to an exchange of different water species within the thin film. Here, the integration area of the O-H peak first reaches a maximum before it decreases. The increase hints toward a strong deuteration of the amide groups and the associated creation of HDO molecules. It is assumed that exchange processes, *i.e.*, excessively present D₂O molecules replace H₂O and HDO molecules within the thin film, occur throughout the swelling in D₂O vapor. Apparently, in the beginning, the effect of deuteration exceeds the exchange processes and results in a maximum of the O-H stretching vibration after roughly one day. While the deuteration eventually slows down, the exchange process continues. Thus, less HDO molecules are created, but still H₂O (initially present) and HDO molecules (due to deuteration) are exchanged by D₂O molecules. Consequently, the integration area of the O-H peak decreases over time.

The integration areas of the protonated amide II and the deuterated amide II' band as a function of time, underline this hypothesis. Both bands show an opposing trend: While the integration area of the amide II band decreases, the integration area of the amide II' band increases, thereby, clearly revealing deuteration processes. Both show a linear regime during the first two days, before the respective increase and decrease of integration area slows down and eventually equilibrates after roughly five days. Hence, a constant deuteration rate is assumed for the first two days. Since the O-H peak features an integration area maximum after one day, it seems that the exchange of H₂O and HDO by D₂O molecules becomes rapidly the dominant factor and outperforms the constantly ongoing deuteration rate. To quantitatively compare the decreasing amide II with the increasing amide II' band, linear and exponential fits are applied to the two regimes. The slopes and decay rates of the linear and the exponential fits, respectively, are very similar for the amide II and II' band (linear: -0.32 d and 0.33 d, exponential: 1.22 d and 1.13 d). This proves a straightforward 1:1 H/D exchange and is in good agreement with the results from the previous Chapter 5.

Analogously to the SR and ToF-NR data, the swelling model can be applied to the integration area of the O-D and O-H peaks as a function of time. Please note that the O-H peak is divided, namely in an increasing and in a decreasing part (marked by a black arrow in Figure 7.7a). The swelling model is applied to both parts individually. All values for χ_{eff} and τ are listed in Table 7.3.

χ_{eff}	τ [d]	extracted from
0.31 ± 0.03	1.3 ± 0.02	O-D stretch. vib. ^a
0.34 ± 0.02	0.5 ± 0.02	O-H stretch. vib. - increase ^a
1.10 ± 0.04	3.2 ± 0.12	O-H stretch. vib. - decrease ^a
1.03 ± 0.08	0.5 ± 0.01	S-O stretch. vib. ^b

Table 7.3: Swelling model applied to the FTIR data shown in Figures 7.7a and 7.8a.

The obtained χ_{eff} values are very similar for the O-D peak and the increasing part of the O-H peak. Since the D₂O uptake governs the O-D peak, and the deuteration of the amide group as well as the exchange of H₂O and HDO by D₂O molecules governs the O-H peak, this suggests, a similar high affinity of the whole DBC and the amide group towards D₂O. In contrast, the τ values differ significantly. The initial increase of the O-H peak occurs faster than the increase of the O-D peak, which indicates a strong deuteration at early stages of the swelling process. In turn, the τ value of the subsequent O-H peak decrease is larger than for the O-D peak increase. Thus, the release of H₂O and HDO molecules takes place on a longer time scale, than the D₂O uptake, due to the still ongoing deuteration process and the creation of HDO molecules. Analogously to the SR and ToF-NR results, the χ_{eff} and τ values obtained from the increasing O-D peak are smaller than the corresponding values obtained in the previous Chapter 5. Thus, the assumption of an at least partly hydrated PSPP block, is also confirmed on a molecular level.

Besides the integration areas of the absorption peaks, also their peak position is of interest, as a shift indicates cooperative hydration effects. At 1038 cm⁻¹ a sharp absorption peak arises that is due to the symmetric S-O stretching vibration of the SO₃⁻ group. This group is located at the end of the PSPP side chain. Due to its location and its negative charge, it is assumed to play a major role during water uptake and release. Figure 7.8 displays its absorption peak maximum as a function of time during the swelling in D₂O vapor. The S-O absorption peak undergoes a distinct shift towards higher wavenumbers upon hydration with D₂O, which equilibrates after approximately five days. The swelling model yields a higher χ_{eff} value and a lower τ value than the corresponding χ_{eff} and τ values for the increasing integration area of the O-D peak. This indicates a lower affinity of the SO₃⁻ group towards D₂O, but simultaneously a faster hydration with respect to the overall D₂O uptake. Apparently, the position of the SO₃⁻ group is easily accessible for D₂O molecules, which leads to a very fast hydration. Thus, the location of a particular group has a considerable impact on its hydration behavior and might even outbalance a reduced affinity towards the solvent. An interesting fact gives the comparison with the previous Chapter 5. There, the χ_{eff} and τ values obtained from the S-O stretching vibration peak shift are lower, while in parallel, the values determined via integration of the O-D stretching vibration are higher than the values obtained in the present chapter. In other words, the difference of the χ_{eff} and τ values, obtained from the here presented S-O and O-D stretching vibration is significantly higher. This might be due to the longer PSPP block, which is assumed to be hydrated (see the discussion above in the SR and ToF-NR section). Hence, the overall D₂O uptake is favored, while, with respect to this favored uptake, the affinity of the SO₃⁻ group towards D₂O is lower. This further corrob-

orates the hypothesis, that at a temperature of 20 °C the PSPP block is hydrated, which is not the case in aqueous solution.

Once the D₂O swelling has equilibrated, a static ToF-NR measurement is performed, as is discussed in the Section 7.1. Immediately after this measurement, the first temperature jump is performed and monitored with SR, kinetic ToF-NR, and FTIR measurements, which will be described in the following.

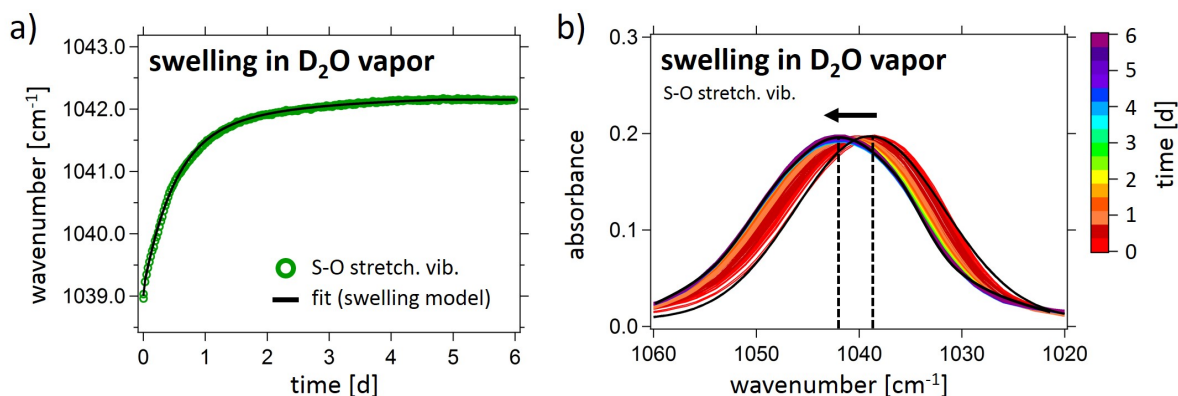


Figure 7.8.: Peak maximum position extracted from FTIR spectra during the swelling in D₂O vapor. (a) The peak position of the symmetric S-O stretching vibration during swelling in D₂O vapor is extracted via an Gaussian fit from the S-O absorption mode shown in (b). A Gaussian fit (applied to all FTIR curves) is shown in (b) as black line for the first and final S-O stretching vibrations. Dashed black lines indicate the peak maxima. The S-O peak position as a function of time is fitted with a swelling model (black line) as explained in the main text. Adapted with permission from AMERICAN CHEMICAL SOCIETY, Copyright 2020 [37].

7.3. Phase transition behavior

Two consecutive temperature jumps are performed: From 20 °C to 40 °C and from 40 °C to 60 °C. First, the swelling ratio and water content obtained with SR and ToF-NR measurements are discussed, and subsequent the molecular information from FTIR spectroscopy complements the discussion. The swelling model is again applied to the data.

Film thickness and water content

Analogously to the swelling in D₂O vapor, the obtained kinetic ToF-NR curves are fitted with a four-layer model (SiO₂, one main polymer layer, and two D₂O enrichment layers at the interfaces). A selection of NR curves together with the corresponding fits can be

found in Figure 7.9. The extracted swelling ratio and water content as a function of time during both temperature jumps are shown in Figure 7.10.

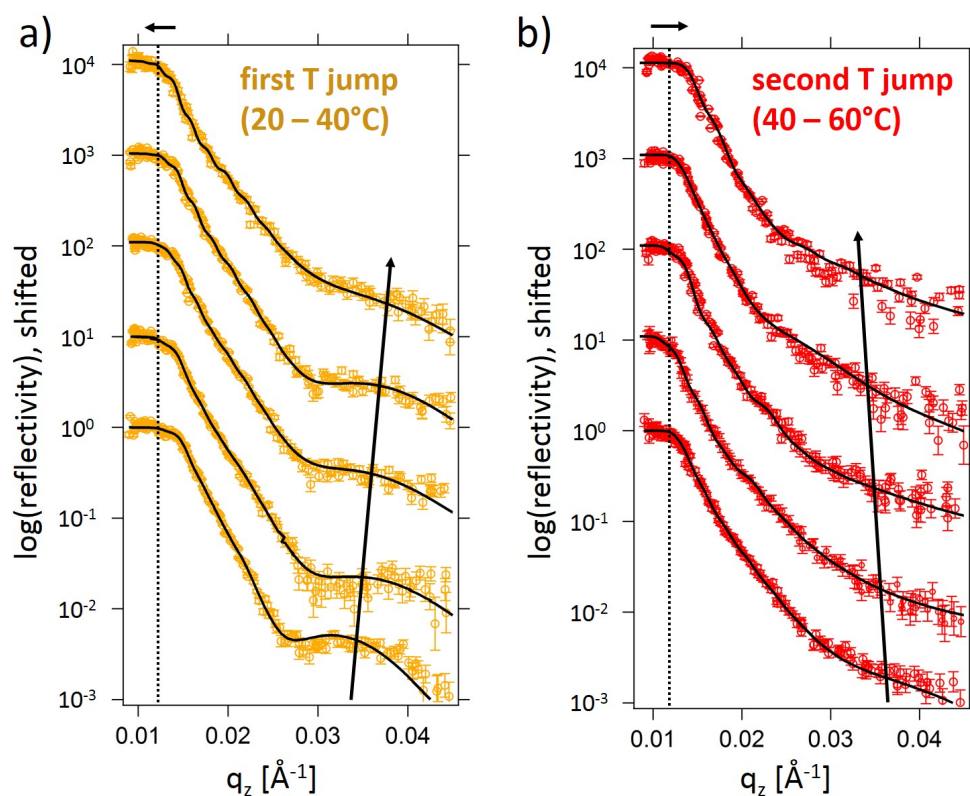


Figure 7.9.: Selected ToF-NR curves during temperature increase. Representative ToF-NR data are shown with best model fits (black lines) for the (a) first and the (b) second temperature jump. From bottom to top the time increases for the first temperature jump: $t = 0.5, 5, 10, 30,$ and 60 min. For the second temperature jump the curves correspond to $t = 0.5, 5, 30, 60,$ and 120 min after the temperature jump is induced. The ToF-NR curves are shifted along the y -axis for clarity. The dashed black lines mark the critical edge of the as-prepared thin films. The black arrows on top of the graphs indicate the shift of the critical edge, while the black arrows inside the graphs indicate the shift of the Kiessig fringes. Adapted with permission from AMERICAN CHEMICAL SOCIETY, Copyright 2020 [37].

SR and ToF-NR reveal a decreasing thin film thickness and D_2O content during the first temperature jump. Upon the second temperature jump, the film thickness and water content slightly increase again. As already stated earlier, the phase diagram of the DBC in aqueous solution (at a polymer concentration of 50 g L^{-1}) features a fully hydrophilic window at 40°C and a partly hydrophilic regime at 20°C (only PNIPMAM block soluble in water) and 60°C (only PSPP block soluble in water). Thus, a further swelling and D_2O uptake upon the first, and a thin film contraction and D_2O release upon the second

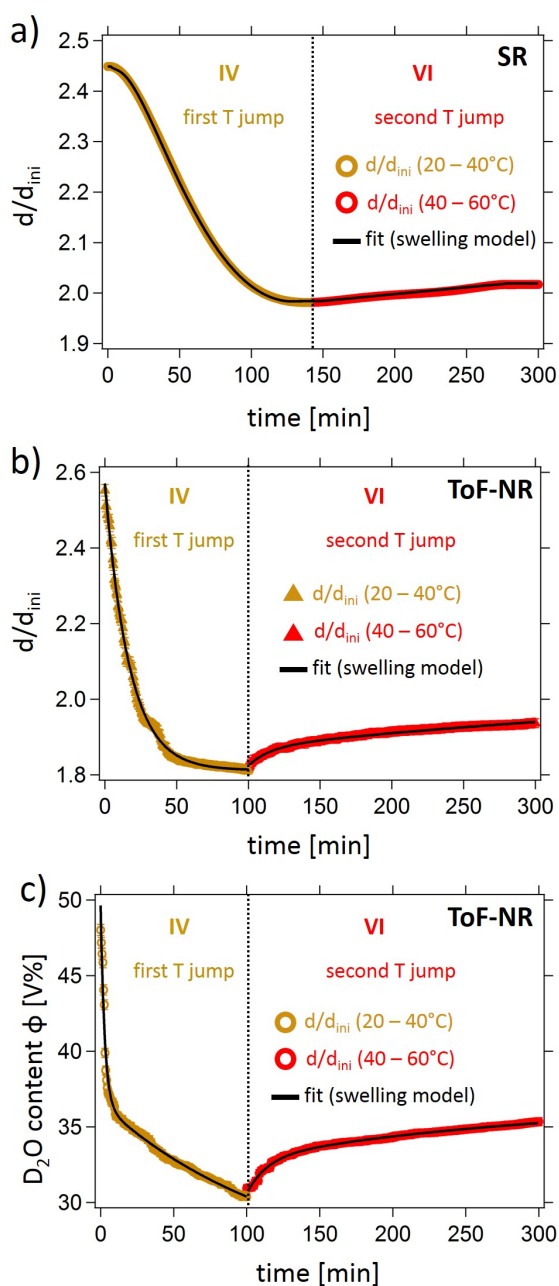


Figure 7.10: First and second temperature jump followed with SR and ToF-NR *in-situ*. The swelling ratio d/d_{ini} as a function of time during both temperature jumps obtained with (a) SR and (b) kinetic ToF-NR measurements. (c) Water content Φ as a function of time obtained with kinetic ToF-NR measurements. The vertical dotted black line divides the first and the second temperature jump. The swelling model is applied to all curves as explained in the main text. Adapted with permission from AMERICAN CHEMICAL SOCIETY, Copyright 2020 [37].

temperature jump, is expected. Here, the opposite behavior is monitored. A strong shift of the swelling temperature of the PSPP block to higher temperature, as well as a shift of the collapse temperature of the PNIPMAM block to lower temperatures would explain the data. Thus, upon the first temperature jump, the decreased collapse temperature is exceeded, while during the second temperature jump the increased swelling temperature is crossed. Based on the results, we assume a hydrated PSPP block, even below the swelling temperature. Also, cooperative hydration effects between both polymer blocks, as is described in the second part of Chapter 6 might contribute to the observed behavior.

The swelling model is applied to the evolution of the swelling ratio and the water content. Since χ_{eff} and τ are sensitive to temperature, a change of these values is expected once the temperature is increased. Table 7.4 summarizes all extracted values. The χ_{eff} values, extracted from SR and ToF-NR during the first temperature jump, are higher as compared to the values extracted during the swelling in D₂O vapor. This indicates a decreasing water compatibility of the DBC and fits to the release of D₂O molecules and the thin film contraction. In comparison, to the very short swelling in D₂O vapor, the extracted τ values suggest, the polymer chains need longer times to re-arrange and to equilibrate. Apparently, even in the swollen state, the polymer chain mobility is low. During the second temperature jump to 60 °C, the following trend is observed. The values for χ_{eff} lie in-between the values obtained from swelling and the first temperature jump, while the τ values are the highest of all dynamic processes. The values again match the observations: Compared to the first temperature jump, the χ_{eff} values decrease, therefore indicating an increased water compatibility and favored polymer-water interactions. This refers to the observed increase in film thickness as D₂O molecules diffuse into the thin film during the second temperature jump. The re-swelling occurs on an even longer time scale as the thin film contraction during the first temperature jump. This seems intuitive, since at 40 °C the thin film is in a partly collapsed state, the mobility of the polymer chains is supposed to be even lower, as compared to the fully swollen state at 20 °C. Generally, the long ongoing re-arrangements of the polymer chains hint towards a change in thin film morphology, which will be discussed in detail in the later Section 7.4.

Table 7.4: Swelling model applied to the SR and ToF-NR data shown in Figure 7.10a,b.

First temperature jump (20 °C to 40 °C)		
χ_{eff}	τ [min]	extracted from
1.3 ± 0.05	33 ± 2	SR (d/d_{ini}) ^a
1.0 ± 0.06	21 ± 1	ToF-NR (d/d_{ini}) ^b
1.5 ± 0.07	30 ± 1	ToF-NR (Φ) ^b
Second temperature jump (40 °C to 60 °C)		
χ_{eff}	τ [min]	extracted from
0.77 ± 0.04	80 ± 3	SR (d/d_{ini}) ^a
0.64 ± 0.04	68 ± 3	ToF-NR (d/d_{ini}) ^b
0.85 ± 0.05	57 ± 2	ToF-NR (Φ) ^b

Polymer-water interactions

To explore the molecular origin of the unexpected thin film behavior upon increasing temperature, FTIR measurements are performed. The obtained FTIR spectra are displayed in Figure 7.11. One has to note that the temperature is increased step-wise (0.5 K h^{-1}), to enable *in-situ* measurements. The characteristic absorption modes of the O-D, the O-H, and the symmetric S-O stretching vibrations as well as the amide I, II, and II' band, can be assigned to the corresponding groups, as explained above in Section 7.2. It is important to know that due to deuteration upon swelling in D_2O vapor, three water species, D_2O , H_2O , and HDO are present within the film prior to temperature increase. Therefore, the absorption peaks of the O-D and the O-D peaks are a combination of $\text{D}_2\text{O}/\text{HDO}$ and $\text{H}_2\text{O}/\text{HDO}$, respectively. Their normalized integration areas are depicted in Figure 7.12.

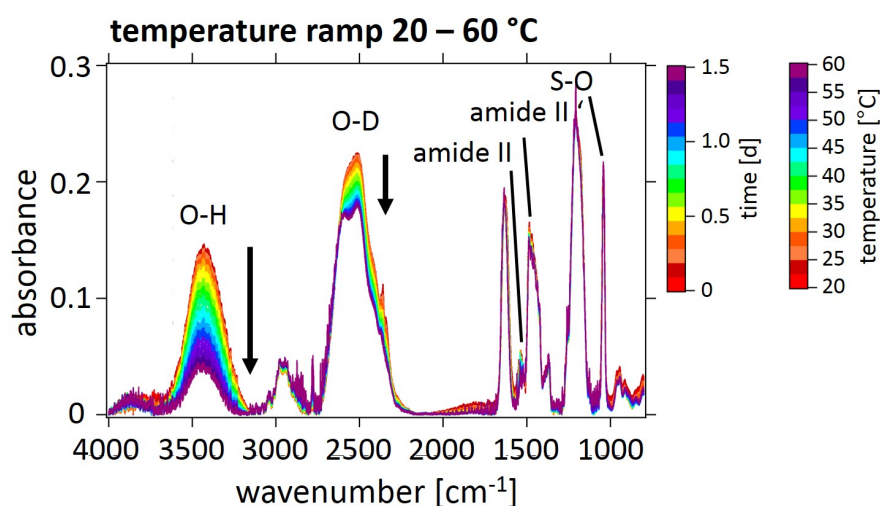


Figure 7.11.: Temperature ramp in D_2O vapor followed with FTIR *in-situ*. The red curve marks the initial ($t = 0$ days), while the purple curve marks the final measurement after 1.5 days. Characteristic absorption peaks are labelled accordingly. Black arrows mark the increase and decrease of the O-H and the O-D stretching vibration. Adapted with permission from AMERICAN CHEMICAL SOCIETY, Copyright 2020 [37].

Both absorption peaks decrease in integration area upon temperature increase, indicating a reduced water amount within the thin film, and presumably also a reduced film thickness. This is only partly in agreement with the findings from SR, and ToF-NR. The re-swelling process, seen during the second temperature jump, is not observed with FTIR. A possible explanation, might be the changed measurement protocol (temperature jump vs. temperature ramp), but also other effects such as differences in the sample size or sample environment might play a role here. This shows, how beneficial combined measurement techniques within one flexible measurement chamber for such complex and

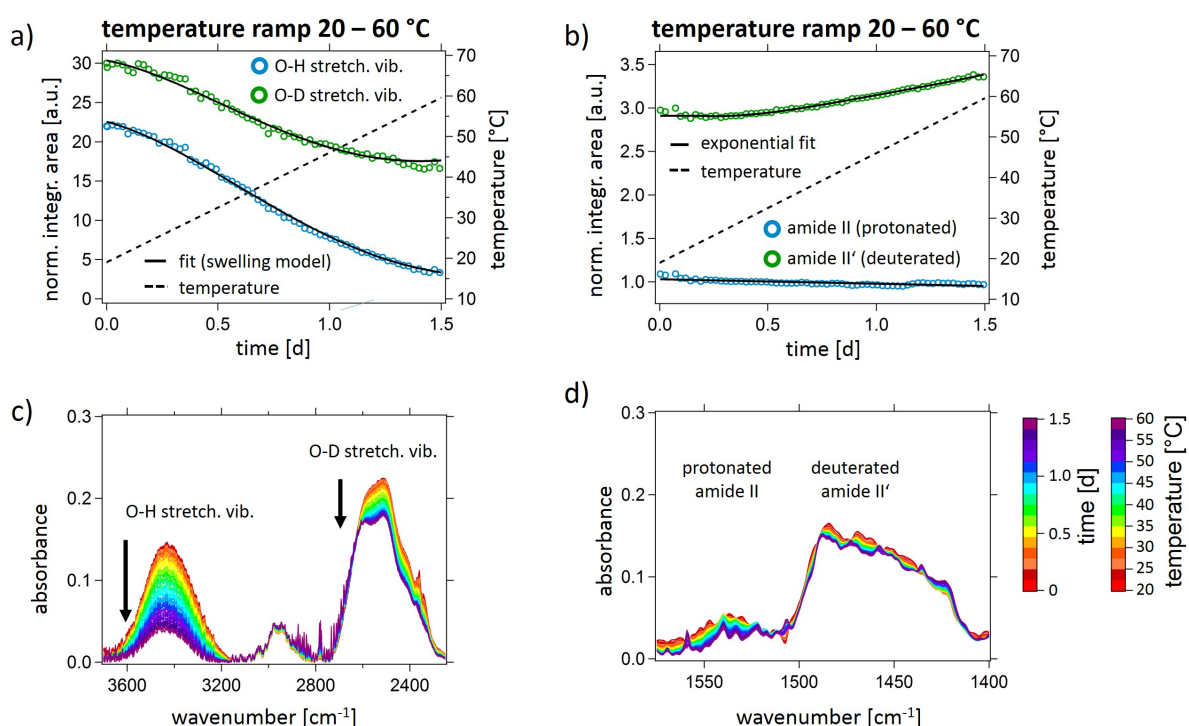


Figure 7.12.: Integration areas extracted from FTIR spectra during temperature increase. Normalized integration areas of the (a) O-H (blue) and O-D (green) peaks, and the (b) protonated (blue) and deuterated (green) amide II and II' peak upon temperature increase. The corresponding absorption modes are imaged below the integration areas in (c,d). The integration areas of the O-H and O-D peaks as a function of time in (a) are fitted with a swelling model (black line), while the integration areas of the amide II and II' peaks in (b) are fitted with an exponential fit as explained in the main text. The temperature is indicated by a dashed black line. Adapted with permission from AMERICAN CHEMICAL SOCIETY, Copyright 2020 [37].

time-consuming experiments are. An approach to overcome these issues is part of the present thesis and is described in Section 3.4. A more detailed study of the integration areas reveal that the area of the O-H peak decreases more strongly than the one of the O-D peak. This hints towards a still ongoing exchange of H₂O and HDO by D₂O molecules. This exchange has slowed down significantly as compared to the swelling in D₂O vapor, since no more HDO molecules are generated by deuteration processes and almost all initially present H₂O molecules are already exchanged by D₂O molecules. The very stable absorption peaks of the amide II and II' bands confirm this. Only at the later stages, deuteration is observed, which is most likely due to an increased D₂O concentration within the thin film as the exchange of H₂O by D₂O molecules still continues. An exponential fit is applied to the integration area of the amide II' band and shows a lower decay rate than for the swelling in D₂O vapor [(0.41 ± 0.01) d vs. (1.13 ± 0.01) d].

The swelling model is applied to the data and the extracted χ_{eff} and τ values are listed in Table 7.5. The χ_{eff} values indicate a higher affinity of the DBC toward D₂O as compared to H₂O, which is not in agreement with results from the previous section about the swelling behavior, as well as from Chapter 5. A possible explanation could be the strong deuteration of the chains, which definitely results in a change of the nature of interactions via hydrogen and deuterium bonds with the different water species. Thus, it seems possible, that a fully deuterated polymer chain, favors interactions with deuterated solvents, while the protonated polymer chain favors rather protonated solvents. As a consequence, more H₂O (and HDO) molecules are released from the thin film upon temperature increase as compared to D₂O (and HDO) molecules. The release of all water species occurs on roughly the same time scale.

χ_{eff}	τ [d]	extracted from
1.08 ± 0.05	0.7 ± 0.03	O-D stretch. vib. ^a
1.31 ± 0.08	0.8 ± 0.06	O-H stretch. vib. ^a
1.20 ± 0.08	0.8 ± 0.02	S-O stretch. vib. ^b

Table 7.5: Swelling model applied to FTIR data shown in Figures 7.12a and 7.13a.

The temperature increase leads to a backshift of the peak maximum position of the symmetric S-O peak to lower wavenumbers as is shown in Figure 7.13. Therefore, the general release of water from the thin film results also in a dehydration of the SO₃⁻ group. It can be seen that the initial position of the as-prepared thin film state (1039 cm⁻¹) is not reached. Thus, we assume the SO₃⁻ group to be still partly hydrated. The de-hydration of this characteristic group within the PSPP block is extremely counter intuitive, as typically the hydrophilicity of an UCST-type polymer increases with temperature. The previous results, regarding the film contraction during the first and its re-swelling during the second temperature jump, could be explained by a certain hydrophilic character of the PSPP block, and a shift of its swelling temperature to higher temperatures. However, the shifted phase transition temperature can not be the origin of the SO₃⁻ dehydration. This demonstrates the high complexity of the hydration and de-hydration mechanisms in thin films, and how greatly they differ from the well-studied mechanisms in aqueous solutions. The obtained χ_{eff} and τ values indicate a similar affinity of the SO₃⁻ group and the whole DBC toward both, H₂O and D₂O. Also, the backshift of the S-O peak, *i.e.*, the dehydration of the SO₃⁻ group occurs on the same time scale as the water release, which suggests a strong synchronization of the de-hydration of the SO₃⁻ group and the general water release from the thin film.

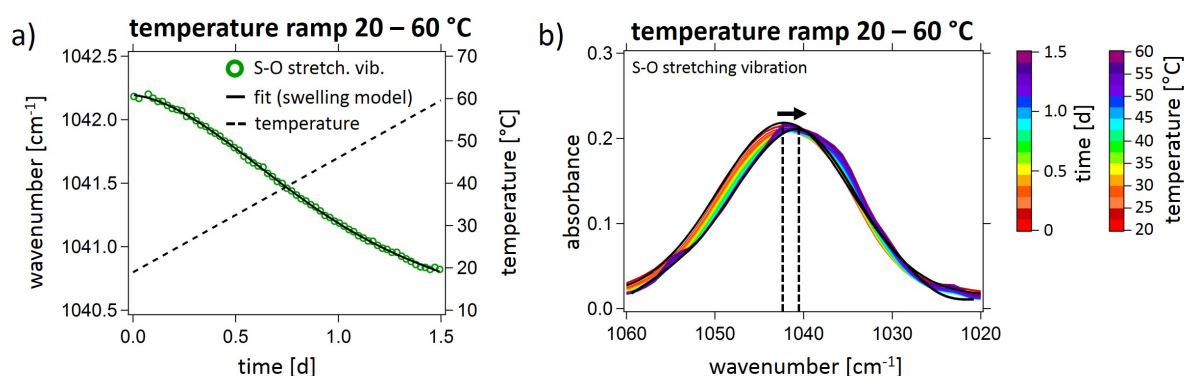


Figure 7.13.: Peak maximum position extracted from FTIR spectra upon increasing temperature. (a) The peak position of the symmetric S-O stretching vibration upon temperature increase is extracted via an Gaussian fit from the S-O absorption mode shown in (b). A Gaussian fit (applied to all FTIR curves) is shown in (b) as black line for the first and final S-O stretching vibration. Dashed black lines indicate the peak maxima. The S-O peak position as a function of time is fitted with a swelling model (black line) as explained in the main text. Adapted with permission from AMERICAN CHEMICAL SOCIETY, Copyright 2020 [37].

7.4. Temperature-dependent thin film morphology

The last part of this chapter focuses on the lateral thin film morphology upon swelling in D_2O vapor and the subsequent temperature jumps. ToF-GISANS probes the equilibrated as-prepared (stage I) and swollen thin film states at 20°C (stage III), 40°C (stage V), and 60°C (stage VII). Due to the ToF mode, surface-near as well as surface-far ('bulk') regions of the thin film are probed. A detailed introduction to the ToF-GISANS measurement technique can be found in Section 2.3.2. Figure 7.14 shows exemplary 2D detector images (with a wavelength band of 10%) of the ToF-GISANS measurement of the swollen thin film at 20°C . The surface- and bulk-sensitive neutron wavelengths are labelled accordingly.

For analysis, vertical line cuts (VLC) along q_z direction at $q_y = 0$ (red box) and horizontal line cuts (HLC) along q_y direction around the Yoneda region (yellow box) are performed. The VLC can be seen in Figure 7.15.

For the as-prepared state (colored in gray), only a very weak Yoneda peak arises, which is attributed to the Si substrate. In contrast to that, two further Yoneda peaks are found for the D_2O swollen states at 20°C , 40°C , and 60°C . This strongly indicates a heterogeneous polymer distribution along the substrate normal. Noteworthy, such regions are also found with static ToF-NR measurements. There, D_2O enrichment layers are observed. By applying a linear regression to the Yoneda position as a function of the neutron wavelength, the SLD values of these D_2O - and polymer-rich regions as well as of the Si substrate are obtained. This is displayed in Figure 7.16.

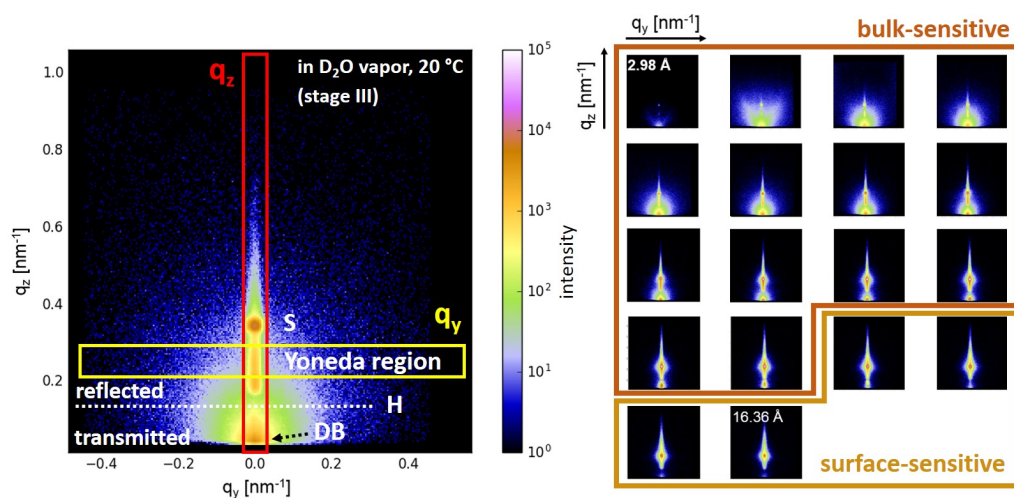


Figure 7.14.: ToF-GISANS 2D detector images. Exemplary 2D detector image of the ToF-GISANS measurement of the swollen thin film at 20 °C (left) with characteristic scattering features: The horizon (H) separates the transmitted (below H) from the scattered (above H) signal. On the bottom of the detector, the direct beam (DB) is still visible. The specular beam is denoted with S. In-between the direct and specular beam, the Yoneda region is visible. For analysis, vertical (red box) and horizontal (yellow box) line cuts along q_z and q_y , respectively are performed. The right side shows 2D detector images of all wavelength slices. The orange and brown boxes indicate surface- and bulk-sensitive incident neutrons. Adapted with permission from AMERICAN CHEMICAL SOCIETY, Copyright 2020 [37].

Table 7.6.: SLD values of the equilibrated thin film states determined by ToF-GISANS and ToF-NR. ^aThe as-prepared state probed with static ToF-NR features a homogeneous vertical SLD distribution.

thin film state	SLD [10^{-6} \AA^{-2}]			SLD [10^{-6} \AA^{-2}]	
	determined with ToF-GISANS			determined with ToF-NR	
	polymer-rich	Si substrate	D ₂ O-rich	polymer-rich	D ₂ O-rich
as-prepared	—	2.070 ± 0.012	—	0.601 ± 0.01^a	
swollen - 20 °C	1.85 ± 0.01	2.07 ± 0.01	4.001 ± 0.02	1.86 ± 0.02	4.01 ± 0.02
swollen - 60 °C	1.40 ± 0.01	2.07 ± 0.01	3.99 ± 0.009	1.44 ± 0.01	3.99 ± 0.02
swollen - 60 °C	1.56 ± 0.01	2.07 ± 0.01	4.01 ± 0.021	1.50 ± 0.02	4.00 ± 0.02

The SLD values for the respective regions at the corresponding temperatures, determined via ToF-GISANS and via ToF-NR, are listed in Table 7.6. While the obtained SLD values for the Si substrate are in good agreement with the literature [69], the two

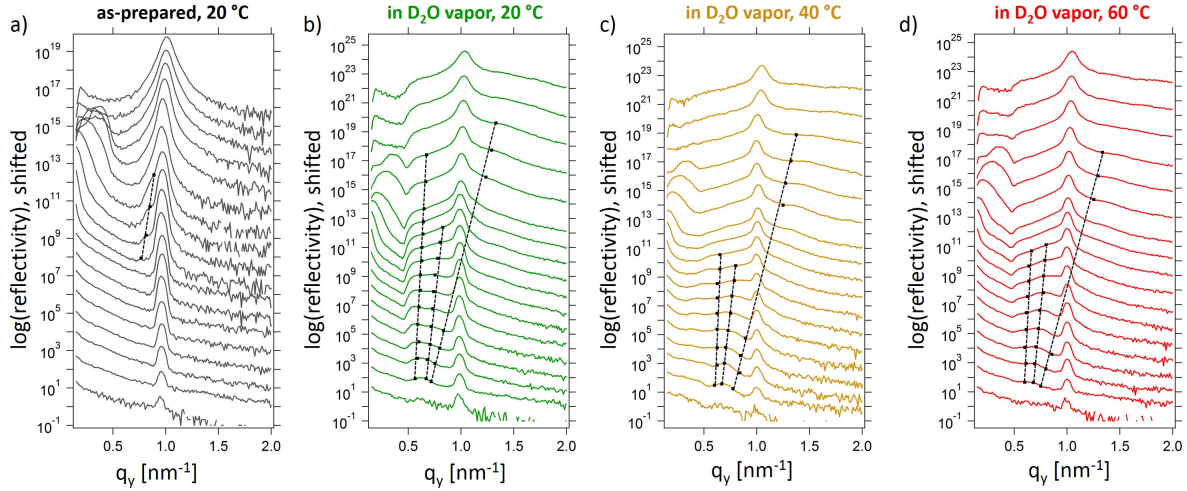


Figure 7.15.: Vertical line cuts. VLC extracted from ToF-GISANS measurements for the (a) as-prepared state and for the swollen states at (b) 20 °C, (c) 40 °C, and (d) 60 °C. The neutron wavelength increases from bottom to top (2.9, 3.2, 3.5, 3.9, 4.3, 4.9, 5.3, 5.8, 6.5, 7.1, 7.9, 8.7, 9.6, 10.7, 11.8, 13.0, 14.4, and 15.9 Å). The black squares indicate the positions of the Yoneda peaks, which is fitted with a linear regression (dashed black lines). Adapted with permission from AMERICAN CHEMICAL SOCIETY, Copyright 2020 [37].

additional Yoneda peaks yield SLD values very similar to the SLD values obtained with ToF-NR. Therefore, the observed Yoneda peaks at the swollen thin film states are assigned to D₂O-rich and polymer-rich (or D₂O-poor) layers within the vertical thin film composition. The determined SLD values result from broad Yoneda peaks, which indicates a heterogeneous and a defect-rich distribution of these layers.

While the VLC obtain information about the vertical thin film distribution, the HLC reveal details about the lateral thin film structures. Thus, HLC at the corresponding Yoneda peak position along q_y direction are performed. Figure 7.17 shows the HLC for the swollen states at 20 °C, 40 °C, and 60 °C.

One peak is visible for all three swollen states at higher q_y values (0.200 - 0.250 nm⁻¹), in particular for the shorter neutron wavelengths. In addition, a less pronounced peak is found at lower q_y values (0.055 - 0.070 nm⁻¹). Both peaks smear out with increasing neutron wavelength, which is due to a broadening of the wavelength band (regarding the 10% slicing), but also suggests a defect-rich and disordered thin film morphology. Therefore, the simplest possible model is used to extract information about the lateral structures from the data. All HLC are modeled with the local monodisperse approximation (LMA) and effective interface approximation (EIA) of standing cylinder-shaped nanodomains distributed on a 1D paracrystal lattice in combination with the distorted-wave Born approximation (cf. Section 3.2). The cylinder-shaped nanodomains are assumed based on

7.4. Temperature-dependent thin film morphology

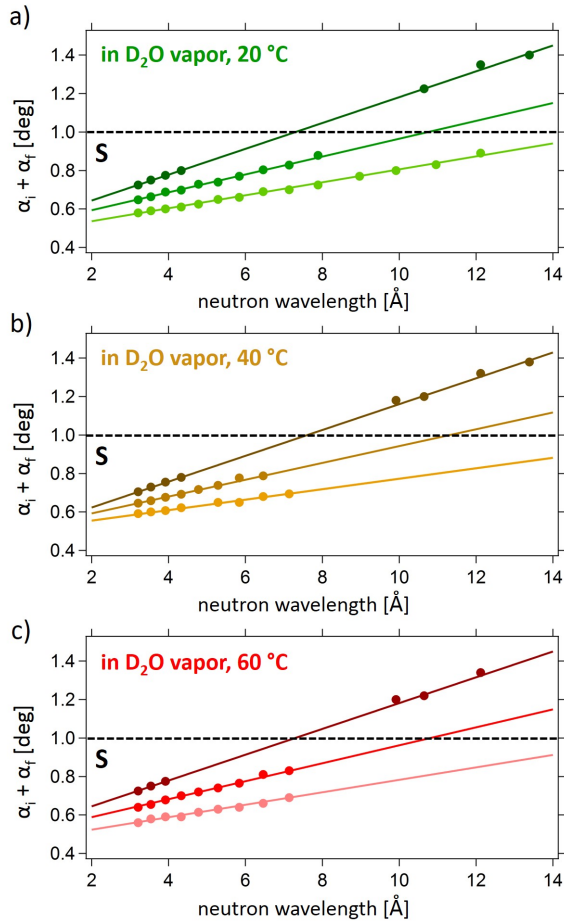


Figure 7.16: Wavelength-dependent Yoneda peak position. The Yoneda peak positions on the detector at an angle of $\alpha_i + \alpha_f$, which is the sum of the incoming and outgoing angle, as a function of the neutron wavelength for the swollen thin film states at (a) 20 °C, (b) 40 °C, and (c) 60 °C. The different colors correspond to a D₂O enrichment layer (dark color, top position), the Si substrate (medium color, middle position), and a polymer enrichment layer (light color, bottom position) regions. The uncertainty bars of the Yoneda peak positions are smaller than the symbol sizes. Linear regression (solid lines) of the data, yields the corresponding SLD values. The specular peak position is marked with a horizontal dashed black line and denoted with S. Adapted with permission from AMERICAN CHEMICAL SOCIETY, Copyright 2020 [37].

the molar mass ratio of the PSPP and PNIPMAM blocks. Since modelling of the HLC with only one structure factor (SF) and form factor (FF) does not result in a proper fit, two FFs and SFs are used. From these factors, small and large cylinder radii (denoted with r_{small} and R_{large}) as well as small and a large center-to-center distances (denoted with d_{small} and D_{large}) are extracted. Table 7.7 summarizes these model values.

Table 7.7.: Values for the cylinder radii and the center-to-center distances extracted from the FFs and SFs obtained from the HLC modelling.

thin film state	r_{small} [nm]	d_{small} [nm]	R_{large} [nm]	D_{large} [nm]
swollen - 20 °C	5 ± 1	28 ± 2	12 ± 1	70 ± 4
swollen - 40 °C	5 ± 1	28 ± 2	12 ± 1	50 ± 5
swollen - 60 °C	5 ± 1	28 ± 2	15 ± 2	60 ± 4

All swollen states feature the same r_{small} and d_{small} , which indicate stable small thin film domains upon increasing temperature. In contrast, R_{large} and D_{large} change with

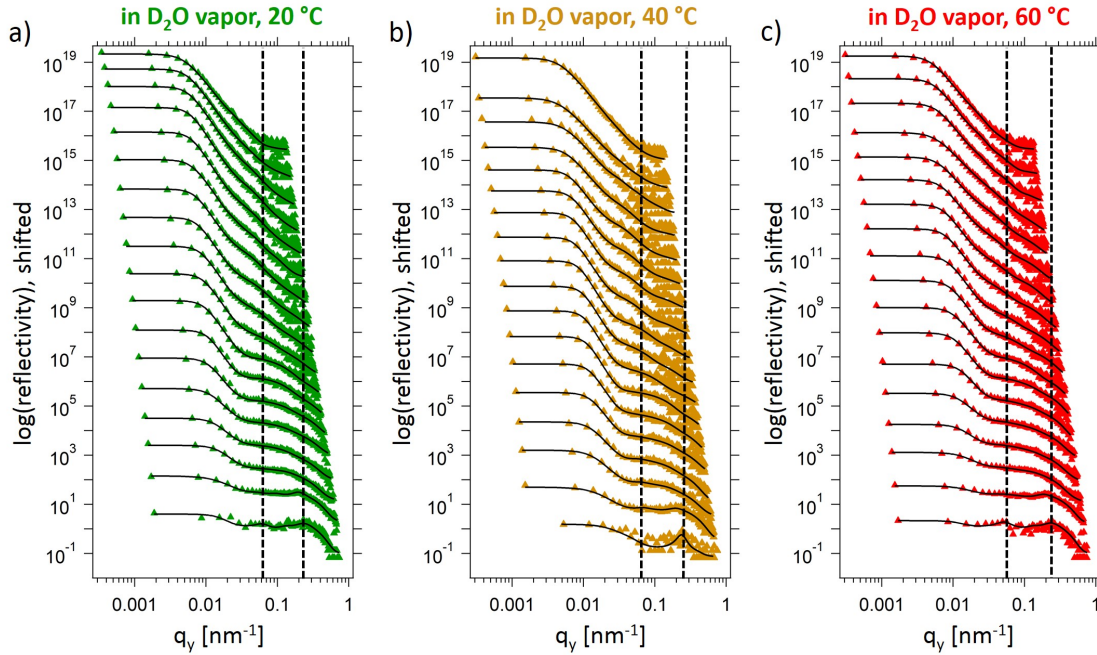


Figure 7.17.: Horizontal line cuts. HLC extracted from ToF-GISANS measurements for the swollen states at (a) 20 °C, (b) 40 °C, and (c) 60 °C. The neutron wavelength increases from bottom to top (2.9, 3.2, 3.5, 3.9, 4.3, 4.9, 5.3, 5.8, 6.5, 7.1, 7.9, 8.7, 9.6, 10.7, 11.8, 13.0, 14.4, and 15.9 Å). A fitting model (solid black line) is applied to the HLC as explained in the text. The dashed black lines mark the determined peak positions. Adapted with permission from AMERICAN CHEMICAL SOCIETY, Copyright 2020 [37].

increasing temperature. R_{large} increases during the second temperature jump, while D_{large} undergoes the most significant changes. It is the largest at 20 °C, decreases during the first temperature jump, and re-increases again during the second temperature jump.

In the following, the values of the cylinder radii and the center-to-center distances (lateral thin film morphology), as well as the results from the analysis of the VLC and the ToF-NR measurements (vertical thin film structure), are used to sketch a possible scenario of how the thin film might look like at different temperatures. From the block length ratio and the volume fractions of the two polymer blocks, we assume cylinder-shaped PNIPMAM nanodomains in a PSPP matrix. Some of the small PNIPMAM nanodomains assemble and form larger domains, which results in the two found length scales for the cylinder radius and the center-to-center distance. Since the peak in the HLC corresponding to the larger, assembled PNIPMAM domains, is relatively broad, also a rather broad and heterogeneous distribution of the larger PNIPMAM domains is expected. FTIR reveals a de-hydration of the SO_3^- group and therefore also of the PSPP block, which correlates to the decreasing D_{large} during the first temperature jump. D_{large} increases during the second temperature jump, which underlines the results found with ToF-NR,

7.4. Temperature-dependent thin film morphology

where a re-swelling of the thin film is observed. During the second temperature jump, R_{large} increases, which can be explained by a further assembly of PNIPMAM nanodomains into larger ones. Since the peak positions of the FFs and SFs remain constant with increasing neutron wavelength (cf. Figure 7.17), an unaltered lateral thin film morphology in vertical direction is assumed. In contrast, the polymer concentration is the highest in the center of the thin film and the lowest at both interfaces. The described thin film morphology is schematically shown in Figure 7.18.

While a re-arrangement of the polymer chains with changing temperature is indeed observed, a structural inversion, as was seen in aqueous solution [31, 235], does not occur. Since the size of the PNIPMAM nanodomains remain constant from 20 °C to 60 °C, either the collapse temperature of PNIPMAM has not been exceeded yet within the applied temperature range, or the chain mobility is so low, and the thin film structure so defect-rich, that a collapse of the PNIPMAM blocks does not occur. The PSPP block undergoes de- and re-hydration upon the first and the second temperature jump, which is also very surprising. Nevertheless, the present chapter (in particular Figure 7.18) demonstrates the advantage of a suited selection of complementary measurement techniques and their *in-situ* utilization. A detailed description of the thermal behavior and thin film morphology of a 'schizophrenic' dual thermo-responsive DBC in thin film geometry is obtained and highlights the extraordinary behavior and versatility of such materials.

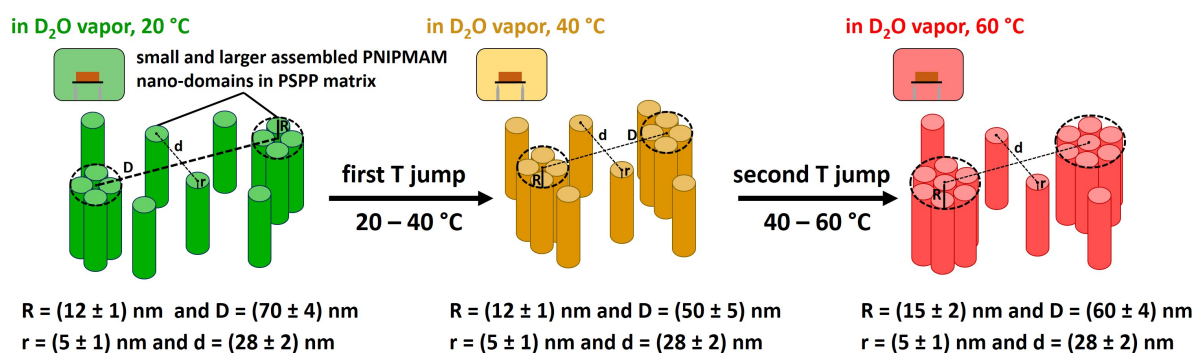


Figure 7.18.: Schematic illustration of a possible scenario of the lateral thin film morphology at different temperatures. Small and larger, assembled cylinder-shaped PNIPMAM domains in a PSPP matrix upon temperature increase from (a) 20 °C to (b) 40 °C, and to (c) 60 °C. The radii and center-to-center distances of the small and large PNIPMAM domains are labelled with r , d and R , D . Adapted with permission from AMERICAN CHEMICAL SOCIETY, Copyright 2020 [37].

7.5. Conclusion

The present chapter investigates the swelling and thermal behavior of a 'schizophrenic' orthogonally dual thermo-responsive PSPP-*b*-PNIPMAM thin film. While ToF-NR and ToF-GISANS reveal the vertical and lateral thin film morphology as well as its general thin film behavior, regarding film thickness and water content, FTIR identifies the molecular origin of the observed behavior and adds a new perspective to the observations. In addition, a swelling model is applied that respects the intrinsic swelling kinetic, *i.e.*, the diffusion of water molecules into and out of the thin film, as well as a non-constant RH. This enables a quantitative analysis of the monitored thin film kinetics and allows for a comparison with similar DBC thin film systems from the previous Chapters [5](#) and [6](#).

During the swelling, a significant D₂O uptake is observed, which is mainly addressed to the good compatibility of the PSPP block with water. The swelling model reveals that D₂O assembles first in air voids within the thin film, while the increase in film thickness is delayed until these voids are filled. With D₂O uptake, deuteration processes start to take place at the amide group, which is present in both polymer blocks. As a result, a third water species, HDO is created. With ongoing D₂O uptake, this HDO species as well as initially present H₂O molecules are exchanged. Regarding the HDO concentration within the thin film, this exchange process competes with the deuteration of the polymer chains and leads to a maximal HDO concentration, before the exchange process outperforms the decelerated deuteration process.

Upon the two temperature jumps, the thin film first contracts before it re-swells, which is accompanied by re-arrangement processes of the polymer chains. These happen on a considerably longer time scale as the D₂O uptake during the swelling, and indicate a very low chain mobility, despite a very high amount of D₂O inside the thin film. The unexpected contraction and re-swelling behavior, might be due to a shift of respective swelling temperature of PSPP, presumably to higher temperatures, and possibly also of the collapse temperature of PNIPMAM, presumably to lower temperatures. The data indicates, the PSPP block is responsible for the thin film contraction during the first as well as for the re-swelling during the second temperature jump. In contrast, the PNIPMAM block remains unchanged in its hydration throughout both temperature jumps. This is either due to a strongly shifted CP_{PNIPMAM} or due to a very low chain mobility that prevents the transition. The obtained lateral thin film morphology confirms these findings. Smaller PNIPMAM nanodomains within a PSPP matrix are present at all temperatures. Apart from a clustering of these nanodomains into larger ones, their sizes remain unaffected by temperature. In contrast, the distance between the smaller and the larger, aggregated PNIPMAM domains varies with temperature, which indicates a collapse and re-swelling of the PSPP matrix. A structural inversion analogous to the 'schizophrenic' behavior

in aqueous solution is not observed, which is most probably due to the very low chain mobility.

The present chapter provides a detailed and insightful first study of the thermal behavior of orthogonally dual thermo-responsive PSPP-*b*-PNIPMAM thin films. The results underline the findings from the previous chapters and unfold the complexity of the thin film mechanisms upon temperature change. The thin film behavior significantly differs from its behavior in dilute aqueous solution, and thereby this chapter contributes to a fundamental understanding of such thermo-responsive DBC thin films.

8. Temperature-dependent cyclic thin film swelling and drying kinetics

This chapter is largely based on the publication 'Cyclic Water Storage Behavior of orthogonally Thermoresponsive Poly(sulfobetaine)-Based Diblock Copolymer Thin Films' (L. P. Kreuzer et al., *Macromolecules* **2020**, 53, 9108–9121; DOI: 10.1021/acs.macromol.0c01335) [38]. Reprinted with the permission from AMERICAN CHEMICAL SOCIETY, Copyright 2020. Experiments were performed in collaboration with master student Nawarah Aldosari [275].

The previous chapters provide a detailed overview of how a changing vapor composition and temperature affect the behavior of poly(sulfobetaine)-based and orthogonally dual thermo-responsive DBC thin films. However, one crucial aspect has been left open so far, namely the reversibility and reproducibility of the dynamic processes. With respect to possible future application fields, *e.g.*, as (nano) switches or artificial muscles, reproducible kinetic processes are essential. Therefore, the following chapter focuses on the cyclic swelling and contraction of thin films in saturated water and dry nitrogen vapors. Regarding potential applications, these vapors provide the safest and most harmless environmental conditions.

Introduction

Polymer thin films can be used as artificial muscles and pumps [2, 3], as (nano) sensors and switches [13, 87, 90, 99, 239, 276–278], and as functionalized surface coatings [7, 8, 10–12]. In these application fields, the polymer is exposed to its surrounding, which in most cases is air, containing a certain amount of water molecules. Driven by the osmotic pressure, this gaseous water is able to diffuse into the thin film, thereby altering the polymer properties. Typically, the diffusion process is accompanied by an increase in film thickness, which can directly be used to move objects or close gaps [279–281]. For a reliable application, reversible and reproducible dynamic thin film processes are essential, *e.g.*, swelling leads to comparable swollen thin films state, regarding film thickness and water content, while drying results in the primordial thin film states.

The previous chapters demonstrate the great potential of orthogonally dual thermo-responsive DBC thin films and their versatile behavior in changing environmental conditions. Chapter 7 highlights that the thin film swelling behavior not only depends on the ambient relative humidity (RH), but also on the ambient temperature and the final swelling degree and water uptake is strongly altered at different temperatures. Therefore, this chapter focuses on the reproducibility of multiple thin film swelling and contraction cycles at different temperatures. Of particular interest are potential differences in the thin film swelling and drying kinetics with increasing cycle number.

The DBC under investigation is PSPP₅₀₀-*b*-PNIPMAM₁₅₀ (Figure 4.2d in Section 4.2). In the following, it will simply be referred to as PSPP-*b*-PNIPMAM. Its thermal behavior upon two consecutive temperature jumps, is described in the previous Chapter 7. The film thickness and water content of the DBC undergo strong changes with increasing temperature, which makes the DBC a promising candidate for potential applications as *e.g.*, artificial muscle in the field of soft robotics. In the present chapter, the cyclic thin film swelling and contraction behavior is analyzed. Within three consecutive swelling (in water vapor) and drying cycles (in dry nitrogen vapor) the reproducibility of these processes is investigated. To further evaluate the effect of temperature, three individual experiments, all including three full swelling and drying cycles, at three different temperatures are performed. Figure 8.1 displays the schematic overview of the measurement protocol.

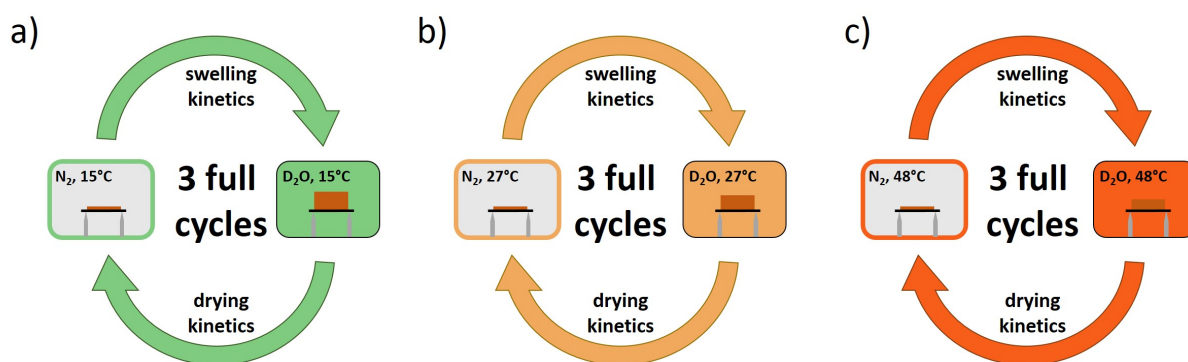


Figure 8.1.: Temperature-dependent cyclic thin film swelling and drying kinetics: Schematic representation of the performed experiments. Three full cycles of swelling in D₂O vapor and drying in N₂ vapor are performed at (a) 15 °C, (b) 27 °C, and (c) 48 °C. The equilibrated dry and swollen thin film states are probed with static ToF-NR measurements, the swelling and drying kinetics are followed *in-situ* with kinetic ToF-NR, SR, and FTIR measurements. The saturated D₂O vapor at 15 °C, 27 °C, and 48 °C is indicated in green, orange, and red, respectively. The dry vapor is colored in gray, the colored frame marks the ambient temperature. Adapted with permission from AMERICAN CHEMICAL SOCIETY, Copyright 2020 [38].

The selected measurement temperatures of 15 °C, 27 °C, and 48 °C differ from the temperature range, that is applied to the thin films in the previous Chapter 7. There, the known transition temperatures of the PSPP and PNIPMAM blocks, determined from aqueous solution, is taken as reference ($CP'_{\text{PSPP}_{\text{DBC}}} = 33.5 \text{ °C}$ and $CP_{\text{PNIPMAM}_{\text{DBC}}} = 49.5 \text{ °C}$). While the results clearly indicate a shift of the swelling and contraction temperature of PSPP and PNIPMAM in thin film geometry, it remains challenging to determine their exact positions. Furthermore, this present chapter is more driven toward potential future thin film applications. Therefore, the applied temperatures are set to a moderate range from 15 °C to approximately 50 °C, as this covers the common range of the majority of thin film applications.

The chapter is structured as follows: The equilibrated thin film states, probed with static time-of-flight neutron reflectivity (ToF-NR), are described first, then the swelling and contraction kinetics, followed *in-situ* with spectral reflectance (SR), kinetic ToF-NR, and Fourier-transform infrared spectroscopy (FTIR), are discussed. Special attention is given to reversibility and reproducibility of the swelling and drying kinetics, as well as to the comparability of the equilibrated states, with respect to the swelling degree and water content, and how the temperature affects both, the dynamic processes as well as the equilibrium states.

The ToF-NR measurements are conducted at the RefSANS instrument at the MLZ neutron source in Garching, Germany [218–220]. Details to the ToF-NR, SR, and FTIR techniques can be found in the Sections 3.2 and 3.3. *In-situ* measurements are realized by using customized sample environments, as described in the subsection 'Pre-existing experimental setup' in Section 3.4. The thin film samples, discussed in the following are prepared and pre-characterized according to Section 4.4. Details to the pre-characterization can be found in the Appendix D. A pre-characterization of the thin film samples is done via optical and atomic force microscopy, and x-ray reflectivity. All techniques reveal highly homogeneous and smooth thin films.

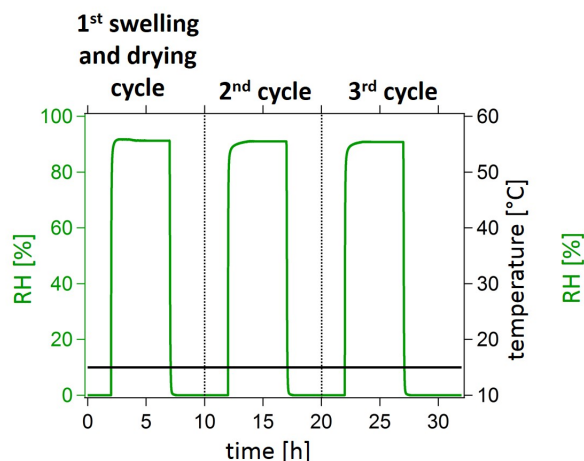
8.1. Comparability of the equilibrated swollen and dry thin film states

Throughout all swelling and contraction cycles, the RH and temperature inside the respective measurement chambers are monitored. Figure 8.2 displays them as a function of measurement time and demonstrates the highly reproducible evolution of the RH upon the three swelling and contraction cycles, here exemplified at a measurement temperature of 15 °C. This provides an excellent experimental basis for the following analysis, and shows the importance of a reliably performing sample environment. The RH and temperature

evolution during the swelling and drying cycles at 27 °C and 48 °C can be found in the Appendix [D](#).

Figure 8.2: RH and temperature during three swelling and drying cycles at 15 °C.

Both parameters, RH (green) and temperature (black), as a function of measurement time during three swelling and drying at 15 °C. The swelling and contraction cycles are labelled accordingly. The RH and T evolution during the swelling and drying cycles at 27 °C and 48 °C can be found in the Appendix [D](#). Adapted with permission from AMERICAN CHEMICAL SOCIETY, Copyright 2020 [\[38\]](#).



In order to get a first insight into the equilibrated states, the swollen and dry thin film states are probed with static ToF-NR. Figure [8.3](#) shows the obtained NR curves. Analogously to Chapter [7](#), the curves of the swollen thin film states are fitted with a four-layer model (SiO₂, one main polymer layer, and two D₂O enrichment layers at the substrate-polymer and the polymer-D₂O vapor interface), while the as-prepared states at 15 °C and 48 °C are fitted with a two-layer model (SiO₂, one polymer layer). The distribution of the as-prepared state at 27 °C is slightly heterogeneous, thus a three-layer model is applied (SiO₂, two polymer layers). The extracted film thickness and average thin film $\langle \text{SLD} \rangle$ values (denoted as SLD in the following) are listed in Table [8.1](#). Since the thin film behavior was found to strongly depend on the initial film thickness [\[74\]](#), particular attention is paid to achieving a similar initial film thickness of the three individual as-prepared thin films. The three samples feature an initial thickness of (63 ± 3) nm, (65 ± 3) nm, and (60 ± 2) nm. In order to rule out slight deviations and to provide a better comparability of the thin film states, the film thickness d is normalized to its initial thickness d_{ini} , which gives the swelling ratio d/d_{ini} . Also the SLD values of the as-prepared thin films are very similar, although they are slightly lower than the theoretical SLD of the DBC. This is due to residual H₂O molecules inside the thin film, as is also described in the previous chapters. From the measured thin film SLD, the D₂O content can be calculated according to Equation [2.13](#). In addition, the SLD profiles are obtained, which are plotted below the corresponding NR curves in Figure [8.3](#). The SLD profiles show a homogeneous and gradient-free polymer distribution of the as-prepared thin film states. Thus, all as-prepared states feature similar thin film conditions. which changes upon the first swelling cycle.

8.1. Comparability of the equilibrated swollen and dry thin film states

Table 8.1.: Film thickness (sum of all polymer layers), swelling ratio d/d_{ini} , average thin film SLD (integration over the respective SLD profiles), and D₂O content Φ extracted from the fits of the static ToF-NR measurements of the swollen and dry thin film states, shown in Figures 8.3 and 8.4.

swollen states				
	thickness	swelling	SLD	D ₂ O
	d [nm]	ratio d/d_{ini}	$[10^{-6} \text{ \AA}^{-2}]$	content Φ [V%]
15 °C				
first cycle	190 ± 4	3.02 ± 0.02	3.55 ± 0.05	47 ± 2
second cycle	194 ± 4	3.08 ± 0.02	3.51 ± 0.05	46 ± 2
third cycle	205 ± 4	3.25 ± 0.02	3.48 ± 0.04	46 ± 2
27 °C				
first cycle	110 ± 2	1.69 ± 0.02	3.05 ± 0.04	38 ± 2
second cycle	112 ± 2	1.72 ± 0.02	2.96 ± 0.04	36 ± 1
third cycle	111 ± 1	1.72 ± 0.02	3.00 ± 0.03	37 ± 2
48 °C				
first cycle	87 ± 2	1.45 ± 0.02	2.75 ± 0.02	32 ± 2
second cycle	87 ± 2	1.45 ± 0.02	2.75 ± 0.01	32 ± 1
third cycle	87 ± 1	1.45 ± 0.02	2.68 ± 0.02	31 ± 2
dry states				
15 °C				
as-prepared	63 ± 3	1.00 ± 0.04	0.91 ± 0.02	8 ± 1 (H ₂ O)
first cycle	63 ± 2	1.00 ± 0.03	1.37 ± 0.02	19 ± 2
second cycle	63 ± 2	1.00 ± 0.03	1.32 ± 0.03	18 ± 2
third cycle	63 ± 2	1.00 ± 0.03	1.31 ± 0.03	18 ± 2
27 °C				
as-prepared	65 ± 3	1.00 ± 0.05	0.85 ± 0.01	12 ± 2 (H ₂ O)
first cycle	65 ± 3	1.00 ± 0.05	1.37 ± 0.03	14 ± 2
second cycle	64 ± 4	0.98 ± 0.06	1.32 ± 0.03	12 ± 2
third cycle	65 ± 3	1.00 ± 0.05	1.31 ± 0.02	12 ± 2
48 °C				
as-prepared	60 ± 2	1.00 ± 0.03	0.90 ± 0.02	8 ± 1 (H ₂ O)
first cycle	63 ± 2	1.05 ± 0.03	1.25 ± 0.02	15 ± 2
second cycle	63 ± 3	1.05 ± 0.03	1.52 ± 0.03	18 ± 2
third cycle	61 ± 2	1.02 ± 0.03	1.38 ± 0.03	16 ± 2

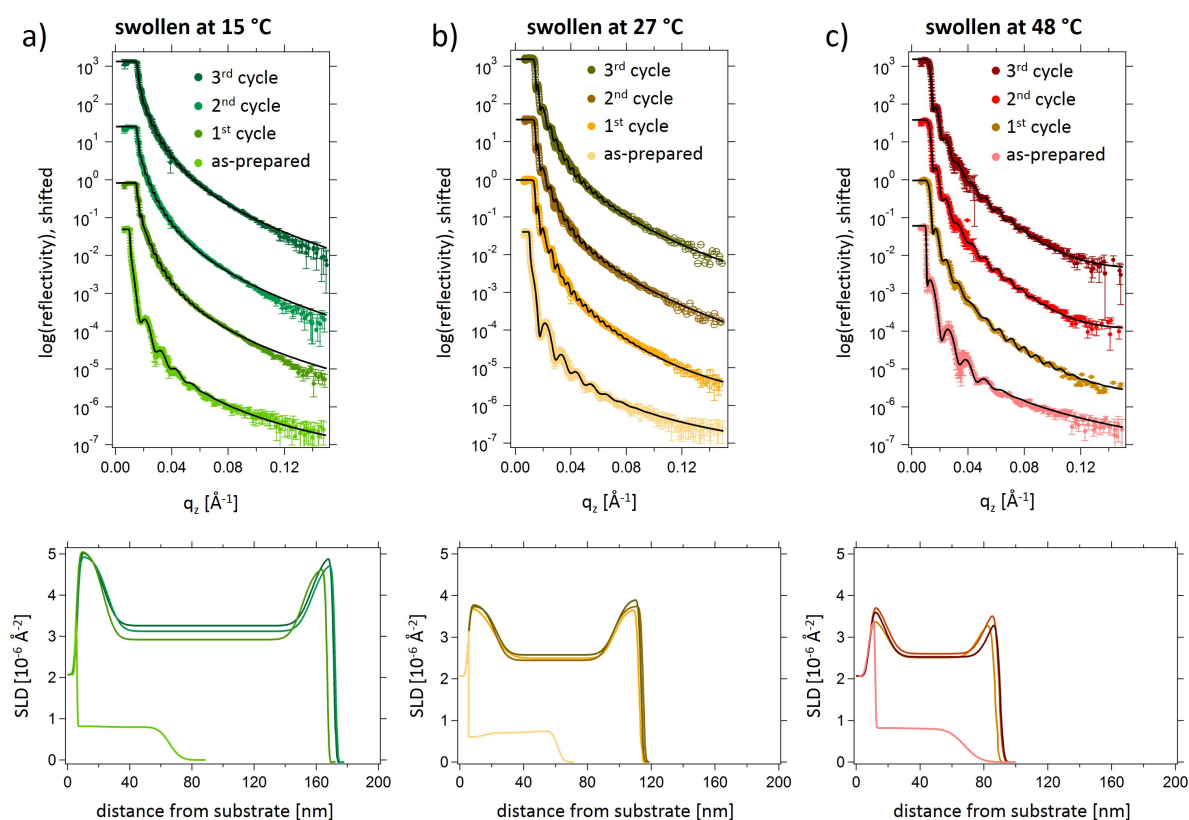


Figure 8.3.: Static ToF-NR measurements of the swollen thin film states. ToF-NR curves of the thin films in their swollen equilibrium states at (a) 15 °C, (b) 27 °C, and (c) 48 °C. The NR curve of the initial, dry and as-prepared thin film state is shown as reference. Best fits are achieved with a two-layer model for the as-prepared [38] state at 15 °C and 48 °C, with a three-layer model for the as-prepared state at 15 °C, and with a four-layer model for the swollen states at all temperatures (black lines). The corresponding SLD profiles are shown below the NR curves. Adapted with permission from AMERICAN CHEMICAL SOCIETY, Copyright 2020 [38].

All swollen thin films show a pronounced increase in film thickness and D₂O content, while with higher temperatures, the increase in thickness and water uptake is less pronounced. While this opposes the behavior found in aqueous solution [26], it confirms the findings from the previous Chapter [7]. Furthermore, D₂O enrichment layers appear independently of the temperature, in all swollen states at the substrate-polymer and the polymer-D₂O vapor interfaces. While the enrichment layer near the substrate is due to attractive interactions between D₂O and the hydrophilic SiO₂ layer (located on top of the Si substrate) [36, 67, 109], the enrichment layer at the polymer-D₂O vapor interface is referred to an accumulation of D₂O (due to the high RH) within the PSPP layer on top of the thin film as is also seen in the Chapter [7] (cf. Section [7.4]). Upon the individual swelling cycles at constant temperature, the thickness remains constant, however with

increasing temperature it becomes smaller. This indicates a hydrated PSPP matrix at lower temperature, which collapses and dehydrates, at least partly, at higher temperatures. Interestingly, the thickness of this enrichment layer at 48 °C is in a similar range as the hydrophilic PSPP shell around the hydrophobic PNIPMAM core in D₂O solution [(15 ± 2) nm] [26]. In addition, we found the highest swelling ratio and water content during each first swelling cycle at the respective temperatures. This hints to a slight hysteresis effect, which disappears after the first swelling and drying cycle. We mainly attribute this to an improved polymer conformation (regarding water uptake), after the first swelling process. The thin film preparation via spin-coating results in a non-equilibrated and kinetically frozen as-prepared thin film state, which equilibrates in the first swollen state due to an increased water content and polymer chain mobility. Such hysteresis effects were found to disappear after the first swelling cycle [282–284]. Apart from these small effects, highly reproducible swollen states are found at the corresponding temperatures.

Figure 8.4 shows the ToF-NR curves obtained from the thin films in their initial as-prepared and their re-dried states. The corresponding SLD profiles are shown below the respective NR curves. After each drying cycle, the thin films reach their initial film thickness. In contrast, the SLD values after each of the applied cycles, are significantly higher than the SLD value of the as-prepared state. Also, the SLD profiles reveal a pronounced heterogeneity, as in particular the SLD of the thin film center increases after the first full swelling/drying cycle. The increase in SLD may be due to residual D₂O molecules from the previous swelling processes. In addition, the polymer chains undergo a selective partial deuteration during swelling in D₂O vapor at the amide moieties, as is analogously described in the previous chapters. As a consequence, an increased deuterium content is present in the dry states, which results in an increased average thin film SLD. Interestingly, the regions near the substrate-polymer and the polymer-D₂O vapor interfaces undergo less dramatic changes as compared to the center of the thin films. This might be related to the D₂O enrichment layers, observed in the swollen states. The thin film can be seen as a physically connected hydrogel with a certain mesh size, which increases upon swelling. ToF-NR reveals a higher D₂O content near the interfaces, thus the mesh size there increases to a stronger degree, as compared to the center. Upon the subsequent drying, D₂O molecules are released from the thin films, leaving behind voids, which are filled with air. These voids are larger at the interfacial regions, thus leading to reduced SLD values.

In the following, the kinetic swelling and contraction processes, in-between the equilibrium states, are discussed, in order to find the origin of *e.g.*, the lower swelling degree and water content at higher temperatures, and the hysteresis of the first swelling cycle.

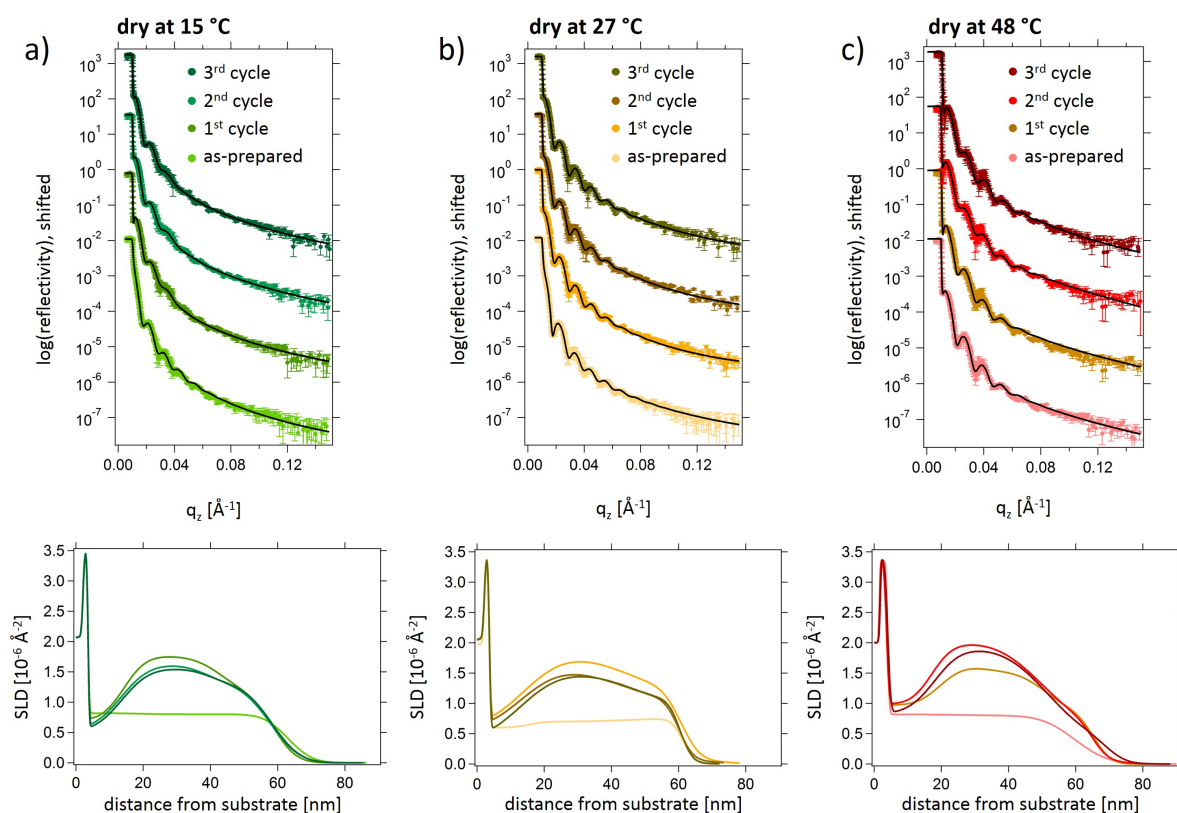


Figure 8.4.: Static ToF-NR measurements of the dry thin film states. ToF-NR curves of the thin films in their dry equilibrium states at (a) 15 °C, (b) 27 °C, and (c) 48 °C. The NR curve of the initial, dry and as-prepared thin film state is shown as reference. Best fits are achieved with a three-layer model, except for the as-prepared state at 15 °C and 48 °C, where a two-layer model is applied (black lines). The corresponding SLD profiles are shown below the NR curves. Adapted with permission from AMERICAN CHEMICAL SOCIETY, Copyright 2020 [38].

8.2. Temperature-dependent cyclic swelling behavior

The first part of this section describes the mesoscopic thin film swelling followed with ToF-NR and SR, while in the second part, FTIR complements the obtained results with molecular information about polymer-polymer and polymer-water interactions. In addition, a swelling model is applied to the data.

Film thickness and water content

The swelling ratio d/d_{ini} and the water content Φ during the three swelling cycles at 15 °C, 27 °C, and 48 °C are extracted from kinetic ToF-NR measurements. Selected kinetic NR curves with the corresponding fits (four-layer model) of each first swelling cycle at all temperatures are shown in Figure 8.5. Both extracted parameters are displayed in Figure

8.2. Temperature-dependent cyclic swelling behavior

8.6 as a function of the measurement time. Analogously to ToF-NR, the swelling kinetics are also followed with SR. Figure D.4 in the Appendix D shows the obtained swelling ratio of the thin films as a function of time.

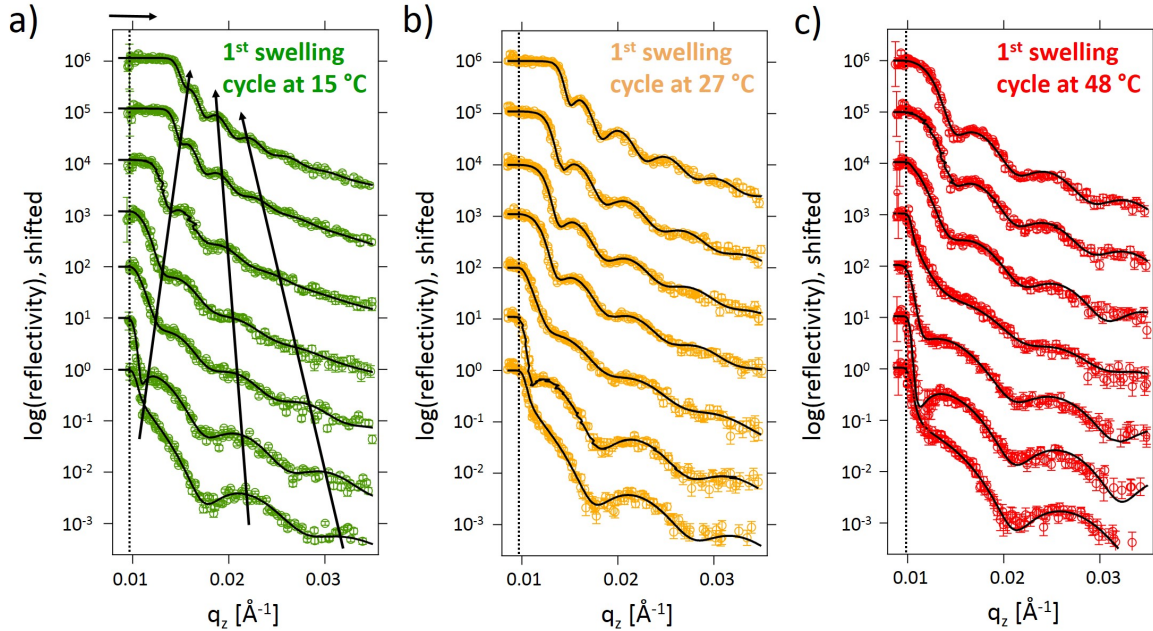


Figure 8.5.: Representative selection of ToF-NR curves for each first swelling cycle in D_2O vapor. Representative ToF-NR data (open circles) with best model fits (black lines) for each first swelling cycles at (a) 15 °C, (b) 27 °C, and (c) 48 °C. From bottom to top the measurement time increases: $t = 0.5, 2, 5, 8, 15,$ and 100 min. The ToF-NR curves are shifted along the y -axis for clarity. The dashed black line marks the critical edge of the as-prepared thin film. The black arrow on top of (a) exemplary marks the shift of the critical edge, while the black arrows inside the graph in (a) indicate the shift of the Kiessig fringes. Adapted with permission from AMERICAN CHEMICAL SOCIETY, Copyright 2020 [38].

In general, all thin films show a highly reproducible swelling behavior, as a comparable swelling ratio and D_2O content is reached after each swelling cycle. With respect to potential application, these are very promising results. In the following, the swelling kinetics are discussed in detail.

At higher temperatures, SR and ToF-NR yield a lower swelling ratio and water content, analogously to static ToF-NR measurements. This is due to a de-hydration of the PSPP block, as is also found Chapter 7. By comparing the final states of the individual swelling cycles, we observe a lower swelling ratio for each first swelling cycle, while the second and third swelling cycle reach a similar swelling degree. The same trend is seen for the water content, which is in good agreement with the results from static ToF-NR, and is referred to a changing polymer conformation during the first swelling cycle. Furthermore, each

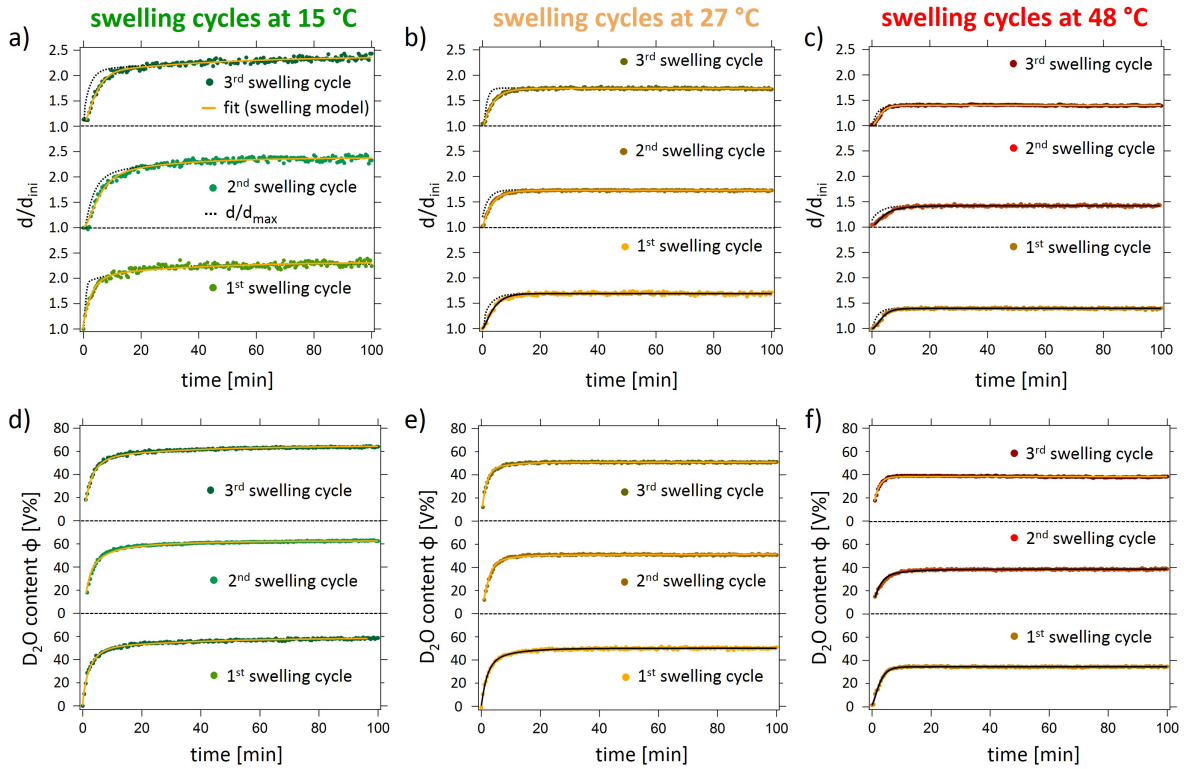


Figure 8.6.: Cyclic thin film swelling in D_2O vapor followed with ToF-NR *in-situ*. The (a-c) swelling ratio d/d_{ini} and (d-f) water content Φ as a function of measurement time during three swelling cycles at (a,d) 15 °C, (b,e) 27 °C, and (c,f) 48 °C. The cycle number increases from bottom (first swelling cycle) to top (third swelling cycle). A swelling model is applied to the data as explained in the main text (solid lines, the color switches between brown and black for better visibility). In addition to the swelling ratio, the maximum swelling ratio d_{max}/d_{ini} is plotted [dashed black lines in (a-c)]. Adapted with permission from AMERICAN CHEMICAL SOCIETY, Copyright 2020 [38].

second and third swelling cycle start with a non-zero amount of D_2O inside the films. Thus, during drying, some D_2O molecules remain inside the films. Deuteration of the polymer chains, which results in an increased deuterium content also contributes to this observation.

By applying a swelling model to the evolution of the swelling ratio and the water content the swelling kinetics are quantified. Section 2.1.2 provides a detailed introduction to the swelling model. From the model, the effective interaction parameter χ_{eff} and the time τ are extracted, which describe polymer-water interaction and the time scale of the occurring swelling processes. Please note, all χ_{eff} and τ values discussed in the following refer to the first swelling cycle at the respective temperature unless stated otherwise. All values are listed in Table 8.2.

Table 8.2.: Swelling model applied to the SR and ToF-NR data shown in Figures ^aD.4 and ^b8.6

D ₂ O swelling	SR ^a			
	χ_{eff}	τ [min]		
15 °C				
first cycle	0.60 ± 0.02	30 ± 1		
second cycle	0.62 ± 0.02	28 ± 2		
third cycle	0.61 ± 0.03	31 ± 1		
27 °C				
first cycle	0.91 ± 0.02	20 ± 1		
second cycle	0.92 ± 0.01	20 ± 1		
third cycle	0.92 ± 0.03	22 ± 2		
48 °C				
first cycle	1.12 ± 0.04	16 ± 1		
second cycle	1.08 ± 0.04	17 ± 1		
third cycle	1.09 ± 0.03	17 ± 1		
kinetic ToF-NR^b				
	determined from d/d_{ini}		determined from Φ	
	$\chi_{eff}(d/d_{ini})$	$\tau(d/d_{ini})$	$\chi_{eff}(\Phi)$	$\tau(\Phi)$
		[min]		[min]
15 °C				
first cycle	0.32 ± 0.02	11 ± 1	0.14 ± 0.01	12 ± 1
second cycle	0.32 ± 0.01	10 ± 1	0.15 ± 0.01	13 ± 1
third cycle	0.33 ± 0.01	10 ± 1	0.14 ± 0.02	13 ± 1
27 °C				
first cycle	0.52 ± 0.01	7 ± 1	0.42 ± 0.02	6 ± 1
second cycle	0.54 ± 0.01	6 ± 1	0.41 ± 0.03	5 ± 1
third cycle	0.52 ± 0.01	6 ± 1	0.41 ± 0.02	6 ± 1
48 °C				
first cycle	0.65 ± 0.03	6 ± 1	0.55 ± 0.02	5 ± 1
second cycle	0.66 ± 0.02	6 ± 1	0.55 ± 0.03	4 ± 1
third cycle	0.66 ± 0.02	6 ± 1	0.54 ± 0.02	4 ± 1

All extracted χ_{eff} values, from the evolution of the swelling ratio (SR and ToF-NR) and water content (ToF-NR) increase at higher temperatures, which corroborates the lower swelling ratio and water content at higher temperatures. In contrast, the extracted τ values are lower at higher temperatures, indicating a faster water uptake. This is due to a reduced water uptake, *i.e.*, less water is absorbed faster. Furthermore, the parameters extracted from the swelling ratio are smaller than the parameters extracted from the water content, which suggests a slower increase in film thickness as compared to the water uptake. This is mainly attributed to air voids within the thin film. These voids are filled first, which leads to an increase in water content, while the thin film is not increasing in thickness. Once they are filled, further water uptake also leads to a swelling of the films. This is in good agreement with the previous chapters. Interestingly, the difference between these values becomes larger during the second and the third swelling cycles. An explanation might be the widening of the polymeric network, in particular at the interfacial areas due to D₂O enrichment layers. As a consequence, the voids become larger, and filling them with water takes longer times. Also, the changed polymer chain conformation after the first swelling cycle might contribute to this effect.

In addition, to the swelling ratio and the model fit, Figure 8.6a-c displays the maximum swelling ratio d_{max}/d_{ini} , which describes the theoretical limit of the swelling ratio at a given RH and χ_{eff} . At early stages of the swelling cycles, a significant offset between the measured and the maximum swelling ratio is observed. This identifies the diffusion as limiting factor until both curves merge, which happens relatively fast (after ≈ 10 min). At this point, the swelling process is limited by the RH. This is in good agreement with the evolution of the RH, shown in Figure 8.2, as after 10 min, the RH is already above 90% and increases only slowly until it equilibrium is reached.

Polymer-water interactions

FTIR measurements yield insights into the polymer-water interactions and how they are affected by multiple swelling/drying cycles. Since an individual FTIR measurement takes approximately 7 min, *in-situ* measurements are enabled by artificially decelerating the RH increase within the FTIR measurement chamber. The resulting FTIR spectra at 15 °C are imaged in Figure 8.7. The obtained FTIR spectra upon each first swelling cycle at 15 °C, 27 °C, and 48 °C can be found in Figure 8.7.

Two very pronounced absorption peaks arise at around 2500 and 3400 cm⁻¹, which are assigned to the O-D and the O-H stretching vibration, respectively. Both modes consist of several sub-bands that correspond to various types of water molecules, *i.e.*, water that is bound by H- (or D-) bonds to the polymer chain, hydrophobic hydration water, or freely moving water [244, 245]. In-between those two peaks, a three-fold peak is located, which

8.2. Temperature-dependent cyclic swelling behavior

corresponds to the symmetric and the asymmetric C-H stretching vibrations of the CH_3 group and the asymmetric C-H stretching vibration of the CH_2 group. Since these CH_3 and CH_2 groups remain mostly unaffected by the swelling process, the FTIR spectra are normalized to these, in order to account for slightly different film thicknesses.

Figure 8.8 displays the normalized integrated areas of the O-D and O-H peaks, which indicate the D_2O and H_2O content as a function of time during the swelling cycles at 15°C , 27°C , and 48°C . A close-up of the O-D and O-H peaks is visible in Figure 8.9. All thin films exhibit a highly reproducible swelling behavior, as a comparable final water content is reached after each swelling cycle. Thus, also on a molecular level, the thin films are suited for potential applications. While the final states are very similar, the mechanisms within the individual cycles strongly differ. This is described and discussed in detail in the following.

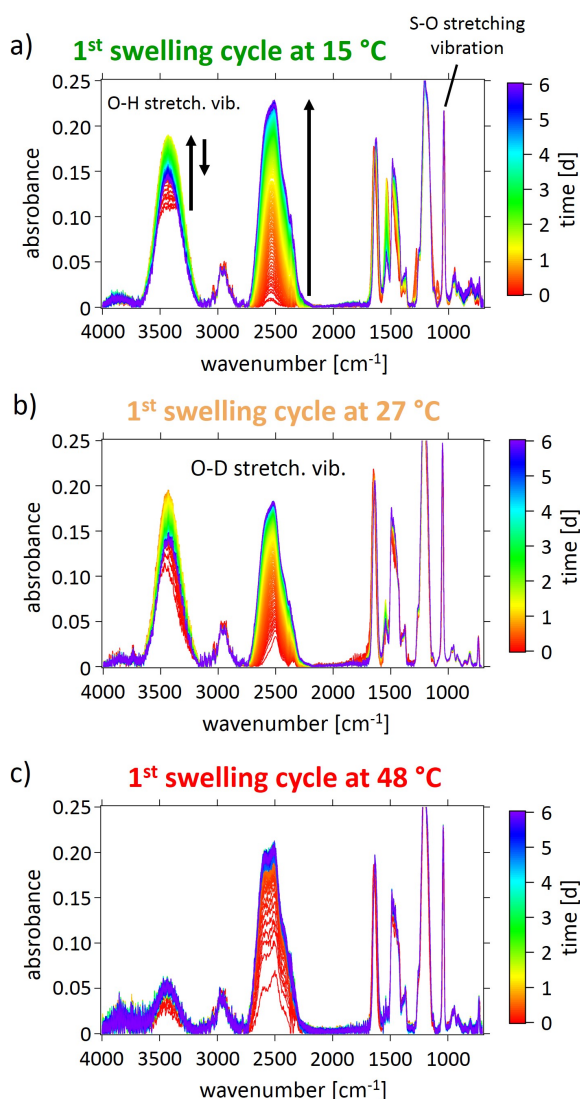


Figure 8.7: The first swelling cycles in D_2O vapor at different temperatures followed with FTIR *in-situ*. FTIR spectra of each first swelling cycle at (a) 15°C , (b) 27°C , and (c) 48°C . The red curve marks the initial ($t = 0$ d) measurement, the purple curve marks the final measurement ($t = 6$ d). Characteristic absorption peaks are labelled accordingly. Black arrows mark the increase and decrease of the O-H and the O-D stretching vibration. The FTIR spectra of the corresponding second and third swelling cycles can be found in the Appendix D. Adapted with permission from AMERICAN CHEMICAL SOCIETY, Copyright 2020 [38].

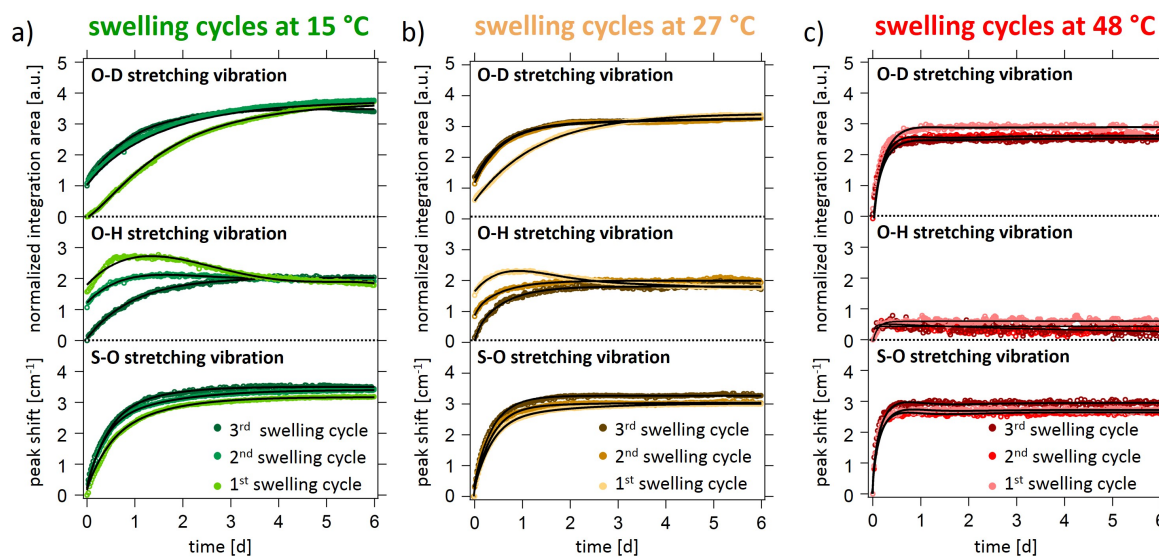


Figure 8.8.: Integration areas and peak shift extracted from FTIR spectra during three swelling cycles in D_2O vapor at different temperatures. The normalized integration areas of the O-D (top row) and the O-H peaks (mid row), as well as the peak shift of the symmetric S-O peak (bottom row) upon three swelling cycles at (a) $15\text{ }^\circ\text{C}$, (b) $27\text{ }^\circ\text{C}$, and (c) $48\text{ }^\circ\text{C}$ are extracted from the FTIR spectra (close-ups) shown in Figure 8.9. The areas indicate the H_2O (O-H peak) and D_2O (O-D peak) content during the swelling cycles. All curves as a function of time are fitted with the swelling model (black line) as explained in the main text. Adapted with permission from AMERICAN CHEMICAL SOCIETY, Copyright 2020 [38].

The normalized area of the O-D stretching vibration increases over time, as D_2O molecules diffuse into the thin film, while the final equilibrated areas decrease with increasing temperature. That means, with increasing temperature less D_2O molecules are present within the thin film, which is consistent with the ToF-NR and SR data. One has to note, this trend is not as pronounced as in the ToF-NR experiments. Noticeable, we observe a considerable difference between the first and the following second and third swelling cycles at $15\text{ }^\circ\text{C}$ and $27\text{ }^\circ\text{C}$. The D_2O uptake during each first swelling cycle is significantly slower than during the second and the third cycle, indicating a changing polymer conformation during the first swelling cycle. A similar behavior is also observed with ToF-NR and thus, a fully reproducible behavior, on the meso- and nanoscale is established once the thin film undergoes one full swelling/drying cycle.

At higher temperatures, the water uptake decreases, while the uptake itself takes shorter times. In particular, the water uptake at $48\text{ }^\circ\text{C}$ is very fast and furthermore, no differences between the first and the following second and third swelling cycles are observed, which is mainly addressed to the short diffusion pathways.

8.2. Temperature-dependent cyclic swelling behavior

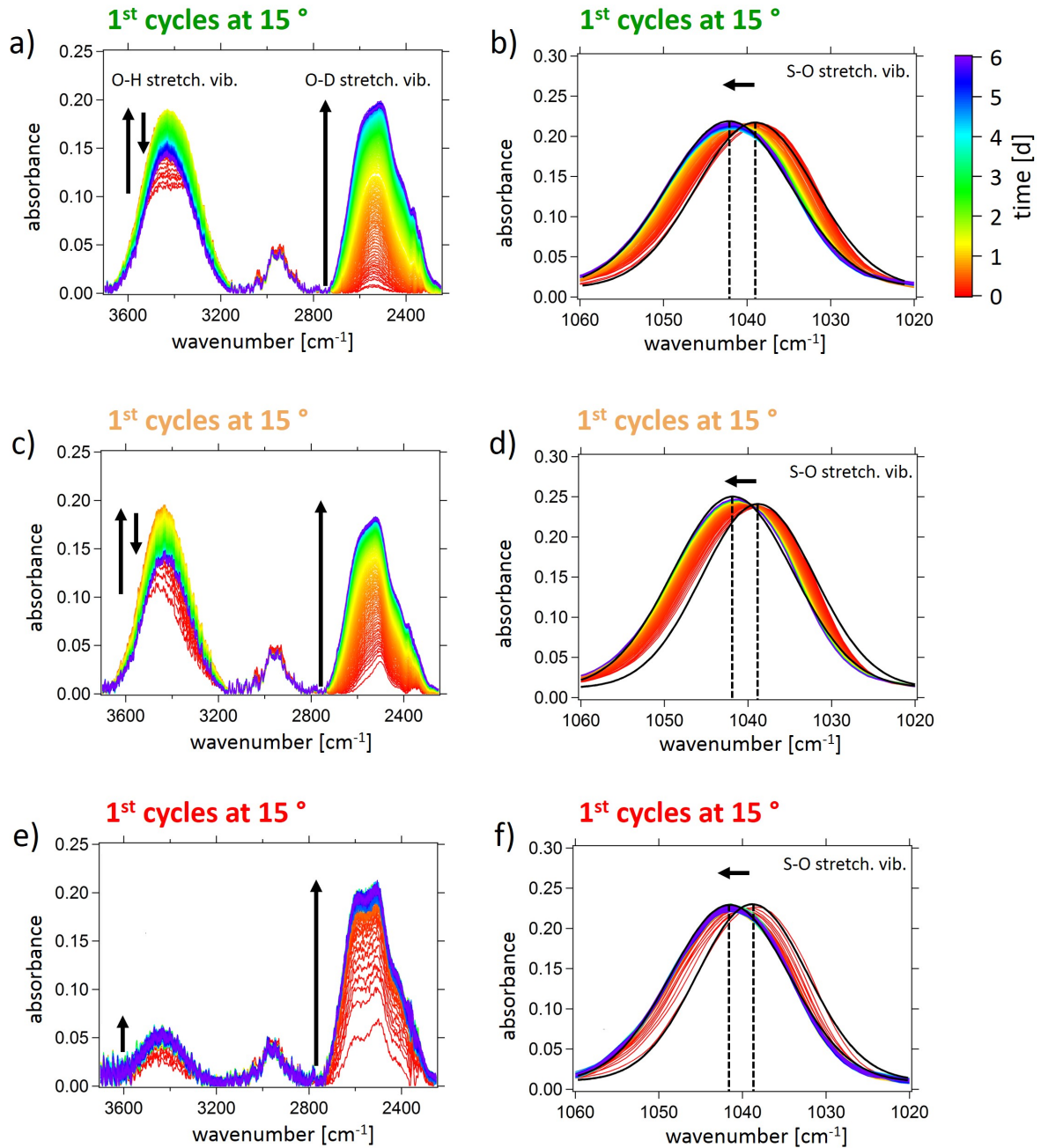


Figure 8.9.: Close-ups of absorption peaks of each first swelling cycle at 15 °C, 27 °C, and 48 °C. (a-c) O-H, O-D, and (d-f) S-O stretching vibrations are labelled accordingly. Black arrows indicate (a-c) increasing and decreasing absorption or (d-f) shifting peak maxima. A Gaussian fit (applied to all FTIR curves) is shown in (d-f) as black line for each first and final absorption peak. Dashed black lines indicate the peak maxima.

The swelling model, introduced in the previous ToF-NR section is also applied to the FTIR data. All χ_{eff} and τ values extracted during the swelling cycles are listed in Table

8.3. With increasing temperature, the analysis of the O-D peak yields higher $\chi_{eff}(\text{O-D})$ and lower $\tau(\text{O-D})$ values, indicating a lower but faster water uptake at higher temperatures. Furthermore, at 15 °C and 27 °C the first swelling cycle takes the longest time, while the second and third swelling cycle are considerably shorter. This underlines the assumption stated earlier. The polymer chain conformation changes during the first swelling cycle, which eventually promotes the water uptake in the following swelling cycles. Interestingly, at the beginning of the second and third swelling cycles, the non-zero integration area of the O-D peak indicates the presence of D₂O molecules, which can also be seen in the ToF-NR data.

Table 8.3.: Swelling model applied to the FTIR data shown in Figure 8.8a (top and mid row).

	FTIR			
	determined from		determined from	
	<i>O – D</i> stretch.	vib. ^a	<i>O – H</i> stretch.	vib. ^b
	$\chi_{eff}(\text{O-D})$	$\tau(\text{O-D})$	$\chi_{eff}(\text{O-H})$	$\tau(\text{O-H})$
15 °C				
first cycle	0.51 ± 0.03	3.1 ± 0.2	0.45 ± 0.02	2.4 ± 0.2
second cycle	0.51 ± 0.02	2.7 ± 0.1	0.44 ± 0.02	1.6 ± 0.02
third cycle	0.53 ± 0.02	2.8 ± 0.1	0.44 ± 0.02	1.6 ± 0.02
27 °C				
first cycle	1.02 ± 0.04	1.8 ± 0.1	0.95 ± 0.03	1.8 ± 0.2
second cycle	1.01 ± 0.04	1.3 ± 0.1	0.94 ± 0.02	1.1 ± 0.02
third cycle	1.00 ± 0.05	1.3 ± 0.1	0.95 ± 0.02	1.1 ± 0.02
48 °C				
first cycle	1.22 ± 0.06	0.5 ± 0.1	1.13 ± 0.04	0.1 ± 0.03
second cycle	1.22 ± 0.07	0.5 ± 0.1	1.12 ± 0.03	0.1 ± 0.03
third cycle	1.24 ± 0.05	0.5 ± 0.1	1.12 ± 0.03	0.1 ± 0.03

The thin film behavior at 48 °C deviates from the behavior at lower temperatures. Water uptake is limited and diffusion pathways are very short. As a consequence, no difference in $\tau(\text{O-D})$ values is observed within the first and the following second and third swelling cycle, as is the case at 15 °C and 27 °C. Furthermore, no D₂O molecules are present in the beginning of the second and third swelling cycles, which suggests, all D₂O molecules are released during the drying processes, most likely due to the extremely low water uptake during swelling and the short diffusion pathways.

8.2. Temperature-dependent cyclic swelling behavior

At 15 °C and 27 °C the O-H peak features a significant different evolution than the O-D peak. A clear O-H signal is detected in the as-prepared state (prior to the first swelling cycle), which corresponds to initially present H₂O molecules. Upon the first swelling cycle, the integration area further increases, reaches a maximum after approximately one day, decreases, and equilibrates after 3.5 d. The initial increase is due to deuteration processes, *i.e.*, the absorbed D₂O molecules deuterate the amide groups of the PSPP and PNIPMAM blocks. As a consequence, HDO molecules are generated, which contribute to the increasing O-H peak. Besides deuteration, an exchange of the protonated water species H₂O and HDO by D₂O molecules is occurring in the thin film. While at early stages, deuteration is more dominant, this changes upon an increasing D₂O content within the thin films. The maximum in integration area marks the time, when the exchange outperforms the deuteration and the generation of HDO molecules. Subsequently, the O-H peak decreases, which means, more H₂O and HDO are released from the film than HDO is generated. Eventually, the equilibrated O-H peak indicates, both competing processes also have equilibrated. During the second and third swelling cycle, the O-H peak evolution changes, as prior to the second swelling cycle less H₂O and HDO molecules, and prior to the third swelling cycle, no H₂O and HDO molecules are present within the thin film. Furthermore, its initial increase slows down with increasing cycle number, as the O-H peak reaches equilibrium after approximately 1.5 and 3.5 d during the second and third swelling cycle, respectively. This suggest a slowed down deuteration rate upon the individual cycles, while the exchange of H₂O and HDO by D₂O molecules is still ongoing. Surprisingly, the equilibrium state after all three swelling cycles is similar. Thus, the amount of applied swelling cycles alters the deuteration and exchange mechanisms, however it does not affect the final equilibrium state, which reflects the final ratio of different water species in the thin films. While the evolution of the O-H peak is the result of two opposing effects, deuteration and the exchange of H₂O and HDO molecules by D₂O, both of these effects are governed by the diffusion process of D₂O into the thin film. Therefore, the swelling model can be applied. The obtained parameters are listed in Table [8.3](#).

Larger $\chi_{eff}(\text{O-D})$ values are obtained at higher temperatures, which follows the trend of the $\chi_{eff}(\text{O-D})$ values obtained earlier and thereby, confirming the decreased water compatibility of the DBC with increasing temperature. Interestingly, the $\chi_{eff}(\text{O-D})$ values are slightly lower than the $\chi_{eff}(\text{O-D})$ values at the corresponding temperatures, which hints toward a higher affinity of the DBC to H₂O as compared to D₂O. This is in agreement with findings from the previous chapters, in particular with Chapters [5](#) and [6](#). Also, the obtained $\tau(\text{O-H})$ values follow the trend of the $\tau(\text{O-D})$ values, as they are lower at higher temperatures, which indicates a faster equilibration of the thin films. In addition, at 15 °C

and 27 °C the first swelling cycle is found to take the longest time. Again, this is ascribed to an improved chain conformation, with respect to water uptake, during the second and third swelling cycle. Moreover, prior to the first swelling cycle, the amide groups are fully protonated, which naturally leads to a maximum deuteration rate and a high amount of HDO molecules present in the films. As a result, the second and third swelling cycle yield lower $\tau(\text{O-H})$ values. The trend of the extracted values changes dramatically for the swelling cycles at 48 °C, as a rapid but small increase in integration area of the O-H peak is observed for all three swelling cycles. Also, all cycles yield similar $\tau(\text{O-H})$ and $\chi_{eff}(\text{O-D})$ values. This underlines, a very fast but very low deuteration rate throughout all swelling cycles. Apparently, deuteration effects become negligible at a very low D₂O content.

In contrast to the integration of the O-D and O-H peaks, which indicates the amount of water inside the thin films, a peak maximum shift indicates a change in local interaction of characteristic groups of the DBC with water. A very sharp peak arises at roughly 1040 cm⁻¹, which is due to the symmetric S-O stretching vibration of the SO₃⁻ group. This group is located at the end of the PSPP side chain and plays a key role in the water uptake and release mechanism. In the recent chapters, we found a deviating behavior in the local hydration of this group and the hydration of the average thin film, regarding the affinity to different water species, and the time scales of hydration. While usually this group is the first one that is hydrated upon water swelling, it features a lower affinity to water as compared to the general affinity of the DBC toward water. The bottom row of Figure 8.8 displays the S-O peak shift as a function of time during the three swelling cycles at 15 °C, 27 °C, and 48 °C. A close-up of the S-O stretching vibration is provided in Figure 8.9. The strongest shift is observed for the swelling at 15 °C, while at 48 °C the shift is the lowest, however the difference in the peak shift is not very pronounced. This indicates a similar hydration at all temperatures. Thus, the hydration behavior of individual characteristic groups, does not necessarily follow along with the hydration of the general thin film.

In contrast to peak shift amount, the time scale on which the shift occurs, changes significantly. At higher temperatures, the peaks shift faster, which is due to the shorter diffusion pathways at higher temperatures. Thus, the lower water compatibility of the DBC at higher temperatures has an effect on how fast but not on how strong the SO₃⁻ group is hydrated. This conclusion is supported by the swelling model. All obtained parameters are listed in Table 8.4. While $\chi_{eff}(\text{S-O})$ values increase with temperature, $\tau(\text{S-O})$ values decrease. This confirms the lower water compatibility of the DBC as well as the faster hydration at higher temperatures. Furthermore, the obtained $\tau(\text{S-O})$ values

8.3. Temperature-dependent cyclic drying behavior

are considerably lower than the $\tau(\text{O-D})$ and $\tau(\text{O-H})$ values, which underlines the very fast hydration around the SO_3^- group in comparison to the remaining polymer chain.

	FTIR	
	determined from	
	$S - O$ stretch. vib. ^a	
	$\chi_{eff}(\text{S-O})$	$\tau(\text{S-O})$ [min]
15 °C		
first cycle	0.31 ± 0.03	91 ± 4
second cycle	0.31 ± 0.02	92 ± 5
third cycle	0.33 ± 0.02	90 ± 5
27 °C		
first cycle	0.73 ± 0.05	57 ± 3
second cycle	0.73 ± 0.04	57 ± 3
third cycle	0.75 ± 0.04	55 ± 4
48 °C		
first cycle	0.98 ± 0.05	26 ± 3
second cycle	1.01 ± 0.05	24 ± 3
third cycle	0.99 ± 0.06	24 ± 2

Table 8.4: Swelling model applied to the FTIR data shown in Figure 8.8 (bottom row).

8.3. Temperature-dependent cyclic drying behavior

The thin film drying kinetics are followed with kinetic ToF-NR *in-situ*. The contraction process is induced by decreasing the RH to 0% (cf. Figure 8.2). Analogously to the swelling cycles, the obtained NR curves are fitted with a four-layer model (SiO_2 , one main polymer layer, and two D_2O enrichment layers). Figure 8.10 provides a selection of NR curves together with the model fits of each first drying cycle at 15 °C, 27 °C, and 48 °C, while Figure 8.11 shows the extracted swelling ratio d/d_{ini} and water content Φ .

Each first drying cycle features a slightly lower initial swelling ratio and water content as compared to the consecutive second and third cycles. This is due to the first swelling cycles, which equilibrated at lower swelling degrees. Since, the DBC has a lower water compatibility at higher temperatures, we expect an accelerated thin film contraction with increasing temperature. While at 15 °C the thin film features the slowest contraction process, the fastest contraction occurs at 27 °C. The applied swelling model confirms the observed trend (cf. Table 8.5).

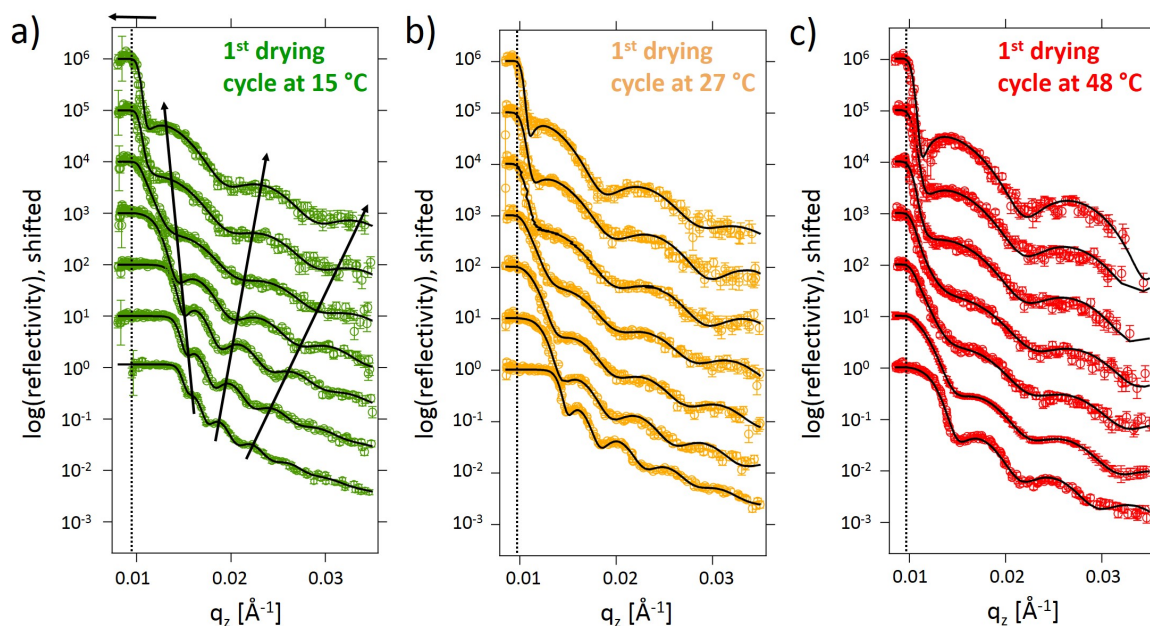


Figure 8.10.: Selected ToF-NR curves during the first drying cycle. Representative ToF-NR data (open circles) with best model fits (black lines) for the first drying cycles at (a) 15 °C, (b) 27 °C, and (c) 48 °C. From bottom to top the measurement time increases: $t = 0.5, 10, 20, 30, 45, 60,$ and 100 min, except for the shown drying cycle at 27 °C, where the measurement time increases from bottom to top according to $t = 0.5, 1.5, 3, 5, 8, 10,$ and 100 min. The ToF-NR curves are shifted along the y -axis for clarity. The dashed black line marks the critical edge of the as-prepared thin film. The black arrow on top of the graphs indicates the shift of the critical edge, while the black arrows inside the graphs indicates the shift of the Kiessig fringes. Adapted with permission from AMERICAN CHEMICAL SOCIETY, Copyright 2020 [38].

The obtained $\tau(d/d_{ini})$ and $\tau(\Phi)$ values indicate the fastest thin film contraction and water release at 27 °C, while these processes are the slowest at 15 °C and occur on an intermediate time scale at 48 °C. In contrast to that, $\chi_{eff}(d/d_{ini})$ and $\chi(\Phi)$ values indicate a decreasing water compatibility of the DBC at higher temperatures, thereby following the expected trend. It should be noted, the χ_{eff} values obtained from the swelling and drying cycles (at the same temperature) differ from each other. Since they are extracted by analyzing either the swelling or the drying process, they refer to water uptake or water release, which is accompanied with a swelling or a contraction of the thin film. Thus, they are compared with each other only within the respective dynamic process, swelling or drying. In addition, the χ_{eff} parameter excludes interactions between the substrate and the DBC, and therefore it cannot be seen as an absolute Flory-Huggins parameter. For that reason, the focus rather lies on the obtained trend of the χ_{eff} than on its absolute values. The unexpected trend is also observed during the swelling cycles, where

8.3. Temperature-dependent cyclic drying behavior

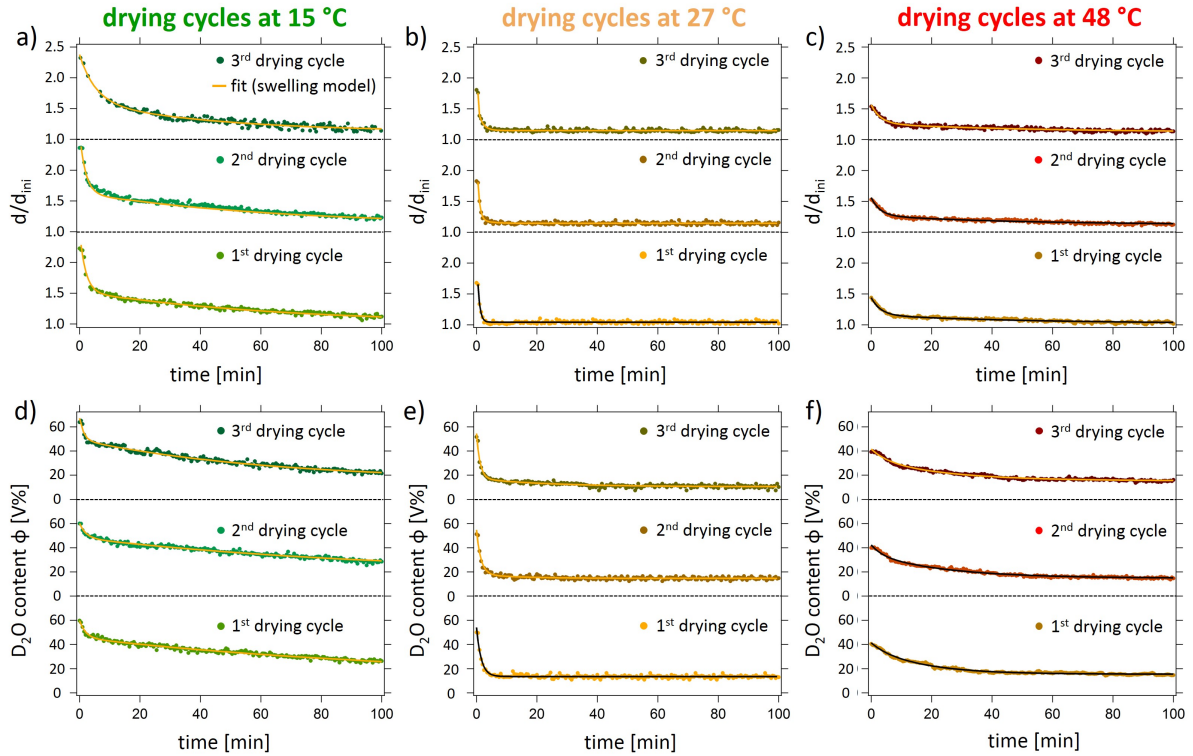


Figure 8.11.: Cyclic thin film drying in N_2 vapor followed with ToF-NR *in-situ*. The (a-c) swelling ratio d/d_{ini} and (d-f) water content Φ as a function of measurement time during three drying cycles at (a,d) 15 °C, (b,e) 27 °C, and (c,f) 48 °C. The cycle number increases from bottom (first swelling cycle) to top (third swelling cycle). A swelling model is applied to the data as explained in the main text (solid lines, the color switches between brown and black for better visibility). Adapted with permission from AMERICAN CHEMICAL SOCIETY, Copyright 2020 [38].

the swelling and the water uptake, takes the longest at 15 °C, but occurs on a similar time scale at 27 °C and 48 °C, even though, at higher temperatures, water compatibility of the DBC thin film is reduced, and therefore, the diffusion pathways are shorter. Upon drying, this trend is even more pronounced, as the contraction process occurs faster at 27 °C as compared to 48 °C. It seems, a temperature of 27 °C represents optimal conditions for a fast water uptake and in particular water release. A possible explanation could be a changing thin film morphology upon temperature change (cf. Chapter 7). Diffusion pathways are shorter at 27 °C than at 15 °C due to the de-hydration of the PSPP matrix. Assuming, water is absorbed and released from the thin film via the hydrophilic DBC part, the thin film at 27 °C bears better conditions for water uptake and release than at 48 °C, since there the PSPP matrix is in a more collapsed state. Thus, the temperature of

Table 8.5.: Swelling model applied to the ToF-NR data shown in Figure [8.11](#)

	kinetic ToF-NR ^a			
	determined from d/d_{ini}		determined from Φ	
	$\chi_{eff}(d/d_{ini})$	$\tau(d/d_{ini})$ [min]	$\chi_{eff}(\Phi)$	$\tau(\Phi)$ [min]
15 °C				
first cycle	0.91 ± 0.03	21 ± 2	1.08 ± 0.04	35 ± 4
second cycle	0.92 ± 0.04	22 ± 3	1.09 ± 0.04	36 ± 4
third cycle	0.89 ± 0.04	21 ± 3	1.09 ± 0.03	36 ± 3
27 °C				
first cycle	1.11 ± 0.04	6 ± 1	1.31 ± 0.04	10 ± 1
second cycle	1.08 ± 0.03	8 ± 2	1.29 ± 0.04	9 ± 1
third cycle	1.08 ± 0.03	8 ± 1	1.29 ± 0.03	10 ± 1
48 °C				
first cycle	1.21 ± 0.05	15 ± 1	1.42 ± 0.04	24 ± 1
second cycle	1.18 ± 0.05	14 ± 2	1.42 ± 0.05	24 ± 1
third cycle	1.20 ± 0.06	14 ± 2	1.39 ± 0.04	23 ± 2

27 °C might provide balanced conditions between short diffusion pathways and a sufficient water compatibility, in order to achieve a fast water uptake and release.

It is noteworthy that similar to the swelling cycles, also during the drying cycles, the τ values differ dependent on whether they are obtained from the swelling ratio or the water content. This trend is independent from the temperature. During all drying cycles, the film thickness decreases faster than the water content, which can be seen as an inversion of the swelling cycles, where the water content increases faster than the film thickness. Immediately after drying is induced, water release leads to a decrease in film thickness, until only the aforementioned voids are still filled with water. The release of water from these voids further reduces the water content, while the thin film thickness already is close to equilibrium. In the final dried thin film states, residual water is still present inside the thin film, even though the RH is decreased to 0%, whereas the swelling ratio returns to roughly its initial value. Thus, also the contraction processes feature a very reproducible behavior and demonstrate the reliable reversibility of the swelling processes.

8.4. Conclusion

The present chapter describes the behavior of the orthogonally dual thermo-responsive PSPP₅₀₀-*b*-PNIPMAM₁₅₀ thin films upon three full swelling and drying cycles at 15 °C, 27 °C, and 48 °C. At all temperatures, the thin films feature a reversible dynamic swelling and drying processes, and reproducible swollen and dry states, respectively. During each first swelling cycle at the different temperatures, the polymer chain conformation changes, which leads to a further improved water uptake capacity. In addition, the thin film behavior can be tuned by a change in temperature, as higher temperatures result in a decreased swelling degree and water uptake. A temperature of 27 °C is found to be optimal for a fast water uptake and release, which is due to a superposition of short diffusion pathways and a sufficient compatibility of the DBC toward water. Thus, the thin films are highly suited for potential future application, *e.g.*, as artificial muscles in the field of soft robotics.

While the equilibrated swollen and dried thin film states exhibit a high reproducibility, the mechanisms of the individual swelling cycles on a molecular level, differ considerably from each other. Various dynamic processes *e.g.*, deuteration, exchange of different water species, and deviating hydration mechanisms, result in a complex interplay of different water species, D₂O, H₂O, and HDO, and eventually to changing swelling mechanisms, dependent on the cycle number. In particular the deuteration as well as the exchange of H₂O and HDO by D₂O, weakened with increasing cycle number, and are expected to fully vanish at some point. A swelling model is applied to the data and the quantitative analysis confirms the decreased water compatibility of the DBC at higher temperatures, as well as the deviating swelling mechanisms on a molecular level.

The presented results provide valuable insights into the temperature-dependent cyclic swelling and drying behavior of orthogonally dual thermo-responsive DBC thin films. While in particular the repeated swelling mechanisms differ on a molecular level, the final swollen, and re-dried states feature high similarities, regarding their swelling degree, water content, and hydration. Although a change in chain conformation during the first swelling cycle is found, an aging process and a decreased water storage ability are not observed. The present chapter clearly demonstrates the potential of such thin films and puts the findings into context to the previous results.

9. Thermal behavior of 'salty' thin films

The following chapter is largely based on a the publication 'Salt Dependent Phase Transition Behavior of orthogonally Thermo-Responsive Poly(sulfobetaine)-Based Diblock Copolymer Thin Films' (L. P. Kreuzer et al., *Langmuir* **2021**, 37, 9179–9191; DOI: 10.1021/acs.macromol.0c02281) [285]. Reprinted with the permission from AMERICAN CHEMICAL SOCIETY, Copyright 2021. Experiments were partly performed in collaboration with bachelor student Christoph Lindenmeir [249].

The previous chapters provide a detailed description of the swelling and thermal behavior of orthogonally thermo-responsive poly(sulfobetaine)-based DBC thin films and demonstrate how effects, such as a high polymer concentration, dominant polymer-polymer interactions, and interfacial effects shape the thermal response of polymer thin films. While in these chapters, one single external stimulus is applied, which is either a changing vapor composition or temperature, the present chapter focuses on two stimuli in parallel, namely temperature and the addition of salt. Therefore, we address the question in how far the presence of salt alters the swelling behavior of orthogonally dual thermo-responsive DBC thin films in dependency of temperature, while special attention is given to a potential superposition and interference of the two applied stimuli.

Introduction

Recent studies demonstrated a strong sensitivity of poly(sulfobetaine)s in solution toward small amounts of added salts, in particular to NaCl and NaBr, which led to a decreased clearing point (CP'_{PSBP}) [127, 242, 273]. Dependent on the monomer architecture, this effect was not linearly correlated in all cases. While for some poly(sulfobetaine)s, the CP'_{PSBP} decreased linearly, it was also found that CP'_{PSBP} first increased at low salt concentrations, and decreased after reaching a maximum [20, 26, 27, 31, 127–130, 235, 242]. In particular, chaotropic anions, according to the Hofmeister series (cf. Section 2.2.1) affected the CP'_{PSBP} significantly. Recently, the effect of monovalent salts, such as NaCl and NaBr, on the solution and self-assembly behavior of orthogonally thermo-responsive DBCs was investigated, that bear a poly(sulfobetaine) and a poly(*N*-isopropylmethacrylamide) (PNIPMAM) block. It was found that the salt alters exclusively the CP'_{PSBP} , while the

cloud point PNIPMAM (CP_{PNIPMAM}) remained relatively stable upon an increasing salt concentration [26, 27, 31, 235]. Thus, the self-assembly behavior in solution was strongly tunable [25-27, 31, 235]. Since in solution, the interplay between salt and temperature enabled in total four different aggregation states as well as phase transitions, these DBCs are highly suited for applications in the field of drug-delivery, emulsification, and smart rheology [28, 29, 103].

The DBC under investigation in this chapter, consists of a zwitterionic poly(4-((3-(methacrylamidopropyl) dimethylammonio) butane-1-sulfonate) (PSPP) block and a non-ionic PNIPMAM block (PSBP₂₄₅-*b*-PNIPMAM₁₀₅). Its chemical structure can be found in Figure 4.2f in Section 4.2. In the following it is referred to as PSBP-*b*-PNIPMAM. In salt-free D₂O solution (50 g L⁻¹), PSBP-*b*-PNIPMAM featured a LCST-type transition at 47 °C, which is addressed to the PNIPMAM block. An analogous UCST-type transition of the PSBP block was not resolved, which suggested a CP'_{PSBP} above 47 °C [31]. This assumption was underlined, by the CP'_{PSBP} of the corresponding PSBP homopolymer (identical molar mass), which in salt-free D₂O solution exceeded 100 °C [273]. At higher NaBr concentrations (≈ 10 mM), the CP'_{PSBP} of the PSBP block was observable and shifted to lower temperatures with rising NaBr concentration. At NaBr concentrations of approximately 15 mM (and higher), the CP'_{PSBP} eventually fell below the CP_{PNIPMAM} [31].

In total, four thin films are prepared by spin-coating DBC salt solutions of different NaBr concentrations ranging from 0 to 20 mM (0, 2, 10, and 20 mM). Based on the polymer concentration in the spin-coating solution (25 g L⁻¹) as well as on the polymer block ratio, this yields thin films with NaBr contents of 0-29 mol% per zwitterionic monomeric group (0, 2.9, 14.5, and 29 mol%). One should add here, that with stoichiometric amounts of NaBr, PSBs form homogeneous and glassy blends in the bulk phase [21, 286]. In order to follow the salt-dependent swelling and thermal thin film behavior, the following measurement protocol is applied. First, the initially dried thin films are exposed to saturated D₂O vapor at 15 °C, before the temperature is increased with a heating rate of + 5 K h⁻¹. After an equilibration period of 2 h, the temperature is reduced again with a cooling rate of - 5 K h⁻¹. While the thin films in their respective equilibrated states (stage I, III, V, and VII) are probed with static time-of-flight neutron reflectivity (ToF-NR), the dynamic swelling, heating, and cooling processes (stage II, IV, and VI) are followed with spectral reflectance (SR), kinetic ToF-NR, and Fourier-transform infrared spectroscopy (FTIR) *in-situ*. The protocol is schematically imaged in Figure 9.1.

The chapter is structured as follows: The static, equilibrated thin film states are described first. Then, the thin film kinetics during the swelling in D₂O vapor and subsequent during the heating and cooling processes are discussed. There, the mesoscopic informa-

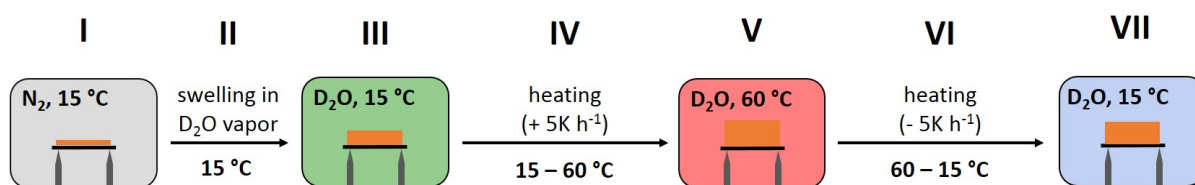


Figure 9.1.: Thermal behavior of 'salty' thin films: Schematic representation of the performed experiments. The swelling in D_2O vapor is followed by a heating ($+ 5 K h^{-1}$) and cooling ramp ($- 5 K h^{-1}$). The thin film states in equilibrium (stage I, III, V, and VII) are probed with static ToF-NR, while the thin film kinetics of the swelling (stage II), the heating (stage IV), and the cooling (stage VI) processes are followed with kinetic ToF-NR, SR, and FTIR *in-situ*. The initial dry N_2 , and the D_2O vapors at $15^\circ C$, $60^\circ C$, and $15^\circ C$ (cooled) are indicated in gray, green, red, and blue, respectively. Adapted with permission from AMERICAN CHEMICAL SOCIETY, Copyright 2021 [285].

tion obtained with SR and ToF-NR are complemented with the molecular findings from the FTIR measurements. In particular, the thermal response of the individual polymer blocks as a function of the salt concentration is of high interest, while the chapter also focuses on a potential superposition of the two applied stimuli.

ToF-NR measurements are performed at the RefSANS instrument at the MLZ neutron source in Garching, Germany [218–220]. Details to the ToF-NR, SR, and FTIR techniques can be found in the Sections 3.2 and 3.3. For realizing *in-situ* measurements, specialized sample environments are used. The swelling, heating, and cooling processes are induced by a custom-made gas flow setup and a thermal bath. Section 3.4 provides a detail description of the used setups. The thin film samples, discussed in the following are prepared according to Section 4.4. A pre-characterization of the thin film samples is done via optical and atomic force microscopy, and x-ray reflectivity. All techniques reveal highly homogeneous and smooth thin films. Details can be found in the Appendix E.

9.1. Investigation of the equilibrated thin film states

Throughout all experiments, the temperature and relative humidity (RH) within the corresponding measurement chambers (ToF-NR/SR and FTIR) are tracked. Both parameters as a function of measurement time are plotted in Figure 9.2. The RH shifts slightly and very slowly to lower values during the heating (approximately 6%) and shifts back to its initial value during the cooling. Since these changes are monotonic and slow, they are not considered to affect the thermal behavior of the thin films. Still, they are taken into account for the analysis.

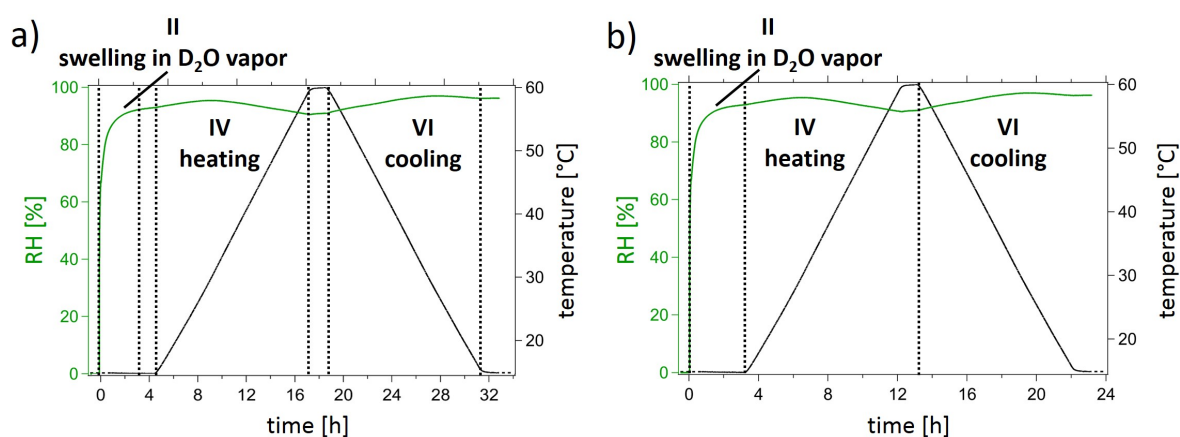


Figure 9.2.: RH and temperature during swelling in water vapor and the subsequent heating and cooling processes. Both parameters, RH (green) and temperature (black), are plotted as a function of time for the (a) ToF-NR and (b) FTIR measurement chamber. The thin film stages are labelled according to Figure 9.1. Adapted with permission from AMERICAN CHEMICAL SOCIETY, Copyright 2021 [285].

The equilibrated dry and swollen states (stage I, III, V, and VII in Figure 9.1) are probed with static ToF-NR measurements to get a first impression about the swelling behavior upon changing salt content and temperature. The obtained NR curves are imaged in Figure 9.3. Fitting the ToF-NR data yields film thickness and the average $\langle \text{SLD} \rangle$ (denoted as SLD in the following), which is transformed into a water content according to Equation 2.13 in Section 2.1.2. A two-layer model is used for the curves of the dry thin film states (SiO_2 and one main polymer layer), while for the curves of the swollen thin film states a three-layer model is applied (SiO_2 layer, one main polymer layer, and one D_2O enrichment layer near the Si substrate). The extracted thin film characteristics are listed in Table 9.1.

Since the film thickness has a significant impact on the swelling behavior [74], particular attention is paid to achieving similar initial film thicknesses [(42 ± 1) nm, (51 ± 2) nm, (56 ± 2) nm, and (45 ± 2) nm]. The film thickness is normalized to the initial value d_{ini} , resulting in a swelling ratio d/d_{ini} , in order to facilitate the comparison of the swelling, heating, and cooling kinetics. Interestingly, the theoretically calculated SLD ($1.02 \times 10^{-6} \text{ \AA}^{-2}$) value of the pure DBC, is higher than the SLD values of the dried DBC thin films [($\approx 0.77 \pm 0.01$) $\times 10^{-6} \text{ \AA}^{-2}$] [182]. This is due to residual H_2O molecules located within the thin films, even at low RH values close to 0%. Besides these values, the fitting routine also yields the SLD profiles, which gives detailed information about the vertical thin film composition. The profiles are provided in Figure 9.4

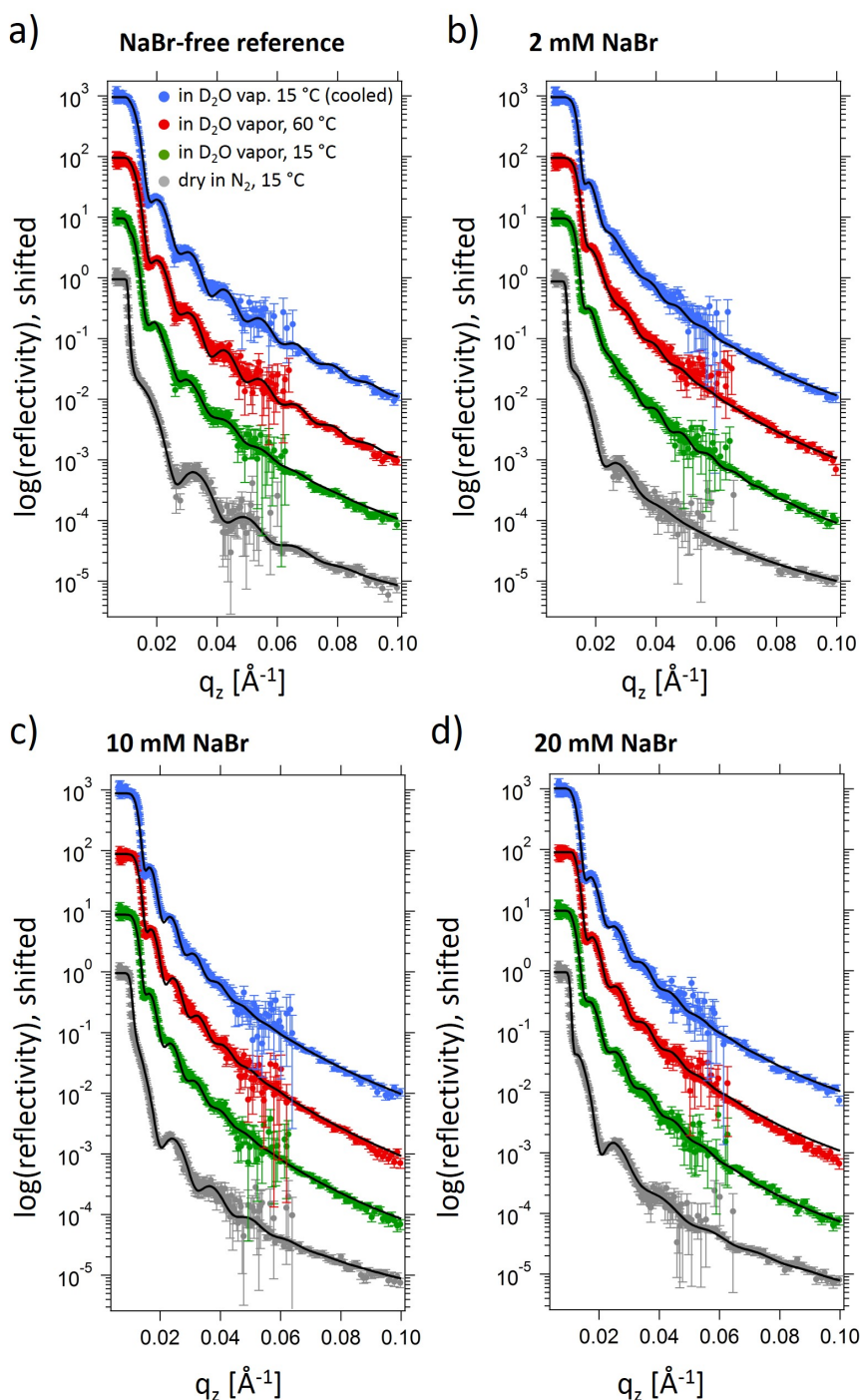


Figure 9.3.: Static ToF-NR measurements. ToF-NR curves of the equilibrated dry (gray), and the swollen states after the swelling in D_2O vapor (green), heating (red), and cooling (blue) for the thin films spin-coated from (a) NaBr-free, (b) 2 mM, (c) 10 mM, and (d) 20 mM NaBr solution. Best fits are achieved with a two-layer model for the dry states and with a three-layer model for all swollen states. For better visibility the q_z range is set from 0.005 - 0.100 \AA . The NR curves over the full q_z range can be found in the Appendix E. Adapted with permission from AMERICAN CHEMICAL SOCIETY, Copyright 2021 [285].

Table 9.1.: Film thickness d (sum of all polymer layers) normalized to the initial film thickness d_{ini} , SLD (integration of the respective SLD profiles), and D_2O content Φ extracted from the fits of the static ToF-NR measurements as is shown in Figure 9.3.

^aThe given values correspond to the NaBr concentration of the respective spin-coating solutions.

[NaBr] ^a	dry - 15 °C			swollen - 15 °C		
	d_{ini} [nm]	SLD [10^{-6} \AA^{-2}]	Φ [V%]	d/d_{ini}	SLD [10^{-6} \AA^{-2}]	Φ [V%]
NaBr-free	42 ± 1	0.78 ± 0.01	—	1.30 ± 0.01	2.74 ± 0.02	34 ± 1
2 mM	51 ± 2	0.77 ± 0.01	—	1.35 ± 0.01	2.85 ± 0.02	36 ± 1
10 mM	56 ± 2	0.78 ± 0.01	—	1.40 ± 0.01	3.02 ± 0.02	39 ± 1
20 mM	45 ± 2	0.77 ± 0.02	—	1.40 ± 0.01	3.03 ± 0.02	39 ± 2
	swollen - 60 °C			swollen - 15 °C - cooled		
	d/d_{ini}	SLD [10^{-6} \AA^{-2}]	Φ [V%]	d/d_{ini}	SLD [10^{-6} \AA^{-2}]	Φ [V%]
NaBr-free	1.33 ± 0.01	3.03 ± 0.02	39 ± 2	1.31 ± 0.01	2.88 ± 0.01	36 ± 2
2 mM	1.38 ± 0.01	3.08 ± 0.04	40 ± 2	1.36 ± 0.01	2.92 ± 0.01	37 ± 3
10 mM	1.42 ± 0.01	3.23 ± 0.04	43 ± 1	1.40 ± 0.01	3.01 ± 0.02	40 ± 3
20 mM	1.43 ± 0.01	3.24 ± 0.03	43 ± 2	1.41 ± 0.02	3.03 ± 0.03	40 ± 2

The dried thin films feature a homogeneous polymer distribution (stage I – gray lines). Upon swelling in D_2O vapor, the average SLD increases, whereas near the Si substrate D_2O enrichment layers are formed, due to attractive interactions between the native hydrophilic SiO_2 layer on top of the Si substrate and D_2O molecules. This is in good agreement with literature, as well as with previous results [36, 67, 109]. The thickness of these enrichment layers remains stable throughout the heating and cooling, while their SLD values changes.

Also the swollen films feature a homogeneous polymer distribution along the surface normal, except the D_2O enrichment layer near the substrate. Since inaccessible with NR, a lateral microphase separation structure might have formed and would require *e.g.*, grazing-incidence small-angle neutron scattering (GISANS) for detection. The lowest SLD value of the enrichment layers is reached after the swelling in D_2O vapor at 15 °C (stage III), while the enrichment layers exhibit the highest SLD value after the heating at 60 °C (stage V). Therefore, they follow along with the trend of the average thin film SLD and water content, respectively (cf. Table 9.1).

After the swelling in D_2O vapor (stage III), all thin films feature a strongly increased film thickness and D_2O content, which even further increases after the heating to 60 °C (from

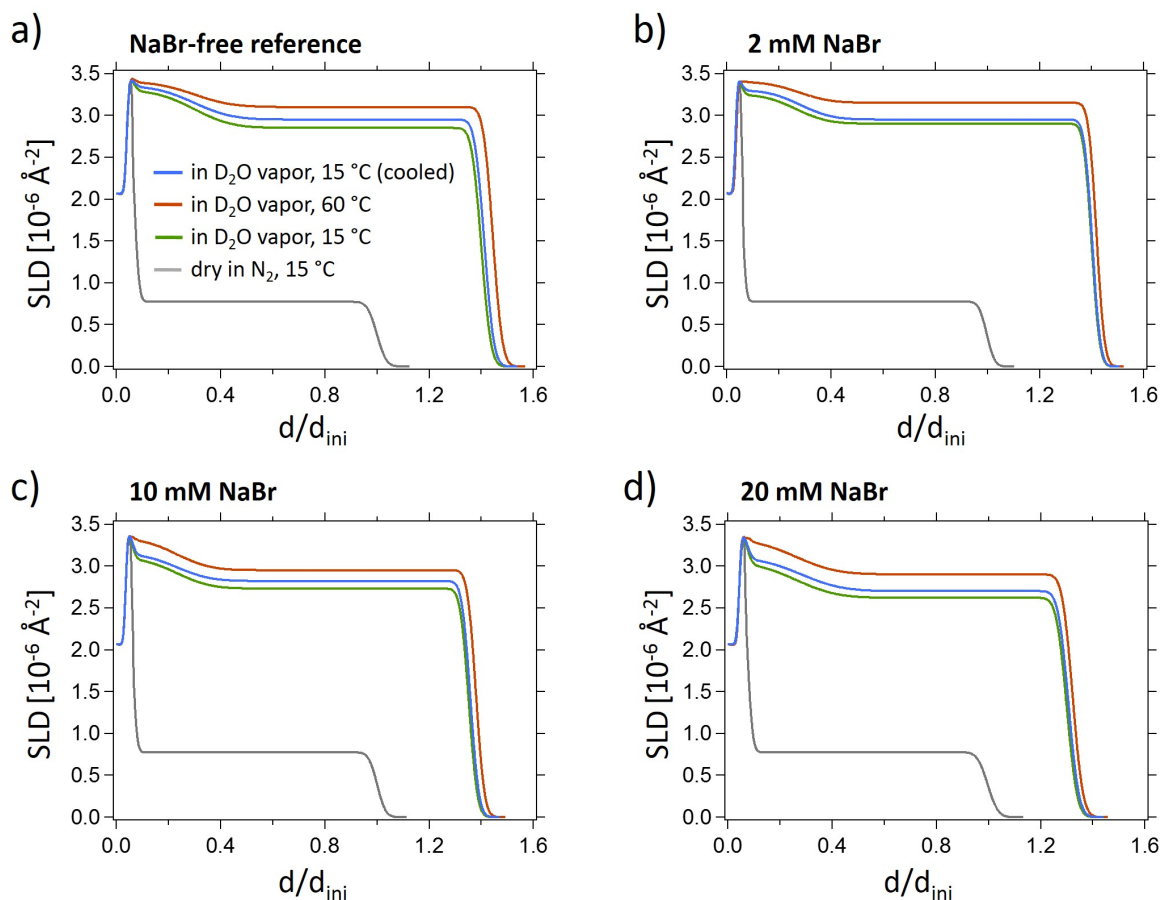


Figure 9.4.: SLD profiles of the dry and the swollen thin films loaded with different salt contents. SLD profiles of the thin films spin-coated from (a) NaBr-free, (b) 2 mM, (c) 10 mM, and (d) 20 mM NaBr solution in their dry state at 15 °C (gray) and their swollen states at 15 °C (green), 60 °C (red), and 15 °C - cooled (blue). Adapted with permission from AMERICAN CHEMICAL SOCIETY, Copyright 2021 [285].

stage III to V). Thus, the water compatibility of the thin films is higher at 60 °C than at 15 °C, which might be due to a crossing of the CP'_{PSBP} . Since the terms cloud and clearing points refer to a polymer solution, in the following 'swelling temperature' and 'collapse temperature' will be used. After cooling back to 15 °C (stage VII), D_2O is released from the films, and also the thickness decreases, thus the inversed behavior is found compared to the heating process. One has to note, after the cooling, both, the thickness and the water content are slightly higher as compared to the swollen thin films before the heating, which is at the same temperature of 15 °C. This indicates a slight thermal hysteresis, which was previously found in similar polymer thin film systems [38, 282-284]. A similar behavior, although during cyclic swelling and drying at a constant temperature is described in Chapter 8. Foremost, the first heating/cooling cycle as well as the first

swelling/drying cycle, yields slightly different final thin film states, regarding thickness and water uptake. With ongoing cycling, these differences eventually vanish, which is mainly addressed to kinetically trapped polymer chains, due to the spin-coating process. These chains thermodynamically equilibrate during swelling. The swelling ratio d/d_{ini} and water content Φ are plotted as a function of NaBr concentration (of the respective spin-coating solution) in Figure 9.5.

While qualitatively, all thin films behave similarly and follow the trends described above, quantitatively, the added NaBr content markedly enhances the absolute amount of incorporated D_2O and the resulting swelling ratio. This effect reaches its maximum strength in the thin film prepared from 10 mM NaBr solution, as the thin film from 20 mM NaBr solution reaches a similar water content and film thickness. This is visualized by an exponential fit in Figure 9.5. Hence, the thin films, spin-coated from 10 mM and 20 mM NaBr solution, exhibit a similar water compatibility at the corresponding states and temperatures. Since the addition of salt does not affect the transition temperature of PNIPMAM, this observed effect is mainly referred to an increased water compatibility of the PSB block. One should add here, the addition of 20 mM NaBr might not be sufficient to cross the swelling temperature of the PSBP block. Since the polymer transition might be distributed over a large temperature range (as is also seen in Chapter 7), the approaching of the swelling temperature might already increase the water compatibility and lead to a partly swollen state of the PSBP block, which would explain the found results.

9.2. Salt-dependent swelling and phase transition behavior

The swelling and the subsequent thermal behavior of the thin films loaded with different NaBr concentrations are followed with ToF-NR and FTIR *in-situ*. First, the results from ToF-NR are described, subsequently, the FTIR results are discussed.

Film thickness and water content

Kinetic ToF-NR measurements give details about the thin film behavior in-between the equilibrated states. In particular, the mechanisms of possible phase transitions are of interest. Selected representative NR curves together with the fits are shown in Figure 9.6.

Analogously to the static ToF-NR measurements, the swelling ratio d/d_{ini} and the water content Φ of the respective thin films are extracted from the fits. They are plotted in Figure 9.7 as a function of time during the swelling in D_2O vapor (stage II), the heating (stage IV), and the cooling process (stage VI). Figure 9.7a also shows the swelling

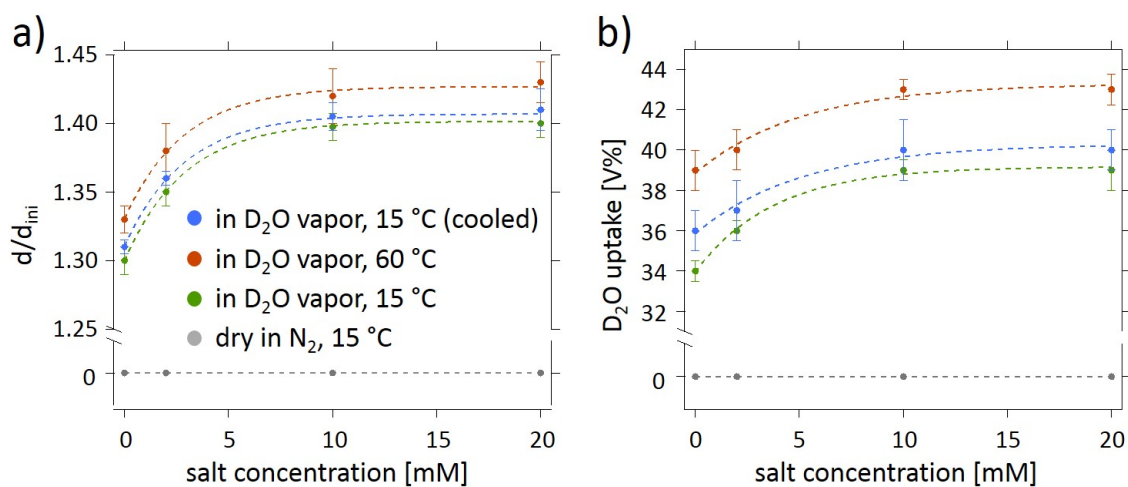


Figure 9.5.: Results from static ToF-NR measurements plotted as function of salt concentration. Swelling ratio d/d_{ini} and D₂O content Φ of the thin films as a function of the salt concentration in their dry state at 15 °C (gray) and their swollen states at 15 °C (green), 60 °C (red), and 15 °C - cooled (blue). The dotted lines are the corresponding exponential fits to the data as described in the main text. Adapted with permission from AMERICAN CHEMICAL SOCIETY, Copyright 2021 [285].

ratio obtained from simultaneous SR measurements. The SR data is consistent with the ToF-NR data. The time window in which no kinetic ToF-NR data points are plotted, correspond to the static ToF-NR measurements, which roughly takes 2 h to measure and during which the conditions, *i.e.*, temperature and RH, are kept constant.

The kinetic data confirm the results obtained from static ToF-NR measurements, regarding the highest swelling ratio and water content at 60 °C (stage V) and the slightly higher swelling ratio and water uptake at 15 °C (stage VII) after the cooling as compared to before the heating (stage III). In-between those equilibrium states, the kinetic ToF-NR measurements reveal that strong, non-monotonic changes in film thickness and water content occur. Upon swelling in D₂O vapor, the thin films significantly increase in film thickness, reaching a swelling ratio of up to 1.4, which corresponds to a strong D₂O uptake of approximately 40 V%. During heating, the thin films first undergo a contraction at around 17 °C, before they re-swell again beyond approx. 50 °C, which may be explained by individual phase transitions of the two polymer blocks. Presumably, the PNIPMAM block collapses first, which results in a contraction of the whole polymer thin film, before the PSBP block swells and the thin film re-swells again with further temperature increase. The results are roughly in line with our expectations of a higher collapse and a lower swelling temperature of the PNIPMAM and PSBP block, respectively, as compared

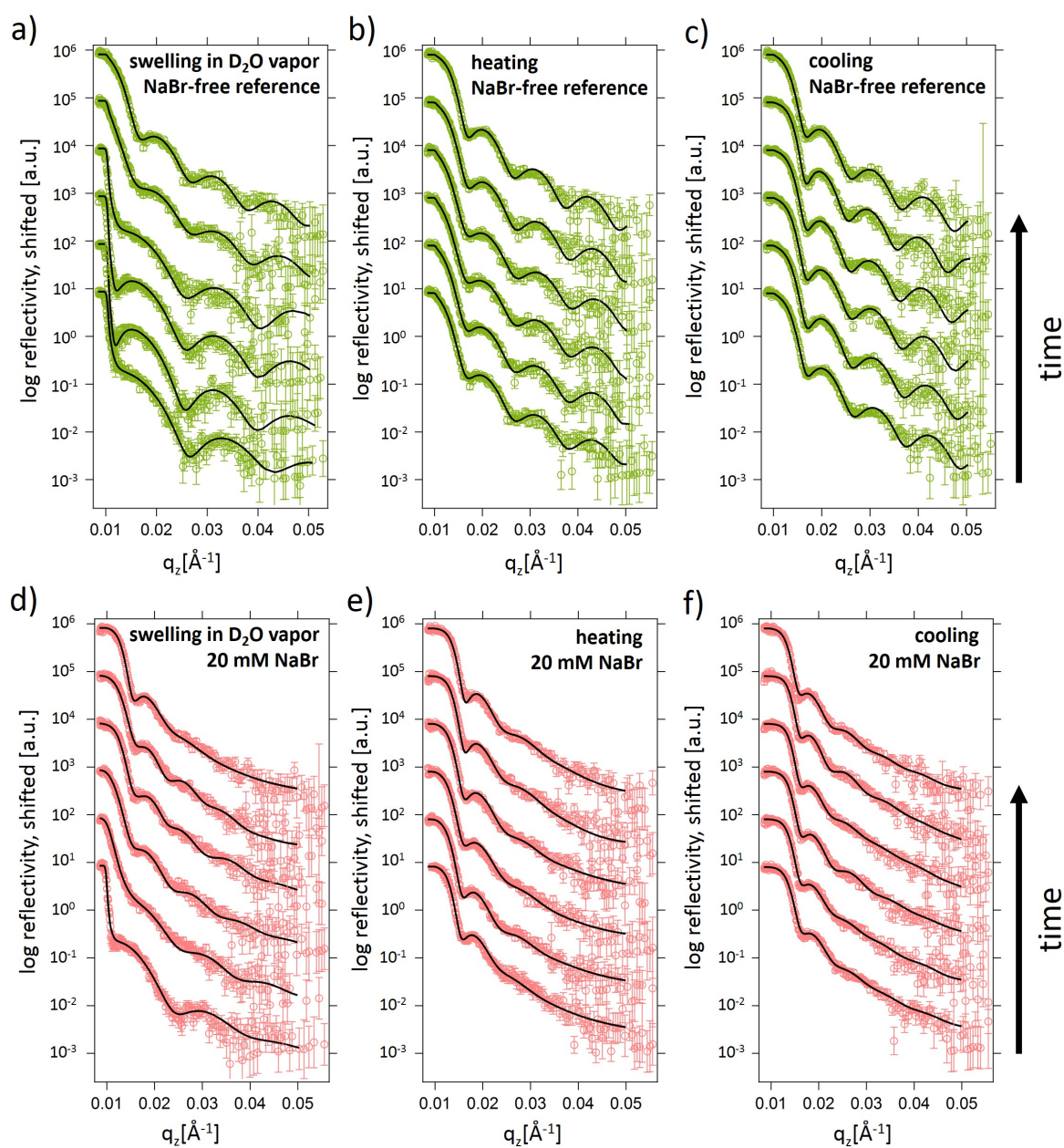


Figure 9.6.: Representative selection of ToF-NR curves for the swelling in D₂O vapor, heating, and cooling. Representative ToF-NR data (open circles) are shown with best model fits (black lines) for the thin films spin-coated from (a-c) NaBr-free and (d-e) 20 mM NaBr solution, during the (a,d) swelling in D₂O vapor, (b,e) heating, and (c,f) cooling. For the swelling in D₂O vapor, the selected curves (bottom to top) are taken at $t = 0.5, 2, 15, 45, 90,$ and 180 min, while for both heating and cooling, the selected curves (bottom to top) are taken at $t = 0.5, 60, 180, 300, 420,$ and 540 min. Selected ToF-NR curves for the thin films spin-coated from 2 and 10 mM NaBr solution are provided in the Appendix [E](#). Adapted with permission from AMERICAN CHEMICAL SOCIETY, Copyright 2021 [\[285\]](#).

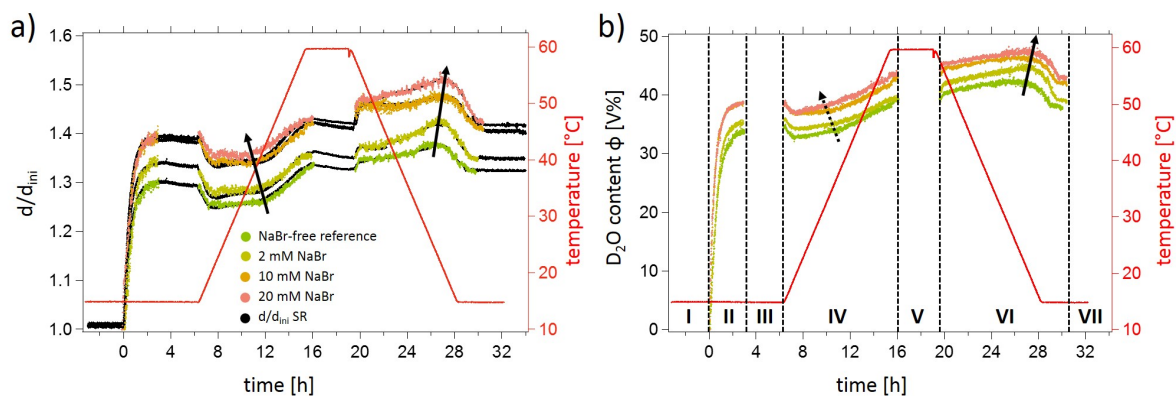


Figure 9.7.: Swelling in D_2O vapor, heating, and cooling followed with SR and ToF-NR *in-situ*. The (a) swelling ratio d/d_{ini} and (b) D_2O content Φ as a function of measurement time during swelling in D_2O vapor, heating, and cooling. The curves correspond to thin films prepared from NaBr-free (green), 2 mM (yellow), 10 mM (orange), and 20 mM (pink) NaBr solution (extracted from ToF-NR). The temperature within the measurement chamber is plotted in red. Vertical dotted lines separate the respective stages according to Figure 9.1. To prevent an overcrowding of the Figure, they are indicated in (b) only. The swelling ratio extracted from SR in (a) is colored in black. No kinetic ToF-NR data is obtained at the stages I, III, V, and VII, where the thin films are in equilibrium. The black arrows in stage IV (a) and VI (a,b) indicate the shift of the swelling temperature of the PSBP block to lower temperatures evidenced by the respective changes in swelling ratio and water content. The shift in stage IV in (b) is not very pronounced, thus it is indicated with a dotted arrow. Adapted with permission from AMERICAN CHEMICAL SOCIETY, Copyright 2021 [285].

to their $CP_{PNIPMAM}$ and CP'_{PSBP} in aqueous solution, which is due to the high polymer concentration in thin film geometry, as discussed above (see also Section 2.1.2).

The contraction process is sharper and faster than the re-swelling process, which indicates a more smeared-out transition of the PSBP block as compared to the PNIPMAM block. Hence, it is possible that the probed temperature range only approaches the CP'_{PSBP} without crossing it. Also, a lower mobility of the longer PSBP chain as compared to the shorter PNIPMAM chain might play a role and further smears out the re-swelling of the thin film. The observed contraction and re-swelling of the thin film during heating are relatively small compared to the pronounced increase in thickness and water uptake during the swelling in D_2O vapor. While the hydration state of the PNIPMAM and PSBP block changes, we assume that both blocks are at least partly hydrated throughout the heating process.

In dilute aqueous solution, the addition of NaBr at amounts below 20 mM reduced CP'_{PSBP} , while $CP_{PNIPMAM}$ remained unchanged [26, 27, 31, 235]. In thin film geometry,

we observe a similar behavior. As the NaBr content increases, the re-swelling of the thin film, due to the PSBP transition is reduced from approximately 45 °C (NaBr-free reference) to approximately 38 °C (20 mM NaBr), which is indicated by a solid black arrow in Figure 9.7a. However, the observed decrease of the swelling temperature in thin film geometry is not as pronounced as in aqueous solution, where CP'_{PSBP} shifts below 48 °C at a NaBr concentration of approximately 15 mM [31]. In contrast, the increasing amount of NaBr barely affects the collapse transition of the non-charged PNIPMAM.

Upon cooling, the situation becomes more complex: The thin films start to swell shortly after the temperature starts decreasing (approximately at 58 °C), which is presumably due to the swelling transition of the PNIPMAM block. Subsequently, the swelling process first weakens before it intensifies again. Eventually the thin films undergo a final contraction, most likely due to the collapse transition of the PSBP block, which is distributed over a broad temperature range at lower temperatures (23 °C – 16 °C). Apparently, upon cooling, the reversed transitions, with respect to the heating process, are shifted along the temperature axis, whereas the PNIPMAM transition shifts to higher temperatures and the PSBP transition shifts to lower temperatures. The latter might be due to the positions of the spinodal and binodal curves in the phase diagram. The spinodal curve is located at higher temperatures than the binodal curve for PNIPMAM, and the opposite is the case for PSBP. In-between both curves, the polymer block is metastable. Since for a mixing or swelling process the binodal is crucial, and for a de-mixing or collapse process, the spinodal is crucial, it is logical, that upon cooling the collapse transition of the PSBP block occurs at lower temperatures. In contrast, the behavior of the PNIPMAM block contradicts the above-described theory. It might be, the collapse temperature of PNIPMAM features a similar shift to lower temperatures during cooling, and therefore is beyond the probed temperature range. Also, one could speculate about a strong coupling of the hydration state of the PSBP block with the hydration state of the PNIPMAM block (cf. Section 6.3.2 in Chapter 6) due to a rather disordered thin film morphology, as is seen in Chapter 7. Hence, upon collapse of the PSBP block, hydration molecules are released, which could have a direct impact on the hydration state of the PNIPMAM polymer block. While this might explain, to a certain extent the observed evolution of the swelling ratio and the D₂O content, further experiments are needed to fully elucidate the ongoing coupled mechanisms during the cooling process.

Summarized, ToF-NR and SR experiments, reveal an increased water compatibility of the PSBP block due to the added NaBr content, which reaches its maximum at a NaBr concentration of 10 mM (of the respective spin-coating solution). Upon heating, the transitions of both, the PNIPMAM and the PSBP blocks are observed, whereas both are shifted to lower temperatures as compared to aqueous solution. The addition of

NaBr further decreased the swelling temperature of the PSBP block. Furthermore, a significantly altered responsive behavior is observed during heating and cooling, which suggests that a huge variety of different parameters impact the overall thin film behavior.

Polymer-water interactions

In order to further investigate the occurring processes within the thin films, FTIR spectroscopy is applied, to study the molecular interactions between the DBC and water molecules. FTIR measurements are performed according to the protocol shown in Figure 9.1. Figure 9.8 provides an overview over the resulting FTIR spectra during the swelling in D₂O vapor, heating, and cooling for the thin films spin-coated from NaBr-free and 20 mM NaBr solution. The FTIR spectra of all thin films can be found in the Appendix E. The evolution of the RH and temperature as a function of measurement time during the dynamic processes is given earlier in Figure 9.2b. The prominent signal peaks of the O-H and O-D stretching vibrations appear at around 3400 cm⁻¹ and 2500 cm⁻¹, respectively. Both consist of several sub-bands that refer to different water types, regarding their orientation with respect to the polymer chain [244, 245]. The peak areas, found by integration, give information about the amount of the different water species, *i.e.*, D₂O and H₂O that are present inside the thin film. As discussed above as well as in previous chapters, a certain amount of H₂O is present within the dried thin films, even though the ambient RH is 0% [36-38, 67]. Typically the H₂O molecules are replaced by D₂O during the swelling in D₂O vapor. Since the O-H peak is barely changing throughout the swelling, we assume that the amount of initially present H₂O molecules is very low. To assure a good comparison between the O-H and O-D stretching vibrations, the molar extinction coefficient λ_e , which is different for O-H and O-D bonds, is taken into account. Furthermore, possible differences in film thickness of the investigated thin film samples are eliminated by normalizing both stretching vibrations to the three-fold peak, that appears in between the O-H and O-D stretching vibrations. These peaks refer to the symmetric and asymmetric C-H stretching vibrations of the -CH₂- and the -CH₃ groups of the backbone and the sidechains of both polymer blocks. The normalized peak areas are displayed in Figure 9.9.

Upon swelling in D₂O vapor, the thin films absorb a significant amount of D₂O. With higher NaBr content, more D₂O molecules are incorporated into the thin films, as evidenced by the increasing peak areas. This agrees well with the results from ToF-NR and SR measurements. Once the thin films have equilibrated in saturated D₂O vapor, the temperature is gradually increased (heating rate + 5 K h⁻¹). As a consequence, D₂O is released from the thin films at a relatively low temperature of approximately 17 °C. The D₂O release process is relatively sharp and resembles the thin film contraction seen in the

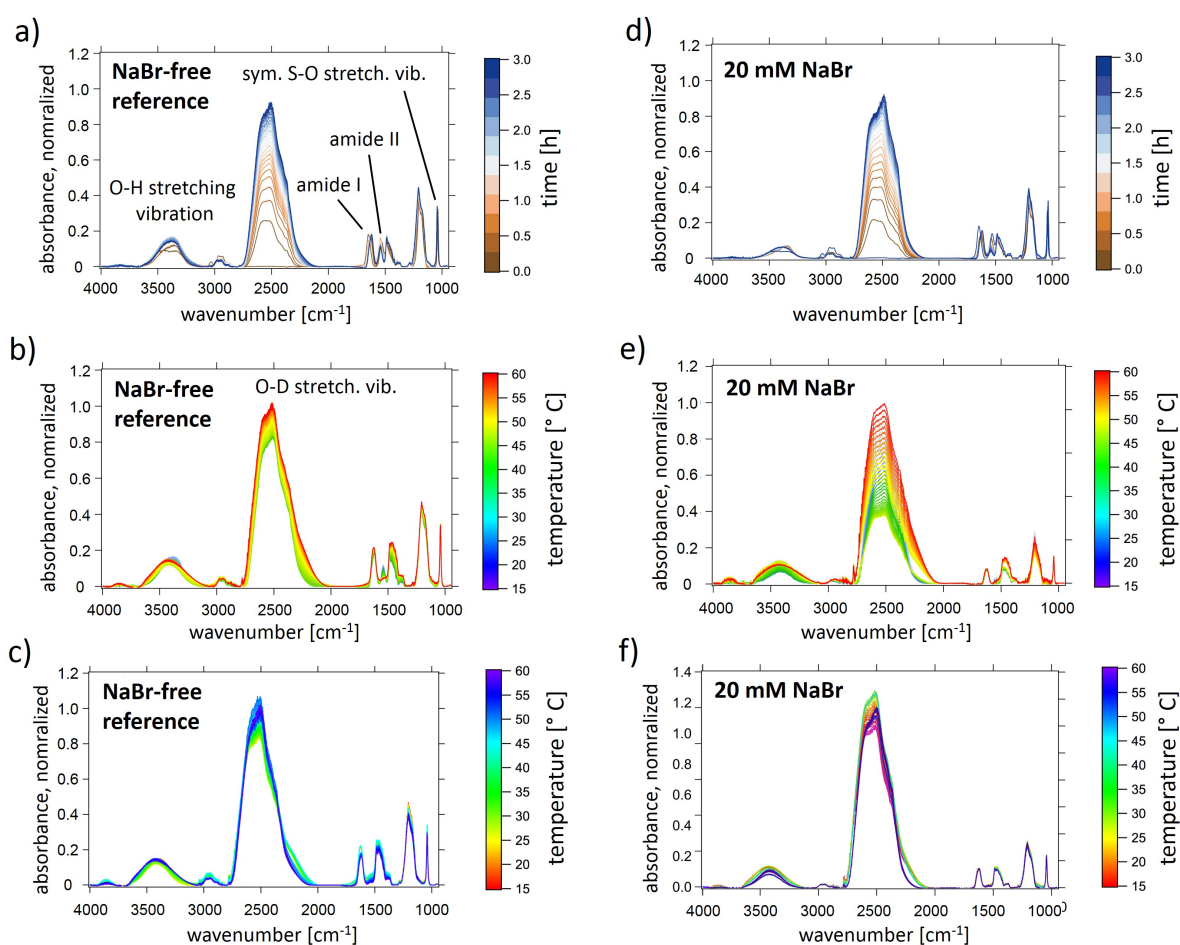


Figure 9.8.: Swelling in D_2O vapor, heating, and cooling followed with FTIR *in-situ*. FTIR spectra of the thin films spin-coated from (a,c,e) NaBr-free reference and (b,d,f) 20 mM NaBr solution during the (a,b) swelling in D_2O vapor, (c,d) heating, and (e,f) cooling. The color bars refer to time in (a,b) to temperature in (c,d and e,f). Characteristic absorption peaks are labelled accordingly. The FTIR spectra for the thin films spin-coated from 2 and 10 mM NaBr solution are provided in the Appendix E. Adapted with permission from AMERICAN CHEMICAL SOCIETY, Copyright 2021 [285].

ToF-NR and SR measurements. Hence, we again address this observation to the collapse transition of the PNIPMAM block. The contraction occurs roughly at the same temperature for all thin films probed, and therefore, the increasing NaBr content has no effect on the collapse temperature of PNIPMAM. At higher temperatures, beyond roughly around 30°C , D_2O molecules are re-absorbed, whereas this process is considerably slower than the contraction at 17°C and distributed over a broader temperature range. Analogous to the findings from ToF-NR and SR, we attribute this to a swelling of the PSBP block. With increasing NaBr content, the re-absorption of D_2O molecules starts at lower tem-

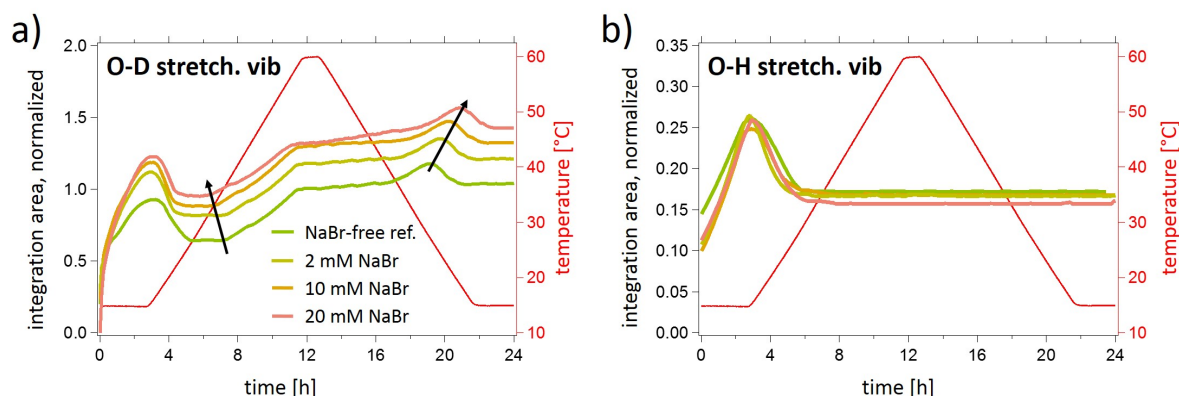


Figure 9.9.: Integration areas extracted from FTIR spectra during the swelling in D₂O vapor, heating, and cooling. The normalized integration areas of the (a) O-D and the (b) O-H speaks are extracted from the FTIR spectra shown in Figure 9.8. The areas indicate the H₂O (O-H peak) and D₂O (O-D peak) content during the swelling in D₂O vapor, heating, and cooling process. The curves correspond to thin films prepared from NaBr-free (green), 2 mM (yellow), 10 mM (orange), and 20 mM (pink) NaBr solution. The temperature within the measurement chamber is plotted in red. The solid black arrow indicate the shifted swelling temperature of the PSBP block during heating and cooling. Adapted with permission from AMERICAN CHEMICAL SOCIETY, Copyright 2021 [285].

peratures ($\approx 35^\circ\text{C}$ for the NaBr-free, and $\approx 30^\circ\text{C}$ for thin film spin-coated from 20 mM NaBr solution), indicating an increasing water compatibility of PSBP. The temperatures, at which this re-adsorption occurs, are in good agreement with the temperatures found with ToF-NR.

Upon cooling, the D₂O content first slightly increases at intermediate temperatures (around 35°C), before it reaches a relatively sharp local maximum at lower temperatures (roughly around 25°C), and finally decreases. The position of the local maximum and the following release of D₂O molecules shifts to lower temperatures with increasing NaBr content. Since a similar shift to lower temperatures of the swelling of the PSBP block with increasing NaBr content is observed during heating, we assume that this reflects the ionic strength dependency of the PSBP block on its coil-to-globule transition during cooling. Analogous to the ToF-NR results, the release of D₂O molecules upon cooling occurs at lower temperatures as compared to the D₂O re-absorption during heating. As opposed to heating, a pronounced change in D₂O content during cooling that could be referred to the PNIPMAM transition is not observed. A possible scenario might be, that both the collapse and swelling temperatures of PNIPMAM and PSBP shifts to lower temperatures, whereas the collapse temperature is then beyond the probed temperature range. Analogous to the ToF-NR and SR data (cf. Figure 9.7), an increase in D₂O content

is seen at the beginning of the cooling process, however, this increase is considerably slower and less pronounced. As described earlier, this might be due to cooperative hydration effects of the individual polymer blocks. Also, still ongoing long-term re-arrangement processes from the heating process are thinkable.

The evolution of the normalized peak area of the O-H stretching vibration during swelling in D₂O vapor, heating, and cooling is shown in Figure 9.9b. With increasing D₂O content, the intensity of the O-H stretching vibration signal increases as well before falling asymptotically to a final value, which is still higher than the starting point. This can be explained by the release of protons into the film upon deuteration of the secondary amide groups, which are present in both polymer blocks. Figure 9.10 shows the decreasing normalized peak area of the protonated amide II mode and the increasing normalized peak area of the deuterated amide II' mode, which demonstrates the exchange of the -CONH- groups by deuterium to -COND- groups. As a result, a third water species, HDO is generated, which also contributes to the O-H stretching vibration. After reaching the maximum, the peak area of the O-H stretching vibration signal decreases. This decrease is due to a slowing down of the deuteration of the polymer chain combined with an ongoing replacement of H₂O/HDO by excessively present D₂O molecules. This finding is consistent with the previous chapters, where deuteration and exchange processes are also observed [36-38]. The H₂O/HDO content equilibrates around a temperature of 30 °C, indicating that these processes are finished. Please note, this temperature corresponds to ≈ 3 h of heating.

While the areas of the O-D and O-H stretching vibration signals can be correlated with the overall water (D₂O, H₂O, and HDO) content inside the thin films, the wavenumber shift of characteristic signals, such as the sulfonate and amide groups, yield information about their particular hydration behavior. Figure 9.11 shows the evolution of the peak maximum positions of the S-O stretching vibration signal (1038 cm⁻¹ in dry state), which arises due to the SO₃⁻ group, and of the amide I mode (1645 cm⁻¹ in dry state), respectively.

Upon swelling, both peaks undergo significant shifts for the S-O stretching vibration signal to higher wavenumbers, and for the amide mode to lower wavenumbers. This is in agreement with literature and the previous chapters of this thesis, and indicates decreasing (SO₃⁻) and increasing (amide I) stretching and bending vibrational energies of the respective bonds [37, 39]. Upon higher NaBr content, these shifts are more pronounced. This demonstrates a stronger hydration of the respective groups and confirms the previous findings of an increased water compatibility of particularly the PSBP block (analogously to the salting-in effect in aqueous solution). Thus, a higher NaBr content leads not only to an overall higher water content within the thin films, but also to a stronger net hy-

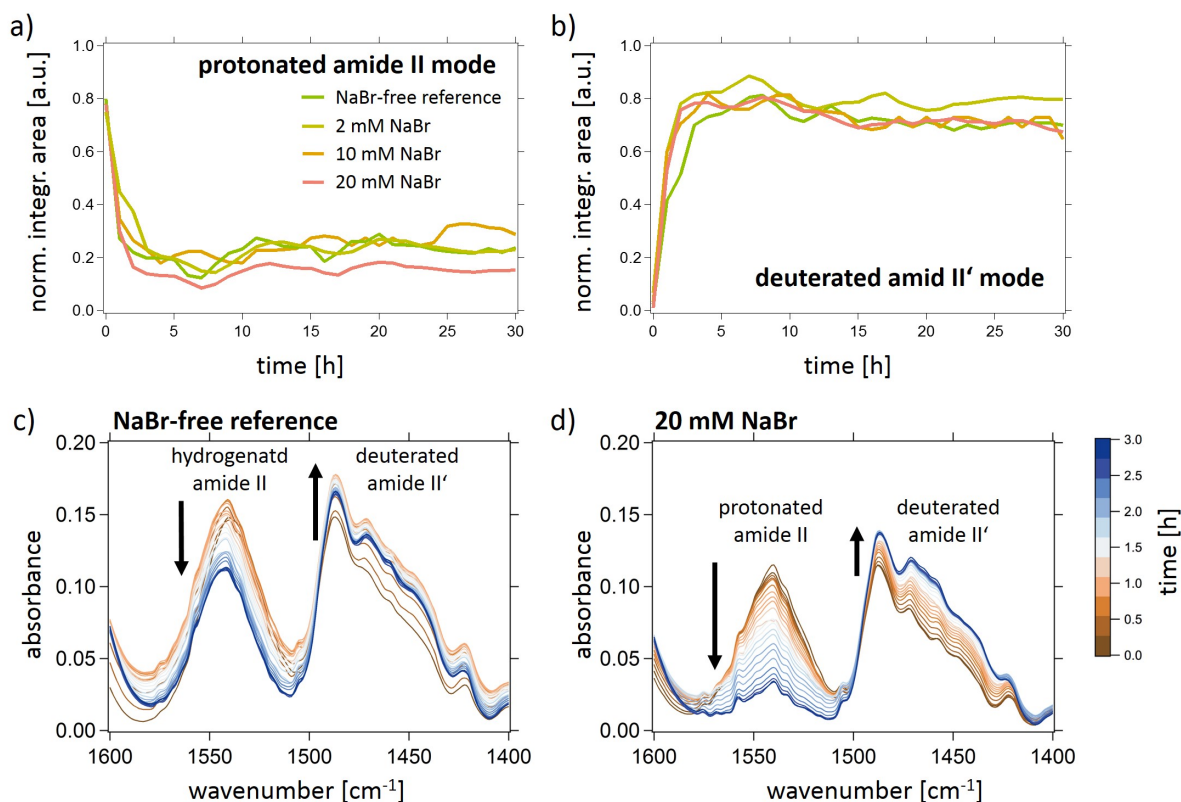


Figure 9.10.: Integration areas extracted from FTIR spectra during the swelling in D_2O vapor, heating, and cooling. Normalized integration areas of the (a) protonated amide II and the (b) deuterated amide II' modes. The curves correspond to thin films prepared from NaBr-free (green), 2 mM (yellow), 10 mM (orange), and 20 mM (pink) NaBr solution. A close-up of the amide II and II' modes are visible below for the thin films spin-coated from (c) NaBr-free and (d) 20mM NaBr solution. Adapted with permission from AMERICAN CHEMICAL SOCIETY, Copyright 2021 [285].

dration of the characteristic groups. Interestingly, during heating and cooling, both peak shifts feature a considerably different trend for the evolution of the D_2O and H_2O/HDO content. Upon heating, the peak maxima shift back slightly, *i.e.*, a displacement to lower wavenumbers for the S-O stretching vibration signal and to higher wavenumbers for the amide I mode is observed. Upon cooling, this trend is reversed, and the peak maxima shift to their initial values of after the swelling in D_2O vapor (stage III). As the peak shifts are monotonic, this indicates a steady de-hydration during heating and a steady re-hydration during cooling. The strong shift of the S-O stretching vibration and the amide I mode upon D_2O swelling, underlines the assumption described above. Both polymer blocks are already at least partly hydrated after the swelling process. Although, upon heating and cooling, the minor shifts indicate a change in hydration state, they are not indicative of

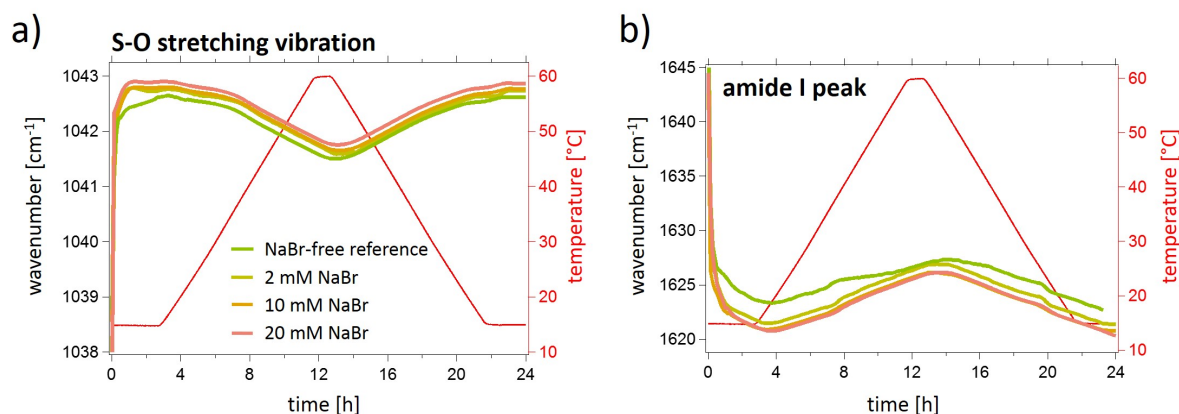


Figure 9.11.: Peak maximum position extracted from FTIR spectra upon swelling in D_2O vapor, heating, and cooling. From the FTIR spectra shown in Figure 9.8, the peak maximum position of the (a) symmetric S-O stretching vibration and the (b) amide I during the swelling in D_2O vapor, heating, and cooling process are extracted by applying a Gaussian fit to the corresponding peaks. The curves correspond to thin films prepared from NaBr-free (green), 2 mM (yellow), 10 mM (orange), and 20 mM (pink) NaBr solution. The temperature within the measurement chamber is plotted in red. Adapted with permission from AMERICAN CHEMICAL SOCIETY, Copyright 2021 [285].

a fully hydration - dehydration. One has to note here that the evolution of the peak shifts parallels the evolution of the RH during heating and cooling. In particular, the very slow changes in RH and peak maximum positions indicate, that the monotonically de- and re-hydration is due to the non-constant RH, but not due to a response of the thin films. This implies, that the phase transitions of both polymer blocks upon heating and cooling lead to non-monotonic changes of the overall water content, but not necessarily to a change in hydration of the characteristic hydrophilic groups, such as the SO_3^- and amide group. This finding is in agreement with the study presented in Chapter 8 on a similar DBC thin film, where the changing water compatibility of the thin film is indeed affecting the overall water content but not the hydration of particular hydrophilic groups [38].

The FTIR results are consistent with the findings from ToF-NR and SR measurements. Upon increasing NaBr content, the PSBP block features a higher compatibility to water, which leads to a stronger water uptake and hydration of the thin films. Furthermore, a shift of the swelling temperature of the PSBP block to lower temperatures with increasing NaBr content is revealed. PNIPMAM shows a relatively sharp collapse at low temperatures during heating, however no clear transition during cooling is observed. Analogous to ToF-NR and SR, this demonstrates the significant difference of the thin film behavior upon heating and cooling. In addition, changes in temperature and NaBr content are

found to induce a change in the hydrophilicity and water content of the thin films, while they affect the hydration of particular hydrophilic groups within the DBC.

9.3. Conclusion

The present chapter describes the behavior of orthogonally dual thermo-responsive DBC thin films as a function of temperature and NaBr content. The DBC consists of a zwitterionic PSBP and a nonionic PNIPMAM block and is spin-coated from solutions of different NaBr concentrations (0-20 mM). Increasing the salt concentration to 10 mM leads to a maximum swelling ratio and water uptake of the thin films and a further increase to 20 mM has no significant additional effect on the swelling ratio and water uptake. These findings mainly originate from the salt-sensitive nature of the zwitterionic PSBP block. Upon heating, the thin film contracts and re-swells, which is attributed to a change of the hydration state of first the PNIPMAM block, and then the PSBP block. The collapse and swelling temperatures of PNIPMAM and PSBP, respectively, are slightly shifted to lower temperatures as compared to the corresponding CP_{PNIPMAM} and CP'_{PSBP} in aqueous solution, which is due to the increased polymer concentration in thin film geometry. In addition, the amount of NaBr decreases the swelling temperature of the PSBP block but not the collapse temperature of PNIPMAM, while the onset temperatures of the respective swelling (PSBP block) and contraction (PNIPMAM block) processes for the different NaBr contents, found with ToF-NR/SR and FTIR are in good agreement.

The subsequent cooling process reveals that the PSBP collapse occurs at lower temperatures than the corresponding swelling during heating, following the behavior expected from the solution phase diagram and the position of the binodal and spinodal. Furthermore, and analogously to the heating process, the swelling temperature of PSBP decreases with increasing NaBr content. In contrast, the behavior of the PNIPMAM block seems to be more complex, as a clear transition during cooling is not detected. A possible scenario might be a strong correlation of the hydration states of the PSBP and PNIPMAM block. Interestingly, particular characteristic groups, such as the non-charged amide or the negative sulfonate group, barely change their hydration state upon changes in temperature as well as in NaBr content.

The observed responsive behavior of the thin film system demonstrates the complex interplay between different, and to some extent competing, external stimuli such as temperature and NaBr content. The high polymer concentration increases the complexity of the system even more by introducing confinement and stronger crowding effects than in solutions. Altered polymer – water interactions, as well as a lower chain mobility have a

significant impact on the overall thin film behavior. In addition, further kinetic processes such as deuteration and the exchange of H₂O/HDO by D₂O also play a role.

10. Summary and outlook

Multi-responsive polymers feature a highly controllable self-assembly behavior and therefore, provide a high level of functionality. While this versatility is the basis of a continuously increasing number of polymer-based applications, it is also accompanied by a massive complexity of the material. A change in the materials dimensions, *i.e.*, from a 3-dimensional polymer solution to a 2-dimensional thin film geometry, results equally in an increased versatility and complexity of the materials response. In the present thesis, the behavior of orthogonally dual thermo-responsive diblock copolymer (DBC) thin films in varying environmental conditions is analyzed. The results and conclusions contribute to resolve this complexity, in order to take full advantage of the versatility, and therefore, the thesis may provide a groundwork for future studies.

In addition, the 'FlexiProb' sample environment is developed together with Tobias Widmann, which allows for a precise control of environmental parameter, *e.g.*, relative humidity, temperature, and vapor composition. Since this setup is mainly used at large scale neutron (and potentially also x-ray) sources, the focus is set to an easy, fast, and space-saving installation and disassembly. Furthermore, it can be coupled with additional measurement techniques, which allows to follow dynamic thin film processes at the exact same environmental parameters from different perspectives. The 'Flexiprob' sample environment has been employed successfully during numerous beamtimes at the MLZ and ILL neutron sources, in Garching, Germany and Grenoble, France, respectively. Chapter [3](#) provides a description of the developed setup.

The DBCs under investigation consist of a zwitterionic poly(sulfobetaine) (PSB) block and a nonionic block, which is either poly(*N*-isopropylacrylamide) (PNIPAM) or poly(*N*-isopropylmethacrylamide) (PNIPMAM). Both blocks are orthogonally responsive towards temperature, *i.e.* the PSB block features a coil-to-globule transition upon cooling, while PNIPAM and PNIPMAM undergo the same transition but upon heating. The transition temperatures of both blocks are sensitive to polymer concentration and as a consequence, they shift considerably in thin film geometry as compared to aqueous solution. Furthermore, the polymer transitions can be tuned dramatically by applying vapors of different isotopes, *e.g.*, H₂O/D₂O and CH₃OH/CD₃OH as well as of different composition, *e.g.*, water/methanol mixtures. Loading the thin films with certain amounts of salt selectively affects the transition temperature of the PSB block.

Mainly, neutron scattering techniques (ToF-NR, ToF-GISANS) and FTIR spectroscopy are used to follow the behavior of the DBC thin films in changing environmental conditions *in-situ*. This combination of measurement techniques allows to link mesoscopic thin film characteristics, *e.g.*, swelling degree, solvent content, (vertical) distribution within the thin films, and a lateral thin film morphology, to molecular information about local hydration of certain functional groups, polymer-polymer, and polymer-solvent interactions.

For a first fundamental understanding, PSB-*b*-PNIPAM DBC thin films are exposed to pure H₂O or D₂O vapor, which is then exchanged by the corresponding other water species (H₂O with D₂O and vice versa). This is described in Chapter 5. Most prominently, the DBC thin films exhibit a higher affinity to H₂O than to D₂O, which results in a larger and faster adsorption of H₂O. This response, is mainly addressed to the isotope sensitivity of the PSB block, and can be seen as the thin film equivalent to a decreased clearing point of the PSB (CP'_{PSB}) in aqueous solution. A deviating thin film behavior in H₂O or D₂O vapor has been expected to a certain level, however, the significance of the observed differences is indeed surprising.

In a next step, methanol is introduced to the thin film/vapor system. Since Chapter 5 reveals the high complexity of, in particular the exchange processes, the individual homopolymers are investigated first, and PSB and PNIPMAM thin films are exposed to pure water and mixed water/methanol vapors. This experiment is described in Chapter 6. Upon swelling in water vapor, the PSB thin film absorbs a significantly higher amount of water than the PNIPMAM thin film, which opposes the expectations from aqueous solution. This difference demonstrates a strong shift of the corresponding transition temperatures of PSB and PNIPMAM in thin film geometry. In mixed water/methanol vapor both thin films contract and equilibrate with a swelling ratio lower than in pure water and methanol vapors. Therefore, a co-nonsolvency-type behavior is attributed to both, the PSB and PNIPMAM thin films. For PNIPMAM, such effect was already found in mixed water/alcohol solutions [92], whereas PSB is insoluble in methanol, and therefore the observed swelling and contraction behavior is highly surprising. Apparently, PSB exhibits a miscible regime on the very substance-rich region of the phase diagram, which eventually leads to a co-nonsolvency effect in thin film geometry. The PSB and PNIPMAM contraction mechanism deviate from each other (one-step PSB vs. two-step PNIPMAM contraction). This difference is attributed to the strong differences in polymer-solvent interactions, based on the different nature of PSPE and PNIPMAM, *i.e.*, zwitterionic vs. nonionic, insoluble vs. soluble in methanol, UCST vs. LCST. Thus, the co-nonsolvency mechanism depends on the specific nature of the polymer thin film, which necessitates

a thin film-specific interpretation of the observed results, rather than a universal co-nonsolvency theory.

Analogous, to this homopolymer study, the corresponding PSB-*b*-PNIPMAM DBC thin films are exposed to pure water and mixed water/methanol vapors. To combine the experiments with the previous Chapter 5 about isotope-sensitivity, different water (H_2O and D_2O) and methanol species (CH_3OH and CD_3OH) are used. Conveniently, the PSB-*b*-PNIPMAM DBC thin film behavior follows the combined results from Chapter 5 and the homopolymer thin film study. While the DBC thin film exhibits a higher compatibility with H_2O , regarding its swelling degree and solvent uptake, it also features the combined contraction mechanisms of the PSB and PNIPMAM homopolymers. The individual contractions occur consecutively and not simultaneously, which results in five different thin film regimes, dependent on the vapor composition: (i) dry, (ii) water-swollen, (iii) after PSB collapse, (iv) after PSB and PNIPMAM collapse, and (v) methanol-swollen. By using different isotopes of water and methanol, these regimes can be further tuned. A co-nonsolvency-type behavior of the DBC thin films is not observed, as the swelling degree in pure methanol vapor is only slightly higher than in mixed water/methanol vapors. Apparently, the covalent bonds between both blocks leads to steric hindrance, repulsive interactions or cooperative hydration effects, which eventually suppress a co-nonsolvency-type behavior of the DBC thin film.

While these first two Chapters 5 and 6 focus on a mixed vapor composition at constant temperature, Chapter 7 describes the thermal behavior of PSB-*b*-PNIPMAM thin films in pure water vapor. Upon two temperature jumps, from 20 °C to 40 °C and from 40 °C to 60 °C, the thin film first contracts and re-swells afterwards, which considerably opposes the expectations from aqueous solution. This is due to a shift of the transition temperatures of both polymer blocks, PSB and PNIPMAM, thereby confirming the results from the previous chapters. Generally, the thin film transitions are very slow (on the order of hours) compared to the transitions observed in solution, indicating a low polymer chain mobility. GISANS measurements reveal a changing lateral thin film morphology, however the changes are rather small, most likely also due to the low chain mobility. A structural inversion upon increasing temperature as was seen in solution [26, 27], is not observed in the thin film geometry.

Chapter 8 describes the cyclic swelling and drying behavior of PSB-*b*-PNIPMAM thin films at three different temperatures (15 °C, 27 °C, and 48 °C), and therefore investigates the suitability of these thin films in potential applications, where reversible and reproducible kinetic processes are essential. All cycles yield highly reproducible swollen and dry thin film states, regarding their film thicknesses and water contents. In contrast to the final equilibrium states of the thin films, their swelling and contraction mechanisms devi-

ate considerably. Deuteration of the amide groups, present in the PSB and PNIPMAM blocks, generates a third water species, HDO, which is exchanged by excessively present D₂O molecules. While the competing deuteration and exchange processes are mainly responsible for the deviating swelling and drying mechanisms, they already weaken upon three full swelling/drying cycles and are supposed to vanish with further increasing cycle number. Also, an increased temperature leads to a lower compatibility of the DBC with water, and eventually results in lower swelling degrees and water absorption. In particular, a temperature of 27 °C is found to provide balanced conditions between short diffusion ways and a sufficient hydrophilic state, and therefore provides ideal conditions for a fast water uptake and release.

Chapter 9 investigates the response of PSB-*b*-PNIPMAM thin films toward two stimuli in parallel, namely temperature and the addition of the monovalent salt NaBr. Upon swelling in D₂O vapor, the addition of NaBr promotes water uptake. In solution, this phenomenon is called 'salting-in' effect. Upon heating and cooling a pronounced shift of the PSB transition temperature to lower temperatures with increasing NaBr content is observed. A PNIPMAM collapse transition is observed as well, however at constant temperature and independently from NaBr addition. Thus, the promoted water uptake mainly originates from the salt-sensitive nature of the zwitterionic PSBP block. During cooling, a superposition of both stimuli, temperature and salt addition, as well as a strong correlation of the hydration states of both polymer blocks is found. The application of two external stimuli results in a highly tunable and versatile, but also complex thin film behavior. The superposition of the external stimuli makes it extremely challenging, to isolate the individual effects of temperature and salt addition on the thin film behavior.

In summary, the present thesis demonstrates a highly versatile behavior of the investigated orthogonally dual thermo-responsive DBC thin films. Their response toward various external stimuli differs significantly from the response of the same material in solution. This difference highlights the impact of polymer concentration and confinement on polymer-polymer and polymer-solvent interactions and eventually on the overall behavior of the material. In parallel, the thin film geometry enables new possibilities. Multiple and reproducible thin film regimes are established that can be tuned by the vapor composition, temperature, and salt additives, and therefore, these thin films are promising candidates for (nano) sensors, (nano) switches, and functional surfaces.

In the future, multi-responsive polymer thin films will become more prominent in fundamental research as well as in polymer-based applications. In particular polymer thin films and polymer interfaces provide great opportunities for multi-component and multi-

responsive systems in spatially confined environments. To realize such systems, precise selectivity of individual building blocks toward single stimuli is required. Furthermore, enhanced mechanical integrity and stability in combination with a short response time and a reversible behavior, will be essential, in particular for fragile polymer hydrogels or free-standing thin films. For future applications, it will be particularly important to integrate these attributes in biocompatible, biodegradable, and non-toxic systems. Since these multi-responsive systems will become more complex and will require precise control of a large number of parameters, the investigation with several measurement techniques simultaneously, will play a crucial role in future experiments. A further future trend focuses on automated measurements, *e.g.*, for tedious parameter screenings, and, as computational power increases, on simulations.

A. Appendix for Chapter 1

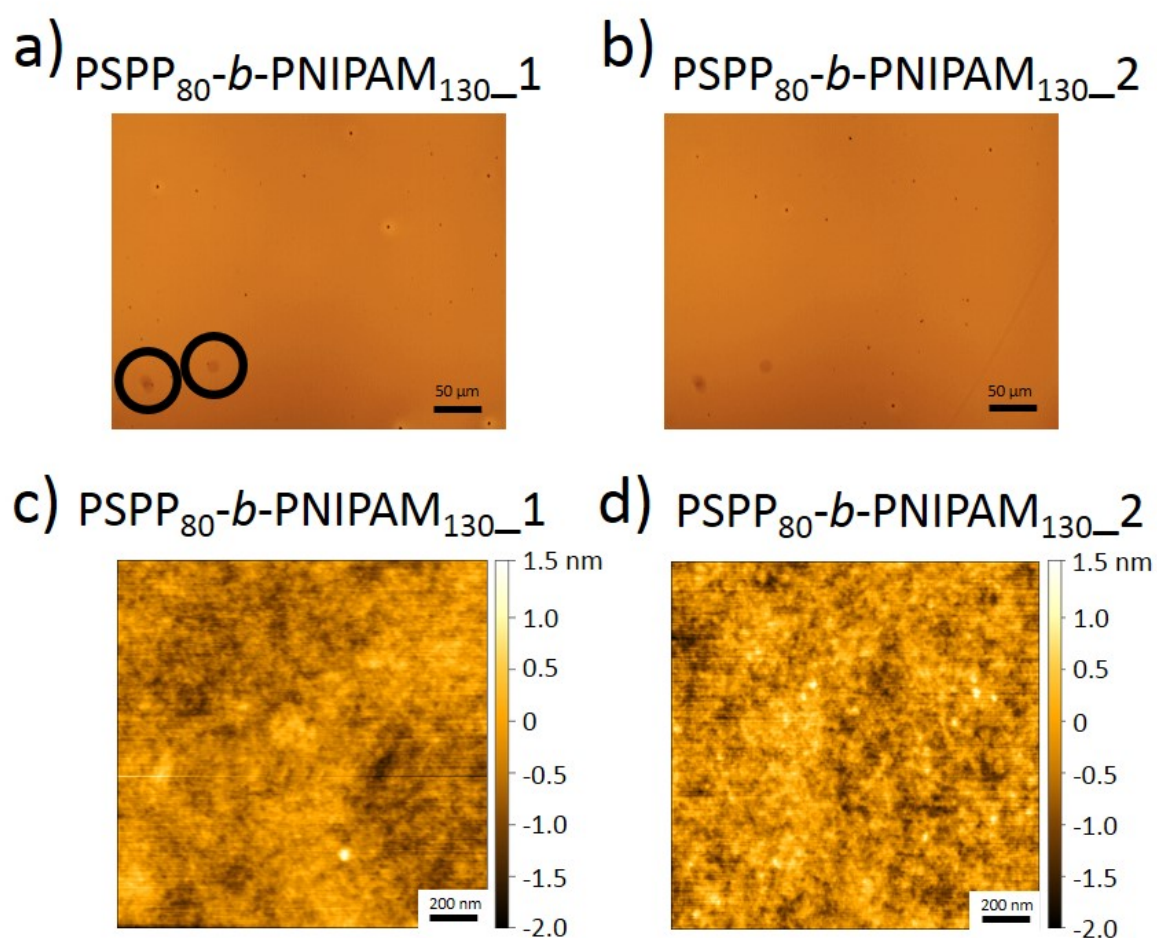


Figure A.1.: Pre-characterization of the two $\text{PSPP}_{80}\text{-}b\text{-PNIPAM}_{130}$ thin films investigated in Chapter 5. (a,b) OM images. The two spots in the lower left corner result from a damaged OM lens. (c,d) AFM topography data.

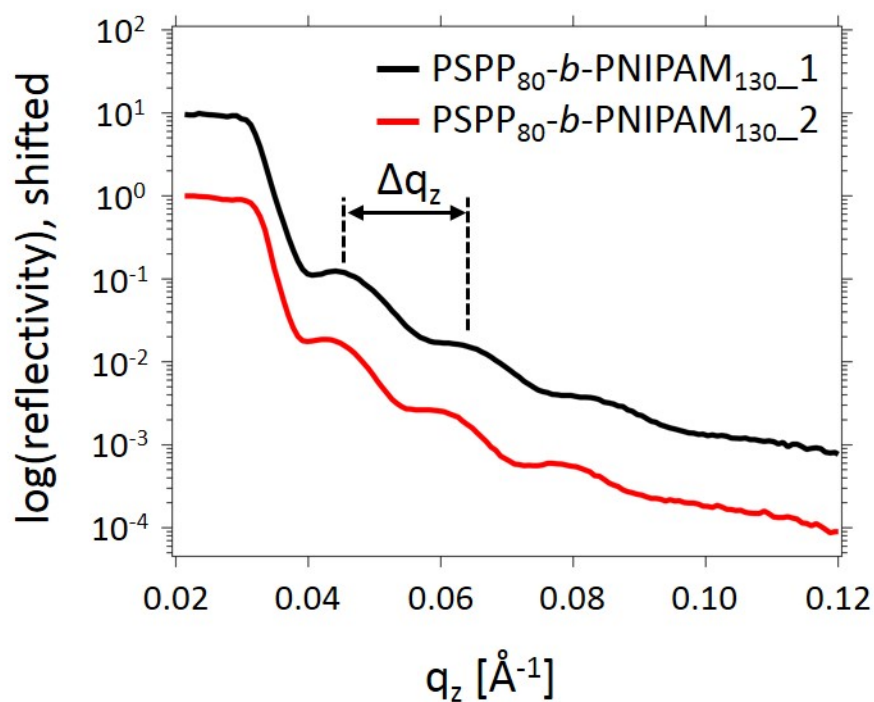


Figure A.2.: XRR data of the two PSPP₈₀-b-PNIPAM₁₃₀ thin films investigated in Chapter 5. The film thickness is calculated via the distance of two oscillation maxima (Δq) according to Equation 2.35.

B. Appendix for Chapter 2

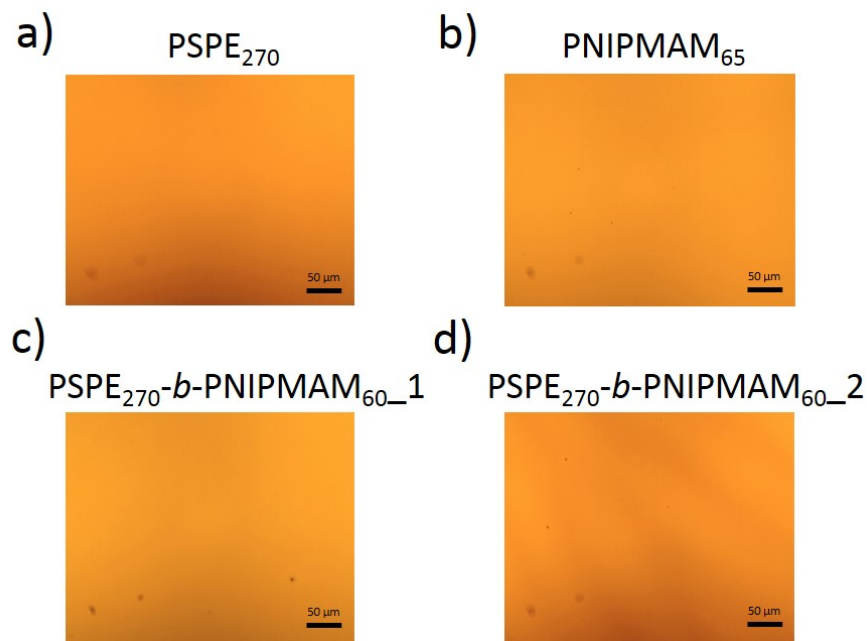


Figure B.1.: OM images of the homopolymer and diblock copolymer (DBC) thin films investigated in Chapter 6. (a,b) PSPE₂₇₀ and PNIPMAM₆₅ homopolymer thin films investigated in the first part and (c,d) PSPE₂₇₀-*b*-PNIPMAM₆₅ DBC thin films investigated in Chapter 6 in Section 6.3. The two spots in the lower left corner marked in (a) result from a damaged OM lens.

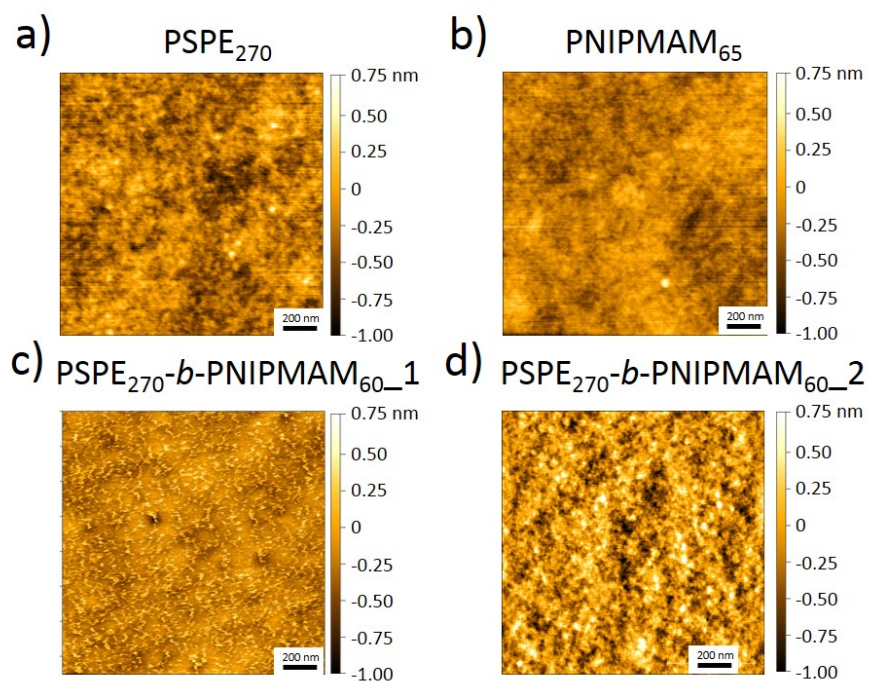


Figure B.2.: AFM topography data of the thin films investigated in Chapter 6. (a,b) PSPE and PNIPMAM homopolymer thin films investigated in the first part and (c,d) PSPE-*b*-PNIPMAM DBC thin film samples investigated Chapter 6 in Section 6.3.

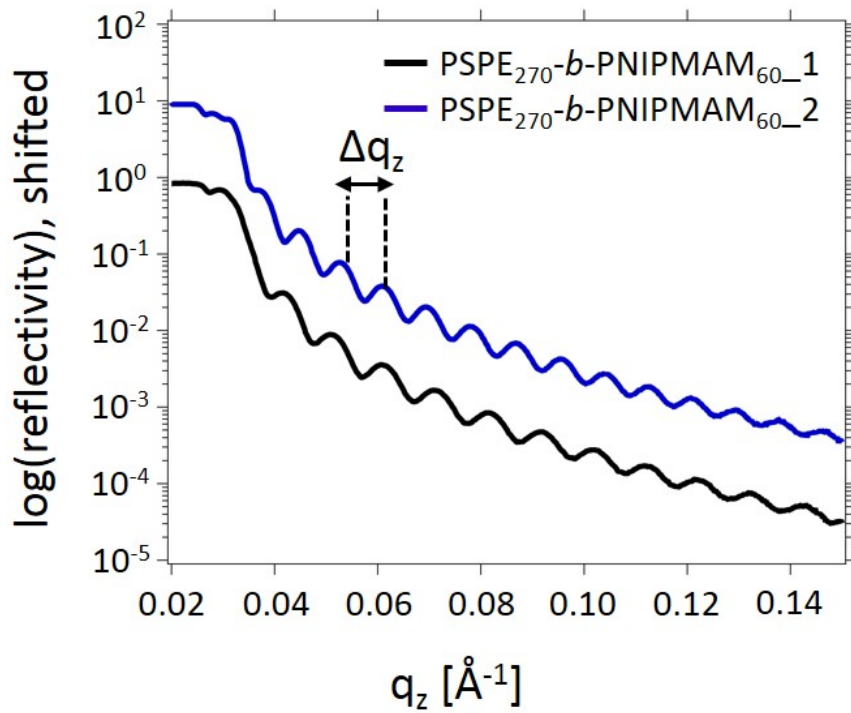


Figure B.3.: XRR data of the thin film samples investigated in Chapter 6 in Section 6.3. The film thickness is calculated via the distance of two oscillation maxima (Δq) according to Equation 2.35.

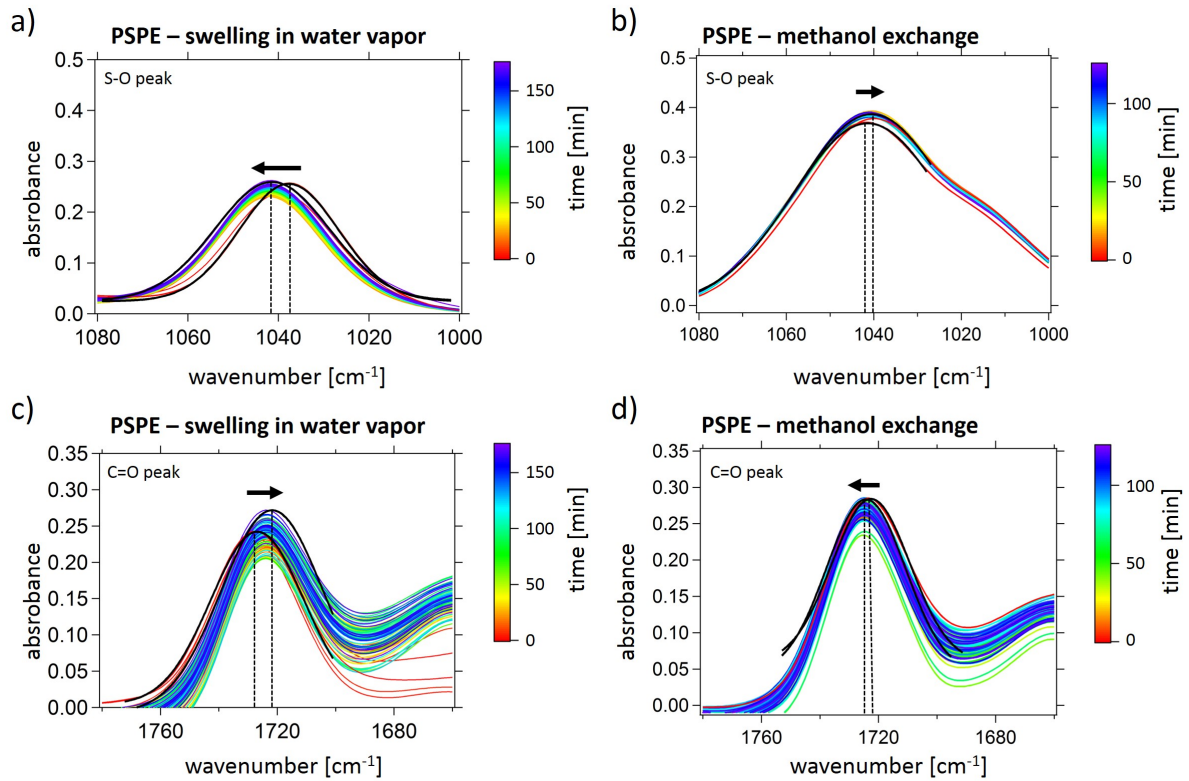


Figure B.4.: Close-up of characteristic stretching vibrations probed with FTIR spectroscopy of the PSPE homopolymer thin film investigated in Chapter 6 in Section 6.1. (a,b) S-O and the (c,d) C=O stretching vibration of the PSPE homopolymer thin film during (a,c) swelling in water vapor and (b,d) methanol addition. A Gaussian fit (applied to all FTIR curves) is shown as black line for each first and final absorption peak. Black dashed lines indicate the peak maxima. The peak shifts as a function of time is shown in Figure 6.6.

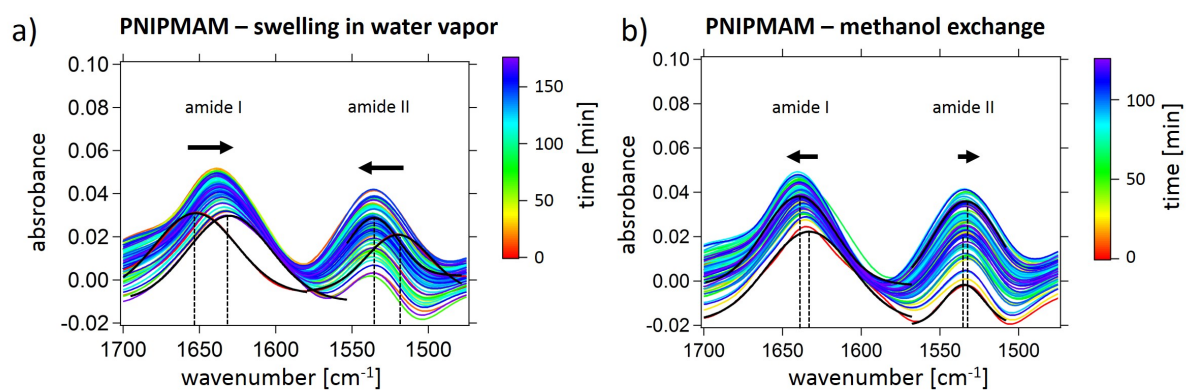


Figure B.5.: Close-up of characteristic stretching vibrations probed with FTIR spectroscopy of the PNIPMAM homopolymer thin film investigated in Chapter 6. Amide I and II peaks of the PNIPMAM homopolymer thin film during (a) swelling in water vapor and (b) methanol addition. A Gaussian fit (applied to all FTIR curves) is shown as black line for each and final first absorption peak. Black dashed lines indicate the peak maxima. The peak shifts as a function of time is shown in Figure 6.6.

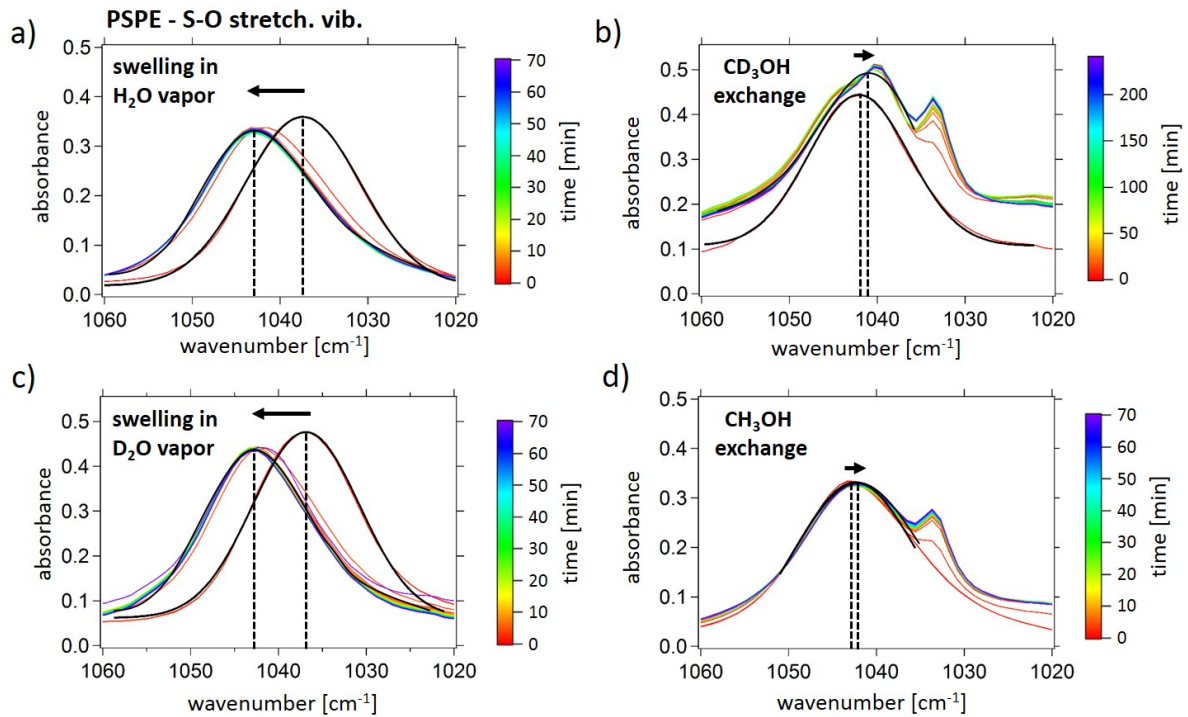


Figure B.6.: Close-up of S-O stretching vibration probed with FTIR spectroscopy of the PSPE-*b*-PNIPMAM DBC thin film investigated in Chapter 6 in Section 6.3. Peak shift (black arrows) of the S-O stretching vibration during (a,b) Experiment A, swelling in H₂O vapor (a) and subsequent addition of CD₃OH (b) and (c,d) Experiment B, swelling in D₂O vapor (c) and subsequent addition of CH₃OH (d). A Gaussian fit (applied to all FTIR curves) is shown as black line for each first and final S-O absorption peak. Black dashed lines indicate the peak maxima. The extracted peak shift is shown in Figure 6.17.

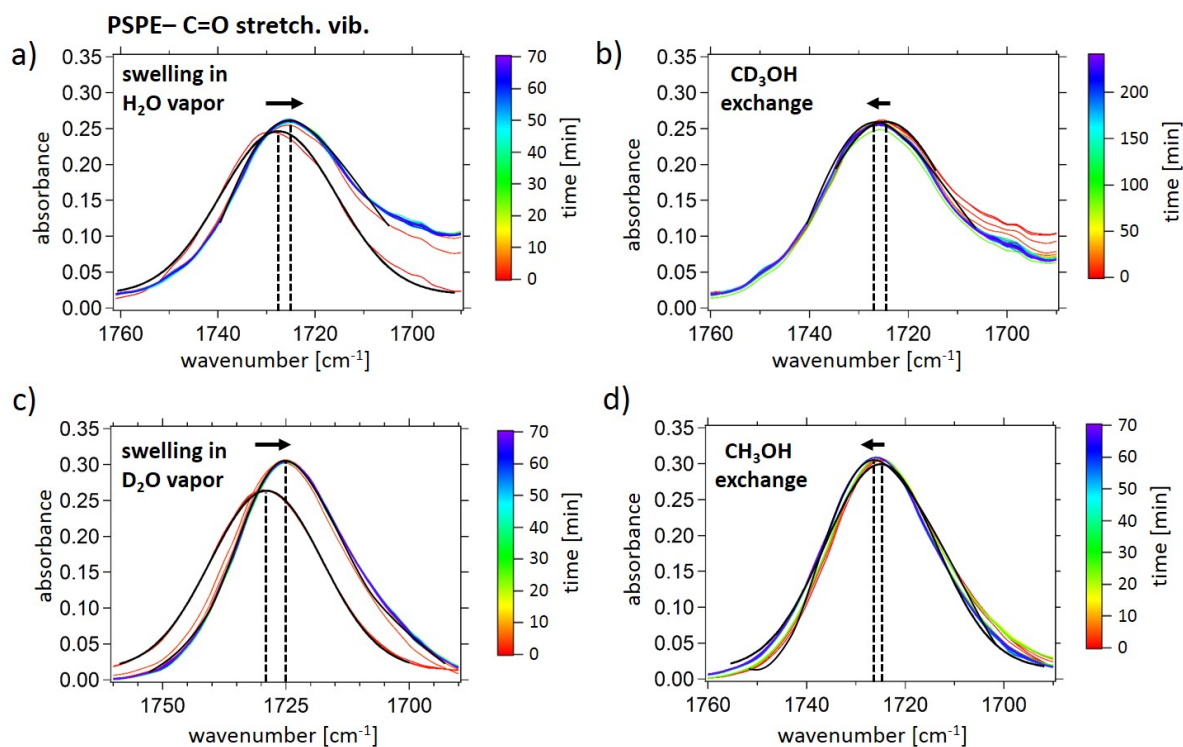


Figure B.7.: Close-up of C=O stretching vibration probed with FTIR spectroscopy of the PSPE-*b*-PNIPMAM DBC thin film investigated in Chapter 6 in Section 6.3. Peak shift (black arrows) of the C=O stretching vibration during (a,b) Experiment A, swelling in H₂O vapor (a) and subsequent addition of CD₃OH (b) and (c,d) Experiment B, swelling in D₂O vapor (c) and subsequent addition of CH₃OH (d). A Gaussian fit (applied to all FTIR curves) is shown as black line for each first and final C=O absorption peak. Black dashed lines indicate the peak maxima. The extracted peak shift is shown in Figure 6.17.

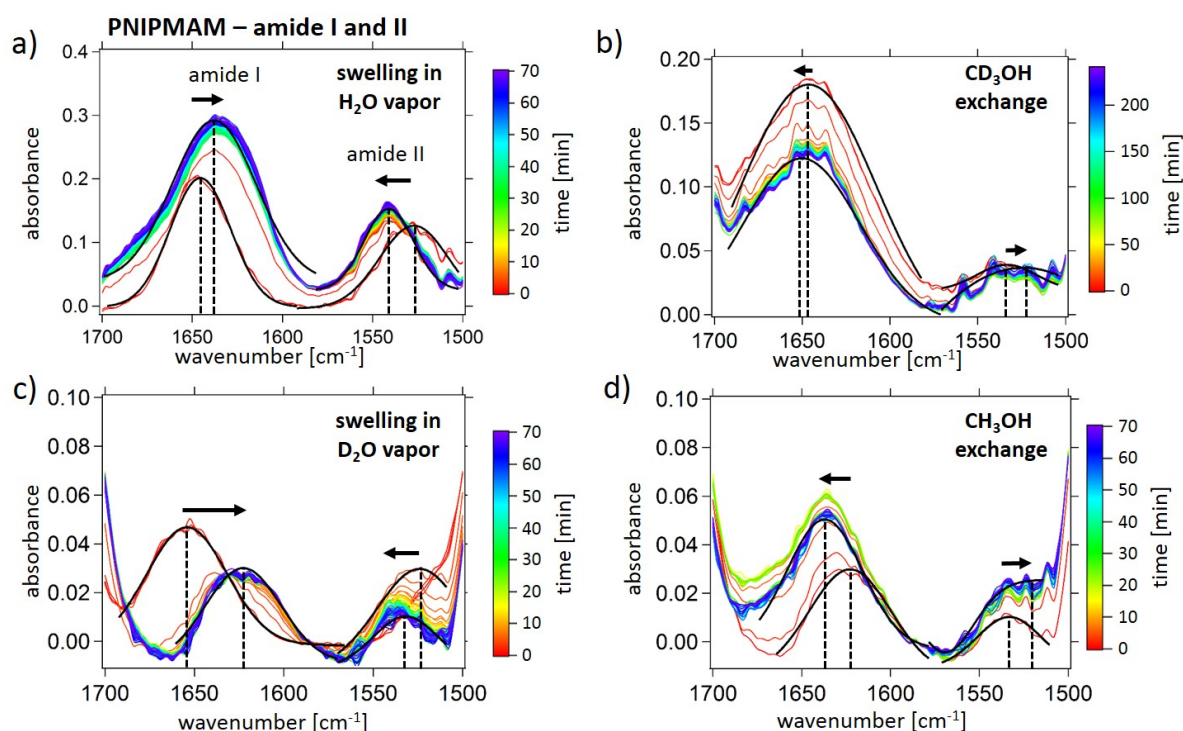


Figure B.8.: Close-up of the amide I and II peaks probed with FTIR spectroscopy of the PSPE-*b*-PNIPMAM DBC thin film investigated in Chapter 6 in Section 6.3. Peak shift (black arrows) of the amide I and II peaks during (a,b) Experiment A, swelling in H₂O vapor (a) and subsequent addition of CD₃OH (b) and (c,d) Experiment B, swelling in D₂O vapor (c) and subsequent addition of CH₃OH (d). A Gaussian fit (applied to all FTIR curves) is shown as black line for each first and final amide I and II absorption peak. Black dashed lines indicate the peak maxima. The extracted peak shift is shown in Figure 6.17.

C. Appendix for Chapter 3

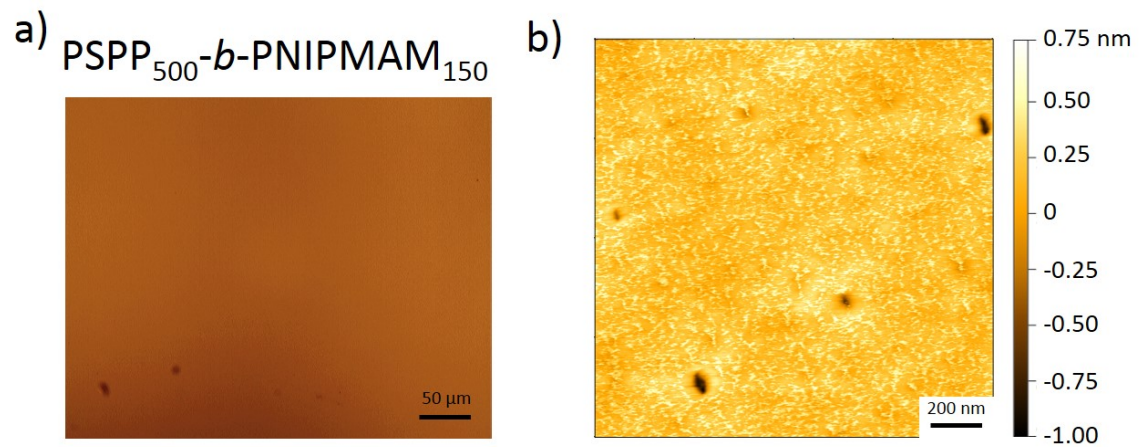


Figure C.1.: Pre-characterization of the PSPP₅₀₀-*b*-PNIPMAM₁₅₀ thin film, investigated in [7](#). (a) OM image. The two spots in the lower left corner result from a damaged OM lens. (b) AFM image. (c) XRR data. The film thickness is calculated via the distance of two oscillation maxima (Δq) according to Equation [2.35](#).

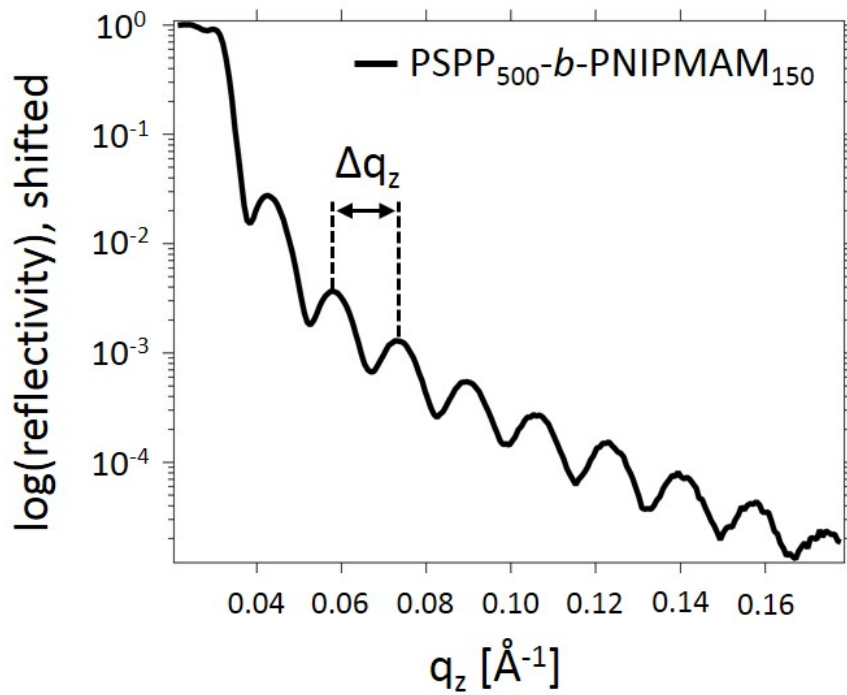


Figure C.2.: of the PSPP₅₀₀-b-PNIPMAM₁₅₀ thin films investigated in Chapter 7. The film thickness is calculated via the distance of two oscillation maxima (Δq) according to Equation 2.35.

D. Appendix for Chapter 4

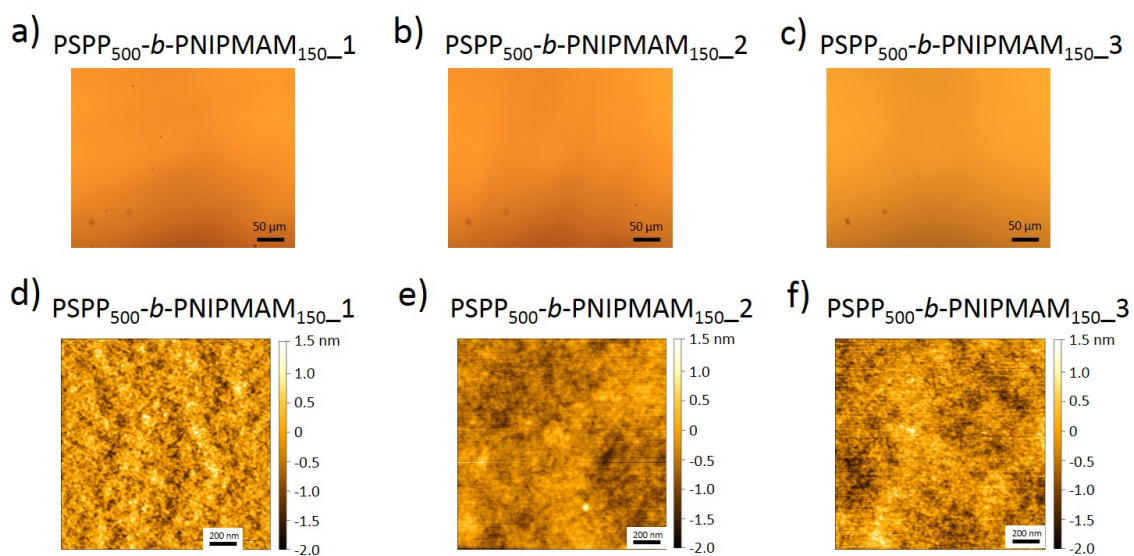


Figure D.1.: Pre-characterization of the three PSPP₅₀₀-*b*-PNIPMAM₁₅₀ thin films investigated in Chapter 8. (a-c) OM images. The two spots in the lower left corner result from a damaged OM lens. (e-f) AFM topography data.

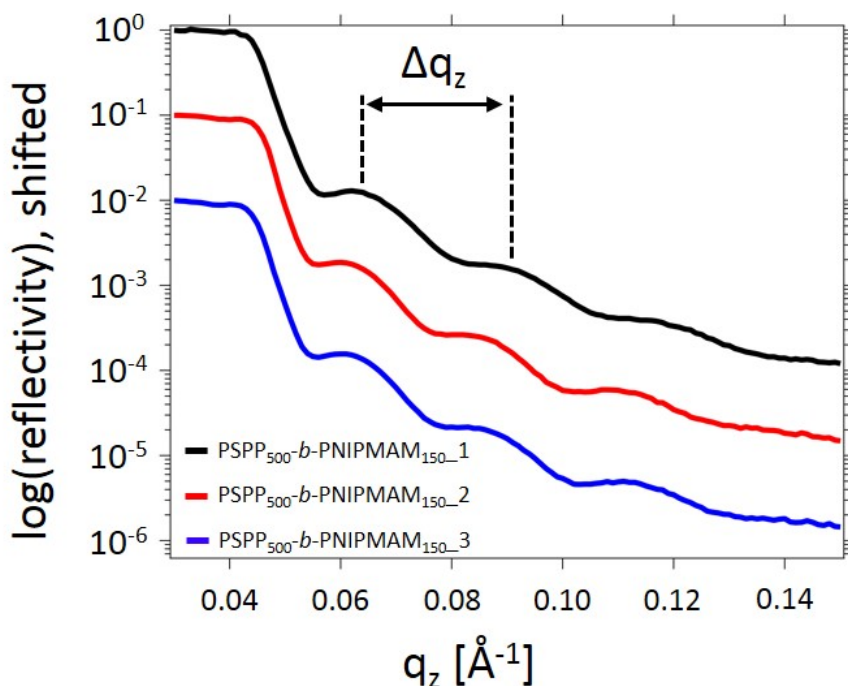


Figure D.2.: XRR data of the PSPP₅₀₀-*b*-PNIPMAM₁₅₀ thin films investigated in Chapter 8. The film thickness is calculated via the distance of two oscillation maxima (Δq) according to Equation 2.35.

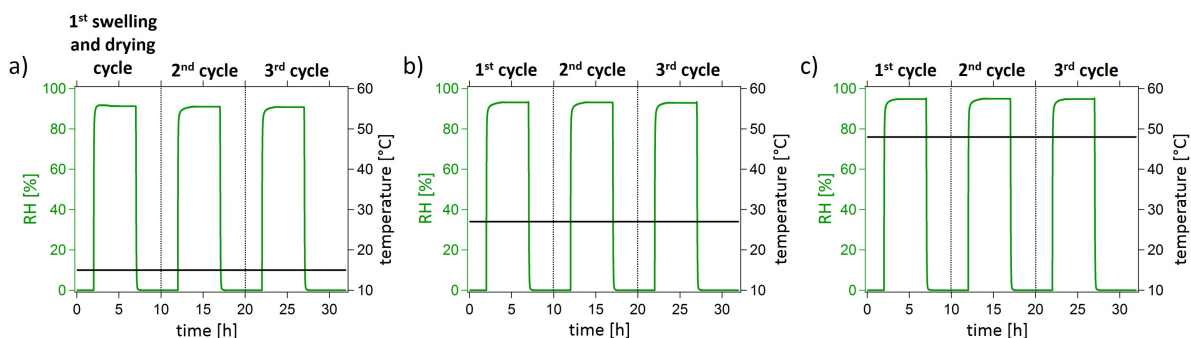


Figure D.3.: RH and temperature during three swelling and drying cycles. Both parameters, RH (green) and temperature (black), as a function of measurement time during three swelling and drying cycles at (a) 15 °C, (b) 27 °C, and (c) 48 °C. The swelling and contraction cycles are labelled accordingly. Adapted with permission from AMERICAN CHEMICAL SOCIETY, Copyright 2020 [38].

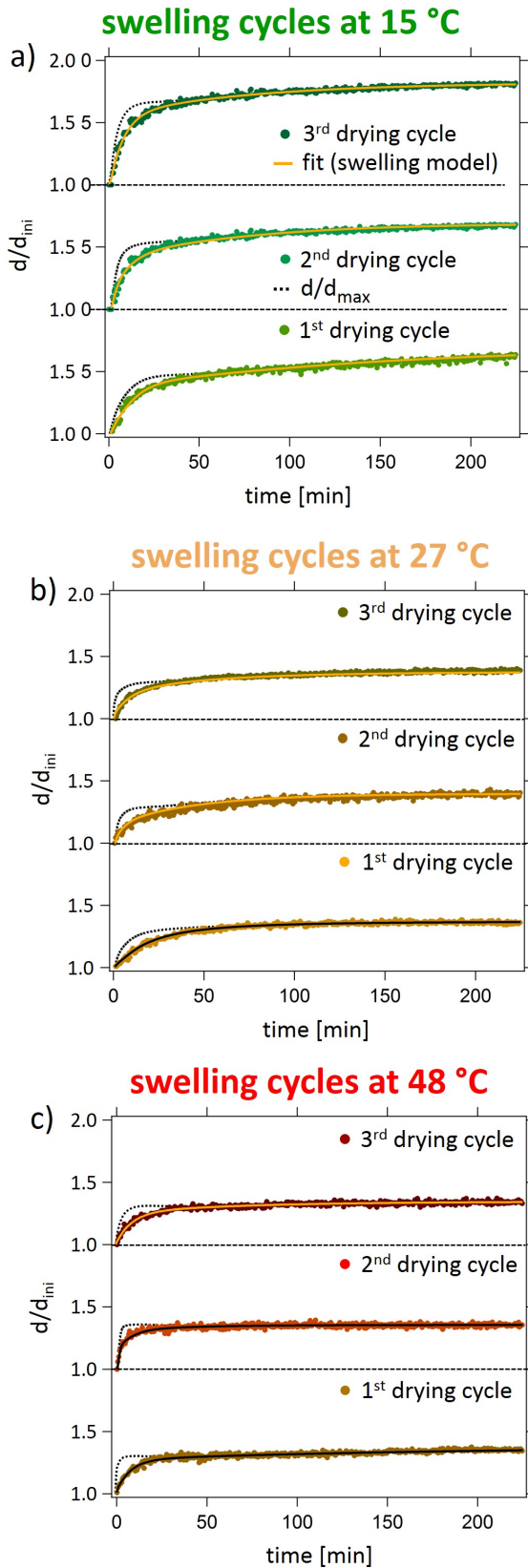


Figure D.4: Cyclic thin film swelling in D_2O vapor followed with SR *in-situ*. The swelling ratio d/d_{ini} as a function of measurement time during three swelling cycles at (a) 15 °C, (b) 27 °C, and (c) 48 °C. The cycle number increases from bottom (first swelling cycle) to top (third swelling cycle). A swelling model is applied to the data as explained in the main text [solid yellow lines, except for the first and second swelling cycle at 48 °C in (c), where it is indicated with a black line]. In addition to the swelling ratio, the maximum swelling ratio d_{max}/d_{ini} is plotted (dashed black lines). Adapted with permission from AMERICAN CHEMICAL SOCIETY, Copyright 2020 [38].

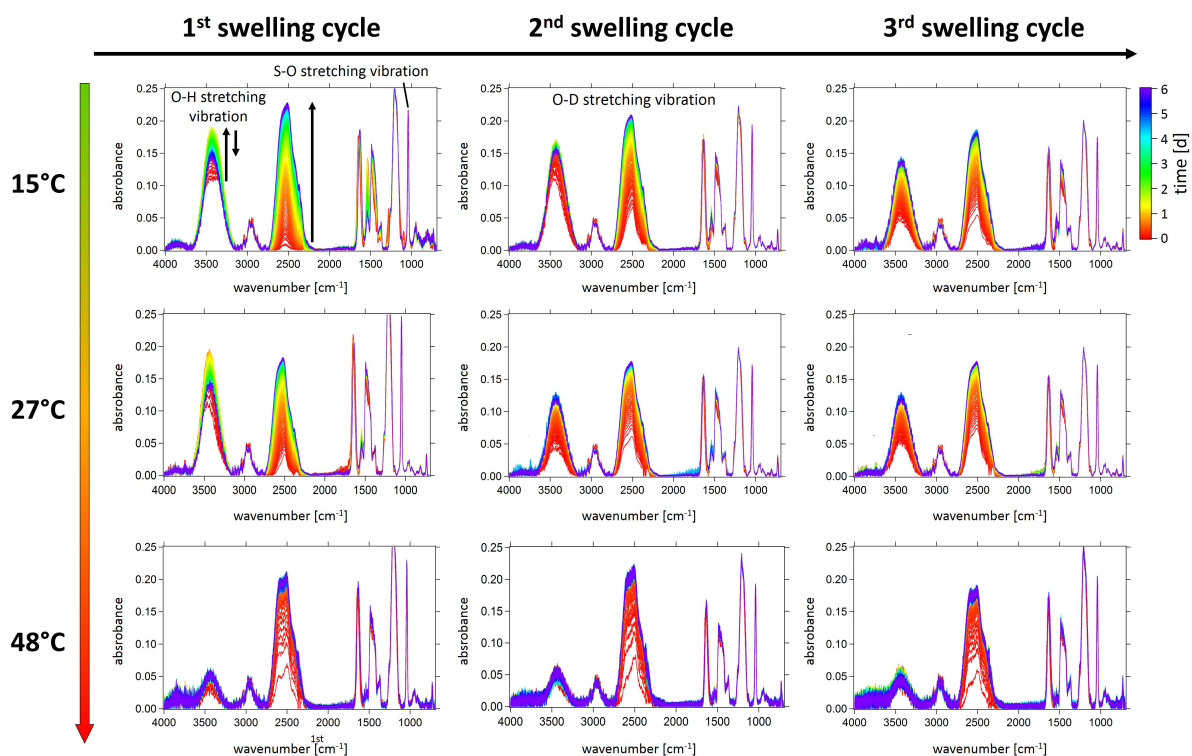


Figure D.5.: FTIR spectra recorded *in-situ* during three swelling cycles in D_2O vapor at different temperatures. From top to bottom the temperature increases, while from left to right the number of swelling cycles increases. In each spectrum, the red curve marks the initial ($t = 0$ days) measurement, the purple curve marks the final measurement after in total 6 days. Characteristic absorption peaks are labelled accordingly. Black arrows mark the increase and decrease of the O-H and the O-D stretching vibration. Adapted with permission from AMERICAN CHEMICAL SOCIETY, Copyright 2020 [38].

E. Appendix for Chapter 5

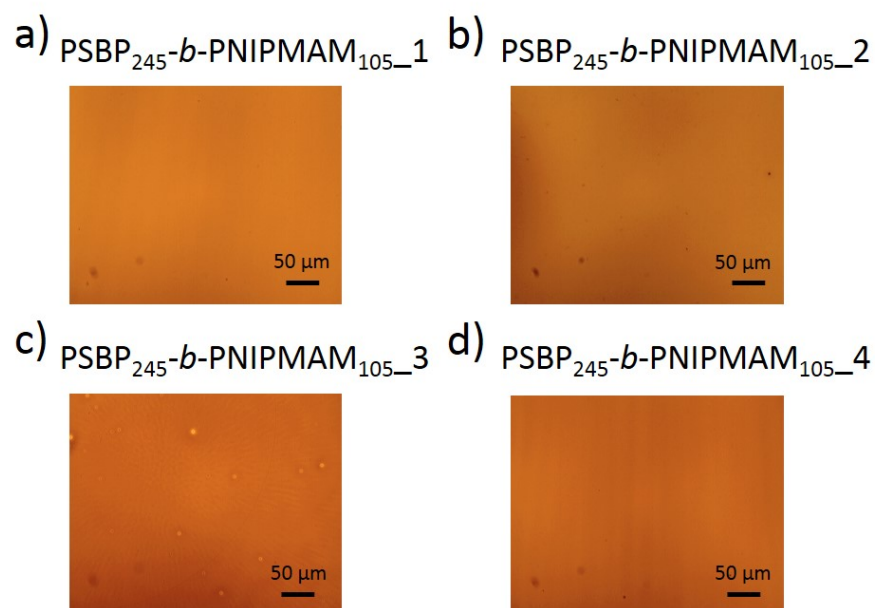


Figure E.1.: OM images of the four PSBP₅₀₀-*b*-PNIPMAM₁₅₀ thin films investigated in Chapter 9. The two spots in the lower left corner result from a damaged OM lens.

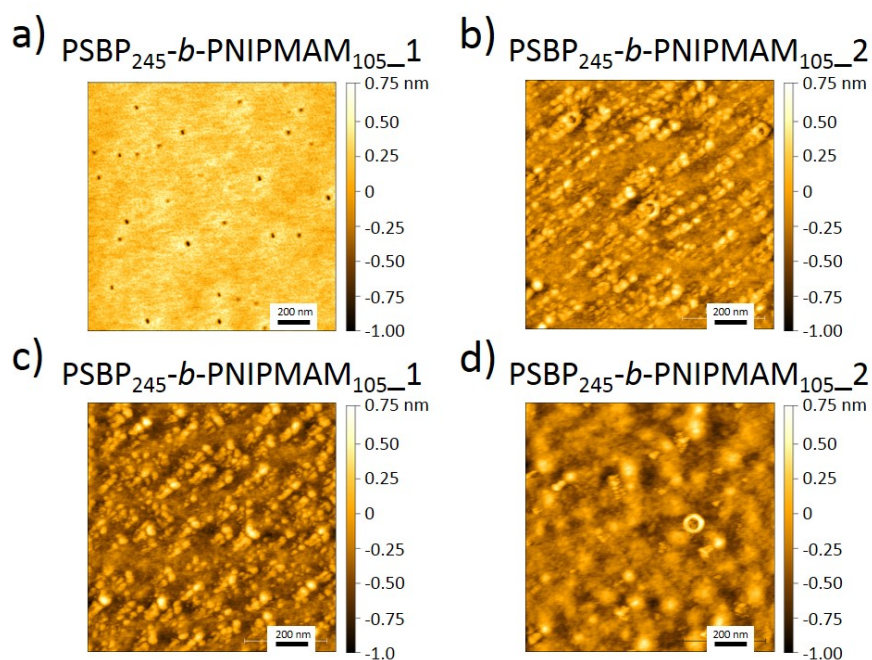


Figure E.2.: AFM topography data of the four $\text{PSBP}_{245}\text{-}b\text{-PNIPMAM}_{105}$ thin films investigated in Chapter 9.

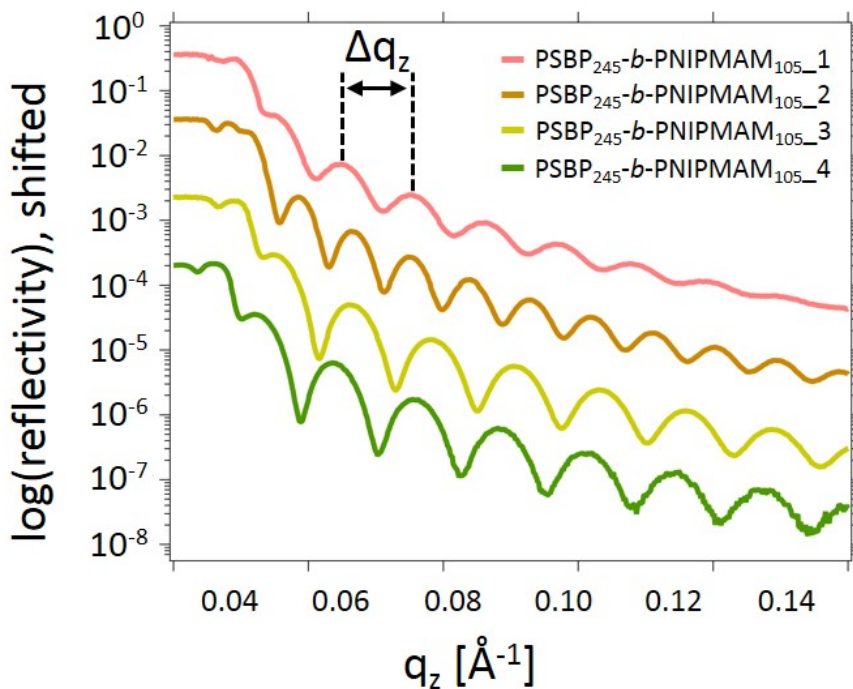


Figure E.3.: XRR data of the $\text{PSBP}_{245}\text{-}b\text{-PNIPMAM}_{105}$ thin films investigated in Chapter 8. The film thickness is calculated via the distance of two oscillation maxima (Δq) according to Equation 2.35.

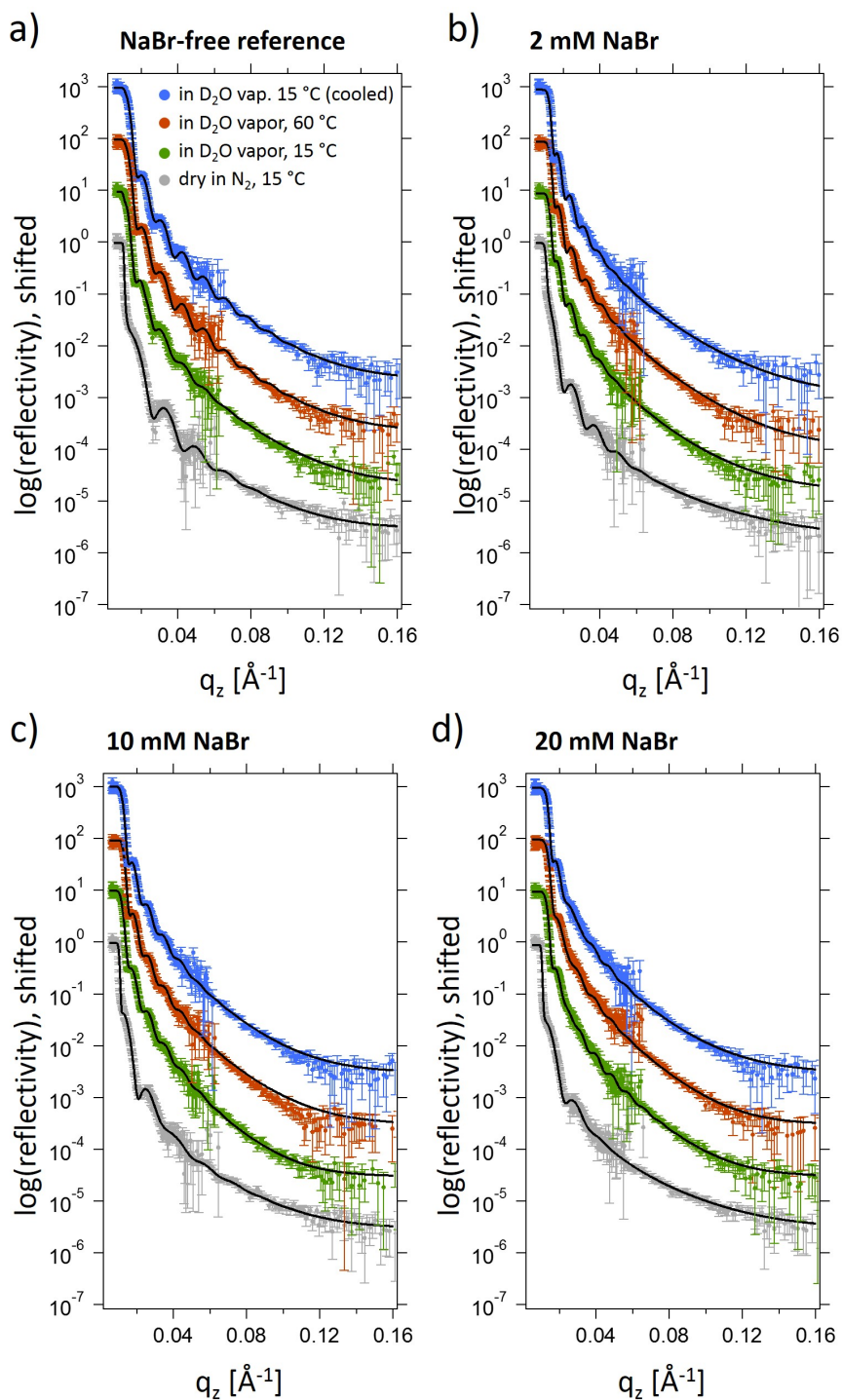


Figure E.4.: Static ToF-NR measurements. ToF-NR curves with the full q_z -range of the equilibrated dry (gray), and the swollen states after the swelling in D_2O vapor (green), heating (red), and cooling (blue) for the thin films spin-coated from (a) NaBr-free, (b) 2 mM, (c) 10 mM, and (d) 20 mM NaBr solution. Best fits are achieved with a two-layer model for the dry state and with a three-layer model for all swollen states.

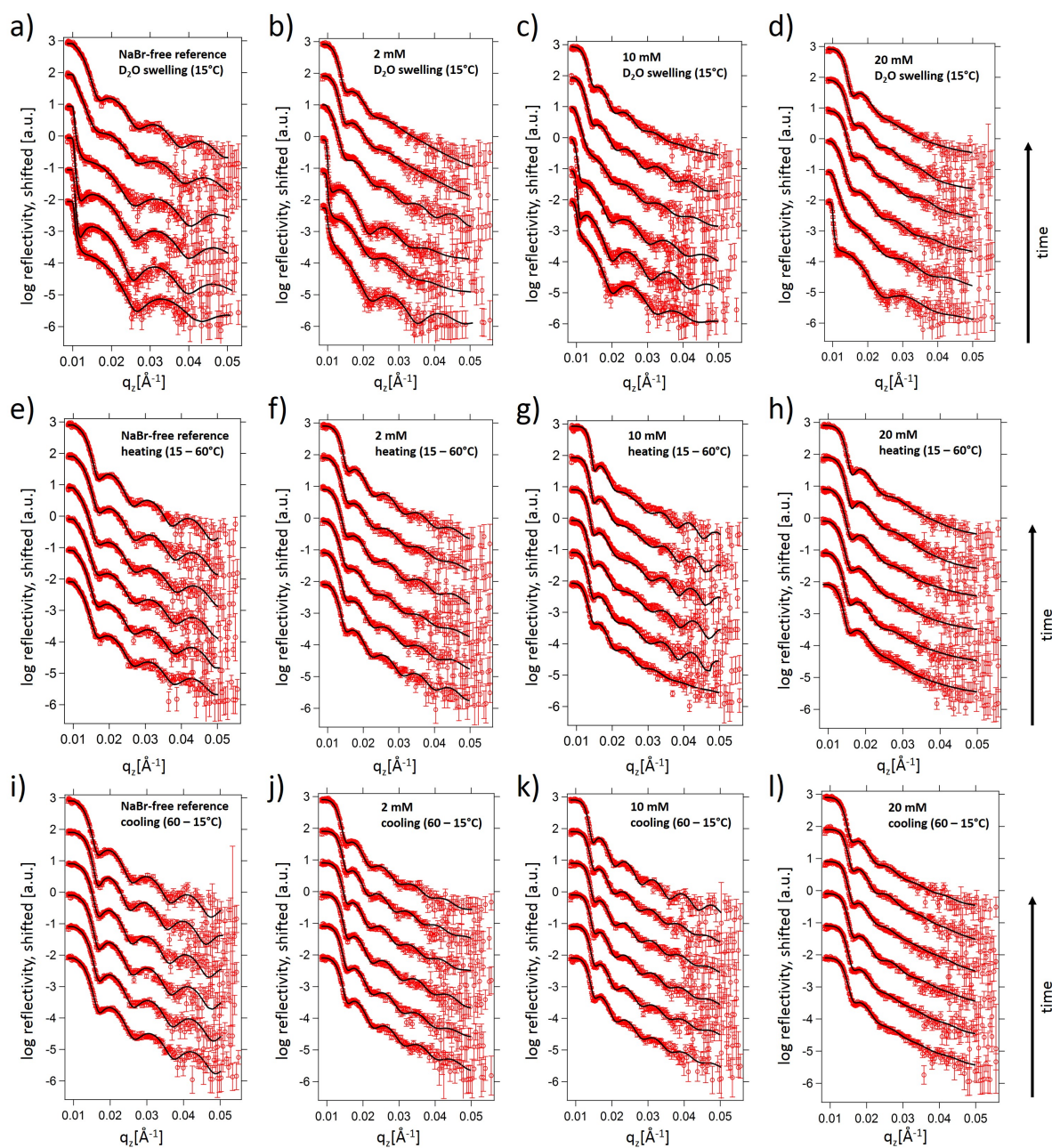


Figure E.5.: Representative selection of ToF-NR curves for the swelling in D_2O vapor, heating, and cooling. Representative ToF-NR data are shown with best model fits (black lines) for the thin films spin-coated from (a,e,i) NaBr-free, (b,f,j) 2 mM, (c,g,k) 10 mM, and (d,h,l) 20 mM NaBr solution, during the (a-d) swelling in D_2O vapor, (e-h) heating, and (i-l) cooling. For the swelling in D_2O vapor, the selected curves (bottom to top) were taken at $t = 0.5, 2, 15, 45, 90,$ and 180 min, while for both heating and cooling, the selected curves (bottom to top) were taken at $t = 0.5, 60, 180, 300, 420,$ and 540 min.

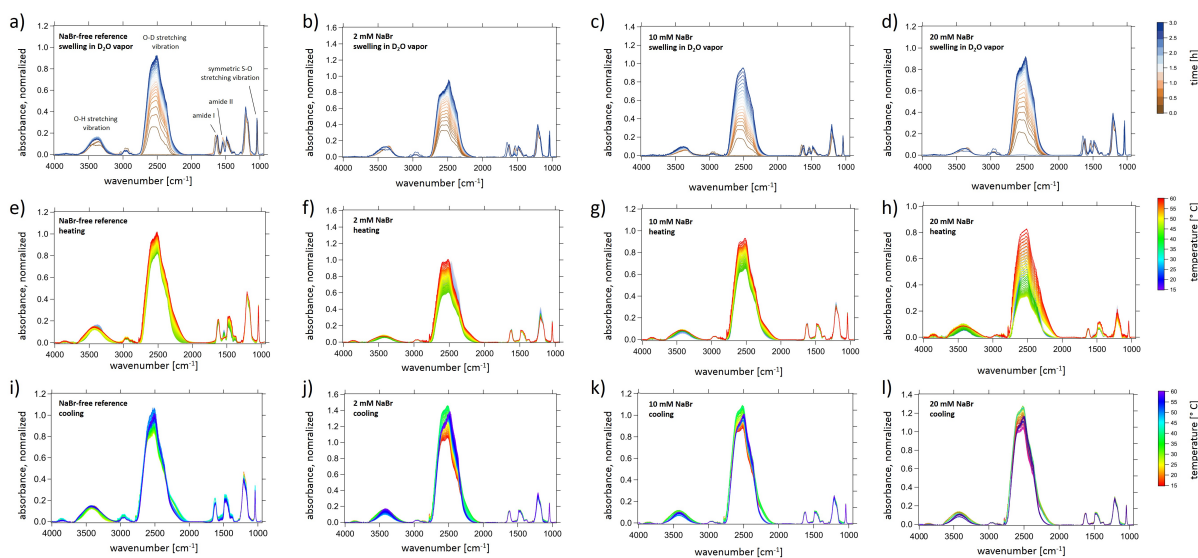


Figure E.6.: FTIR spectra recorded *in-situ* during the swelling in D_2O vapor, heating, and cooling. FTIR spectra of the thin films spin-coated from (a,e,i) NaBr-free reference, (b,f,j) 2 mM, (c,g,k) 10 mM, and (d,h,l) 20 mM NaBr solution, during the (a-d) swelling in D_2O vapor, (e-h) heating, and (i-l) cooling. The color bars refer to time in (a-d) to temperature in (e-l). Characteristic absorption peaks are labelled accordingly.

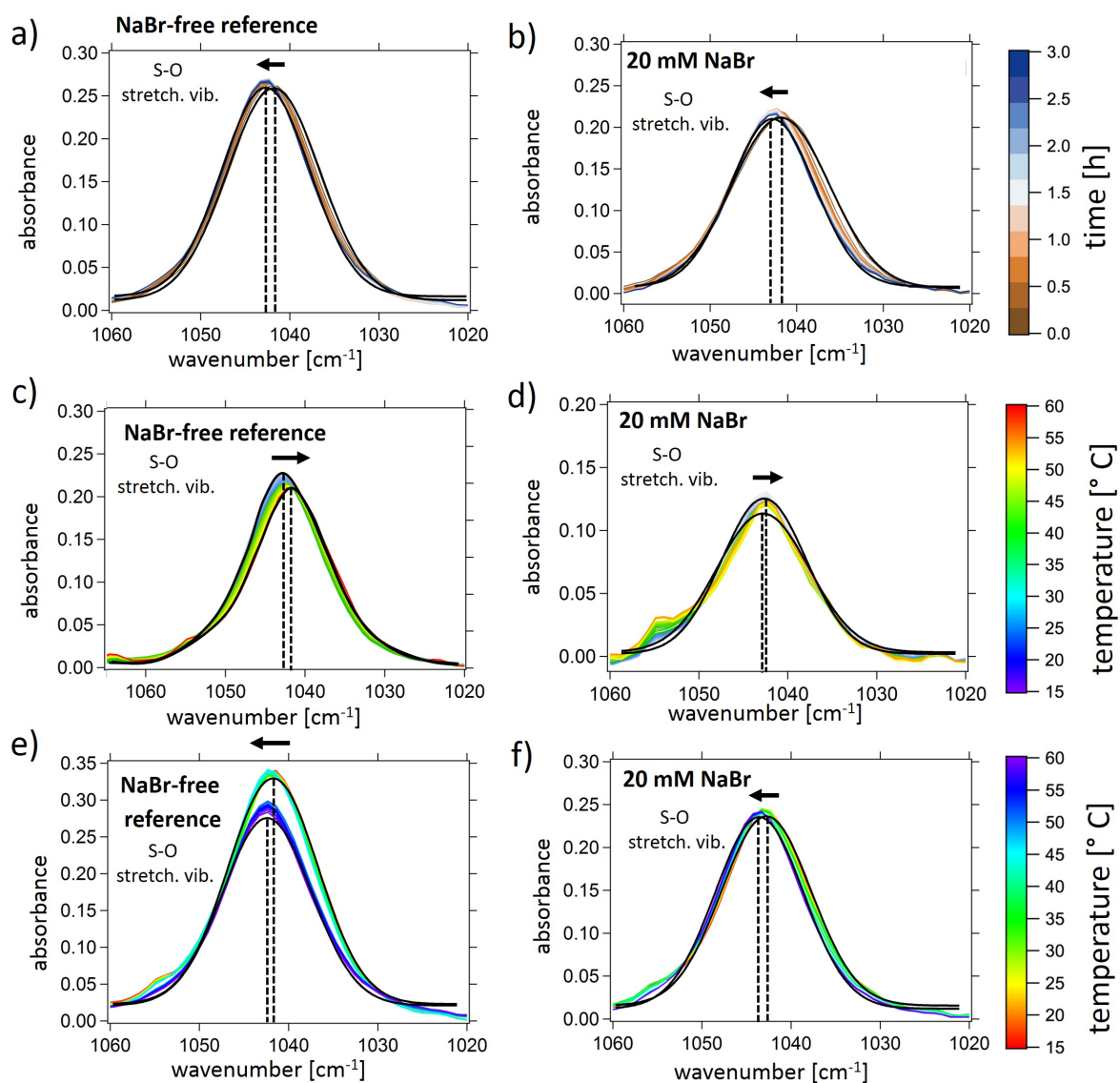


Figure E.7.: Close-up of the S-O stretching vibration probed with FTIR spectroscopy of the PSBP-*b*-PNIPMAM DBC thin film investigated in Chapter 9. Peak shift (black arrows) of the S-O peak during (a,b) swelling, (c,d) heating, and (e,f) cooling of PSBP-*b*-PNIPMAM thin films spin-coated from (a,c,e) NaBr-free and (b,d,f) 20 mM NaBr solution. The Gaussian fit (applied to all FTIR curves) is shown as black line for each first and final S-O absorption peak. Black dashed lines indicate the peak maxima. The extracted peak shift is shown in Figure 9.11.

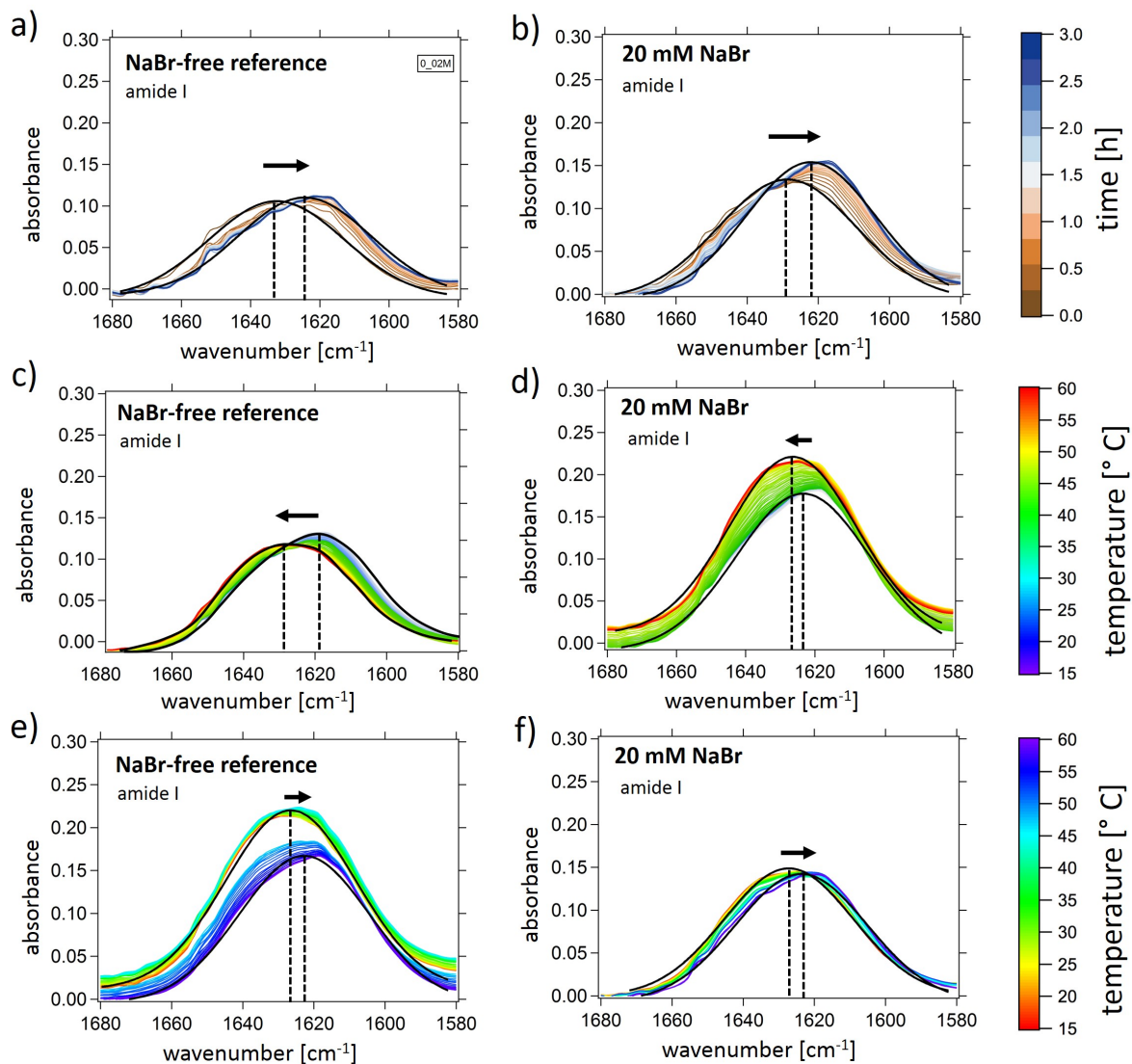


Figure E.8.: Close-up of the amide I peak probed with FTIR spectroscopy of the PSBP-*b*-PNIPMAM DBC thin film investigated in Chapter 9. Peak shift (black arrows) of the amide I peak during (a,b) swelling, (c,d) heating, and (e,f) cooling of PSBP-*b*-PNIPMAM thin films spin-coated from (a,c,e) NaBr-free and (b,d,f) 20 mM NaBr solution. The Gaussian fit (applied to all FTIR curves) is shown as black line for each first and final amide I absorption peak. Black dashed lines indicate the peak maxima. The extracted peak shift is shown in Figure 9.11

Bibliography

- [1] M. A. C. Stuart, W. T. S. Huck, J. Genzer, M. Müller, C. Ober, M. Stamm, G. B. Sukhorukov, I. Szleifer, V. V. Tsukruk, M. Urban, F. Winnik, S. Zauscher, I. Luzinov, and S. Minko, “Emerging applications of stimuli-responsive polymer materials”, *Nat. Mater.*, vol. 9, no. 2, pp. 101–113, 2010. DOI: [10.1038/nmat2614](https://doi.org/10.1038/nmat2614).
- [2] S. M. Mirvakili and I. W. Hunter, “Artificial muscles: Mechanisms, applications, and challenges”, *Adv. Mater.*, vol. 30, no. 6, p. 1704407, 2018. DOI: [10.1002/adma.201704407](https://doi.org/10.1002/adma.201704407).
- [3] A. Ghosh, C. Yoon, F. Ongaro, S. Scheggi, F. M. Selaru, S. Misra, and D. H. Gracias, “Stimuli-responsive soft untethered grippers for drug delivery and robotic surgery”, *Front. Mech. Eng.*, vol. 3, p. 73, 2017. DOI: [10.3389/fmech.2017.00007](https://doi.org/10.3389/fmech.2017.00007).
- [4] H. Priya James, R. John, A. Alex, and K. Anoop, “Smart polymers for the controlled delivery of drugs – a concise overview”, *Acta Pharm. Sin. B.*, vol. 4, no. 2, pp. 120–127, 2014. DOI: <https://doi.org/10.1016/j.apsb.2014.02.005>.
- [5] S. Lakkadwala, S. Nguyen, J. Nesamony, A. S. Narang, and S. H. Boddu, “Smart polymers in drug delivery”, in *Excipient Applications in Formulation Design and Drug Delivery*, A. S. Narang and S. H. S. Boddu, Eds.: Springer International Publishing, 2015, pp. 169–199. DOI: [10.1007/978-3-319-20206-8_7](https://doi.org/10.1007/978-3-319-20206-8_7).
- [6] X. Fu, L. Hosta-Rigau, R. Chandrawati, and J. Cui, “Multi-stimuli-responsive polymer particles, films, and hydrogels for drug delivery”, *Chem.*, vol. 4, no. 9, pp. 2084–2107, 2018. DOI: <https://doi.org/10.1016/j.chempr.2018.07.002>.
- [7] E. Wischerhoff, N. Badi, A. Laschewsky, and J.-F. Lutz, “Smart polymer surfaces: Concepts and applications in biosciences”, *Adv. Polym. Sci.*, vol. 240, pp. 1–33, 2011. DOI: [10.1007/12_2010_88](https://doi.org/10.1007/12_2010_88).
- [8] D. Roy, W. L. A. Brooks, and B. S. Sumerlin, “New directions in thermoresponsive polymers”, *Chem. Soc. Rev.*, vol. 42, no. 17, pp. 7214–7243, 2013. DOI: [10.1039/c3cs35499g](https://doi.org/10.1039/c3cs35499g).

- [9] S. Nagappan, M. S. Moorthy, K. M. Rao, and C.-S. Ha, “Stimuli-responsive smart polymeric coatings: An overview”, in *Industrial Applications for Intelligent Polymers and Coatings*, M. Hosseini and A. S. H. Makhlof, Eds. Cham: Springer International Publishing, 2016, pp. 27–49. DOI: [10.1007/978-3-319-26893-4_2](https://doi.org/10.1007/978-3-319-26893-4_2).
- [10] K. Nagase and T. Okano, “Thermoresponsive-polymer-based materials for temperature-modulated bioanalysis and bioseparations”, *Journal of Materials Chemistry B*, vol. 4, no. 39, pp. 6381–6397, 2016. DOI: [10.1039/C6TB01003B](https://doi.org/10.1039/C6TB01003B).
- [11] P. Esmailzadeh and T. Groth, “Switchable and obedient interfacial properties that grant new biomedical applications”, *ACS Appl. Mater. Interfaces*, vol. 11, no. 29, pp. 25 637–25 653, 2019. DOI: [10.1021/acsami.9b06253](https://doi.org/10.1021/acsami.9b06253).
- [12] L. D. Blackman, P. A. Gunatillake, P. Cass, and K. E. S. Locock, “An introduction to zwitterionic polymer behavior and applications in solution and at surfaces”, *Chem. Soc. Rev.*, vol. 48, no. 3, pp. 757–770, 2019. DOI: [10.1039/c8cs00508g](https://doi.org/10.1039/c8cs00508g).
- [13] M. Wei, Y. Gao, X. Li, and M. J. Serpe, “Stimuli-responsive polymers and their applications”, *Polym. Chem.*, vol. 8, no. 1, pp. 127–143, 2017. DOI: [10.1039/C6PY01585A](https://doi.org/10.1039/C6PY01585A).
- [14] M. Heskins and J. E. Guillet, “Solution properties of poly(*N*-isopropylacrylamide)”, *Journal of Macromolecular Science: Part A - Chemistry*, vol. 2, no. 8, pp. 1441–1455, 1968. DOI: [10.1080/10601326808051910](https://doi.org/10.1080/10601326808051910).
- [15] S. Dai, P. Ravi, and K. C. Tam, “pH-responsive polymers: Synthesis, properties and applications”, *Soft Matter*, vol. 4, pp. 435–449, 3 2008. DOI: [10.1039/B714741D](https://doi.org/10.1039/B714741D).
- [16] T. Tanaka, I. Nishio, S. T. Sun, and S. Ueno-Nishio, “Collapse of gels in an electric field”, *Science*, vol. 218, pp. 467–469, 1982. DOI: [10.1126/science.218.4571.467](https://doi.org/10.1126/science.218.4571.467).
- [17] J. Thévenot, H. Oliveira, O. Sandre, and S. Lecommandoux, “Magnetic responsive polymer composite materials”, *Chem. Soc. Rev.*, vol. 42, pp. 7099–7116, 17 2013. DOI: [10.1039/C3CS60058K](https://doi.org/10.1039/C3CS60058K).
- [18] Y. L. Colson and M. W. Grinstaff, “Biologically responsive polymeric nanoparticles for drug delivery”, *Adv. Mater.*, vol. 24, pp. 3878–3886, 2012. DOI: [10.1002/adma.201200420](https://doi.org/10.1002/adma.201200420).
- [19] V. Aseyev, H. Tenhu, and F. M. Winnik, “Non-ionic thermoresponsive polymers in water”, *Adv. Polym. Sci.*, vol. 242, no. 1, pp. 29–89, 2011. DOI: [10.1007/12_2010_57](https://doi.org/10.1007/12_2010_57).

- [20] Schulz, D., N., Pfeiffer, D., G., K. Agarwal P., Laraee J., J. Kaladas J., Soni L, Handwerker B., and T. Garner R., “Phase behaviour and solution properties of sulphobetaine polymers”, *Polymer*, no. 27, pp. 1734–1742, 1986. DOI: [10.1016/0032-3861\(86\)90269-7](https://doi.org/10.1016/0032-3861(86)90269-7).
- [21] P. Köberle, A. Laschewsky, and T. D. Lomax, “Interactions of a zwitterionic polysoap and its cationic analog with inorganic salts”, *Macromol. Chem. Rapid Commun.*, vol. 12, pp. 427–433, 1991. DOI: [10.1002/marc.1991.030120709](https://doi.org/10.1002/marc.1991.030120709).
- [22] J. Seuring and S. Agarwal, “Polymers with upper critical solution temperature in aqueous solution”, *Macromol. Rapid Commun.*, vol. 33, no. 22, pp. 1898–1920, 2012. DOI: [10.1002/marc.201200433](https://doi.org/10.1002/marc.201200433).
- [23] J. Seuring and S. Agarwal, “Polymers with upper critical solution temperature in aqueous solution: Unexpected properties from known building blocks”, *ACS Macro Letters*, vol. 2, no. 7, pp. 597–600, 2013. DOI: [10.1021/mz400227y](https://doi.org/10.1021/mz400227y).
- [24] H. Yoshimitsu, E. Korchagina, A. Kanazawa, S. Kanaoka, F. M. Winnik, and S. Aoshima, “Shape-switching self-assembly of new diblock copolymers with UCST-type and LCST-type segments in water”, *Polym. Chem.*, vol. 7, pp. 2062–2068, 11 2016. DOI: [10.1039/C5PY01976A](https://doi.org/10.1039/C5PY01976A).
- [25] C. M. Papadakis, P. Müller-Buschbaum, and A. Laschewsky, “Switch it inside-out: ”schizophrenic” behavior of all thermoresponsive UCST-LCST diblock copolymers”, *Langmuir*, vol. 35, no. 30, pp. 9660–9676, 2019. DOI: [10.1021/acs.langmuir.9b01444](https://doi.org/10.1021/acs.langmuir.9b01444).
- [26] N. S. Vishnevetskaya, V. Hildebrand, B.-J. Niebuur, I. Grillo, S. K. Filippov, A. Laschewsky, P. Müller-Buschbaum, and C. M. Papadakis, “Schizophrenic micelles from doubly thermoresponsive polysulfobetaine-*b*-poly(*N*-isopropylmethacrylamide) diblock copolymers”, *Macromolecules*, vol. 50, no. 10, pp. 3985–3999, 2017. DOI: [10.1021/acs.macromol.7b00356](https://doi.org/10.1021/acs.macromol.7b00356).
- [27] N. S. Vishnevetskaya, V. Hildebrand, M. A. Dyakonova, B.-J. Niebuur, K. Kyriakos, K. N. Raftopoulos, Z. Di, P. Müller-Buschbaum, A. Laschewsky, and C. M. Papadakis, “Dual orthogonal switching of the schizophrenic self-assembly of diblock copolymers”, *Macromolecules*, vol. 51, no. 7, pp. 2604–2614, 2018. DOI: [10.1021/acs.macromol.8b00096](https://doi.org/10.1021/acs.macromol.8b00096).
- [28] C. Cummings, H. Murata, R. Koepsel, and A. J. Russell, “Dramatically increased pH and temperature stability of chymotrypsin using dual block polymer-based protein engineering”, *Biomacromolecules*, vol. 15, no. 3, pp. 763–771, 2014. DOI: [10.1021/bm401575k](https://doi.org/10.1021/bm401575k).

- [29] M. Ranka, H. Katepalli, D. Blankschtein, and T. A. Hatton, “Schizophrenic diblock-copolymer-functionalized nanoparticles as temperature-responsive pickering emulsifiers”, *Langmuir*, vol. 33, no. 46, pp. 13 326–13 331, 2017. DOI: [10.1021/acs.langmuir.7b03008](https://doi.org/10.1021/acs.langmuir.7b03008).
- [30] E. G. Kelley, J. N. L. Albert, M. O. Sullivan, and T. H. Epps, “Stimuli-responsive copolymer solution and surface assemblies for biomedical applications”, *Chem. Soc. Rev.*, vol. 42, pp. 7057–7071, 2013. DOI: [10.1039/C3CS35512H](https://doi.org/10.1039/C3CS35512H).
- [31] N. S. Vishnevetskaya, V. Hildebrand, N. M. Nizardo, C.-H. Ko, Z. Di, A. Radulescu, L. C. Barnsley, P. Müller-Buschbaum, A. Laschewsky, and C. M. Papadakis, “All-in-one ”schizophrenic” self-assembly of orthogonally tuned thermoresponsive diblock copolymers”, *Langmuir*, vol. 35, no. 19, pp. 6441–6452, 2019. DOI: [10.1021/acs.langmuir.9b00241](https://doi.org/10.1021/acs.langmuir.9b00241).
- [32] H. Yamauchi and Y. Maeda, “LCST and UCST behavior of poly(*N*-isopropylacrylamide) in DMSO/water mixed solvents studied by IR and micro-Raman spectroscopy”, *J. Phys. Chem. B*, vol. 111, no. 45, pp. 12 964–12 968, 2007. DOI: [10.1021/jp072438s](https://doi.org/10.1021/jp072438s).
- [33] P. W. Zhu and D. H. Napper, “Volume phase transitions of poly(*N*-isopropylacrylamide) Latex Particles in Mixed Water/*N,N*-dimethylformamide solutions”, *Chem. Phys. Lett.*, vol. 256, pp. 51–56, 1996. DOI: [10.1016/0009-2614\(96\)00420-4](https://doi.org/10.1016/0009-2614(96)00420-4).
- [34] K. Dalkas G. Pagonis and G. Bokias, “Control of the lower critical solution temperature-type cononsolvency properties of poly(*N*-isopropylacrylamide) in water-dioxane mixtures through copolymerisation with acrylamide”, *Polymer*, vol. 47, no. 1, pp. 243–248, 2006. DOI: [10.1016/j.polymer.2005.10.115](https://doi.org/10.1016/j.polymer.2005.10.115).
- [35] R. Brighenti, Y. Li, and F. J. Vernerey, “Smart polymers for advanced applications: A mechanical perspective review”, *Frontiers in Materials*, vol. 7, p. 196, 2020, ISSN: 2296-8016. DOI: [10.3389/fmats.2020.00196](https://doi.org/10.3389/fmats.2020.00196).
- [36] L. P. Kreuzer, T. Widmann, N. Hohn, K. Wang, L. Bießmann, L. Peis, J.-F. Moulin, V. Hildebrand, A. Laschewsky, C. M. Papadakis, and P. Müller-Buschbaum, “Swelling and exchange behavior of poly(sulfobetaine)-based block copolymer thin films”, *Macromolecules*, vol. 52, no. 9, pp. 3486–3498, 2019. DOI: [10.1021/acs.macromol.9b00443](https://doi.org/10.1021/acs.macromol.9b00443).
- [37] L. P. Kreuzer, T. Widmann, L. Bießmann, N. Hohn, J. Pantle, R. Märkl, J.-F. Moulin, V. Hildebrand, A. Laschewsky, C. M. Papadakis, and P. Müller-Buschbaum, “Phase transition kinetics of doubly thermoresponsive poly(sulfobetaine)-based diblock copolymer thin films”, *Macromolecules*, vol. 53, no. 8, pp. 2841–2855, 2020. DOI: [10.1021/acs.macromol.0c00046](https://doi.org/10.1021/acs.macromol.0c00046).

- [38] L. P. Kreuzer, T. Widmann, N. Aldosari, L. Bießmann, G. Mangiapia, V. Hildebrand, A. Laschewsky, C. M. Papadakis, and P. Müller-Buschbaum, “Cyclic water storage behavior of doubly thermoresponsive poly(sulfobetaine)-based diblock copolymer thin films”, *Macromolecules*, vol. 53, no. 20, pp. 9108–9121, 2020. DOI: [10.1021/acs.macromol.0c01335](https://doi.org/10.1021/acs.macromol.0c01335).
- [39] L. P. Kreuzer, C. Lindenmeir, C. Geiger, T. Widmann, V. Hildebrand, A. Laschewsky, C. M. Papadakis, and P. Müller-Buschbaum, “Poly(sulfobetaine) versus poly(*N*-isopropylmethacrylamide): Co-nonsolvency-type behavior of thin films in a water/methanol atmosphere”, *Macromolecules*, 2021. DOI: [10.1021/acs.macromol.0c02281](https://doi.org/10.1021/acs.macromol.0c02281).
- [40] F. S. Bates and G. H. Fredrickson, “Block copolymer thermodynamics: Theory and experiment”, *Annu. Rev. Phys. Chem.*, vol. 41, no. 1, pp. 525–557, 1990. DOI: [10.1146/annurev.pc.41.100190.002521](https://doi.org/10.1146/annurev.pc.41.100190.002521).
- [41] G. H. Fredrickson and F. S. Bates, “Dynamics of block copolymers: Theory and experiment”, *Annu. Rev. Mater. Sci.*, vol. 26, no. 1, pp. 501–550, 1996. DOI: [10.1146/annurev.ms.26.080196.002441](https://doi.org/10.1146/annurev.ms.26.080196.002441).
- [42] G. R. Strobl, “The physics of polymers: Concepts for understanding their structures and behavior”, *Springer*, 2007. DOI: [10.1007/978-3-540-68411-4](https://doi.org/10.1007/978-3-540-68411-4).
- [43] P. J. Flory, “Thermodynamics of high polymer solutions”, *J. Chem. Phys.*, vol. 10, no. 1, pp. 51–61, 1942. DOI: [10.1063/1.1723621](https://doi.org/10.1063/1.1723621).
- [44] M. L. Huggins, “Thermodynamic properties of solutions of long-chain compounds”, *Ann. N. Y. Acad. Sci.*, vol. 43, no. 1, pp. 1–32, 1942. DOI: [10.1111/j.1749-6632.1942.tb47940.x](https://doi.org/10.1111/j.1749-6632.1942.tb47940.x).
- [45] I. W. Hamley, “Introduction to soft matter”, *John Wiley & Sons*, 2007. DOI: [10.1002/9780470517338](https://doi.org/10.1002/9780470517338).
- [46] L. Leibler, “Theory of microphase separation in block copolymers”, *Macromolecules*, vol. 13, no. 13, pp. 1602–1617, 1980. DOI: [10.1021/ma60078a047](https://doi.org/10.1021/ma60078a047).
- [47] I. Teraoka, “Polymer solutions: An introduction to physical properties”, *John Wiley & Sons*, 2002. DOI: [10.1002/0471224510](https://doi.org/10.1002/0471224510).
- [48] G. Riess, “Micellization of block copolymers”, *Prog. Polym. Sci.*, vol. 28, pp. 1107–1170, 2003. DOI: [doi:10.1016/S0079-6700\(03\)00015-7](https://doi.org/10.1016/S0079-6700(03)00015-7).
- [49] J.-F. Gohy, “Block copolymer micelles”, *Block Copolymers II; Abetz, V., Ed.; Springer Berlin Heidelberg: Berlin, Heidelberg*, pp. 65–136, 2005. DOI: [10.1007/12_048](https://doi.org/10.1007/12_048).

- [50] A. F. Hannon, W. Bai, A. Alexander-Katz, and C. A. Ross, “Simulation methods for solvent vapor annealing of block copolymer thin films”, *Soft Matter*, vol. 11, pp. 3794–3805, 2015. DOI: [10.1039/C5SM00324E](https://doi.org/10.1039/C5SM00324E).
- [51] T. G. Fox, “Influence of diluent and of copolymer composition on the glass temperature of a polymer system”, *Bull. Am. Phys. Soc.*, vol. 1, p. 123, 1956.
- [52] M. A. Chavis, D.-M. Smilgies, U. B. Wiesner, and C. K. Ober, “Widely tunable morphologies in block copolymer thin films through solvent vapor annealing using mixtures of selective solvents”, *Adv. Funct. Mater.*, vol. 25, pp. 3057–3065, 2015. DOI: [10.1002/adfm.201404053](https://doi.org/10.1002/adfm.201404053).
- [53] T. P. Lodge, B. Pudil, and K. J. Hanley, “The full phase behavior for block copolymers in solvents of varying selectivity”, *Macromolecules*, vol. 35, pp. 4707–4717, 2002. DOI: [10.1021/ma0200975](https://doi.org/10.1021/ma0200975).
- [54] C. A. Jung Y. S.; Ross, “Solvent-vapor-induced tunability of self-assembled block copolymer patterns”, *Adv. Mater*, vol. 21, pp. 2540–2545, 2009. DOI: [10.1002/adma.200802855](https://doi.org/10.1002/adma.200802855).
- [55] M. Y. Paik, J. K. Bosworth, D.-M. Smilgies, E. L. Schwartz, X. Andre, and C. K. Ober, “Reversible morphology control in block copolymer films via solvent vapor processing: An in situ GISAXS study”, *Macromolecules*, vol. 43, pp. 4253–4260, 2010. DOI: [10.1021/ma902646t](https://doi.org/10.1021/ma902646t).
- [56] K. W. Gotrik, A. F. Hannon, J. G. Son, B. Keller, A. Alexander-Katz, and C. A. Ross, “Morphology control in block copolymer films using mixed solvent vapors”, *ACS Nano*, vol. 6, pp. 8052–8059, 2012. DOI: [10.1021/nn302641z](https://doi.org/10.1021/nn302641z).
- [57] A. V. Berezkin, F. Jung, D. Posselt, D.-M. Smilgies, and C. M. Papadakis, “In situ tracking of composition and morphology of a diblock copolymer film with GISAXS during exchange of solvent vapors at elevated temperatures”, *Adv. Funct. Mater.*, vol. 41, p. 1706226, 2018. DOI: [10.1002/adfm.201706226](https://doi.org/10.1002/adfm.201706226).
- [58] T. Graves-Abe, F. Pschenitzka, H. Z. Jin, B. Bollman, J. C. Sturm, and R. A. Register, “Solvent-enhanced dye diffusion in polymer thin films for polymer light-emitting diode application”, *J. Appl. Phys.*, vol. 96, no. 12, pp. 7154–7163, 2004. DOI: [10.1063/1.1806548](https://doi.org/10.1063/1.1806548).
- [59] W. Wang, E. Metwalli, J. Perlich, C. M. Papadakis, R. Cubitt, and P. Müller-Buschbaum, “Cyclic switching of water storage in thin block copolymer films containing poly(*N*-isopropylacrylamide)”, *Macromolecules*, vol. 42, no. 22, pp. 9041–9051, 2009. DOI: [10.1021/ma901751n](https://doi.org/10.1021/ma901751n).

- [60] S. Bhattacharya, D. K. Sharma, S. Saurabh, S. De, A. Sain, A. Nandi, and A. Chowdhury, “Plasticization of poly(vinylpyrrolidone) thin films under ambient humidity: Insight from single-molecule tracer diffusion dynamics”, *J. Phys. Chem. B*, vol. 117, no. 25, pp. 7771–7782, 2013. DOI: [10.1021/jp401704e](https://doi.org/10.1021/jp401704e).
- [61] H. Tang, B. Zhang, and P. Wu, “On the two-step phase transition behavior of the poly(*N*-isopropylacrylamide) (PNIPAM) Brush: Different zones with different orders”, *Soft Matter*, vol. 10, no. 37, pp. 7278–7284, 2014. DOI: [10.1039/c4sm01182a](https://doi.org/10.1039/c4sm01182a).
- [62] I. Bischofberger and V. Trappe, “New aspects in the phase behaviour of poly-*N*-isopropylacrylamide: Systematic temperature dependent shrinking of PNiPAM assemblies well beyond the lcst”, *Sci. Rep.*, vol. 5, p. 15520, 2015. DOI: [10.1038/srep15520](https://doi.org/10.1038/srep15520).
- [63] S. Micciulla, O. Soltwedel, O. Löhmann, and R. von Klitzing, “Temperature responsive behavior of polymer brush/polyelectrolyte multilayer composites”, *Soft Matter*, vol. 12, no. 4, pp. 1176–1183, 2016. DOI: [10.1039/c5sm02256h](https://doi.org/10.1039/c5sm02256h).
- [64] D. W. Janes, V. Chandrasekar, S. E. Woolford, and K. B. Ludwig, “Predicting the effects of composition, molecular size and shape, plasticization, and swelling on the diffusion of aromatic additives in block copolymers”, *Macromolecules*, vol. 50, no. 16, pp. 6137–6148, 2017. DOI: [10.1021/acs.macromol.7b00690](https://doi.org/10.1021/acs.macromol.7b00690).
- [65] N. Vergadou and D. N. Theodorou, “Molecular modeling investigations of sorption and diffusion of small molecules in glassy polymers”, *Membranes*, vol. 9, no. 8, p. 98, 2019. DOI: [10.3390/membranes9080098](https://doi.org/10.3390/membranes9080098).
- [66] M. J. Serpe, K. A. Yarmey, C. M. Nolan, and L. A. Lyon, “Doxorubicin uptake and release from microgel thin films”, *Biomacromolecules*, vol. 6, no. 1, pp. 408–413, 2005. DOI: [10.1021/bm049455x](https://doi.org/10.1021/bm049455x).
- [67] T. Widmann, L. P. Kreuzer, N. Hohn, L. Bießmann, K. Wang, S. Rinner, J.-F. Moulin, A. J. Schmid, Y. Hannappel, O. Wrede, M. Kühnhammer, T. Hellweg, R. von Klitzing, and P. Müller-Buschbaum, “Hydration and solvent exchange induced swelling and deswelling of homogeneous poly(*N*-isopropylacrylamide) Microgel Thin Films”, *Langmuir*, vol. 35, no. 49, pp. 16341–16352, 2019. DOI: [10.1021/acs.langmuir.9b03104](https://doi.org/10.1021/acs.langmuir.9b03104).
- [68] W. Wang, E. Metwalli, J. Perlich, K. Troll, C. M. Papadakis, R. Cubitt, and P. Müller-Buschbaum, “Water storage in thin films maintaining the total film thickness as probed with in situ neutron reflectivity”, *Macromol. Rapid Commun.*, vol. 30, no. 2, pp. 114–119, 2009. DOI: [10.1002/marc.200800576](https://doi.org/10.1002/marc.200800576).

- [69] Y. Li and T. Tanaka, “Kinetics of swelling and shrinking of gels”, *J. Chem. Phys.*, vol. 92, no. 2, pp. 1365–1371, 1990. DOI: [10.1063/1.458148](https://doi.org/10.1063/1.458148).
- [70] J. Jaczewska, I. Raptis, A. Budkowski, D. Goustouridis, J. Raczowska, M. Sano-poulou, E. Pamuła, A. Bernasik, and J. Rysz, “Swelling of poly(3-alkylthiophene) films exposed to solvent vapors and humidity: Evaluation of solubility parameters”, *Synth. Met.*, vol. 157, no. 18-20, pp. 726–732, 2007. DOI: [10.1016/j.synthmet.2007.07.015](https://doi.org/10.1016/j.synthmet.2007.07.015).
- [71] C. Wu and C. Y. Yan, “Studies of the swelling and drying kinetics of thin gelatin gel films by in-situ interferometry”, *Macromolecules*, vol. 27, 4516-4520, 1994. DOI: [10.1021/ma00094a013](https://doi.org/10.1021/ma00094a013).
- [72] D. W. Schubert and T. Dunkel, “In-situ interferometry studies of the drying and swelling kinetics of an ultrathin poly(*N*-isopropylacrylamide) Gel Film below and above Its Volume Phase Transition Temperature”, *Mater. Res. Innov.*, vol. 29, 4998-5001, 1996. DOI: [10.1007/s10019-003-0270-2](https://doi.org/10.1007/s10019-003-0270-2).
- [73] D. Magerl, M. Philipp, X.-P. Qiu, F. M. Winnik, and P. Müller-Buschbaum, “Swelling and thermoresponsive behavior of linear versus cyclic poly(*N*-isopropyl acrylamide) Thin Films”, *Macromolecules*, vol. 48, no. 9, pp. 3104–3111, 2015. DOI: [10.1021/acs.macromol.5b00436](https://doi.org/10.1021/acs.macromol.5b00436).
- [74] D. Magerl, M. Philipp, E. Metwalli, P. Gutfreund, X.-P. Qiu, F. M. Winnik, and P. Müller-Buschbaum, “Influence of confinement on the chain conformation of cyclic poly(*N*-isopropylacrylamide)”, *ACS Macro Letters*, vol. 4, no. 12, pp. 1362–1365, 2015. DOI: [10.1021/acsmacrolett.5b00676](https://doi.org/10.1021/acsmacrolett.5b00676).
- [75] L. Bießmann, “Functional layers for enhanced photon extraction in ito-free oleds”, *PhD thesis. München: Technische Universität München, Fakultät für Physik*, 2019.
- [76] L. Klouda, “Thermoresponsive hydrogels in biomedical applications: A seven-year update”, *Eur. J. Pharm.*, vol. 97, no. Pt B, pp. 338–349, 2015. DOI: [10.1016/j.ejpb.2015.05.017](https://doi.org/10.1016/j.ejpb.2015.05.017).
- [77] N. Badi, “Non-linear PEG-based thermoresponsive polymer systems”, *Prog. Polym. Sci.*, vol. 66, pp. 54–79, 2017. DOI: [10.1016/j.progpolymsci.2016.12.006](https://doi.org/10.1016/j.progpolymsci.2016.12.006).
- [78] M. Hruby, P. Štěpánek, J. Pánek, and C. M. Papadakis, “Crosstalk between responsiveness to various stimuli in multiresponsive polymers: Change in polymer chain and external environment polarity as the key factor”, *Colloid Polym. Sci.*, vol. 297, no. 11-12, pp. 1383–1401, 2019. DOI: [10.1007/s00396-019-04576-5](https://doi.org/10.1007/s00396-019-04576-5).

- [79] D. Mukherji, C. M. Marques, and K. Kremer, “Smart responsive polymers: Fundamentals and design principles”, *Annu. Rev. Condens. Matter Phys.*, vol. 11, no. 1, pp. 271–299, 2020. DOI: [10.1146/annurev-conmatphys-031119-050618](https://doi.org/10.1146/annurev-conmatphys-031119-050618).
- [80] A. S. Hoffman, “Applications of thermally reversible polymers and hydrogels in therapeutics and diagnostics”, *J. Control. Release*, vol. 6, no. 1, pp. 297–305, 1987. DOI: [https://doi.org/10.1016/0168-3659\(87\)90083-6](https://doi.org/10.1016/0168-3659(87)90083-6).
- [81] E. Cabane, X. Zhang, K. Langowska, C. G. Palivan, and W. Meier, “Stimuli-responsive polymers and their applications in nanomedicine”, *Biointerphases*, vol. 7, no. 9, pp. 1–27, 2012. DOI: [10.1007/s13758-011-0009-3](https://doi.org/10.1007/s13758-011-0009-3).
- [82] N. Vijayakameswara Rao, H. Ko, J. Lee, and J. H. Park, “Recent progress and advances in stimuli-responsive polymers for cancer therapy”, *Front. Bioeng. Biotechnol.*, vol. 6, no. 110, pp. 1–15, 2018. DOI: [10.3389/fbioe.2018.00110](https://doi.org/10.3389/fbioe.2018.00110).
- [83] I. Tokarev and S. Minko, “Stimuli-responsive hydrogel thin films”, *Soft Matter*, vol. 5, no. 3, pp. 511–524, 2009. DOI: [10.1039/B813827C](https://doi.org/10.1039/B813827C).
- [84] E. M. White, J. B. Yatvin J. and Grubbs III, J. A. Bilbrey, and J. Locklin, “Advances in smart materials: Stimuli-responsive hydrogel thin films”, *J. Polym. Sci. B Polym. Phys.*, vol. 51, pp. 1084–1099, 2013. DOI: [10.1002/polb.23312](https://doi.org/10.1002/polb.23312).
- [85] B. D. Kieviet, P. M. Schön, and G. Vancso, “Stimulus-responsive polymers and other functional polymer surfaces as components in glass microfluidic channels”, *Lab Chip*, vol. 14, pp. 4159–4170, 2014. DOI: [10.1039/C4LC00784K](https://doi.org/10.1039/C4LC00784K).
- [86] J.-K. Chen and C.-J. Chang, “Fabrications and applications of stimulus-responsive polymer films and patterns on surfaces: A review.”, *Materials*, vol. 7, pp. 805–875, 2014. DOI: [10.3390/ma7020805](https://doi.org/10.3390/ma7020805).
- [87] Richter A., Paschew G., Klatt S., Lienig J., Arndt K.-F., and Adler H.-J. P., “Review on hydrogel-based pH sensors and microsensors”, *Sensors*, no. 8, pp. 561–581, 2008. DOI: [10.3390/s8010561](https://doi.org/10.3390/s8010561).
- [88] D. Wang, L. Tao, Y. Jun, and L. Shiyong, “Stimuli-responsive fluorescent poly(*N*-isopropylacrylamide) microgels labeled with phenylboronic acid moieties as multifunctional ratiometric probes for glucose and temperatures”, *Macromolecules*, vol. 44, no. 7, pp. 2282–2290, 2011. DOI: [10.1021/ma200053a](https://doi.org/10.1021/ma200053a).
- [89] J. Kim, S. Nayak, and L. A. Lyon, “Bioresponsive hydrogel microlenses”, *J. Am. Chem. Soc.*, vol. 127, no. 26, pp. 9588–9592, 2005. DOI: [10.1021/ja0519076](https://doi.org/10.1021/ja0519076).
- [90] J. Hu and S. Liu, “Responsive polymers for detection and sensing applications: Current status and future developments”, *Macromolecules*, vol. 43, no. 20, pp. 8315–8330, 2010. DOI: [10.1021/ma1005815](https://doi.org/10.1021/ma1005815).

- [91] Schild H. G., Muthukumar M., and Tirrell D. A., “Cononsolvency in mixed aqueous solutions of poly(*N*-isopropylacrylamide)”, *Macromolecules*, vol. 24, pp. 948–952, 1991. DOI: [10.1021/ma00004a022](https://doi.org/10.1021/ma00004a022).
- [92] Winnik F. M., Ringsdorf H, and Venzmer J., “Methanol-water as a co-nonsolvent system for poly(*N*-isopropylacrylamide)”, *Macromolecules*, vol. 23, pp. 2415–2416, 1990. DOI: [10.1021/ma00210a048](https://doi.org/10.1021/ma00210a048).
- [93] Y. Lu, K. Zhou, Y. Ding, G. Zhang, and C. Wu, “Origin of hysteresis observed in association and dissociation of polymer chains in water”, *Phys. Chem. Chem. Phys.*, vol. 12, pp. 3188–3194, 13 2010. DOI: [10.1039/B918969F](https://doi.org/10.1039/B918969F).
- [94] J. Seuring, F. M. Bayer, K. Huber, and S. Agarwal, “Upper critical solution temperature of poly(*N*-acryloyl glycinamide) in water: A concealed property”, *Macromolecules*, vol. 45, no. 1, pp. 374–384, 2012. DOI: [10.1021/ma202059t](https://doi.org/10.1021/ma202059t).
- [95] C. Zhao, Z. Ma, and X. X. Zhu, “Rational design of thermoresponsive polymers in aqueous solutions: A thermodynamics map.”, *Prog. Polym. Sci.*, vol. 90, pp. 269–291, 2019. DOI: [10.1016/j.progpolymsci.2019.01.001](https://doi.org/10.1016/j.progpolymsci.2019.01.001).
- [96] J. Niskanen and H. Tenhu, “How to manipulate the upper critical solution temperature (UCST)?”, *Polym. Chem.*, vol. 8, no. 1, pp. 220–232, 2017. DOI: [10.1039/C6PY01612J](https://doi.org/10.1039/C6PY01612J).
- [97] A. S. Hoffman, “Stimuli-responsive polymers: Biomedical applications and challenges for clinical translation”, *Adv. Drug Delivery Rev.*, vol. 65, pp. 10–16, 2013. DOI: [10.1016/j.addr.2012.11.004](https://doi.org/10.1016/j.addr.2012.11.004).
- [98] A. Laschewsky, P. Müller-Buschbaum, and C. M. Papadakis, “Thermoresponsive amphiphilic di- and triblock copolymers based on poly(*N*-isopropylacrylamide) and Poly(methoxy diethylene glycol acrylate): Aggregation and hydrogel formation in bulk solution and in thin films”, *Prog. Colloid Polym. Sci.*, vol. 140, pp. 15–34, 2013. DOI: [10.1007/978-3-319-01683-2_2](https://doi.org/10.1007/978-3-319-01683-2_2).
- [99] H. R. Culver, J. R. Clegg, and N. A. Peppas, “Analyte-responsive hydrogels: Intelligent materials for biosensing and drug delivery.”, *Acc. Chem. Res.*, vol. 50, pp. 170–178, 2017. DOI: [10.1021/acs.accounts.6b00533](https://doi.org/10.1021/acs.accounts.6b00533).
- [100] I. Dimitrov, B. Trzebicka, A. H. E. Müller, A. Dworak, and C. B. Tsvetanov, “Thermosensitive water-soluble copolymers with doubly responsive reversibly interacting entities”, *Prog. Polym. Sci.*, vol. 32, pp. 1275–1343, 2007. DOI: [10.1016/j.progpolymsci.2007.07.001](https://doi.org/10.1016/j.progpolymsci.2007.07.001).

- [101] P. Schattling, F. D. Jochum, and P. Theato, “Multi-stimuli responsive polymers - the all-in-one talents”, *Polym. Chem.*, vol. 5, pp. 25–36, 2014. DOI: [10.1039/C3PY00880K](https://doi.org/10.1039/C3PY00880K).
- [102] S. Strandman and X. X. Zhu, “Thermo-responsive block copolymers with multiple phase transition temperatures in aqueous solutions”, *Prog. Polym. Sci.*, vol. 42, pp. 154–176, 2015. DOI: [10.1016/j.progpolymsci.2014.10.008](https://doi.org/10.1016/j.progpolymsci.2014.10.008).
- [103] Y. Kotsuchibashi, M. Ebara, T. Aoyagi, and R. Narain, “Recent advances in dual temperature responsive block copolymers and their potential as biomedical applications”, *Polymers*, vol. 8, no. 11, 2016. DOI: [10.3390/polym8110380](https://doi.org/10.3390/polym8110380).
- [104] K. Skrabania, J. Kristen, A. Laschewsky, O. Akdemir, A. Hoth, and J.-F. Lutz, “Design, synthesis, and aqueous aggregation behavior of nonionic single and multiple thermoresponsive polymers”, *Langmuir*, vol. 23, no. 1, pp. 84–93, 2007. DOI: [10.1021/1a061509w](https://doi.org/10.1021/1a061509w).
- [105] J. Weiss and A. Laschewsky, “Temperature-induced self-assembly of triple-responsive triblock copolymers in aqueous solutions”, *Langmuir*, vol. 27, no. 8, pp. 4465–4473, 2011. DOI: [10.1021/1a200115p](https://doi.org/10.1021/1a200115p).
- [106] M. Arotçaréna, B. Heise, S. Ishaya, and A. Laschewsky, “Switching the inside and the outside of aggregates of water-soluble block copolymers with double thermoresponsivity”, *J. Am. Chem. Soc.*, vol. 124, no. 14, pp. 3787–3793, 2002. DOI: [10.1021/ja012167d](https://doi.org/10.1021/ja012167d).
- [107] J. Virtanen, M. Arotçaréna, B. Heise, S. Ishaya, A. Laschewsky, and H. Tenhu, “Dissolution and aggregation of a poly(nipa-block-sulfobetaine) copolymer in water and saline aqueous solutions”, *Langmuir*, vol. 18, no. 14, pp. 5360–5365, 2002. DOI: [10.1021/1a0118208](https://doi.org/10.1021/1a0118208).
- [108] M. Mertoglu, S. Garnier, A. Laschewsky, K. Skrabania, and J. Storsberg, “Stimuli responsive amphiphilic block copolymers for aqueous media synthesised via reversible addition fragmentation chain transfer polymerisation (RAFT)”, *Polymer*, vol. 46, no. 18, pp. 7726–7740, 2005. DOI: [10.1016/j.polymer.2005.03.101](https://doi.org/10.1016/j.polymer.2005.03.101).
- [109] Y. Cai, Y. Tang, and S. P. Armes, “Direct synthesis and stimulus-responsive micellization of y-shaped hydrophilic block copolymers”, *Macromolecules*, vol. 37, no. 26, pp. 9728–9737, 2004. DOI: [10.1021/ma0487756](https://doi.org/10.1021/ma0487756).
- [110] Y. Cai and S. P. Armes, “Synthesis of well-defined y-shaped zwitterionic block copolymers via atom-transfer radical polymerization”, *Macromolecules*, vol. 38, no. 2, pp. 271–279, 2005. DOI: [10.1021/ma048511j](https://doi.org/10.1021/ma048511j).

- [111] J. V. M. Weaver, S. P. Armes, and V. Bütün, “Synthesis and aqueous solution properties of a well-defined thermo-responsive schizophrenic diblock copolymer”, *Chem. Commun. (Cambridge, U. K.)*, no. 18, pp. 2122–2123, 2002. DOI: [10.1039/b207251n](https://doi.org/10.1039/b207251n).
- [112] V. Bütün, S. Liu, J. Weaver, X. Bories-Azeau, Y. Cai, and S. P. Armes, “A brief review of ‘schizophrenic’ block copolymers”, *React. Funct. Polym.*, vol. 66, pp. 157–165, 2006. DOI: [10.1016/j.reactfunctpolym.2005.07.021](https://doi.org/10.1016/j.reactfunctpolym.2005.07.021).
- [113] A. B. Lowe and C. L. McCormick, “Synthesis and solution properties of zwitterionic polymers”, *Chem. Rev.*, vol. 102, pp. 4177–4190, 2002.
- [114] A. Laschewsky, “Structures and synthesis of zwitterionic polymers”, *Polymers*, vol. 6, pp. 1544–1601, 2014. DOI: [10.1021/cr020371t](https://doi.org/10.1021/cr020371t).
- [115] J. C. Galin, “Polyzwitterions (overview)”, *Polymer Materials Encyclopedia*, vol. 9, 1996.
- [116] J. B. Schlenoff, “Zwitteration: Coating surfaces with zwitterionic functionality to reduce nonspecific adsorption”, *Langmuir*, vol. 30, no. 32, pp. 9625–9636, 2014. DOI: [10.1021/la500057j](https://doi.org/10.1021/la500057j).
- [117] B. Mojtaba, K. Maryam, and D. U. Larry, “Poly(ethylene glycol) and poly(carboxy betaine) based nonfouling architectures: Review and current efforts”, *Proteins at Interfaces III State of the Art (ACS Symposium Series, 1120)*, vol. 1120, pp. 621–643, 2012. DOI: [10.1021/bk-2012-1120.ch028](https://doi.org/10.1021/bk-2012-1120.ch028).
- [118] T. Moro, Y. Takatori, K. Ishihara, T. Konno, Y. Takigawa, and T. Matsushita, “Surface grafting of artificial joints with a biocompatible polymer for preventing periprosthetic osteolysis”, *Nat. Mater.*, vol. 3, pp. 829–836, 2004. DOI: [10.1038/nmat1233](https://doi.org/10.1038/nmat1233).
- [119] P. A. Woodfield, Y. Zhu, Y. Pei, and P. J. Roth, “Hydrophobically modified sulfobetaine copolymers with tunable aqueous UCST through postpolymerization modification of poly (pentafluorophenyl acrylate)”, *Macromolecules*, vol. 47, p. 750, 2014. DOI: [10.1021/ma402391a](https://doi.org/10.1021/ma402391a).
- [120] J. Wu, W. Lin, Z. Wang, S. Chen, and Y. Chang, “Investigation of the hydration of nonfouling material poly(sulfobetaine methacrylate) by low-field nuclear magnetic resonance”, *Langmuir*, vol. 28, pp. 7436–7441, 2012. DOI: [10.1021/la300394c](https://doi.org/10.1021/la300394c).
- [121] J. Yuan, X. Huang, P. Li, L. Li, and K. Shen, “Surface-initiated RAFT polymerization of sulfobetaine from cellulose membranes to improve hemocompatibility and antibiofouling property”, *Polym. Chem.*, vol. 4, pp. 5074–5085, 2013. DOI: [10.1039/C3PY00565H](https://doi.org/10.1039/C3PY00565H).

- [122] V. A. Vasantha, S. Jana, A. Parthiban, and J. G. Vancso, “Water swelling, brine soluble imidazole based zwitterionic polymers—synthesis and study of reversible UCST behaviour and gel-sol transitions”, *Chem. Commun. (Cambridge, U. K.)*, vol. 50, no. 1, pp. 46–48, 2014. DOI: [10.1039/c3cc44407d](https://doi.org/10.1039/c3cc44407d).
- [123] A. Laschewsky, R. Touillaux, P. Hendlinger, and A. Vierengel, “Characterization of sulfobetaine monomers by nuclear magnetic resonance spectroscopy: A note”, *Polymer*, vol. 36, pp. 3045–3049, 1995. DOI: [10.1016/0032-3861\(95\)94357-Y](https://doi.org/10.1016/0032-3861(95)94357-Y).
- [124] P. Köberle, A. Laschewsky, and D. van den Boogaard, “Self-organization of hydrophobized polyzwitterions”, *Polymer*, vol. 33, pp. 4029–4039, 1992. DOI: [10.1016/0032-3861\(92\)90601-R](https://doi.org/10.1016/0032-3861(92)90601-R).
- [125] V. M. Monroy Soto and J. C. Galin, “Poly(sulphopropylbetaines): 2. Dilute solution properties”, *Polymer*, no. 25, pp. 254–262, 1984. DOI: [10.1016/0032-3861\(84\)90334-3](https://doi.org/10.1016/0032-3861(84)90334-3).
- [126] V. Hildebrand, “Twofold switchable blockcopolymers based on new polyzwitterions”, *PhD thesis. Potsdam: Universität Potsdam, Institut für Chemie*, 2016.
- [127] V. Hildebrand, A. Laschewsky, M. Päch, P. Müller-Buschbaum, and C. M. Papadakis, “Effect of the zwitterion structure on the thermo-responsive behaviour of poly(sulfobetaine methacrylates)”, *Polym. Chem.*, vol. 8, no. 1, pp. 310–322, 2017. DOI: [10.1039/C6PY01220E](https://doi.org/10.1039/C6PY01220E).
- [128] J. Yu, Y. Liu, S. Song, G. Gao, and F. Liu, “Phase behavior of a high-concentration sulfobetaine zwitterionic polymer solution”, *Polym. J.*, vol. 49, no. 11, pp. 767–774, 2017. DOI: [10.1038/pj.2017.51](https://doi.org/10.1038/pj.2017.51).
- [129] V. Hildebrand, M. Heydenreich, A. Laschewsky, H. M. Möller, P. Müller-Buschbaum, C. M. Papadakis, D. Schanzenbach, and E. Wischerhoff, “Schizophrenic self-assembly of dual thermoresponsive block copolymers bearing a zwitterionic and a non-ionic hydrophilic block”, *Polymer*, vol. 122, pp. 347–357, 2017. DOI: [10.1016/j.polymer.2017.06.063](https://doi.org/10.1016/j.polymer.2017.06.063).
- [130] B.-J. Niebuur, J. Puchmayr, C. Herold, L. P. Kreuzer, V. Hildebrand, P. Müller-Buschbaum, A. Laschewsky, and C. M. Papadakis, “Polysulfobetaines in aqueous solution and in thin film geometry”, *Materials*, vol. 11, no. 5, p. 850, 2018. DOI: [10.3390/ma11050850](https://doi.org/10.3390/ma11050850).
- [131] T. A. Wielema and Engberts, J. B. F. N., “Zwitterionic polymers - III. Salt effects on the solubility of poly(vinyl sulphobetaines) in aqueous solution”, *Eur. Polym. J.*, vol. 6, no. 26, pp. 639–642, 1990. DOI: [10.1016/0014-3057\(90\)90220-X](https://doi.org/10.1016/0014-3057(90)90220-X).

- [132] J. C. Salamone, W. Volksen, A. P. Olson, and S. C. Israel, “Aqueous solution properties of a poly(vinyl imidazolium sulphobetaine)”, *Polymer*, no. 19, pp. 1157–1162, 1978. DOI: [10.1016/0032-3861\(78\)90064-2](https://doi.org/10.1016/0032-3861(78)90064-2).
- [133] Y. Zhang and P. S. Cremer, “Interactions between macromolecules and ions: The Hofmeister series”, *Curr. Opin. Chem. Biol.*, vol. 10, pp. 658–663, 2006. DOI: [10.1016/j.cbpa.2006.09.020](https://doi.org/10.1016/j.cbpa.2006.09.020).
- [134] P. Lo Nostro and B. W. Ninham, “Hofmeister phenomena: An update on ion specificity in biology”, *Chem. Rev.*, vol. 112, no. 4, pp. 2286–2322, 2012. DOI: [10.1021/cr200271j](https://doi.org/10.1021/cr200271j).
- [135] K. D. Collins, “Charge density-dependent strength of hydration and biological structure”, *Biophys. J.*, no. 72, pp. 65–76, 1997. DOI: [10.1016/S0006-3495\(97\)78647-8](https://doi.org/10.1016/S0006-3495(97)78647-8).
- [136] A. Salis and B. W. Ninham, “Models and mechanisms of Hofmeister effects in electrolyte solutions, and colloid and protein systems revisited”, *Chem. Soc. Rev.*, vol. 43, no. 21, pp. 7358–7377, 2014. DOI: [10.1039/c4cs00144c](https://doi.org/10.1039/c4cs00144c).
- [137] W. Kunz, “Specific ion effects in colloidal and biological systems”, *Curr. Opin. Colloid Interface Sci.*, vol. 15, pp. 34–39, 2010. DOI: [10.1016/j.cocis.2009.11.008](https://doi.org/10.1016/j.cocis.2009.11.008).
- [138] Schild H. G., “Poly(*N*-isopropylacrylamide): Experiment, Theory and Application”, *Prog. Polym. Sci.*, vol. 17, no. 17, pp. 163–249, 1992. DOI: [10.1016/0079-6700\(92\)90023-R](https://doi.org/10.1016/0079-6700(92)90023-R).
- [139] A. Halperin, M. Kröger, and F. M. Winnik, “Poly(*N*-isopropylacrylamide) Phase Diagrams: Fifty years of research”, *Angew. Chem., Int. Ed.*, vol. 54, no. 51, pp. 15 342–15 367, 2015. DOI: [10.1002/anie.201506663](https://doi.org/10.1002/anie.201506663).
- [140] S. Fujishige, “Phase transition of aqueous solutions of poly(*N*-isopropylacrylamide) and Poly(*N*-isopropylmethacrylamide)”, *J. Phys. Chem.*, no. 93, pp. 3311–3313, 1989. DOI: [10.1021/j100345a085](https://doi.org/10.1021/j100345a085).
- [141] Tiktopulo. E. I., V. N. Uversky, V. B. Lushchik, S. I. Klenin, V. E. Bychkova, and O. B. Ptitsyn, “Domain coil-globule transitions in homopolymers”, *Macromolecules*, no. 28, pp. 7519–7524, 1995.
- [142] J. Spěvák and J. Dybal, “Temperature-induced phase separation and hydration in aqueous polymer solutions studied by nmr and ir spectroscopy: Comparison of poly(*N*-vinylcaprolactam) and acrylamide-based polymers”, *Macromolecular Symposia*, vol. 336, no. 1, pp. 39–46, 2014. DOI: [10.1002/masy.201300002](https://doi.org/10.1002/masy.201300002).

- [143] V. Chytrý, M. Netopilík, M. Bohdanecký, and K. Ulbrich, “Phase transition parameters of potential thermosensitive drug release systems based on polymers of n-alkylmethacrylamides”, *J. Biomater. Sci. Polym.*, vol. 8, no. 11, pp. 817–824, 1997. DOI: [10.1163/156856297x00010](https://doi.org/10.1163/156856297x00010).
- [144] Y. Guan and Y. Zhang, “PnIPAM microgels for biomedical applications: From dispersed particles to 3d assemblies”, *Soft Matter*, vol. 7, pp. 6375–6384, 14 2011. DOI: [10.1039/C0SM01541E](https://doi.org/10.1039/C0SM01541E).
- [145] X. Xu, Y. Liu, W. Fu, M. Yao, Z. Ding, J. Xuan, D. Li, S. Wang, Y. Xia, and M. Cao, “Poly(N-isopropylacrylamide)-based thermoresponsive composite hydrogels for biomedical applications”, *Polymers*, vol. 12, no. 3, 2020, ISSN: 2073-4360. DOI: [10.3390/polym12030580](https://doi.org/10.3390/polym12030580).
- [146] C.-H. Ko, K.-L. Claude, B.-J. Niebuur, F. A. Jung, J.-J. Kang, D. Schanzenbach, H. Frielinghaus, L. C. Barnsley, B. Wu, V. Pipich, A. Schulte, P. Müller-Buschbaum, A. Laschewsky, and C. M. Papadakis, “Temperature-dependent phase behavior of the thermoresponsive polymer poly(*N*-isopropylmethacrylamide) in an Aqueous Solution”, *Macromolecules*, vol. 53, no. 16, pp. 6816–6827, 2020. DOI: [10.1021/acs.macromol.0c01256](https://doi.org/10.1021/acs.macromol.0c01256).
- [147] P. Kujawa and F. M. Winnik, “Volumetric studies of aqueous polymer solutions using pressure perturbation calorimetry: A new look at the temperature-induced phase transition of poly(*N*-isopropylacrylamide) in water and D₂O”, *Macromolecules*, vol. 34, pp. 4130–4135, 2001. DOI: [10.1021/ma002082h](https://doi.org/10.1021/ma002082h).
- [148] H. Crowther and B. Vincent, “Swelling behavior of poly-*N*-isopropylacrylamide microgel particles in alcoholic solutions”, *Colloid Polym. Sci.*, no. 276, pp. 46–51, 1998. DOI: [10.1007/s003960050207](https://doi.org/10.1007/s003960050207).
- [149] R. O. R. Costa and R. F. S. Freitas, “Phase behavior of poly(*N*-isopropylacrylamide) in Binary Aqueous Solutions”, *Polymer*, vol. 43, pp. 5879–5885, 2002. DOI: [10.1016/S0032-3861\(02\)00507-4](https://doi.org/10.1016/S0032-3861(02)00507-4).
- [150] F. M. Winnik, M. F. Ottaviani, S. H. Bossman, W. Pan, M. Garcia-Garibay, and N. J. Turro, “Phase separation of poly(*N*-isopropylacrylamide) in Water: A spectroscopic study of a polymer tagged with a fluorescent dye and a spin label”, *J. Phys. Chem.*, vol. 97, pp. 12998–13005, 1993. DOI: [10.1021/j100151a058](https://doi.org/10.1021/j100151a058).
- [151] K. Kyriakos, M. Philipp, J. Adelsberger, S. Jaksch, A. Berezkin, A. V. Lugo, W. Richtering, I. Grillo, A. Miasnikova, A. Laschewsky, P. Müller-Buschbaum, and C. M. Papadakis, “Cononsolvency of water/methanol mixtures for PNIPAM and PS-*b*-PNIPAM: Pathway of aggregate formation investigated using time-resolved

- SANS”, *Macromolecules*, vol. 47, no. 19, pp. 6867–6879, 2014. DOI: [10.1021/ma501434e](https://doi.org/10.1021/ma501434e).
- [152] Z. Chen, S. Yu, D. Liu, S. Shi, and W. Shen, “Solvation behaviors of poly(acrylic acid) in mixed solvents of 2-butoxyethanol + water”, *J. Solution Chem.*, vol. 47, no. 9, pp. 1539–1552, 2018. DOI: [10.1007/s10953-018-0809-x](https://doi.org/10.1007/s10953-018-0809-x).
- [153] S. Edmondson, N. T. Nguyen, A. L. Lewis, and S. P. Armes, “Co-nonsolvency effects for surface-initiated poly(2-(methacryloyloxy)ethyl phosphorylcholine) brushes in alcohol/water mixtures”, *Langmuir*, vol. 26, no. 10, pp. 7216–7226, 2010. DOI: [10.1021/la904346j](https://doi.org/10.1021/la904346j).
- [154] H. Kojima, F. Tanaka, C. Scherzinger, and W. Richtering, “Temperature dependent phase behavior of PNIPAM microgels in mixed water/methanol solvents”, *J. Polym. Sci. Part B: Polym. Phys.*, vol. 51, no. 14, pp. 1100–1111, 2013. DOI: [10.1002/polb.23194](https://doi.org/10.1002/polb.23194).
- [155] S. Maccarrone, C. Scherzinger, O. Holderer, O. Lindner, M. Sharp, W. Richtering, and D. Richter, “Cononsolvency effects on the structure and dynamics of microgels”, *Macromolecules*, vol. 47, no. 17, pp. 5982–5988, 2014. DOI: [10.1021/ma500954t](https://doi.org/10.1021/ma500954t).
- [156] J.-U. Sommer, “Adsorption–attraction model for co-nonsolvency in polymer brushes”, *Macromolecules*, vol. 50, no. 5, pp. 2219–2228, 2017. DOI: [10.1021/acs.macromol.6b02231](https://doi.org/10.1021/acs.macromol.6b02231).
- [157] A. Galuschko and J.-U. Sommer, “Co-nonsolvency response of a polymer brush: A molecular dynamics study”, *Macromolecules*, vol. 52, no. 11, pp. 4120–4130, 2019. DOI: [10.1021/acs.macromol.9b00569](https://doi.org/10.1021/acs.macromol.9b00569).
- [158] G. Park and Y. Jung, “Many-chain effects on the co-nonsolvency of polymer brushes in a good solvent mixture”, *Soft Matter*, vol. 15, no. 39, pp. 7968–7980, 2019. DOI: [10.1039/c9sm01123d](https://doi.org/10.1039/c9sm01123d).
- [159] X. Wang, H. Huang, H. Liu, F. Rehfeldt, X. Wang, and K. Zhang, “Multi-responsive bilayer hydrogel actuators with programmable and precisely tunable motions”, *Macromol. Chem. Phys.*, vol. 220, no. 6, p. 1800562, 2019. DOI: [10.1002/macp.201800562](https://doi.org/10.1002/macp.201800562).
- [160] Y. Zhang, W. S. P. Carvalho, C. Fang, and M. J. Serpe, “Organic compound vapor detection with responsive microgel-based etalons”, *Sens. Actuators, B*, vol. 290, pp. 520–526, 2019. DOI: [10.1016/j.snb.2019.03.147](https://doi.org/10.1016/j.snb.2019.03.147).

- [161] S. Keßler, F. Schmid, and K. Drese, “Modeling size controlled nanoparticle precipitation with the co-solvency method by spinodal decomposition”, *Soft Matter*, vol. 12, no. 34, pp. 7231–7240, 2016. DOI: [10.1039/c6sm01198e](https://doi.org/10.1039/c6sm01198e).
- [162] Y. Yu, R. A. La Lopez de Cruz, B. D. Kieviet, H. Gojzewski, A. Pons, G. Julius Vancso, and S. de Beer, “Pick up, move and release of nanoparticles utilizing co-non-solvency of PNIPAM brushes”, *Nanoscale*, vol. 9, no. 4, pp. 1670–1675, 2017. DOI: [10.1039/c6nr09245d](https://doi.org/10.1039/c6nr09245d).
- [163] Y. Yu, M. Cirelli, B. D. Kieviet, E. S. Kooij, G. J. Vancso, and S. de Beer, “Tunable friction by employment of co-non-solvency of PNIPAM brushes”, *Polymer*, vol. 102, pp. 372–378, 2016. DOI: <https://doi.org/10.1016/j.polymer.2016.08.029>.
- [164] E. Krieg and W. M. Shih, “Selective nascent polymer catch-and-release enables scalable isolation of multi-kilobase single-stranded DNA”, *Angew. Chem. Int. Ed.*, vol. 57, no. 3, pp. 714–718, 2018. DOI: [10.1002/anie.201710469](https://doi.org/10.1002/anie.201710469).
- [165] C. Geiger, J. Reitenbach, L. P. Kreuzer, T. Widmann, P. Wang, R. Cubitt, C. Henschel, A. Laschewsky, C. M. Papadakis, and P. Müller-Buschbaum, “PMMA-*b*-PNIPAM thin films display cononsolvency-driven response in mixed water/methanol vapors”, *Macromolecules*, vol. 54, no. 7, pp. 3517–3530, 2021. DOI: [10.1021/acs.macromol.1c00021](https://doi.org/10.1021/acs.macromol.1c00021).
- [166] C. Geiger, J. Reitenbach, C. Henschel, L. P. Kreuzer, T. Widmann, P. Wang, G. Mangiapia, J.-F. Moulin, C. M. Papadakis, A. Laschewsky, and P. Müller-Buschbaum, “Ternary nanoswitches realized with multiresponsive PMMA-*b*-PNIPAM films in mixed water/acetone vapor atmospheres”, *Adv. Eng. Mater.*, p. 2100191, 2021. DOI: [10.1002/adem.202100191](https://doi.org/10.1002/adem.202100191).
- [167] D. Mukherji, C. M. Marques, and K. Kremer, “Polymer collapse in miscible good solvents is a generic phenomenon driven by preferential adsorption”, *Nat. Commun.*, vol. 5, p. 4882, 2014. DOI: [10.1038/ncomms5882](https://doi.org/10.1038/ncomms5882).
- [168] J. Walter, J. Sehart, J. Vrabec, and H. Hasse, “Molecular dynamics and experimental study of conformation change of poly(*N*-isopropylacrylamide) Hydrogels in Mixtures of Water and Methanol”, *J. Phys. Chem. B*, vol. 116, no. 17, pp. 5251–5259, 2012. DOI: [10.1021/jp212357n](https://doi.org/10.1021/jp212357n).
- [169] J. Heyda, A. Muzdalo, and J. Dzubiella, “Rationalizing polymer swelling and collapse under attractive cosolvent conditions”, *Macromolecules*, vol. 46, no. 3, pp. 1231–1238, 2013. DOI: [10.1021/ma302320y](https://doi.org/10.1021/ma302320y).

- [170] D. Mukherji and K. Kremer, “Coil–globule–coil transition of PNIPAm in aqueous methanol: Coupling all-atom simulations to semi-grand canonical coarse-grained reservoir”, *Macromolecules*, vol. 46, no. 22, pp. 9158–9163, 2013. DOI: [10.1021/ma401877c](https://doi.org/10.1021/ma401877c).
- [171] F. Rodríguez-Ropero, T. Hajari, and N. F. A. van der Vegt, “Mechanism of polymer collapse in miscible good solvents”, *J. Chem. Phys. B*, vol. 119, no. 51, pp. 15 780–15 788, 2015. DOI: [10.1021/acs.jpcc.5b10684](https://doi.org/10.1021/acs.jpcc.5b10684).
- [172] A. K. Tucker and M. J. Stevens, “Study of the polymer length dependence of the single chain transition temperature in syndiotactic poly(*N*-isopropylacrylamide) Oligomers in Water”, *Macromolecules*, vol. 45, p. 6697, 2012. DOI: [10.1021/ma300729z](https://doi.org/10.1021/ma300729z).
- [173] F. Tanaka, T. Koga, H. Kojima, N. Xue, and F. M. Winnik, “Preferential adsorption and co-nonsolvency of thermoresponsive polymers in mixed solvents of water/methanol”, *Macromolecules*, vol. 44, no. 8, pp. 2978–2989, 2011. DOI: [10.1021/ma102695n](https://doi.org/10.1021/ma102695n).
- [174] S. Backes, P. Krause, W. Tabaka, M. U. Witt, D. Mukherji, K. Kremer, and R. von Klitzing, “Poly(*N*-isopropylacrylamide) microgels under alcoholic intoxication: When a LCST polymer shows swelling with increasing temperature”, *ACS Macro Letters*, vol. 6, no. 10, pp. 1042–1046, 2017. DOI: [10.1021/acsmacrolett.7b00557](https://doi.org/10.1021/acsmacrolett.7b00557).
- [175] P.-W. Zhu and L. Chen, “Effects of cosolvent partitioning on conformational transitions and chain flexibility of thermoresponsive microgels”, *Phys. Rev. E*, vol. 99, no. 2-1, p. 022 501, 2019. DOI: [10.1103/PhysRevE.99.022501](https://doi.org/10.1103/PhysRevE.99.022501).
- [176] I. Bischofberger, D. C. E. Calzolari, and V. Trappe, “Co-nonsolvency of PNIPAM at the transition between solvation mechanisms”, *Soft Matter*, vol. 10, no. 41, pp. 8288–8295, 2014. DOI: [10.1039/c4sm01345j](https://doi.org/10.1039/c4sm01345j).
- [177] J. Daillant and A. Gibaud, “X-ray and neutron reflectivity: Principles and applications”, *Lect. Notes Phys. 770 (Springer, Berlin Heidelberg 2009)*, 2009.
- [178] J. S. Higgins and H. C. Benoit, “Polymers and neutron scattering”, *Oxford Clarendon Press*, 1996.
- [179] M. Tolan, “X-ray scattering from soft-matter thin films”, *Springer Tracts in Modern Physics*, vol. 148, 1978. DOI: [10.1007/BFb0112834](https://doi.org/10.1007/BFb0112834).
- [180] J. Lekner, “Reflection theory and the analysis of neutron reflection data”, *Physica B*, vol. 173, no. 1, pp. 99–111, 1991. DOI: [10.1016/0921-4526\(91\)90040-L](https://doi.org/10.1016/0921-4526(91)90040-L).

- [181] P. Müller-Buschbaum, “GISAXS and GISANS as metrology technique for understanding the 3D morphology of block copolymer thin films”, *Eur. Polym. J.*, vol. 81, pp. 470–493, 2016. DOI: [10.1016/j.eurpolymj.2016.04.007](https://doi.org/10.1016/j.eurpolymj.2016.04.007).
- [182] V. F. Sears, “Neutron scattering lengths and cross sections”, *Neutron News*, vol. 3, no. 3, pp. 26–37, 2006. DOI: [10.1080/10448639208218770](https://doi.org/10.1080/10448639208218770).
- [183] A. Hexemer and P. Müller-Buschbaum, “Advanced grazing-incidence techniques for modern soft-matter materials analysis”, *IUCrJ*, vol. 2, no. 1, pp. 106–125, 2015. DOI: [10.1107/S2052252514024178](https://doi.org/10.1107/S2052252514024178).
- [184] P. Müller-Buschbaum, J. S. Gutmann, R. Cubitt, and M. Stamm, “Probing the in-plane composition of thin polymer films with grazing-incidence small-angle neutron scattering and atomic force microscopy”, *Colloid Polym. Sci.*, vol. 277, no. 12, pp. 1193–1199, 1999. DOI: [10.1007/s003960050509](https://doi.org/10.1007/s003960050509).
- [185] B. Jacrot, “The study of biological structures by neutron scattering from solution”, *Rep. Prog. Phys.*, vol. 39, no. 10, pp. 911–953, 1976. DOI: [10.1088/0034-4885/39/10/001](https://doi.org/10.1088/0034-4885/39/10/001).
- [186] G. Squires, “Introduction to the theory of thermal neutron scattering”, *Dover Publications, 1996 [originally published by Cambridge University Press (1978)]*, 1978. DOI: [10.1017/CB09781139107808.016](https://doi.org/10.1017/CB09781139107808.016).
- [187] G. Renaud, R. Lazzari, and F. Leroy, “Probing surface and interface morphology with grazing incidence small angle x-ray scattering”, *Surf. Sci. Rep.*, vol. 64, no. 8, pp. 255–380, 2009. DOI: [10.1016/j.surfrep.2009.07.002](https://doi.org/10.1016/j.surfrep.2009.07.002).
- [188] L. Parratt, “Solid surface studies by total reflection of x-rays”, *Phys. Rev.*, vol. 95, no. 2, pp. 359–369, 1954.
- [189] W. A. Hamilton, “Conformation, directed self-assembly and engineered modification: Some recent near surface structure determinations by grazing incidence small angle x-ray and neutron scattering”, *Curr. Opin. Colloid Interface Sci.*, vol. 9, no. 6, pp. 390–395, 2005. DOI: [10.1016/j.cocis.2004.10.005](https://doi.org/10.1016/j.cocis.2004.10.005).
- [190] P. Müller-Buschbaum, “A basic introduction to grazing incidence small-angle x-ray scattering”, *Applications of Synchrotron Light to Scattering and Diffraction in Materials and Life Sciences. Berlin, Heidelberg: Springer Berlin Heidelberg*, vol. 26, no. 46, pp. 61–89, 2009. DOI: [doi:10.1007/978-3-540-95968-7_3](https://doi.org/doi:10.1007/978-3-540-95968-7_3).
- [191] P. Müller-Buschbaum, E. Metwalli, J.-F. Moulin, V. Kudryashov, M. Haese-Seiller, and R. Kampmann, “Time of flight grazing incidence small angle neutron scattering”, *Eur. Phys. J. Spec. Top.*, vol. 167, no. 1, pp. 107–112, 2009. DOI: [10.1140/epjst/e2009-00944-5](https://doi.org/10.1140/epjst/e2009-00944-5).

- [192] S. Nouhi, M. S. Hellsing, V. Kapaklis, and A. R. Rennie, “Grazing-incidence small-angle neutron scattering from structures below an interface”, *J. Appl. Crystallogr.*, vol. 50, no. Pt 4, pp. 1066–1074, 2017. DOI: [10.1107/S1600576717007518](https://doi.org/10.1107/S1600576717007518).
- [193] M. Wolff, “Grazing incidence scattering”, *EPJ Web of Conferences*, vol. 188, no. 2, p. 04002, 2018. DOI: [10.1051/epjconf/201818804002](https://doi.org/10.1051/epjconf/201818804002).
- [194] P. Müller-Buschbaum, “Grazing incidence small-angle neutron scattering: Challenges and possibilities”, *Polymer Journal*, vol. 45, no. 1, pp. 34–42, 2012. DOI: [10.1038/pj.2012.190](https://doi.org/10.1038/pj.2012.190).
- [195] R. Lazzari, “IsGISAXS: A program for grazing-incidence small-angle x-ray scattering analysis of supported islands”, *J. Appl. Crystallogr.*, vol. 35, no. 4, pp. 406–421, 2002.
- [196] G. H. Vineyard, “Grazing-incidence diffraction and the distorted-wave approximation for the study of surfaces”, *Phys. Rev. B*, vol. 26, pp. 4146–4159, 1982. DOI: [10.1103/PhysRevB.26.4146](https://doi.org/10.1103/PhysRevB.26.4146).
- [197] S. Dietrich and H. Wagner, “Critical surface scattering of x-rays at grazing angles”, *Condens. Matter*, vol. 56, no. 3, pp. 207–215, 1984. DOI: [10.1007/BF01304174](https://doi.org/10.1007/BF01304174).
- [198] S. Dietrich and H. Wagner, “Critical magnetic surface scattering of neutrons at grazing angles”, *Z. Phys. B Condens. Matter*, vol. 59, no. 1, pp. 35–42, 1985. DOI: [10.1007/BF01325380e](https://doi.org/10.1007/BF01325380e).
- [199] D. Babonneau, “Fitgisaxs: Software package for modelling and analysis of GISAXS data using IGOR Pro”, *J. Appl. Crystallogr.*, vol. 43, no. 4, pp. 929–936, 2013. DOI: [10.1107/S0021889810020352](https://doi.org/10.1107/S0021889810020352).
- [200] D. Burle, C. Durniak, J. M. Fisher, M. Ganeva, G. Pospelov, W. van Herck, J. Wuttke, and D. Yurov, “Bornagain - software for simulating and fitting x-ray and neutron small-angle scattering at grazing incidence - Ed. by MLZ Garching”, <http://www.bornagainproject.org/> (visited on 12/04/2021), 2018.
- [201] Y. Yoneda, “Anomalous surface reflection of x-rays”, *Phys. Rev.*, no. 131, pp. 2010–2014, 1963. DOI: [10.1103/PhysRev.131.2010](https://doi.org/10.1103/PhysRev.131.2010).
- [202] T. Salditt, T. H. Metzger, J. Peisl, and G. Goerigk, “Non-specular x-ray scattering from thin films and multilayers with small-angle scattering equipment”, *J. Phys. D Appl. Phys.*, vol. 28, no. 4A, pp. 236–240, 1995. DOI: [10.1088/0022-3727/28/4a/046](https://doi.org/10.1088/0022-3727/28/4a/046).

- [203] P. Müller-Buschbaum, “Grazing incidence small-angle x-ray scattering: An advanced scattering technique for the investigation of nanostructured polymer films”, *Anal. Bioanal. Chem.*, vol. 376, no. 1, pp. 3–10, 2003. DOI: [doi:10.1007/s00216-003-1869-2](https://doi.org/10.1007/s00216-003-1869-2).
- [204] P. Müller-Buschbaum, “The active layer morphology of organic solar cells probed with grazing incidence scattering techniques”, *Adv. Mater.*, vol. 26, no. 46, pp. 7692–7709, 2014. DOI: [doi:10.1002/adma.201304187](https://doi.org/10.1002/adma.201304187).
- [205] S. K. Sinha, E. B. Sirota, S. Garoff, and H. B. Stanley, “X-ray and neutron scattering from rough surfaces”, *Phys. Rev. B*, vol. 38, pp. 2297–2311, 1988. DOI: [doi:10.1103/PhysRevB.38.2297](https://doi.org/10.1103/PhysRevB.38.2297).
- [206] C. J. Schaffer, “Morphological degradation in polymer-fullerene solar cells”, *PhD thesis. München: Technische Universität München, Fakultät für Physik*, 2016.
- [207] J. Schlipf, “The morphology of hybrid perovskite thin films for photovoltaic application. formation & disintegration”, *PhD thesis. München: Technische Universität München, Fakultät für Physik*, 2018.
- [208] R. Hosemann, W. Vogel, D. Weick, and F. J. Baltá-Calleja, “Novel aspects of the real paracrystal”, *Acta Cryst.*, vol. 37, no. 1, pp. 85–91, 1981. DOI: [doi:10.1107/S0567739481000156](https://doi.org/10.1107/S0567739481000156).
- [209] C. J. Schaffer, C. M. Palumbiny, M. A. Niedermeier, C. Jendrzejewski, G. Santoro, S. V. Roth, and P. Müller-Buschbaum, “A direct evidence of morphological degradation on a nanometer scale in polymer solar cells”, *Adv. Mater.*, vol. 25, no. 146, pp. 6760–6764, 2013. DOI: [doi:10.1002/adma.2013028543](https://doi.org/10.1002/adma.2013028543).
- [210] D. G. Bucknall, S. A. Butler, and J. S. Higgins, “Neutron reflectivity of polymer interface”, *J. Phys. Chem. Solids*, vol. 60, no. 8, pp. 1273–1277, 1999. DOI: [doi:10.1016/S0022-3697\(99\)00101-8](https://doi.org/10.1016/S0022-3697(99)00101-8).
- [211] T. Gutberlet, R. Steitz, G. Fragneto, and K. B., “Phospholipid bilayer formation at a bare Si surface: A time-resolved neutron reflectivity study”, *J. Phys. Condens. Matter.*, vol. 16, no. 26, S2469–S2476, 2004. DOI: [doi:10.1088/0953-8984/16/26/020](https://doi.org/10.1088/0953-8984/16/26/020).
- [212] P. Müller-Buschbaum, E. Bauer, E. Maurer, A. Nelson, and R. Cubitt, “In-situ neutron reflectometry probing competitive swelling and de-swelling of thin polystyrene films”, *pss (RRL)*, vol. 1, no. 2, R68–R70, 2007. DOI: [10.1002/pssr.200600066](https://doi.org/10.1002/pssr.200600066).

- [213] W. Kreuzpaintner, J.-F. Moulin, D. Lott, R. Kampmann, M. Haese-Seiller, M. Störmer, and A. Schreyer, “Time of flight grazing incidence small angle neutron scattering on Gd nanowires”, *Eur. Phys. J. Spec. Top.*, vol. 167, no. 1, pp. 73–79, 2009. DOI: [10.1140/epjst/e2009-00939-2](https://doi.org/10.1140/epjst/e2009-00939-2).
- [214] R. Asmatulu and W. S. Khan, “Characterization of electrospun nanofibers”, in *Synthesis and Applications of Electrospun Nanofibers*, ser. Micro and Nano Technologies, R. Asmatulu and W. S. Khan, Eds., Elsevier, 2019, pp. 41–61. DOI: [10.1016/B978-0-12-813914-1.00013-4](https://doi.org/10.1016/B978-0-12-813914-1.00013-4).
- [215] D. Nečas and P. Klapetek, “Gwyddion: An open-source software for spm data analysis”, *Open Physics*, vol. 10, no. 1, p. 99, 2012. DOI: [10.2478/s11534-011-0096-2](https://doi.org/10.2478/s11534-011-0096-2).
- [216] R. Dalglish, “Application of off-specular scattering of x-rays and neutron to the study of soft matter”, *Current Opinion in Colloid & Interface Science*, vol. 7, pp. 244–248, 2002. DOI: [10.1016/S1359-0294\(02\)00054-7](https://doi.org/10.1016/S1359-0294(02)00054-7).
- [217] A. Nelson, “Co-refinement of multiple-contrast neutron/x-ray reflectivity data using motofit”, *Journal of Applied Crystallography*, vol. 39, no. 2, pp. 273–276, 2006. DOI: [10.1107/S0021889806005073](https://doi.org/10.1107/S0021889806005073).
- [218] R. Kampmann, M. Marmotti, M. Haese-Seiller, and V. Kudryashov, “2D-MWPC for the new reflectometer REFSANS/FRM-II: Performance of the prototype”, *Nucl. Instrum. Methods Phys. Res.*, vol. 529, no. 1-3, pp. 342–347, 2004. DOI: [10.1016/j.nima.2004.05.009](https://doi.org/10.1016/j.nima.2004.05.009).
- [219] R. Kampmann, M. Haese-Seiller, V. Kudryashov, V. Deriglazov, M. Trisl, C. Daniel, B. Toperverg, A. Schreyer, and E. Sackmann, “The potential of the horizontal reflectometer REFSANS/FRM-II for measuring low reflectivity and diffuse surface scattering”, *Physica B*, vol. 350, no. 1-3, E763–E766, 2004. DOI: [10.1016/j.physb.2004.03.198](https://doi.org/10.1016/j.physb.2004.03.198).
- [220] R. Kampmann, M. Haese-Seiller, V. Kudryashov, B. Nickel, C. Daniel, W. Fenzl, A. Schreyer, E. Sackmann, and J. Rädler, “Horizontal tof-neutron reflectometer REFSANS at FRM-II Munich/Germany: First tests and status”, *Physica B*, vol. 385-386, pp. 1161–1163, 2006. DOI: [10.1016/j.physb.2006.05.399](https://doi.org/10.1016/j.physb.2006.05.399).
- [221] R. Cubitt and G. Fragneto, “D17: The new reflectometer at the ILL”, *Applied Physics A: Materials Science & Processing*, vol. 74, no. 0, s329–s331, 2002. DOI: [10.1007/s003390201611](https://doi.org/10.1007/s003390201611).

- [222] T. Saerbeck, R. Cubitt, A. Wildes, G. Manzin, K. H. Andersen, and P. Gutfreund, “Recent upgrades of the neutron reflectometer D17 at ILL”, *Journal of Applied Crystallography*, vol. 51, no. 2, pp. 249–256, 2018. DOI: [10.1107/S160057671800239X](https://doi.org/10.1107/S160057671800239X).
- [223] P. R. Griffiths, “Fourier transform infrared spectrometry”, *Science*, vol. 222, pp. 297–302, 1983. DOI: [10.1126/science.6623077](https://doi.org/10.1126/science.6623077).
- [224] J. S. Gaffney, N. A. Marley, and D. E. Jones, “Fourier transform infrared (ftir) spectroscopy”, In *Characterization of Materials; Kaufmann, E. N., Ed.; John Wiley & Sons*, pp. 1104–1135, 2012. DOI: [10.1002/0471266965.com107.pub2](https://doi.org/10.1002/0471266965.com107.pub2).
- [225] P. Panteleimon, “Selbstorganisation und strukturbildung multiskaliger polymermischungsfilm”, *PhD thesis. München: Technische Universität München, Fakultät für Physik*, 2006.
- [226] W. Wang, “Structure and kinetic of stimuli-responsive thin hydrogel films”, *PhD thesis. München: Technische Universität München, Fakultät für Physik*, 2010.
- [227] M. H. Futscher, M. Philipp, P. Müller-Buschbaum, and A. Schulte, “The role of backbone hydration of poly(*N*-isopropyl acrylamide) Across the Volume Phase Transition Compared to its Monomer”, *Sci. Rep.*, vol. 7, no. 1, p. 17012, 2017. DOI: [10.1038/s41598-017-17272-7](https://doi.org/10.1038/s41598-017-17272-7).
- [228] C. Herold, “Multi-stimuli-responsive polymer thin films”, *Master thesis. München: Technische Universität München, Fakultät für Physik*, 2017.
- [229] T. Widmann, L. P. Kreuzer, G. Mangiapia, M. Haese, H. Frielinghaus, and P. Müller-Buschbaum, “3D printed spherical environmental chamber for neutron reflectometry and grazing-incidence small-angle neutron scattering experiments”, *Review of Scientific Instruments*, vol. 91, no. 11, p. 113903, 2020. DOI: [10.1063/5.0012652](https://doi.org/10.1063/5.0012652).
- [230] T. Widmann, L. P. Kreuzer, M. Kühnhammer, A. J. Schmid, L. Wiehemeier, S. Jaksch, H. Frielinghaus, O. Löhmann, H. Schneider, A. Hiess, R. von Klitzing, T. Hellweg, and P. Müller-Buschbaum, “Flexible sample environment for the investigation of soft matter at the european spallation source: Part II—the GISANS setup”, *Appl. Sci.*, vol. 11, no. 9, p. 4036, 2021. DOI: [10.3390/app11094036](https://doi.org/10.3390/app11094036).
- [231] A. J., L. Wiehemeier, S. Jaksch, H. Schneider, A. Hiess, T. Bögershausen, T. Widmann, J. Reitenbach, L. P. Kreuzer, M. Kühnhammer, O. Löhmann, G. Brandl, H. Frielinghaus, P. Müller-Buschbaum, R. von Klitzing, and T. Hellweg, “Flexible sample environments for the investigation of soft matter at the european spallation source: Part i—the in situ SANS/DLS setup”, *Appl. Sci.*, vol. 11, no. 9, p. 4089, 2021. DOI: [10.3390/app11094089](https://doi.org/10.3390/app11094089).

- [232] M. Kühnhammer, T. Widmann, L. P. Kreuzer, A. J. Schmid, L. Wiehemeier, A. Löhmann, H. Frielinghaus, S. Jaksch, T. Bögershausen, P. Barron, H. Schneider, Hiess, P. Müller-Buschbaum, T. Hellweg, and R. von Klitzing, “Flexible sample environments for the investigation of soft matter at the european spallation source: Part III – the macroscopic foam cell”, *Appl. Sci.*, vol. 11, no. 11, p. 5116, 2021. DOI: [10.3390/app11115116](https://doi.org/10.3390/app11115116).
- [233] K. Batkov, A. Takibayev, L. Zanini, and F. Mezei, “Unperturbed moderator brightness in pulsed neutron sources”, *Nuclear Instruments and Methods in Physics Research Section A: Accelerators, Spectrometers, Detectors and Associated Equipment*, vol. 729, pp. 500–505, 2013. DOI: [10.1016/j.nima.2013.07.031](https://doi.org/10.1016/j.nima.2013.07.031).
- [234] A. M. Bivigou-Koumba, E. Görnitz, A. Laschewsky, P. Müller-Buschbaum, and C. M. Papadakis, “Thermoresponsive amphiphilic symmetrical triblock copolymers with a hydrophilic middle block made of poly(*N*-isopropylacrylamide): Synthesis, self-organization, and hydrogel formation”, *Colloid and Polymer Science*, vol. 288, no. 5, pp. 499–517, 2010. DOI: [10.1007/s00396-009-2179-9](https://doi.org/10.1007/s00396-009-2179-9).
- [235] N. S. Vishnevetskaya, V. Hildebrand, B.-J. Niebuur, I. Grillo, S. K. Filippov, A. Laschewsky, P. Müller-Buschbaum, and C. M. Papadakis, “Aggregation behavior of doubly thermoresponsive polysulfobetaine-*b*-poly(*N*-isopropylacrylamide) Diblock Copolymers”, *Macromolecules*, vol. 49, no. 17, pp. 6655–6668, 2016. DOI: [10.1021/acs.macromol.6b01186](https://doi.org/10.1021/acs.macromol.6b01186).
- [236] P. Müller-Buschbaum, “Influence of surface cleaning on dewetting of thin polystyrene films”, *Eur. Phys. J. E: Soft Matter*, vol. 12, no. 3, pp. 443–448, 2003. DOI: [10.1140/epje/e2004-00014-7](https://doi.org/10.1140/epje/e2004-00014-7).
- [237] D. W. Schubert and T. Dunkel, “Spin coating from a molecular point of view: Its concentration regimes, influence of molar mass and distribution”, *Mater. Res. Innov.*, vol. 7, no. 5, pp. 314–321, 2003. DOI: [10.1007/s10019-003-0270-2](https://doi.org/10.1007/s10019-003-0270-2).
- [238] L. Peis, “Role of molecular interactions for stimuli-responsive polymers of potential use in soft robotics”, *Bachelor thesis. München: Technische Universität München, Fakultät für Physik*, 2017.
- [239] D. Buenger, F. Topuz, and J. Groll, “Hydrogels in sensing applications”, *Prog. Polym. Sci.*, vol. 37, no. 12, pp. 1678–1719, 2012. DOI: [10.1016/j.progpolymsci.2012.09.001](https://doi.org/10.1016/j.progpolymsci.2012.09.001).
- [240] K. Kubota, K. Hamano, N. Kuwahara, S. Fujishige, and I. Ando, “Characterization of poly(*N*-isopropylmethacrylamide) in Water”, *Polym. J.*, no. 22, pp. 1051–1057, 1990. DOI: [10.1295/polymj.22.1051](https://doi.org/10.1295/polymj.22.1051).

- [241] M. Kano and E. Kokufuta, “On the temperature-responsive polymers and gels based on *N*-propylacrylamides and *N*-propylmethacrylamides”, *Langmuir*, vol. 25, no. 15, pp. 8649–8655, 2009. DOI: [10.1021/1a804286j](https://doi.org/10.1021/1a804286j).
- [242] V. Hildebrand, A. Laschewsky, and D. Zehm, “On the hydrophilicity of polyzwitterion poly(*N,N*-dimethyl-*N*-(3-(methacrylamido)propyl)ammonio)propane sulfonate) in Water, Deuterated Water, and Aqueous Salt Solutions”, *J. Biomater. Sci., Polym. Ed.*, vol. 25, no. 14-15, pp. 1602–1618, 2014. DOI: [10.1080/09205063.2014.939918](https://doi.org/10.1080/09205063.2014.939918).
- [243] Q. Zhong, E. Metwalli, G. Kaune, M. Rawolle, A. M. Bivigou-Koumba, A. Laschewsky, C. M. Papadakis, R. Cubitt, and P. Müller-Buschbaum, “Switching kinetics of thin thermo-responsive hydrogel films of poly(monomethoxy-diethyleneglycol-acrylate) probed with in situ neutron reflectivity”, *Soft Matter*, vol. 8, no. 19, p. 5241, 2012. DOI: [10.1039/c2sm25401h](https://doi.org/10.1039/c2sm25401h).
- [244] Q. Sun, “The Raman OH stretching bands of liquid water”, *Vib. Spectrosc.*, vol. 51, no. 2, pp. 213–217, 2009. DOI: [10.1016/j.vibspec.2009.05.002](https://doi.org/10.1016/j.vibspec.2009.05.002).
- [245] R. Vyumvuhore, A. Tfayli, H. Duplan, A. Delalleau, M. Manfait, and A. Baillet-Guffroy, “Effects of atmospheric relative humidity on stratum corneum structure at the molecular level: Ex vivo Raman spectroscopy analysis”, *Analyst*, vol. 138, no. 14, pp. 4103–4111, 2013. DOI: [10.1039/c3an00716b](https://doi.org/10.1039/c3an00716b).
- [246] S. K. J. Bandekar, “Vibrational analysis of peptides, polypeptides, and proteins”, *Int. J. Peptide Protein Res.*, vol. 26, no. 26, pp. 407–415, 1985.
- [247] N. A. Besley and K. A. Metcalf, “Computation of the amide I band of polypeptides and proteins using a partial Hessian approach”, *J. Chem. Phys.*, vol. 126, no. 3, p. 035 101, 2007. DOI: [10.1063/1.2426344](https://doi.org/10.1063/1.2426344).
- [248] Z. Ahmed, E. A. Gooding, K. V. Pimenov, L. Wang, and S. A. Asher, “UV resonance Raman determination of molecular mechanism of poly(*N*-isopropylacrylamide) Volume Phase Transition”, *The Journal of Physical Chemistry B*, vol. 113, no. 13, pp. 4248–4256, 2009. DOI: [10.1021/jp810685g](https://doi.org/10.1021/jp810685g).
- [249] C. Lindenmeir, “Dünne hydrogelfilme und deren potentielle anwendung in der soft-robotik”, *Bachelor thesis. München: Technische Universität München, Fakultät für Physik*, 2020.
- [250] L. P. Kreuzer, C. Geiger, T. Widmann, P. Wang, R. Cubitt, V. Hildebrand, A. Laschewsky, C. M. Papadakis, and P. Müller-Buschbaum, “Solvation behavior of poly(sulfobetaine)-based diblock copolymer thin films in mixed water/methanol

- vapors”, *Macromolecules*, vol. 54, no. 15, pp. 7147–7159, 2021. DOI: [10.1021/acs.macromol.1c01179](https://doi.org/10.1021/acs.macromol.1c01179).
- [251] I. Bischofberger, D. C. E. Calzolari, P. de Los Rios, I. Jelezarov, and V. Trappe, “Hydrophobic hydration of poly-*N*-isopropylacrylamide: A matter of the mean energetic state of water”, *Scientific reports*, vol. 4, p. 4377, 2014. DOI: [10.1038/srep04377](https://doi.org/10.1038/srep04377).
- [252] G. Zhang and C. Wu, “Reentrant coil-to-globule-to-coil transition of a single linear homopolymer chain in a water/methanol mixture”, *Phys. Rev. Lett.*, vol. 86, no. 5, pp. 822–825, 2001. DOI: [10.1103/PhysRevLett.86.822](https://doi.org/10.1103/PhysRevLett.86.822).
- [253] M. J. A. Hore, B. Hammouda, Y. Li, and H. Cheng, “Co-nonsolvency of poly(*N*-isopropylacrylamide) in Deuterated Water/Ethanol Mixtures”, *Macromolecules*, vol. 46, no. 19, pp. 7894–7901, 2013. DOI: [10.1021/ma401665h](https://doi.org/10.1021/ma401665h).
- [254] C. Scherzinger, A. Schwarz, A. Bardow, K. Leonhard, and W. Richtering, “Cononsolvency of poly-*N*-Isopropyl Acrylamide (PNIPAM): Microgels versus linear chains and macrogels”, *Curr. Opin. Colloid Interface Sci.*, vol. 19, no. 2, pp. 84–94, 2014. DOI: [10.1016/j.cocis.2014.03.011](https://doi.org/10.1016/j.cocis.2014.03.011).
- [255] D. Mukherji, C. M. Marques, T. Stuehn, and K. Kremer, “Co-non-solvency: Mean-field polymer theory does not describe polymer collapse transition in a mixture of two competing good solvents”, *J. Chem. Phys.*, vol. 142, no. 11, p. 114903, 2015. DOI: [10.1063/1.4914870](https://doi.org/10.1063/1.4914870).
- [256] Y. Hirokawa and T. Tanaka, “Volume phase transition in a nonionic gel”, *Int. J. Chem. Phys.*, vol. 81, no. 12, pp. 6379–6380, 1984. DOI: [10.1063/1.447548](https://doi.org/10.1063/1.447548).
- [257] X. Sui, Q. Chen, M. A. Hempenius, and G. J. Vancso, “Probing the collapse dynamics of poly(*N*-isopropylacrylamide) Brushes by AFM: Effects of co-nonsolvency and grafting densities”, *Small (Weinheim an der Bergstrasse, Germany)*, vol. 7, no. 10, pp. 1440–1447, 2011. DOI: [10.1002/smll.201002229](https://doi.org/10.1002/smll.201002229).
- [258] I. N. Heppner, M. R. Islam, and M. J. Serpe, “Unexpected cononsolvency behavior of poly (*N*-isopropylacrylamide)-Based Microgels”, *Macromolecular Rapid Communications*, vol. 34, no. 21, pp. 1708–1713, 2013. DOI: <https://doi.org/10.1002/marc.201300626>.
- [259] Q. Chen, E. S. Kooij, X. Sui, C. J. Padberg, M. A. Hempenius, P. M. Schön, and G. J. Vancso, “Collapse from the top: Brushes of poly(*N*-isopropylacrylamide) in co-nonsolvent mixtures”, *Soft Matter*, vol. 10, pp. 3134–3142, 17 2014. DOI: [10.1039/C4SM00195H](https://doi.org/10.1039/C4SM00195H).

- [260] H. Yong, E. Bittrich, P. Uhlmann, A. Fery, and J.-U. Sommer, “Co-nonsolvency transition of poly(*N*-isopropylacrylamide) Brushes in a Series of Binary Mixtures”, *Macromolecules*, vol. 52, no. 16, pp. 6285–6293, 2019. DOI: [10.1021/acs.macromol.9b01286](https://doi.org/10.1021/acs.macromol.9b01286).
- [261] J. Spěvák and J. Dybal, “Stimuli-responsive polymers in solution investigated by nmr and infrared spectroscopy”, *Macromolecular Symposia*, vol. 303, no. 1, pp. 17–25, 2011. DOI: [10.1002/masy.201150503](https://doi.org/10.1002/masy.201150503).
- [262] H. Kouřilová, L. Hanyková, and J. Spěvák, “Nmr study of phase separation in d2o/ethanol solutions of poly(*N*-isopropylmethacrylamide) Induced by Solvent Composition and Temperature”, *Eur. Polym. J.*, vol. 45, no. 10, pp. 2935–2941, 2009. DOI: [10.1016/j.eurpolymj.2009.06.011](https://doi.org/10.1016/j.eurpolymj.2009.06.011).
- [263] G. Zhang and C. Wu, “The water/methanol complexation induced reentrant coil-to-globule-to-coil transition of individual homopolymer chains in extremely dilute solution”, *Journal of the American Chemical Society*, vol. 123, no. 7, pp. 1376–1380, 2001. DOI: [10.1021/ja003889s](https://doi.org/10.1021/ja003889s).
- [264] A. Laschewsky and I. Zerbe, “Polymerizable and polymeric zwitterionic surfactants: 1. synthesis and bulk properties”, *Polymer*, no. 32, pp. 2070–2080, 1991. DOI: [10.1016/0032-3861\(91\)90175-I](https://doi.org/10.1016/0032-3861(91)90175-I).
- [265] T. Sato, T. Miyoshi, and M. Seno, “Kinetic study on the radical polymerization of 2-methacryloyloxyethyl phosphorylcholine”, *J. Polym. Sci. A Polym. Chem.*, no. 38, pp. 509–515, 2000. DOI: [10.1002/\(SICI\)1099-0518\(20000201\)38:3<509::AID-POLA17>3.0.CO;2-M](https://doi.org/10.1002/(SICI)1099-0518(20000201)38:3<509::AID-POLA17>3.0.CO;2-M).
- [266] T. E. de Oliveira, P. A. Netz, D. Mukherji, and K. Kremer, “Why does high pressure destroy co-non-solvency of PNIPAm in aqueous methanol?”, *Soft Matter*, vol. 11, no. 44, pp. 8599–8604, 2015. DOI: [10.1039/c5sm01772f](https://doi.org/10.1039/c5sm01772f).
- [267] K. Kyriakos, M. Philipp, L. Silvi, W. Lohstroh, W. Petry, P. Müller-Buschbaum, and C. M. Papadakis, “Solvent dynamics in solutions of PNIPAM in water/methanol mixtures—a quasi-elastic neutron scattering study”, *J. Phys. Chem. B*, vol. 120, no. 20, pp. 4679–4688, 2016. DOI: [10.1021/acs.jpcc.6b01200](https://doi.org/10.1021/acs.jpcc.6b01200).
- [268] J. Dybal, M. Trchová, and P. Schmidt, “The role of water in structural changes of poly(*N*-isopropylacrylamide) and Poly(*N*-isopropylmethacrylamide) Studied by FTIR, Raman spectroscopy and quantum chemical calculations”, *Vib. Spectrosc.*, vol. 51, no. 1, pp. 44–51, 2009. DOI: [10.1016/j.vibspec.2008.10.003](https://doi.org/10.1016/j.vibspec.2008.10.003).

- [269] S. Sbeih, P. S. Mohanty, M. R. Morrow, and A. Yethiraj, “Structural parameters of soft pnipam microgel particles as a function of crosslink density”, *Journal of colloid and interface science*, vol. 552, pp. 781–793, 2019. DOI: [10.1016/j.jcis.2019.05.047](https://doi.org/10.1016/j.jcis.2019.05.047).
- [270] M. Cors, L. Wiehemeier, J. Oberdisse, and T. Hellweg, “Deuteration-induced volume phase transition temperature shift of pnipmam microgels”, *Polymers*, vol. 11, no. 4, 2019. DOI: [10.3390/polym11040620](https://doi.org/10.3390/polym11040620).
- [271] J. Pantle, “Role of molecular interactions for stimuli-responsive polymers of potential use in soft robotics”, *Bachelor thesis. München: Technische Universität München, Fakultät für Physik*, 2018.
- [272] Y. Maeda, H. Mochiduki, and I. Ikeda, “Hydration changes during thermosensitive association of a block copolymer consisting of lcst and ucst blocks”, *Macromolecular Rapid Communications*, vol. 25, no. 14, pp. 1330–1334, 2004. DOI: [10.1002/marc.200400062](https://doi.org/10.1002/marc.200400062).
- [273] V. Hildebrand, A. Laschewsky, and E. Wischerhoff, “Modulating the solubility of zwitterionic poly((3-methacrylamidopropyl)ammonioalkane sulfonate)s in water and aqueous salt solutions via the spacer group separating the cationic and the anionic moieties”, *Polym. Chem.*, vol. 7, no. 3, pp. 731–740, 2016. DOI: [10.1039/C5PY01642H](https://doi.org/10.1039/C5PY01642H).
- [274] J. Bandekar and S. Krimm, “Vibrational analysis of peptides, polypeptides, and proteins”, *Int. J. Pept. Protein Res.*, vol. 26, pp. 407–415, 2007.
- [275] N. Aldosari, “Smart nano-sensors made of stimuli-responsive polymers in thin films”, *Master thesis. München: Technische Universität München, Fakultät für Physik*, 2019.
- [276] J. E. Stumpel, D. J. Broer, and A. P. H. J. Schenning, “Stimuli-responsive photonic polymer coatings”, *Chem. Commun.*, vol. 50, no. 100, pp. 15 839–15 848, 2014. DOI: [10.1039/c4cc05072j](https://doi.org/10.1039/c4cc05072j).
- [277] W. Chen, Y. Ma, J. Pan, Z. Meng, G. Pan, and B. Sellergren, “Molecularly imprinted polymers with stimuli-responsive affinity: Progress and perspectives”, *Polymers*, vol. 7, no. 9, pp. 1689–1715, 2015. DOI: [10.3390/polym7091478](https://doi.org/10.3390/polym7091478).
- [278] J.-P. Couturier, M. Sütterlin, A. Laschewsky, C. Hettrich, and E. Wischerhoff, “Responsive inverse opal hydrogels for the sensing of macromolecules”, *Angew. Chem., Int. Ed.*, vol. 54, no. 22, pp. 6641–6644, 2015. DOI: [10.1002/anie.201500674](https://doi.org/10.1002/anie.201500674).

- [279] J. Shang, X. Le, J. Zhang, T. Chen, and P. Theato, “Trends in polymeric shape memory hydrogels and hydrogel actuators”, *Polym. Chem.*, vol. 10, no. 9, pp. 1036–1055, 2019. DOI: [10.1039/C8PY01286E](https://doi.org/10.1039/C8PY01286E).
- [280] D. Kaneko, J. P. Gong, and Y. Osada, “Polymer gels as soft and wet chemomechanical systems—an approach to artificial muscles”, *J. Mater. Chem.*, vol. 12, no. 8, pp. 2169–2177, 2002. DOI: [10.1039/B109981G](https://doi.org/10.1039/B109981G).
- [281] Z. Lei, Q. Wang, and P. Wu, “A multifunctional skin-like sensor based on a 3d printed thermo-responsive hydrogel”, *Materials Horizons*, vol. 4, no. 4, pp. 694–700, 2017. DOI: [10.1039/C7MH00262A](https://doi.org/10.1039/C7MH00262A).
- [282] W. P. Kalisvaart, H. Fritzsche, and W. Mérida, “Water uptake and swelling hysteresis in a nafion thin film measured with neutron reflectometry”, *Langmuir*, vol. 31, no. 19, pp. 5416–5422, 2015. DOI: [10.1021/acs.langmuir.5b00764](https://doi.org/10.1021/acs.langmuir.5b00764).
- [283] K. E. Secrist and A. J. Nolte, “Humidity swelling/deswelling hysteresis in a polyelectrolyte multilayer film”, *Macromolecules*, vol. 44, no. 8, pp. 2859–2865, 2011. DOI: [10.1021/ma101983s](https://doi.org/10.1021/ma101983s).
- [284] H. Cheng, L. Shen, and C. Wu, “LLS and FTIR studies on the hysteresis in association and dissociation of poly(*N*-isopropylacrylamide) Chains in Water”, *Macromolecules*, vol. 39, no. 6, pp. 2325–2329, 2006. DOI: [10.1021/ma052561m](https://doi.org/10.1021/ma052561m).
- [285] L. P. Kreuzer, T. Widmann, C. Geiger, P. Wang, A. Vagias, J. E. Heger, M. Haese, V. Hildebrand, A. Laschewsky, C. M. Papadakis, and P. Müller-Buschbaum, “Salt-dependent phase transition behavior of doubly thermoresponsive poly(sulfobetaine)-based diblock copolymer thin films”, *Langmuir*, vol. 37, no. 30, pp. 9179–9191, 2021. DOI: [10.1021/acs.langmuir.1c01342](https://doi.org/10.1021/acs.langmuir.1c01342).
- [286] P. Köberle and A. Laschewsky, “Hydrophobically modified zwitterionic polymers: Synthesis, bulk properties, and miscibility with inorganic salts”, *Macromolecules*, vol. 27, pp. 2165–2173, 1994. DOI: [10.1021/ma00086a028](https://doi.org/10.1021/ma00086a028).

List of publications

Publications related to the dissertation

- L. P. Kreuzer, T. Widmann, N. Hohn, K. Wang, L. Bießmann, L. Peis, J.-F. Moulin, V. Hildebrand, A. Laschewsky, C. M. Papadakis, P. Müller-Buschbaum, "Swelling and exchange behavior of poly(sulfobetaine)-based block copolymer thin films", *Macromolecules* **52**, 9, 3486-3498 (2019)
(DOI: [10.1021/acs.macromol.9b00443](https://doi.org/10.1021/acs.macromol.9b00443))
- L. P. Kreuzer, T. Widmann, L. Bießmann, N. Hohn, J. Pantle, R. Märkl, J.-F. Moulin, V. Hildebrand, A. Laschewsky, C. M. Papadakis, P. Müller-Buschbaum, "Phase transition kinetics of doubly thermoresponsive poly(sulfobetaine)-based diblock copolymer thin films", *Macromolecules* **53**, 8, 2841-2855 (2020)
(DOI: [10.1021/acs.macromol.0c00046](https://doi.org/10.1021/acs.macromol.0c00046))
- L. P. Kreuzer, T. Widmann, N. Aldosari, L. Bießmann, G. Mangiapia, V. Hildebrand, A. Laschewsky, C. M. Papadakis, P. Müller-Buschbaum, "Cyclic water storage behavior of doubly thermoresponsive poly(sulfobetaine)-based diblock copolymer thin films", *Macromolecules* **53**, 20, 9108–9121 (2020)
(DOI: [10.1021/acs.macromol.0c01335](https://doi.org/10.1021/acs.macromol.0c01335))
- L. P. Kreuzer, C. Lindemeier, C. Geiger, T. Widmann, V. Hildebrand, A. Laschewsky, C. M. Papadakis, P. Müller-Buschbaum, "Poly(sulfobetaine) versus poly(*N*-isopropyl methacrylamide): Co-nonsolvency-type behavior of thin films in a water/methanol vapor atmosphere", *Macromolecules* **54**, 3, 1548–1556 (2021)
(DOI: [10.1021/acs.macromol.0c02281](https://doi.org/10.1021/acs.macromol.0c02281))
- L. P. Kreuzer, T. Widmann, C. Geiger, P. Wang, A. Vagias, J. E. Heger, M. Haese, V. Hildebrand, A. Laschewsky, C. M. Papadakis, P. Müller-Buschbaum, "Salt-dependent phase transition behavior of doubly thermo-responsive poly(sulfobetaine)-based diblock copolymer thin films", *Langmuir* **37**, 30, 9179–9191 (2021)
(DOI: [10.1021/acs.langmuir.1c01342](https://doi.org/10.1021/acs.langmuir.1c01342))

- L. P. Kreuzer, C. Geiger, T. Widmann, P. Wang, R. Cubitt, V. Hildebrand, A. Laschewsky, C. M. Papadakis, P. Müller-Buschbaum, "Solvation behavior of poly (sulfobetaine)-based diblock copolymer thin films in water/methanol vapor atmosphere", *Macromolecules* **54**, 15, 7147–7159 (2021)

(DOI: [10.1021/acs.macromol.1c01179](https://doi.org/10.1021/acs.macromol.1c01179))

Further publications

- L. P. Kreuzer, M. J. Männel, J. Schubert, R. P. M. Höller, M. Chanana "Enzymatic catalysis at nanoscale: Enzyme-coated nanoparticles as colloidal biocatalyst for polymerization reactions", *ACS Omega* **2**, 7305-7312 (2017)

(DOI: [10.1021/acsomega.7b00700](https://doi.org/10.1021/acsomega.7b00700))

- M. J. Männel, L. P. Kreuzer, C. Goldhahn, J. Schubert, M. J. Hartl, M. Chanana "Catalytically active protein coatings: Toward enzymatic cascade reactions at the intercolloidal level", *ACS Catalysis* **7**, 1664-1672 (2017)

(DOI: [10.1021/acscatal.6b03072](https://doi.org/10.1021/acscatal.6b03072))

- L. Bießmann, L. P. Kreuzer, T. Widmann, N. Hohn, J.-F. Moulin, P. Müller-Buschbaum "Monitoring the swelling behavior of PEDOT:PSS electrodes under high humidity", *ACS Appl. Mater. Interfaces* **10.11**, 9865-9872 (2018)

(DOI: [10.1021/acsami.8b00446](https://doi.org/10.1021/acsami.8b00446))

- B.-J. Niebuur, J. Puchmayer, C. Herold, L. P. Kreuzer, V. Hildebrand, P. Müller-Buschbaum, A. Laschewsky C. M. Papadakis "Polysulfobetaines in aqueous solution and thin film geometry", *Materials* **11**, 850 (2018) **10.11**, 9865-9872 (2018)

(DOI: [10.3390/ma11050850](https://doi.org/10.3390/ma11050850))

- K. Wang, S. Xia, W. Cao, N. Hohn, S. Grott, L. P. Kreuzer, M. Schwartzkopf, S. V. Roth, P. Müller-Buschbaum "Comparison of UV-irradiation and sintering on mesoporous sponge-like ZnO films prepared from PS-*b*-P4VP templated sol-gel synthesis", *ACS Appl. Nano Mater.* **1.12**, 7139-7148 (2018)

(DOI: [10.1021/acsanm.8b02039](https://doi.org/10.1021/acsanm.8b02039))

- K. Wang, N. Hohn, L. P. Kreuzer, T. Widmann, M. Haese, J.-F. Moulin, P. Müller-Buschbaum "Morphology tuning of ZnO/P3HT/P3HT-*b*-PEO hybrid films deposited via spray or spin coating", *ACS Appl. Mater. Interfaces* **11.11**, 10998-11005 (2019)

(DOI: [10.1021/acsami.9b00599](https://doi.org/10.1021/acsami.9b00599))

- W. Chen, J. Zhong, J. Li, N. Saxena, L. P. Kreuzer, H. Liu, L. Song, B. Su, D. Yang, K. Wang, J. Schlipf, V. Körstgens, T. He, K. Wang, P. Müller-Buschbaum "Structure and charge carrier dynamics in colloidal PbS quantum dot solids", *J. Phys. Chem. Lett.* **10.9**, 2058-2065 (2019)

(DOI: [10.1021/acs.jpcllett.9b00869](https://doi.org/10.1021/acs.jpcllett.9b00869))

- C. J. Brett, N. Mittal, W. Ohm, M. Gensch, L. P. Kreuzer, V. Körstgens, M. Månsson, H. Frielinghaus, P. Müller-Buschbaum, L. D. Söderberg, S. V. Roth "Water-induced structural rearrangements on the nanoscale in ultrathin nanocellulose films", *Macromolecules* **52**, 4721-4728 (2019)

(DOI: [10.1021/acs.macromol.9b00531](https://doi.org/10.1021/acs.macromol.9b00531))

- M. Gensch, M. Schwartzkopf, W. Ohm, C. J. Brett, P. Pandit, S. K. Vayalil, L. Bießmann, L. P. Kreuzer, J. Drewes, O. Polonskyi, T. Strunskus, F. Faupel, A. Stierle, P. Müller-Buschbaum, S. V. Roth "Correlating nanostructure, optical and electronic properties of nanogranular silver layers during polymer-template assisted sputter deposition", *ACS Appl. Mater. Interfaces* **11**32, 29416-29426 (2019)

(DOI: [10.1021/acsami.9b08594](https://doi.org/10.1021/acsami.9b08594))

- T. Widmann, L. P. Kreuzer, N. Hohn, L. Bießmann, K. Wang, S. Rinner, J.-F. Moulin, A. J. Schmid, Y. Hannappel, O. Wrede, M. Kühnhammer, T. Hellweg, R. von Klitzing, P. Müller-Buschbaum, S. V. Roth "Hydration and solvent exchange induced swelling and deswelling of homogeneous poly(*N*-isopropylacrylamide) microgel thin films", *Langmuir* **35**49, 16341-16352 (2019)

(DOI: [10.1021/acs.langmuir.9b03104](https://doi.org/10.1021/acs.langmuir.9b03104))

- W. Cao, S. Xia, Y. Jiang, M. Appold, M. Opel, M. Plank, R. Schaffrinna, L. P. Kreuzer, S. Yin, M. Gallei, M. Schwartzkopf, S. V. Roth, P. Müller-Buschbaum, S. V. Roth "Self-assembly of large magnetic nanoparticles in ultrahigh molecular weight linear diblock copolymer films", *ACS Appl. Mater. Interfaces* **12**6, 7557-7564 (2020)

(DOI: [10.1021/acsami.9b20905](https://doi.org/10.1021/acsami.9b20905))

- K. Sparnacci, R. Chiarcos, V. Gianotti, M. Laus, T. J. Giammaria, M. Perego, G. Munaò, G. Milano, A. De Nicola, M. Haese, L. P. Kreuzer, T. Widmann, P. Müller-Buschbaum "Effect of trapped solvent on the interface between PS-*b*-PMMA thin films and P(*S-r*-MMA) brush layers", *ACS Appl. Mater. Interfaces* **12**6, 7777-7787 (2020)

(DOI: [10.1021/acsami.9b20801](https://doi.org/10.1021/acsami.9b20801))

- R. S. Märkl, N. Hohn, E. Hupf, L. Bießmann, V. Körstgens, L. P. Kreuzer, G. Mangiapia, M. Pomm, A. Kriele, E. Rivard, P. Müller-Buschbaum "Comparing the backfilling of mesoporous titania thin films with hole conductors of different sizes sharing the same mass density", *I. U. Cr. J.* **7**, 2, 268-275 (2020)

(DOI: [10.1107/S2052252520000913](https://doi.org/10.1107/S2052252520000913))

- N. Hohn, X. Wang, M. A. Giebel, S. Yin, D. Müller, A. Hetzenecker, L. Bießmann, L. P. Kreuzer, G. E. Möhl, H. Yu, J. G. C. Veinot, T. F. Fässler, Y.-J. Cheng, P. Müller-Buschbaum "Mesoporous GeOx/Ge/C as highly reversible anode material with high specific capacity for Lithium ion batteries", *ACS Appl. Mater. Interfaces* **12** 41, 47002-47009 (2020)

(DOI: [10.1021/acsami.0c13560](https://doi.org/10.1021/acsami.0c13560))

- W. Chen, S. Lian, F. C. Löhner, S. J. Scharper, N. Li, W. Cao, L. P. Kreuzer, H. Liu, H. Tang, V. Körstgens, M. Schwartzkopf, K. Wang, X. W. Sun, S. V. Roth, P. Müller-Buschbaum "In situ grazing-incidence small-angle x-ray scattering observation of gold sputter deposition on a PbS quantum dot solid", *ACS Appl. Mater. Interfaces* **12** 41, 46942-46952 (2020)

(DOI: [10.1021/acsami.0c12732](https://doi.org/10.1021/acsami.0c12732))

- W. Chen, H. Tang, Y. Chen, J. E. Heger, N. Li, L. P. Kreuzer, Y. Xie, D. Li, C. Anthony, Z. Pikramenou, K. W. Ng, X. W. Sun, K. Wang, P. Müller-Buschbaum "Spray-deposited PbS colloidal quantum dot solid for near-infrared photodetectors", *Nano Energy* **78**, 105254 (2020)

(DOI: [10.1016/j.nanoen.2020.105254](https://doi.org/10.1016/j.nanoen.2020.105254))

- T. Widmann, L. P. Kreuzer, G. Mangiapia, M. Haese, H. Frielinghaus, P. Müller-Buschbaum "3D printed spherical environmental chamber for neutron reflectometry and grazing-incidence small-angle neutron scattering experiments", *Rev. Sci. Instrum.* **91**, 113903 (2020)

(DOI: [10.1063/5.0012652](https://doi.org/10.1063/5.0012652))

- Y. Zou, R. Guo, A. Buyruk, W. Chen, T. Xiao, S. Yin, X. Jiang, L. P. Kreuzer, C. Mu, T. Ameri, M. Schwartzkopf, S. V. Roth, P. Müller-Buschbaum "Sodium dodecylbenzene sulfonate interface modification of methylammonium lead iodide for surface passivation of perovskite solar cells", *ACS Appl. Mater. Interfaces* **12**, 47, 52643–52651 (2020)

(DOI: [10.1021/acsami.0c14732](https://doi.org/10.1021/acsami.0c14732))

- W. Cao, S. Yin, M. Plank, A. P. Chumakov, M. Opel, W. Chen, L. P. Kreuzer, J. E. Heger, M. Gallei, C. J. Brett, M. Schwartzkopf, A. A. Eliseev, E. O. Anokhin, L. A. Trusov, S. V. Roth, P. Müller-Buschbaum "Spray-deposited anisotropic ferromagnetic hybrid polymer films of PS-*b*-PMMA and strontium hexaferrite magnetic nanoplatelets", *ACS Appl. Mater. Interfaces* **13**, 1, 1592–1602 (2020)

(DOI: [10.1021/acsami.0c19595](https://doi.org/10.1021/acsami.0c19595))

- X. Zhang, L. P. Kreuzer, D. M. Schwaiger, M. Lu, Z. Mao, R. Cubitt, P. Müller-Buschbaum, Q. Zhong "Abnormal fast dehydration and rehydration of light- and thermo- dual-responsive copolymer films triggered by UV radiation", *Soft Matter* **17**, 2603-2613 (2021)

(DOI: [10.1039/D0SM02007A](https://doi.org/10.1039/D0SM02007A))

- C. Geiger, J. Reitenbach, L. P. Kreuzer, T. Widmann, P. Wang, R. Cubitt, C. Henschel, A. Laschewsky, C. M. Papadakis, P. Müller-Buschbaum "PMMA-*b*-PNIPAM thin films display cononsolvency-driven response in mixed water/methanol vapors", *Macromolecules* **54**, 3517-3530 (2021)

(DOI: [10.1021/acs.macromol.1c00021](https://doi.org/10.1021/acs.macromol.1c00021))

- M. Gensch, M. Schwarzkopf, C. Brett, S. Schaper, L. P. Kreuzer, N. Li, W. Chen, L. Suhze, J. Drewes, O. Polonskyi, T. Strunskus, F. Faupel, P. Müller-Buschbaum, S. V. Roth "Selective silver nanocluster metallization on conjugated diblock copolymer templates for sensing and photovoltaic applications", *ACS Appl. Nano Mater.* **4**, 4245–4255 (2021)

(DOI: [10.1021/acsanm.1c00829](https://doi.org/10.1021/acsanm.1c00829))

- T. Widmann, L. P. Kreuzer, M. Kühnhammer, A. J. Schmid, L. Wiehemeier, S. Jaksch, H. Frielinghaus, O. Löhmann, H. Schneider, A. Hiess, R. von Klitzing, T. Hellweg, P. Müller-Buschbaum "Flexible sample environment for the investigation of soft matter at the European Spallation Source: Part II — The GISANS setup", *Appl. Sci.* **11**, 4036 (2021)

(DOI: [10.3390/app11094036](https://doi.org/10.3390/app11094036))

- A. J. Schmid, L. Wiehemeier, S. Jaksch, H. Schneider, A. Hiess, T. Bögershaus, T. Widmann, J. Reitenbach, L. P. Kreuzer, M. Kühnhammer, O. Löhmann, G. Brandl, H. Frielinghaus, P. Müller-Buschbaum, R. von Klitzing, T. Hellweg "Flexible sample environments for the investigation of soft matter at the European Spallation Source: Part I — The in situ SANS/DLS setup", *Appl. Sci.* **11**, 4089 (2021)

(DOI: [10.3390/app11094089](https://doi.org/10.3390/app11094089))

- W. Chen, R. Guo, H. Tang, K. Wienhold, N. Li, Z. Jiang, J. Tang, X. Jiang, L. Haochen, M. Schwartzkopf, X. W. Sun, S. V. Roth, K. Wang, B. Xu, P. Müller-Buschbaum "Operando structure degradation study of PbS quantum dot solar cells", *Energy Environ. Sci.*, 2021, advanced article

(DOI: [10.1039/D1EE00832C](https://doi.org/10.1039/D1EE00832C))

- C. Geiger, J. Reitenbach, C. Henschel, L. P. Kreuzer, T. Widmann, P. Wang, G. Mangiapia, J.-F. Moulin, C. M. Papadakis, A. Laschewsky, P. Müller-Buschbaum "Ternary nanoswitches realized with multiresponsive PMMA-*b*-PNIPMAM films in mixed water/acetone vapor atmospheres", *Adv. Eng. Mater.*, 2100191 (2021)

(DOI: [10.1002/adem.202100191](https://doi.org/10.1002/adem.202100191))

- C. J. Brett, O. K. Forslund, E. Nocerino, L. P. Kreuzer, T. Widmann, L. Porcar, M. L. Yamada, N. Matsubara, M. Månsson, P. Müller-Buschbaum, L. D. Söderberg, S. V. Roth "Humidity-induced nanoscale restructuring in PEDOT:PSS and cellulose nanofibrils reinforced biobased organic electronics", *Adv. Electron. Mater.*, 2100137 (2021)

(DOI: [10.1002/aelm.202100137](https://doi.org/10.1002/aelm.202100137))

- M. Kühnhammer, T. Widmann, L. P. Kreuzer, A. J. Schmid, L. Wiehemeier, O. Löhmann, H. Frielinghaus, S. Jaksch, T. Bögershaus, P. Barron, H. Schneider, A. Hiess, P. Müller-Buschbaum, T. Hellweg, R. von Klitzing "Flexible sample environments for the investigation of soft matter at the European Spallation Source: Part III – The macroscopic foam cell", *Appl. Sci.* **11**, 5116 (2021)

(DOI: [10.3390/app11115116](https://doi.org/10.3390/app11115116))

- A. Vagias, A. Papagiannopoulos, L. P. Kreuzer, D. Giaouzi, S. Busch, S. Pispas, P. Müller-Buschbaum "Effects of polymer block length asymmetry and temperature on the nanoscale morphology of thermoresponsive double hydrophilic block copolymers in aqueous solutions", *Macromolecules* **54**, 7298-7313 (2021)

(DOI: [10.1021/acs.macromol.1c01005](https://doi.org/10.1021/acs.macromol.1c01005))

Scientific reports

- L. P. Kreuzer, T. Widmann, V. Hildebrand, A. Laschewsky, J.-F. Moulin, M. Haese, P. Müller-Buschbaum, "H₂O-D₂O exchange kinetics of thermoresponsive block copolymer films followed with in-situ time-of-flight neutron reflectometry", *Lehrstuhl für Funktionelle Materialien, Annual Report*, 2016.
- L. P. Kreuzer, T. Widmann, N. Hohn, K. Wang, J.-F. Moulin, Hildebrand, A. Laschewsky, C. M. Papadakis, P. Müller-Buschbaum, "Water swelling and exchange kinetics in multi-stimuli responsive polymer thin films followed with in-situ time-of-flight neutron reflectometry", *Lehrstuhl für Funktionelle Materialien, Annual Report*, 2017.
- L. P. Kreuzer, T. Widmann, L. Bießmann, J.-F. Moulin, V. Hildebrand, A. Laschewsky, C. M. Papadakis, P. Müller-Buschbaum, "In-situ investigation of phase transition kinetics in stimuli-responsive block copolymer thin films", *Lehrstuhl für Funktionelle Materialien, Annual Report*, 2018.
- L. P. Kreuzer, T. Widmann, L. Bießmann, N. Hohn, J. Pantle, J.-F. Moulin, V. Hildebrand, A. Laschewsky, C. M. Papadakis, P. Müller-Buschbaum, "Phase transition kinetics of doubly thermo-responsive poly(sulfobetaine)-based diblock copolymer thin films", *Lehrstuhl für Funktionelle Materialien, Annual Report*, 2019.
- L. P. Kreuzer, T. Widmann, L. Bießmann, N. Hohn, J. Pantle, J.-F. Moulin, V. Hildebrand, A. Laschewsky, C. M. Papadakis, P. Müller-Buschbaum, "Swelling and exchange behaviour of poly(sulfobetaine)-based block copolymer thin films", *Joint Annual Report 2019 of the MLZ and FRM II*, 2019.
- L. P. Kreuzer, V. Hildebrand, A. Laschewsky, C. M. Papadakis, P. Müller-Buschbaum, "Cyclic swelling and drying of doubly thermoresponsive poly(sulfobetaine)- based diblock copolymer thin films", *Lehrstuhl für Funktionelle Materialien, Annual Report*, 2020.

Scientific talks

- L. P. Kreuzer, T. Widmann, and P. Müller-Buschbaum
FlexiProb sample environment for neutron scattering experiments on polymer thin films
FlexiProb Cooperation Meeting, Lund, 29 May 2017

- L. P. Kreuzer, T. Widmann, N. Hohn, K. Wang, J. F. Moulin, A. Laschewsky, C. M. Papadakis, and P. Müller-Buschbaum
In-situ neutron reflectivity investigations of D₂O-H₂O exchange kinetics in thermo-responsive PNIPAM based block copolymers
3rd Internal Biennial Science Meeting of the MLZ, Grainau, 19 – 22 Jun 2017
- L. P. Kreuzer, T. Widmann, N. Hohn, K. Wang, J. F. Moulin, A. Laschewsky, C. M. Papadakis, and P. Müller-Buschbaum
In-situ ToF NR study of the swelling and exchange kinetics of multi-stimuli responsive PNIPAM-based block copolymers
JCNS Workshop 2017, Tutzing, 10 – 13 Oct 2017
- L. P. Kreuzer, T. Widmann, N. Hohn, K. Wang, J.-F. Moulin, V. Hildebrand, A. Laschewsky, C. M. Papadakis, and P. Müller-Buschbaum
Multi-stimuli responsive polymer films analyzed by in-situ neutron reflectometry
29. Edgar Lüscher Seminar, Klosters, Switzerland 3 – 9, Feb 2018
- L. P. Kreuzer, T. Widmann, N. Hohn, K. Wang, J.-F. Moulin, V. Hildebrand, A. Laschewsky, C. M. Papadakis, and P. Müller-Buschbaum
Water swelling and exchange kinetics of multi-stimuli responsive polymer thin films
DPG-Frühjahrstagung, Berlin, 11 – 16 Mar 2018
- L. P. Kreuzer, T. Widmann, N. Hohn, K. Wang, J.-F. Moulin, V. Hildebrand, A. Laschewsky, C. M. Papadakis, and P. Müller-Buschbaum
Water swelling and exchange kinetics in multi-stimuli responsive polymer thin films followed with in-situ time of flight neutron reflectometry
Macro 18 Conference, Cairns, Australia, 1 – 5 Jul 2018
- L. P. Kreuzer, F. Löhner, and T. Widmann
Fourier transform infrared spectroscopy
Polymer Physics Summer School, Obertauern, Austria, 12 – 15 Jun 2018
- L. P. Kreuzer, T. Widmann, V. Körstgens, and P. Müller-Buschbaum
Flexible sample environment for the investigation of soft matter for implementation at the ESS
Verbundprojekttreffen FlexiProb, Bielefeld, 10 Dez 2018
- L. P. Kreuzer, T. Widmann, L. Bießmann, N. Hohn, J. Pantle, R. Märkl, J.-F. Moulin, V. Hildebrand, A. Laschewsky, C. M. Papadakis, and P. Müller-Buschbaum
Phase transition kinetics in a doubly thermo-responsive block copolymer thin film
European Conference on Neutron Scattering, St. Petersburg, 30 June – 05 July 2019

- L. P. Kreuzer, T. Widmann, L. Bießmann, J.-F. Moulin, V. Hildebrand, A. Laschewsky, C. M. Papadakis, and P. Müller-Buschbaum
Potential use of thermo-responsive polymers as self-cooling window surface coatings
9th MSE Colloquium, Garching, 01 August 2019
- L. P. Kreuzer, T. Widmann, L. Bießmann, N. Hohn, J. Pantle, R. Märkl, J.-F. Moulin, V. Hildebrand, A. Laschewsky, C. M. Papadakis, and P. Müller-Buschbaum
Phase transition kinetics in a doubly thermo-responsive diblock copolymer thin film
MLZ User Meeting, Munich 10 December – 11 December 2019
- L. P. Kreuzer, T. Widmann, and P. Müller-Buschbaum
Flexible sample environment for the investigation of soft matter for implementation at the ESS
Verbundprojekttreffen Flexiprob Meeting, München, 13 December 2019
- L. P. Kreuzer, C. Lindemeir, C. Geiger, T. Widmann, P. Wang, R. Cubitt, V. Hildebrand, A. Laschewsky, C. M. Papadakis, and P. Müller-Buschbaum
Co-nonsolvency-type behavior of polymer thin films in mixed water/methanol vapor
ACS Spring Meeting - virtual conference, 13 April 2021

Conference poster presentations

- L. P. Kreuzer, T. Widmann, N. Hohn, K. Wang, J.-F. Moulin, V. Hildebrand, A. Laschewsky, C. M. Papadakis, P. Müller-Buschbaum
H₂O-D₂O exchange kinetics in PNIPAM based block copolymer films followed with in-situ neutron reflectivity
DPG-Frühjahrstagung, Dresden, 19 – 24 Mar 2017
- L. P. Kreuzer
Scattering on multi-stimuli responsive block copolymers
TUM Graduate School Kick-Off Meeting, Raitenhaslach, 8 – 10 May 2017
- L. P. Kreuzer, T. Widmann, N. Hohn, K. Wang, J.-F. Moulin, V. Hildebrand, A. Laschewsky, C. M. Papadakis, P. Müller-Buschbaum
Potential use of thermo-responsive polymers as smart windows
7th Colloquium of the Munich School of Engineering, Garching, 13 Jul 2017

- L. P. Kreuzer, T. Widmann, N. Hohn, K. Wang, J.-F. Moulin, V. Hildebrand, A. Laschewsky, C. M. Papadakis, P. Müller-Buschbaum
In-situ analysis of swelling and exchange kinetics in multi-stimuli responsive PNIPAM based block copolymers
Kolloid-Tagung "Multiresponsive systems", 9 – 11 Oct 2017
- L. P. Kreuzer, T. Widmann, N. Hohn, K. Wang, J.-F. Moulin, V. Hildebrand, A. Laschewsky, C. M. Papadakis, P. Müller-Buschbaum
Water swelling and exchange kinetics in multi-stimuli responsive PNIPAM-based block copolymer thin films
4th German SNI Conference, Garching, 17 – 19 Sep 2018
- L. P. Kreuzer, T. Widmann, N. Hohn, K. Wang, J.-F. Moulin, V. Hildebrand, A. Laschewsky, C. M. Papadakis, P. Müller-Buschbaum
Water swelling and exchange kinetics in multi-stimuli responsive PNIPAM-based block copolymer thin films
ILL & ESS European User Meeting, Grenoble, France, 10 – 12 Oct 2018
- L. P. Kreuzer, T. Widmann, L. Bießmann, N. Aldosari, G. Mangiapia, V. Hildebrand, A. Laschewsky, C. M. Papadakis, P. Müller-Buschbaum
Thermo-responsive polymers as self-cooling window surface coatings
3rd interdisciplinary Winter School 2019 „Food and Energy”, Raitenhaslach, 18 – 22 February 2019.
- L. P. Kreuzer, T. Widmann, L. Bießmann, N. Aldosari, G. Mangiapia, V. Hildebrand, A. Laschewsky, C. M. Papadakis, P. Müller-Buschbaum
Switchable thermo-responsive polymer coatings as self-cooling approach for buildings
10th Colloquium of the Munich School of Engineering, Garching, 31 Jul 2020.
- L. P. Kreuzer, T. Widmann, L. Bießmann, N. Hohn, J. Pantle, R. Märkl, J.-F. Moulin, V. Hildebrand, A. Laschewsky, C. M. Papadakis, P. Müller-Buschbaum
Phase transition kinetics in a doubly thermo-responsive poly(sulfobetaine)-based block copolymer thin film
MLZ User Meeting & German Neutron Scattering Conference 2020, Munich, 08 – 10 Dec 2020.

- L. P. Kreuzer, C. Lindemeir, C. Geiger, T. Widmann, P. Wang, R. Cubitt, V. Hildebrand, A. Laschewsky, C. M. Papadakis, and P. Müller-Buschbaum
Co-nonsolvency-type behavior in poly(sulfobetaine) and poly(N-isopropylmethacrylamide) thin films
Osmolyte and Cosolvent Effects in Stimuli-Responsive Soft Matter Systems - virtual workshop, 25 – 26 Feb 2021
- L. P. Kreuzer, C. Lindemeir, C. Geiger, T. Widmann, R. Cubitt, V. Hildebrand, A. Laschewsky, C. M. Papadakis, and P. Müller-Buschbaum
Co-nonsolvency-type behavior of a poly(sulfobetaine) and a poly(N-isopropylmethacrylamide) thin film in water/methanol vapor
DPG-Frühjahrstagung, virtual conference, 22 – 24 Mar 2021

Acknowledgments

When I think back to my first day at E13, to my application talk, and my first meeting with the group, I didn't know what was ahead of me. If I would have known, I would have been the happiest person on earth. Now, 4.5 years later, I am this happiest person and full of gratitude. This section is dedicated to all the people, who contributed to this work and who accompanied me during the last years and beyond. It takes a village to grow and you are my village. Thank you!

First, I would like to thank Prof. Dr. Peter Müller-Buschbaum for giving me the opportunity to work on a PhD project at his chair. Being a PhD student at E13 comes with a lot of privileges, and I am foremost grateful for the freedom to develop and realize own scientific ideas and approaches. Within this freedom, I had the opportunity to work in national and international collaborations, I was able to perform experiments at various neutron facilities, I enjoyed the privilege to supervise and mentor bachelor and master students, and I was given the possibility to present my results on many conferences, workshops, summer and winter schools. During my PhD I could always count on Peter's support, and in consequence, I was not only able to grow as a scientist, but also as a colleague, collaboration partner, supervisor, and friend. I was able to reflect on my professional and personal strengths as well as on my weaknesses, because of the supportive environment he created at E13. Eventually, I even retrieved a long-gone excitement and enthusiasm for the academic system and how it could look like in the future. For this, I am truly grateful! Thank you, Peter!

I am just as grateful to have Prof. Dr. Christine M. Papadakis as my mentor. In the truest sense of the word, she guided me through the, often confusing, field of polymer physics, gave me immensely helpful feedback during data analysis, and assisted me (A LOT!) during scientific writing. Thank you, Christine!

This thesis is the product of many collaborations, in particular with Prof. Dr. André Laschewsky and Dr. Viet Hildebrand from the University of Potsdam. I have to thank them for many things, foremost for the synthesis and characterization of the polymers I was able to investigate, but also for fruitful discussions about polymer chemistry and physics, the scientific writing assistance, as well as the refreshing off-topic chats about German history and humor.

I also want to thank the whole FlexiProb community. Thank you Prof. Dr. Regine von Klitzing, Matthias Kühnhammer, Dr. Olaf Soltwedel, and Dr. Oliver Löhmann from the University of Darmstadt, Prof. Dr. Thomas Hellweg, Dr. Andreas Schmid, Dr. Yvonne Hannappel, and Dr. Lars Wiehemeier from the University of Bielefeld, Harald Schneider, Dr. Arno Hiess, Dr. Judith Houston, Enrico Rojas, and Torsten Bögershausen from the European Spallation Source in Lund, Sweden, Dr. Sebastian Jaksch and Dr. Henrich Frielinghaus from the Forschungszentrum Jülich, and my E13 colleagues Tobias Widmann and Julija Reitenbach. The FlexiProb project started, when I started my PhD and being part of the team from the very beginning was enormously instructive. I learned how to build-up and foster a collaboration, how to organize collaboration meetings, and how to communicate between the individual partners. The common project goal was extremely ambitious, and I think we all did a great job there. The results speak for themselves. Thank you for this experience and all the great memories, in particular the various tours over the construction site of the ESS.

Another collaboration that was extremely successful (and fun!) was with Prof. Dr. Stephan V. Roth, Dr. Calvin Brett, Marc Gensch, and Dr. Martin Månsson and many more from KTH, Stockholm, Sweden. It never ceases to amaze me, how caring, supportive, and productive our beamtimes were. I learned a lot from you, and in stressful moments during my PhD, I often thought back and asked myself, how you guys would have handled this situation. It always helped!

I also want to thank Prof. Dr. Alfons Schulte for his constant support and help with FTIR measurements and analysis. I profited a lot from his experimental expertise and his deep knowledge about polymer physics.

Besides these long term collaborations, I also enjoyed very much the smaller joint projects and beamtimes. In particular, I want to thank Erik Bergendal from KTH, Stockholm for the joint beamtime at the FIGARO instrument at ILL. Special thanks also to our local contact Dr. Philipp Gutfreund, who patiently answered all our questions about neutron scattering (there were a lot! and even more). I also want to thank Dr. Qi Zhong from University of Hangzhou, with whom I shared my first ILL beamtime, Dr. Hezhen Xie from the University of Alberta for a joint beamtime at RefSANS (FRM II, Garching, Germany) and the introduction to the field of batteries, and Tomasso Giammaria, for a very relaxed beamtime at RefSANS.

From all my collaborators, I want to especially thank Prof. Dr. Stephan V. Roth, who never failed to inspire me, be it scientifically or personally. Thank you for your trust, your advice, and your support! I am really looking forward to future collaborations, conferences, and beamtimes with you! Thank you, Stephan!

A special thanks goes to the people operating the RefSANS instrument at the MLZ

neutron source. Thank you Dr. Jean-François Moulin, Martin Haese-Seiler, Dr. Gaetano Mangiapia, and Dr. Sebastian Busch. The pro-active support, we experienced throughout every single beamtimes was extraordinary! Also, I want to thank Matthias Pomm, who invested hour after hour, for meeting all of our (partly very spontaneously) experimental requirements. Thank you as well for the 'open instrument' tour, which provided a deep insight in neutron scattering from an instrumental perspective. I am convinced, the friendly and relaxed atmosphere at RefSANS significantly contributed to the awesome results we obtained.

Also, I want to thank the local contacts of the various neutron instruments, where I was able to perform experiments. No matter how busy you were, you made sure, we felt comfortably, no question was left unanswered, and the experiment was going as good as it could be. I experienced this neutron community as an incredibly supportive group of people. Thank you Dr. Robert Cubitt, Dr. Thomas Saerbeck, Dr. Samantha Micciulla, Dr. Philipp Gutfreund, Dr. Armando Maestro, Dr. Lionel Porcar, Dr. Sarah Rogers, Dr. Andrew Church, Dr. Henrich Frielinghaus, Dr. Sebastian Jaksch, and Dr. Alexandros Koutsoumpas.

Also, I want to express my gratitude to the Hydrogel Group. I always enjoyed our weekly/monthly meetings, our joint beamtimes, and the great atmosphere between all of us. Thank you, Christina Geiger, Gintare Budryte, Julija Reitenbach, Tobias Widmann, Julian Heger, Peixi Wang, Apostolos Vagias, and all the other BA and MA students who, over the years, were part of the Hydrogel Group. Thank you, swellas!

This work would not have been possible without the help of my students and I am very grateful to have had the opportunity to supervise you! Thank you Leander Peis, Johannes Pantle, and Christoph Lindenmeir, who did an amazing job during their bachelor theses. Also thank you Nawarah Aldosari for an outstanding master thesis. You all contributed to this work beyond words and I hope you learned as much from me as I learned from you. Being your advisor has really enriched me and I am very grateful, that you were part of this journey. All the best for your future, I am sure, we will meet again from time to time. I am already looking forward to this.

The Chair of Functional Materials, commonly known as E13 is something special. The very first day at the chair felt like home coming and throughout the last years, this feeling never changed. Thank you for everything Johnny Schlipf, Nitin Saxena, Lorenz Bießmann, Nuri Hohn, Volker Körstgens, Franzi Löhner, Marc Gensch, Simon Schaper, Lin Song, Bo Su, Senlin Xia, Ray Wang, Kun Wang, Dan Yang, Wei Chen, Wei Cao, Xinyu Jian, Nian Li, Shanshan Yin, and Ezzeldin Metwalli. Also a big thanks to the Herzig Group, Jenny Lebert, Stephan Pröller, Oliver Filonik, and Mihael Čorić, as well as to the Papadakis Group, Bart-Jan Niebuur, Florian Jung, Chia-Hsin Ko, Jia-Jhen Kang, Xiaohan Zhang,

and Anatoly Berezkin. Also a big thanks to all master students, in particular to Gilles E. H. K. Moehl, Markus Trunks, Adalbert Haussmann, Fabien Guelle, Andreas Hetzenecker, Christian Herold, Christoph Bilko, Raphael Märkl, Kiran Mathew John, Kaltrina Shehu, Gintare Budyte, and Oleg Shindelov.

Tobias Widmann and Sebastian Grott started their PhD journeys on the same day I started my journey and I could not have wished for better colleagues, partners in science, and friends. The innate resilience of Tobi and Sebi's given love for details never ceases to amaze and inspire me. You guys always put a smile on my face, no matter how stressed I was. I am very lucky to have you as my friends!

A special place in this section and in my heart is reserved for Shambavi Pratap. My dear Sana, you are a never-ending source of inspiration, kindness, love, and bullshit. You are amplifying and completing me in so many ways, and for that I cannot be grateful enough!

I also want to thank the 'new' generation of PhD colleagues. Just as I thought, I have figured everything out, you brought a breath of fresh air to things. And this was exactly what I needed! Thank you Lennart Reb, Anna-Lena Oechsle, Manuel Scheel, Dominik Schwaiger, Kerstin Wienhold, Roy Schaffrinna, Christian Weindl, and Peixi Wang! In particular, I want to thank Julian Heger and Christina Geiger, for their constant scientific input, their ability to think outside the box, their unconditional dependability, their great sense of humor, and for their friendship.

Among all the science, one easily might forget, there are some people, mostly in the background, who actually keep our chair running. Thank you Carola Kappauf and Marion Waletzki, for all the help and the support with the administrative and bureaucratic tasks. Placing orders, applying for traveling money, and handling reimbursement claims, regularly showed me my limits, and thanks to Carola and Marion, I survived this bureaucratic nightmare.

An equally big thank you, goes to Reinhold Funer and his colleagues from the workshop. You guys are the real MVPs of E13. I lost track, how many times you saved our beamtimes and experiments, by working an extra hour, and I am convinced, Reinhold had a huge impact on the quality of our work and scientific results. Thank you!

One of the greatest things about my time at E13 was the formation of the Polymer Music Band. I want to thank all the people, who were part of the band. Making music with you really cleared my head and was super fun! Thank you Johannes Schlipf, Jenny Lebert, Simon Schaper, Wei Chen, Regina Kluge, Gilles Möhl, Fabien Guelle, and Shambhavi Pratap. Eventually the Polymer Music Band evolved into Neutronic Nomads with a fixed line-up. This transition was even more fun. Thank you Christina Geiger, Chia-Hsin Ko,

Nitin Saxena, and Julian Heger, for countless rehearsals, jams, and gigs, lots of creativity, fun, love, and for an almost finished first album!

I also want to thank the academic Twitter community for their immediate, constructive, and overwhelming support. Being part of a most diverse group of young academics changed my perception and made me aware of things I wouldn't have thought of. Thank you for this! (follow me on Twitter [@neutronic_nomad](#)).

Finally and most importantly, I would like to thank my family for their unconditional support. Thank you Mama, after 30 years I still haven't learned all your lessons! Thank you Papa, becoming your friend is one of the things I enjoy the most. Thank you Julian, for being a constant source of energy and motivation for me. And at the very end, I would like to express my deepest gratitude to Connie, the person who understands and knows me best, the person who cares the most about me when I am down or stressed, the person who stays with me, and the person I love.

